IMPERIAL

Development of natural fibre yarn-reinforced cement composites under enforced carbonation conditions

Yixiu Zhuge

Supervisors:
Dr. Rupert J. Myers
Prof. Hong S. Wong

Submitted in part fulfilment of the requirements for the degree of Doctor of Philosophy

Centre for Infrastructure Materials
Department of Civil and Environmental Engineering
Imperial College London

January 2026

Abstract

Enforced carbonation can increase early-age strength and CO_2 uptake in cement-based materials, but its effectiveness is limited by restricted CO_2 transport into the interior. This thesis investigates whether placed natural fibre yarns can enhance CO_2 ingress, carbonation extent, and CO_2 uptake while maintaining acceptable mechanical performance.

A phenolphthalein-based image analysis method was developed to quantify heterogeneous carbonation at defined depths and linked to thermogravimetric measurements of CO_2 uptake. It was applied to single-yarn cement paste specimens containing different natural yarns, followed by mechanistic studies of jute yarns with controlled moisture states and surface treatments. The study was extended to multi-yarn paste and mortar systems containing yarn meshes, with compressive strength and sorptivity assessed under different post-curing regimes.

Under enforced carbonation (20 vol.% CO_2, 25 ± 0.5 °C, and 64 ± 2% RH), all natural yarns increased CO_2 uptake relative to fibre-free paste, with bast fibres producing the strongest effect. After seven days, hemp increased depth-averaged CO_2 uptake from 5.64 to 8.19 wt.% and enabled measurable uptake at 50 mm depth after one day. Carbonation was governed by moisture retention, pore connectivity, and interfacial transport. Pre-saturation increased carbonation, whereas epoxy sealing strongly reduced it. Across yarns and treatments, 24-hour water absorption was the strongest predictor of effective carbonation radius, typically 2–3 mm at 10 mm depth.

Bulk hydration was only marginally affected, confirming that enhanced carbonation arose mainly from yarn-assisted transport. Although increasing fibre content reduced compressive strength, a single-layer mesh with 5 mm spacing provided a practical balance. At mortar scale, saturated jute yarn meshes performed better than dispersed fibres at the same replacement level. Seven-day carbonation followed by air curing produced the

highest strength. Overall, placed natural fibre yarns can form controlled internal transport networks that enhance carbonation and CO_2 uptake, although their long-term durability requires further study.

Table of contents

Abstract III

Table of contents V

Declaration X

Publications arising from this thesis XI

Acknowledgement XII

List of Tables XIII

List of Figures XIV

Nomenclature XXI

Chapter 1 Introduction 1

1.1. Background 1
1.2. Aims and objectives 5
1.3. Thesis outline 6

Chapter 2 Literature review 8

2.1. Carbon capture, utilisation and storage and mineral carbonation 8
2.2. Carbonation of cement-based materials under enforced conditions 9
2.2.1. Carbonation mechanisms in cement-based materials 9
2.2.2. Enforced carbonation and governing parameters 11
2.2.3. Effect of carbonation on phase evolution and composite performance 13
2.2.4. Current application in industry 15
2.3. Carbonation assessment methods 17
2.3.1. Overview and classification of assessment techniques 17
2.3.2. Carbonation depth and CO_2 uptake quantification 19
2.3.3. Phenolphthalein-based image analysis methods 20
2.4. Fibre reinforced cementitious composites 22
2.4.1. Fibre reinforcement in cement-based materials 22

2.4.2. Fibre–matrix interfaces and interfacial porosity 24
2.4.3. Effects of fibres on cracking control and transport-related durability 26
2.4.4. Textile-reinforced mortars and structured fibre systems 27
2.5. Natural fibre reinforced cementitious composites 29
2.5.1. Properties of natural fibres 29
2.5.2. Natural fibres in cement composites 31
2.5.3. Fibre conditioning and pre-treatment 33
2.5.4. Internal curing and moisture regulation via natural fibres 34
2.6. Fibre-enhanced carbonation behaviour and practical implications 35
2.7. Summary 38

Chapter 3 Materials and methods 40

3.1. Research design and scope 40
3.2. Materials 41
3.3. Sample preparation 45
3.4. Curing regimes 47
3.4.1. Enforced carbonation curing 47
3.4.2. Air-curing 49
3.4.3. Post-conditioning 49
3.5. Characterisation tests 49
3.5.1. Isothermal calorimetry 50
3.5.2. Thermogravimetric analysis 51
3.5.3. X-ray diffraction 53
3.5.4. X-ray fluorescence 54
3.5.5. Fourier-transform infrared spectroscopy 55
3.5.6. Scanning electron microscopy 55
3.6. Image analysis 56
3.6.1. Yarn compactness 56
3.6.2. Phenolphthalein indicator test 58
3.6.3. Porosity quantification 59
3.7. Compressive strength test 60
3.8. Transport and absorption measurements 60
3.8.1. Yarn water absorption test 60
3.8.2. Sorptivity test 61

Chapter 4 Development of a phenolphthalein-based image analysis method 62

4.1. Introduction 62
4.2. Materials and imaging setup 64
4.2.1. Sample preparation 64
4.2.2. Imaging setup 65
4.2.3. Region of interest 66
4.3. Method development 66
4.3.1. Background subtraction 66
4.3.2. Colour deconvolution 67
4.3.3. Threshold and segmentation 68
4.3.4. Quantification of carbonated area fraction 69
4.4. Sensitivity analysis 70
4.5. Validation of the method 72
4.5.1. Carbonated area fraction derived from image analysis 72
4.5.2. Thermogravimetric analysis 74
4.5.3. X-ray diffraction 76
4.5.4. Fourier-transform infrared spectroscopy 78
4.6. Discussion 79
4.6.1. Comparison between image analysis and mass- and phase-based characterisation results 79
4.6.2. Strength and limitations 82
4.6.3. Implications for future work 83
4.7. Conclusion 84
Chapter 5 Feasibility study on natural fibre-enhanced CO_2 transport and uptake 85
5.1. Introduction 85
5.2. Materials and methods 86
5.2.1. Materials and sample preparation 86
5.2.2. Enforced carbonation curing and sampling 87
5.2.3. Phenolphthalein indicator test 88
5.2.4. Scanning electron microscopy 89
5.2.5. Thermogravimetric analysis 89
5.3. Results and analysis 90
5.3.1. Image analysis 90
5.3.2. Scanning electron microscopy 93
5.3.3. Thermogravimetric analysis 95

5.4. Discussion 99
5.4.1. Natural-fibre induced modifications in carbonation mechanisms 99
5.4.2. Effect of natural fibre properties on CO_2 transport and carbonation rate 101
5.4.3. Natural fibre yarn composites under enforced carbonation conditions 103
5.4.4. Carbonation profile assessments 105
5.5. Conclusion 106

Chapter 6 Influence of fibre treatments on carbonation and hydration in yarn-cement composites 108

6.1. Introduction 108
6.2. Materials and methods 110
6.2.1. Materials 110
6.2.2. Sample preparation 112
6.2.3. Phenolphthalein indicator test 112
6.2.4. Scanning electron microscopy 113
6.2.5. Characterisation test 114
6.3. Results and analysis 115
6.3.1. Carbonated area fraction and CO_2 uptake 115
6.3.2. Heat of hydration and phase assemblages 117
6.3.3. Microstructure of yarn-cement composites 121
6.4. Discussion 125
6.4.1. Hydration and carbonation mechanisms in yarn-cement paste composites 125
6.4.2. Microstructural and quantitative influence of yarn properties on carbonation 126
6.4.3. Practical implications 130
6.5. Conclusions 131

Chapter 7 Hardened properties of carbonation-cured natural fibre yarn-reinforced cement pastes and mortars 133

7.1. Introduction 133
7.2. Materials and methods 135
7.2.1. Materials 135
7.2.2. Sample preparation 136
7.2.3. Curing procedure 138

7.2.4. Compressive strength test 139
7.2.5. Sorptivity test 139
7.3. Results and analysis 139
7.3.1. Screening of mesh configurations using cement paste cubes 139
7.3.2. Compressive strength of yarn-reinforced mortars 142
7.3.3. Sorptivity of yarn-reinforced mortars 145
7.4. Discussion 148
7.4.1. Transferability of paste-scale strength trends to mortar systems 148
7.4.2. Effect of carbonation curing and post-curing conditions on strength development 150
7.4.3. Practical implications for natural fibre yarn-reinforced cement composites 152
7.4.4. Durability considerations for yarn-reinforced composites 154
7.5. Conclusions 156
Chapter 8 Conclusions and future work 157
8.1. Conclusions 157
8.2. Limitations 159
8.3. Recommendations for future work 163
References 167
Appendix 1. Supporting tables for literature review 194
Appendix 2. Image analysis trials and sensitivity analysis 196
Appendix 3. Supplementary information on carbonation geometry and phase evolution in yarn-embedded cement pastes 203
Appendix 4. Supplementary characterisation results supporting carbonation and hydration behaviour of yarn-cement composites 208
Appendix 5. Supplementary compressive strength results for yarn-reinforced cement paste cubes 213

Declaration

I hereby declare that this thesis and the work reported herein was composed by and originated entirely from me. Information derived from the published and unpublished work of others has been acknowledged in the text and a list of references is given in the bibliography.

The copyright of this thesis rests with the author. Unless otherwise indicated, its contents are licensed under a Creative Commons Attribution-Non Commercial 4.0 International Licence (CC BY-NC). Under this licence, you may copy and redistribute the material in any medium or format. You may also create and distribute modified versions of the work. This is on the condition that: you credit the author and do not use it, or any derivative works, for a commercial purpose. When reusing or sharing this work, ensure you make the licence terms clear to others by naming the licence and linking to the licence text. Where a work has been adapted, you should indicate that the work has been changed and describe those changes. Please seek permission from the copyright holder for uses of this work that are not included in this licence or permitted under UK Copyright Law.

Yixiu Zhuge

10 January 2026

Publications arising from this thesis

Journal articles

Zhuge, Y., Ong, P.B., Wong, H.S. and Myers, R.J. (2024) Natural fibre-enhanced CO_2 transport and uptake in cement pastes subjected to enforced carbonation. *Journal of CO_2 Utilization*, 90, 102983. https://doi.org/10.1016/j.jcou.2024.102983.

Zhuge, Y., Wong, H.S. and Myers, R.J. (2026) Influence of fibre treatments on early-age carbonation in yarn–cement paste composites under enforced carbonation. *Cement and Concrete Composites*, 173, 106737. https://doi.org/10.1016/j.cemconcomp.2026.106737.

Conference contributions

Zhuge, Y., Ong, P.B., Wong, H.S. and Myers, R.J. (2024) Natural fibre-enhanced CO_2 transport and uptake in cement pastes subjected to enforced carbonation. *Proceedings of the 2nd International Conference on Innovation in Low-Carbon Cement & Concrete Technology*, 8–10 July 2024, London, UK. Poster presentation.

Zhuge, Y., Ong, P.B., Wong, H.S. and Myers, R.J. (2024) Natural fibre-enhanced CO_2 transport and uptake in cement pastes subjected to enforced carbonation. *Proceedings of the 43rd Cement and Concrete Science Conference*, 9–10 September 2024, Belfast, UK. Oral presentation.

Zhuge, Y., Wong, H.S. and Myers, R.J. (2023) Fibre-induced carbonation of cement pastes under ambient conditions. *Proceedings of the 42nd Cement and Concrete Science Conference*, 11–12 September 2023, London, UK. Poster presentation.

Acknowledgement

I would like to offer my sincere gratitude to my supervisors, Dr. Rupert J. Myers and Prof. Hong S. Wong. Their steady guidance and patience have been instrumental in shaping both the trajectory of this thesis and my growth as a researcher. I am grateful for the trust they placed in me, allowing me the space to think and learn at every stage.

I extend my thanks to the technical staff and laboratory teams in the UKCRIC Advanced Infrastructure Materials Laboratory at Imperial College London; their expertise and care supported the daily experimental work upon which this study rests. I also thank my colleagues and friends for their thoughtful conversations and encouragement, which helped maintain my perspective and steady my spirits.

My family has been the essential foundation beneath my efforts. Their support provided a sense of calm during more demanding periods, and I am especially grateful for the stability they afforded me, which allowed me to focus on this research with peace of mind.

Finally, my deepest thanks go to my husband. We have spent the defining years of our twenties walking this path together. He stood beside me through the long days and late nights, offering stability when I was restless and perspective when the work felt heavy. This thesis marks the end of a long chapter; I am just glad we finished it side by side.

List of Tables

Table 3.1. Basic properties of selected natural and synthetic fibre yarns. 42
Table 3.2. Chemical composition of the CEM I 52.5N Portland cement (wt.%). Loss on ignition was 1.72 wt.% for cement 1 and 2.01 wt.% for cement 2. 44

Table 4.1. Validation of overflow-based image segmentation against manual segmentation for different threshold scaling factors. Agreement is quantified for the carbonated area fraction using mean absolute error, standard error, and coefficient of determination. Threshold values correspond to the lower and upper bounds applied to the deconvoluted binary images. 71

Table 6.1. Properties of the treated jute yarn variants. 111

Table A1.1. Effects of supplementary cementitious materials on carbonation reactions. 194
Table A1.2. Effects of key exposure and material parameters on carbonation rate in cement-based materials under enforced carbonation, summarised from the literature (Castellote et al., 2008; Ashraf, 2016; Ashraf, Olek & Atakan, 2016; Morandeau, Thiéry & Dangla, 2014; Šavija & Luković, 2016; Yang et al., 2015; von Greve-Dierfeld et al., 2020; Liu & Meng, 2021; Zhang, Ghouleh & Shao, 2017). 194

Table A2.1. Application of various global (histogram-derived) threshold methods on the green channel of a carbonated jute yarn sample (J-D7-20) using ImageJ Tool. 198
Table A2.2. Difference in effective carbonation radius ($\Delta r_{carbonated}$) and carbonated area fraction ($\Delta f_{carbonated}$) derived from threshold with different correction factor (1.0 – 1.4) to manual threshold counterparts. 200

Table A5.1. Compressive strength of yarn–cement composites under air and carbonation curing at 1, 3, and 7 days for all mesh configurations. 214

List of Figures

Figure 1.1 Conceptual comparison of internal CO_2 transport pathways in cement-based materials: (a) fibre-free matrix with surface-limited CO_2 ingress; (b) matrix with short, randomly dispersed fibres showing localised, discontinuous transport paths; and (c) matrix containing a placed fibre yarn, introducing a continuous internal pathway..... 5

Figure 2.1. Classification of fibres and optimum replacement percentage by volume (vol.%) of some natural fibres in cement composites (Abdalla et al., 2023). 22
Figure 2.2. Textile category and structure. 27

Figure 3.1. Schematic overview of the experimental sequence adopted in this thesis.. 40
Figure 3.2. Selection of natural fibre yarns; (a) jute, (b) hemp, (c) cotton (super slim), (d) cotton (slim), (e) cotton (thick), (f) wool (slim), (g) wool (thick), (h) Acrylic, (i) Nylon, (j) Polypropylene. 42
Figure 3.3. Sieve analysis of siliceous sand. 45
Figure 3.4. Preparation of specimens. (a–b) Cylindrical (centrifuge-tube-cast) single-yarn cement paste specimens showing curing within the tubes for the first 24 hours and subsequent removal of the tube cap and upper section to expose the paste surface. (c) Cement paste and mortar cubes reinforced with yarn meshes prepared using a layer-by-layer casting approach. 46
Figure 3.5. Schematic illustration of curing regimes applied in this study: (a) enforced carbonation curing of centrifuge-cast cement paste specimens and cement paste and mortar cubes in a controlled CO_2 incubator; and (b) alternative curing and post-conditioning regimes, including air curing for comparison and post-conditioning by water bath curing or air curing in a fog room, depending on the experimental programme adopted in each result chapter..... 48
Figure 3.6 (a) Example of using tangential method to determine the mass loss (in wt.%) due to portlandite and calcium carbonate decomposition. (b) TG-DTG curves of raw jute, hemp, cotton and wool fibres. All chosen natural fibres experienced decomposition

between 300 °C and 400 °C, culminating in a weight reduction to roughly 0% - 25% of their original weights at 1050 °C. 52
Figure 3.7. Schematic overview of SEM sample preparation. (a) Sectioning of cylindrical specimens into discs; (b) hydration stoppage by solvent exchange; (c) epoxy resin impregnation in plastic moulds; (d) vacuum-assisted air removal and curing; (e) sequential grinding and polishing with intermittent acetone cleaning; (f) storage in a desiccator for ≥48 hours to remove residual acetone and moisture prior to coating; and (g) carbon coating before BSE-SEM imaging (h). 56
Figure 3.8. Yarn compactness determination: (a) fluorescence micrograph of a resin-impregnated hemp yarn cross-section; (b) threshold image showing segmented fibre filaments; (c) hemp yarn cross-section embedded in cement paste; and (d) manually defined convex area of the yarn bundle. 58
Figure 3.9. Sorptivity test setup and mass measurement schedule. 61

Figure 4.1. Experimental setup for phenolphthalein-stained discs. (a) Preparation of cement paste cylinders and depth-resolved sectioning for image analysis, XRD and TGA/FTIR sampling, followed by phenolphthalein spraying. (b) Microscope setup with controlled oblique lighting and calibrated XY stage. (c) Region of interest showing cement paste, yarn area, carbonated zone, and exclusion of the plastic rim. 64
Figure 4.2. Image processing workflow for a representative phenolphthalein-stained disc (J-C-D7). (a) Raw RGB image with ROI defined. (b) Rolling-ball background subtraction at 100 pixels. (c) Colour deconvolution using standardised vectors: (c-1) phenolphthalein stain; (c-2) cement matrix paste; and (c-3) residual colour. (d) Threshold determination using the overflow segmentation method. (e) Binary mask of carbonated area before and after the correction factor (×1.25) applied. (f) Schematic illustration of carbonated area fraction. 67
Figure 4.3. Representative phenolphthalein-stained cross-sections of J-C-D7 specimens at increasing depths from the CO_2-exposed surface (0–40 mm, top to bottom). (a) Original images. (b) Corresponding colour-deconvoluted binary images. (c) Manual segmentation based on visual interpretation of the phenolphthalein boundary. (d–i) Automated segmentation using the overflow-based thresholding method with correction factors of 1.00 (original threshold), 1.10, 1.20, 1.25, 1.30, and 1.40, respectively. 70
Figure 4.4. Correlation between carbonated area fraction determined by manual segmentation and by overflow segmentation method. Coefficient of determination (R^2) is obtained from linear regression. 72

Figure 4.5. Carbonated area fraction profiles for (a) reference paste and (b) jute-embedded composites after 1, 3, 5, and 7 days of enforced carbonation. 73
Figure 4.6. Representative TG–DTG curves for surface, partially carbonated, and bottom discs 75
Figure 4.7. CO_2 uptake (wt.%) calculated from TG curves for (a) reference paste and (b) jute-embedded composites after 1, 3, 5, and 7 days of enforced carbonation. 76
Figure 4.8. (a) XRD patterns of (i) uncarbonated bottom disc, (ii) partially carbonated disc, (iii) mostly carbonated sample (surface disc). *Unreacted cement phases include C_3S, C_2S, C_3A and C_4AF. Phase compositions of (b) top (1 – 10 mm) and (c) bottom (50-60 mm) reference and jute-embedded samples carbonation cured for 1 and 7 days. 77
Figure 4.9. Evolution of the FTIR spectra of jute-embedded discs (J-C-D5) subjected to 5 days of enforced carbonation; (a) stacked overview; (b) position and broadening of C-O bonds; (c) position and shifting of Si-O bonds. 78
Figure 4.10. (a) Relationship between carbonated area fraction (image analysis) and CO_2 uptake from TGA. (b) Comparison of calcite contents from quantitative XRD and calcium carbonate contents from TGA plotted against carbonated area fraction. 80

Figure 5.1. Schematic diagram of disc extraction for phenolphthalein indicator testing and complementary characterisation tests. 87
Figure 5.2. (a) Selected region of interest of a carbonated jute yarn sample (J-D7-20); (b-d) colour deconvolution and the corresponding histograms in (b*-d*) using ImageJ; (e) overflow segmentation method to obtain the threshold range of carbonated zone; (f) schematic illustration of carbonated area fraction based on image analysis. 89
Figure 5.3. Carbonated area fraction in specimens exposed to CO_2 curing; (a) 1-day carbonation curing; (b) 3-day carbonation curing; (c) 5-day carbonation curing; (d) 7-day carbonation curing. VP-REF: vertical carbonation depth of reference samples. 91
Figure 5.4. Microstructure of carbonated natural fibre cementitious composites. Panels (a-d) show the carbonated areas in samples containing (a) jute (J-C-D7-20), (b) hemp (H-C-D7-20), (c) cotton (CT-C-D7-20), and (d) wool (WT-C-D7-20) yarns. SEM-BSE images (e-h) detailing the paste-fibre interface for (e) jute (J-C-D7-11), (f) hemp (H-C-D7-11), (g) cotton (CT-C-D7-11), and (h) wool yarns (WT-C-D7-11). Images (i-k) further illustrate the microstructural variations in (i) the transition zone featuring the porous hemp yarns adjacent to carbonated cement pastes, (j) internal structure of hemp fibre, (k) a dense calcium-rich carbonated area, and (n) an uncarbonated reference zone. (l) 2-tone inner C-S-H with residual alite observed in carbonated area, (m) inner and outer C-S-H

surrounding alite in uncarbonated area. Annotations: (I) natural fibre yarn, (II) porous interfacial transition zone, (III) carbonate-rich zone, (IV) uncarbonated reference zone. 93

Figure 5.5. TGA-MS analysis of selected (a) mostly carbonated disc (H-C-D7-0) at surface and (b) partially carbonated disc (H-C-D7-50) at bottom. TGA-DTG curves of (c) reference and (d) hemp-embedded samples at different depths after 5-day enforced carbonation. 97

Figure 5.6. (a) CO_2 uptake by wt.% for reference (REF-D1, REF-D3, REF-D5, REF-D7) and hemp-embedded (H-D1, H-D3, H-D5, H-D7) samples subjected to carbonation curing of 1, 3, 5, and 7 days, determined by *Equation 3.2.* (b) Comparison between the carbonated area fraction obtained by image analysis against the degree of carbonation measured by TGA. 98

Figure 5.7. (a) Schematic illustration of fibre-enhanced carbonation mechanism; (b) Vertical carbonation profile (0-15 mm) of a hemp-embedded sample subjected to 5 days of enforced carbonation (c) CO_2 transport pathways in natural fibre (hemp) embedded cement paste (5× magnification, darkfield, light intensity 50.2%). 100

Figure 6.1. Representative morphology and schematic illustration of the treated jute yarns. (a) oven-dried jute (ODJ), (b) water-saturated jute (SJ), (c) oven-dried slurry-coated jute (ODMJ), (d) saturated slurry-coated jute (SMJ), (e) epoxy-coated jute (EJ). All micrographs were acquired at 10× magnification and 46.1% brightness. 111

Figure 6.2. Schematic diagram of cylindrical specimen geometry and sectioning strategy for depth-resolved carbonation and microstructural analysis. 112

Figure 6.3. Carbonation front geometry and quantitative carbonation assessments. (a–h) Stereomicrographs of phenolphthalein-stained disc cross-sections at 20 mm depth after 7 days enforced carbonation: (a) ODJ, (b) SJ, (c) ODMJ, (d) SMJ, (e) EJ, (f) acrylic, (g) nylon and (h) polypropylene. (i–l) Carbonated area fractions from 0 to 40 mm depth measured at different curing durations: (i) 1 day, (j) 3 days, (k) 5 days, and (l) 7 days. 116

Figure 6.4. Thermogravimetric analysis of yarn–cement composites. (a) TG–DTG curves of saturated jute (SJ) after 7 days of carbonation. (b-c): Depth profiles of (b) $CaCO_3$ contents after 7 days; (c) corresponding $Ca(OH)_2$ contents. (d) Linear correlation between CO_2 uptake and effective carbonation radius. 119

Figure 6.5. (a) XRD patterns of saturated jute–cement discs after 7 days of enforced carbonation, sampled from 0–40 mm depths; cement phases include alite, belite,

tricalcium aluminate, and tetracalcium aluminoferrite. (b) Carbonation-to-hydration ratios of yarn–cement discs after 7 days of curing. 120
Figure 6.6. SEM-BSE micrographs of air-cured yarn–cement composites after 7 days of sealed curing at 20 mm depth. Four distinct zones are identified: (I) yarn cross-section, (II) interfacial transition zone (ITZ), (III) porous matrix region, and (IV) outer unmodified matrix. Panels (a1–a4) correspond to oven-dried jute (ODJ-A-D7), (b1–b4) to saturated jute (SJ-A-D7), and (c1–c2) to nylon (N-A-D7). 121
Figure 6.7. SEM-BSE images illustrating the microstructural features of yarn–cement composites after 7 days of enforced carbonation at 20 mm depth. Four characteristic zones are identified: (I) yarn cross-section; (II) interfacial transition zone (ITZ); (III) porous or partially carbonated matrix; and (IV) uncarbonated matrix. Panels (a1–a5): ODJ-C-D7, showing an (a1) overview at 200× and (a2–a5) corresponding Zones I–IV at 500×. Panels (b1–b5): SJ-C-D7, with (b1) overview and (b2–b5) corresponding Zones I–IV. Panels (c1–c3): N-C-D7, showing Zones I–III. (d) Carbonated reference paste at zone IV.... 123
Figure 6.8. Relationship between yarn properties and the depth-averaged effective carbonation radius measured over 10–40 mm after 7 days of enforced carbonation curing: (a) 24 h water absorption, (b) average tightened yarn diameter, and (c) fibre compactness. 130

Figure 7.1. Schematic illustration of sample preparation and test configurations. (a) Mesh configurations for cement paste cubes: (i–vi) tested arrangements varying in in-plane yarn spacing (10 or 5 mm) and number of vertical yarn layers (1L to 3L). (b) Mortar specimen types: (i) plain reference mortar, (ii) yarn-reinforced mortar, and (iii) dispersed fibre reinforced mortar. 137
Figure 7.2. Curing procedures applied to mortar specimens. Specimens were subjected to four curing regimes: (a) continuous air curing; (b) initial air curing followed by water curing; (c) initial carbonation curing followed by air curing; and (d) initial carbonation curing followed by water curing. Compressive strength was measured after 1, 3, 7, and 28 days of curing, with specimens transferred to the secondary curing environment after the initial 1, 3, or 7 days where applicable. 138
Figure 7.3. Compressive strength of yarn–reinforced cement paste as a function of fibre type, curing regime, curing duration, and fibre volume. (a–c) Strength development at 1, 3, and 7 days for oven-dried jute (ODJ), saturated jute (SJ), and nylon (N) composites under air and carbonation curing, using (a) 5-1L, (b) 5-2L, and (c) 5-3L mesh configurations. The larger grey bars represent the fibre-free reference cement pastes under

air curing (REF-A) and carbonation curing (REF-C), included as benchmarks for comparison with the yarn-reinforced specimens. (d–f) Compressive strength variation with fibre volume fraction (replacement level) for (d) ODJ, (e) SJ, and (f) N composites at 1, 3, and 7 days, under both curing regimes. Error bars represent ± standard error of the mean (n = 3). Linear trendlines are included for visual reference. 140
Figure 7.4. Compressive strength development of mortar specimens under different curing sequences. Panels (a–c) show specimens initially air cured for 1, 3, and 7 days, respectively, followed by either continued air curing or water curing to 28 days. Panels (d–f) show specimens initially subjected to carbonation curing for 1, 3, and 7 days, respectively, followed by either air curing or water curing to 28 days. Results are shown for plain reference mortars, yarn-reinforced mortars (SJ), and dispersed fibre reinforced mortars (DJ). The red dotted line indicates the 28-day compressive strength of the plain reference mortar cured continuously in air, shown as a benchmark for comparison. .. 144
Figure 7.5. Water absorption behaviour of mortar specimens plotted as mass change versus the square root of time. (a) Plain reference mortars and (b) dispersed fibre reinforced mortars (DJ) subjected to carbonation curing for 1, 3, and 7 days, with and without subsequent water curing to 28 days. (c) Yarn-reinforced mortars (SJ) after carbonation curing for 1, 3, and 7 days, including specimens air cured or water cured to 28 days. (d) Enlarged view of the boxed region in (c), highlighting early-stage absorption behaviour. 146

Figure A2.1. Cross-sectional (top), vertical (middle) interface bond and phenolphthalein-stained cross-sections of (a) jute, (b) hemp, (c) cotton, and (d) wool fibre string and cement matrix (darkfield, Zeiss Axio Imager Z2m digital microscope). 196
Figure A2.2. (a) Region of interest of a carbonated jute yarn sample (J-D7-20); (b-d) Colour channel split images in red, blue and green; (e-f) binary images obtained by different thresholding methods using ImageJ Tool. 197
Figure A2.3. Application of various global (histogram-derived) threshold methods on the green channel in Figure A2.2(d) (J-D7-20) using ImageJ Tool. 199

Figure A3.1. Carbonated area geometry of jute (J), hemp (H), thick cotton (CT) and thick wool (WT) embedded samples at 0-50 mm depths after 1, 3, 5, and 7 days of carbonation curing. 203
Figure A3.2. TGA-DTG curves of reference and hemp-embedded samples subjected to CO_2 curing for 1,3,5 and 7 days; (a) 1-day carbonation curing on reference sample; (b) 1-

day carbonation curing on hemp-embedded sample; (c) 3-day carbonation curing on reference sample; (d) 3-day carbonation curing on hemp-embedded sample; (e) 5-day carbonation curing on reference sample; (f) 5-day carbonation curing on hemp-embedded sample; (g) 7-day carbonation curing on reference sample. (h) 7-day carbonation curing on hemp-embedded sample. 205
Figure A3.3. Evolution of calcium carbonate (CC) and calcium hydroxide (CH) content of hemp-embedded and reference samples subjected to CO_2 curing for (a) 1, (b) 3, (c) 5, (d) 7 days. The weight percentages are normalised to per gram of anhydrous cement.206
Figure A3.4. Example resin impregnated sample under fluorescence microscopy. (a) jute, (b) hemp, (c) cotton, and (d) wool fibre yarn. 207

Figure A4.1. Isothermal conduction calorimetry results for pastes containing oven-dried (ODJ, ODN, ODA, ODP) and saturated (SJ, SN, SA, SP) yarns, alongside a paste control (PC). (a) Normalised heat flow curves over 7 days. (b) Normalised cumulative heat release over 7 days..... 208
Figure A4.2. Thermogravimetric analysis of selected yarn-cement paste composites. (a–d) TG and DTG curves of saturated jute (SJ) paste at different depths (0–40 mm) under (a) 1-day air curing and (b) 1-day enforced carbonation, (c) 7-day air curing and (d) 7-day carbonation..... 209
Figure A4.3. Stacked phase assemblages (wt.%) obtained by quantitative XRD of (a) 1-day air-cured; (b) 1-day carbonation cured; (c) 7-day air-cured; (d) 7-day carbonation-cured. 211
Figure A4.4. Pore area fraction (μ_p) distributions in yarn–cement composites after 7 days of air curing and enforced carbonation. Graphs (a–f) present μ_p (%) as a function of depth (1–41 mm), segmented into four characteristic microstructural zones: yarn (I), inner rim (II), middle rim (III), and outer rim (IV). The left y-axis shows the relative area of each zone (stacked bars), while the right y-axis denotes μ_p within each zone (scatter lines) across depths. Accompanying schematics (a*–f*) illustrate the radial positions of each zone and corresponding average μ_p. Samples include: (a, a*) ODJ-A-D7; (b, b*) ODJ-C-D7; (c, c*) SJ-A-D7; (d, d*) SJ-C-D7; (e, e*) N-A-D7; and (f, f*) N-C-D7. 212

Figure A5.1. Schematic illustration of the additional 2.5 mm mesh configurations used to assess the influence of extreme yarn spacing on fibre volume and mechanical response. 213

Nomenclature

Symbols and Variables

A_c	Area of carbonated region within region of interest (mm²)
A_f	Cross-sectional or convex area of fibre yarn bundle (mm²)
A_{ROI}	Area of region of interest (mm²)
DoC	Degree of carbonation (%)
DoH	Degree of hydration (%)
f	Correction factor of overflow segmentation method
$f_{carbonated}$	Carbonated area fraction (%)
m_{CO_2}	CO_2 uptake (wt.% of binder)
$r_{carbonated}$	Effective carbonation radius around yarns (mm)
R^2	Coefficient of determination (–)
RH	Relative humidity
μ_p	Pore area fraction (%)

Phases and Mineralogy

AFm	Aluminate–ferrite–monosulfate hydrate phases
AFt	Aluminate–ferrite–trisulfate hydrate phases (ettringite-type)
$CaCO_3$	Calcium carbonate
$Ca(OH)_2$ / CH	Calcium hydroxide (portlandite)
CO_2	Carbon dioxide
C–S–H	Calcium silicate hydrate

Abbreviations

ATR	Attenuated total reflection
BSE	Backscattered electron

CCUS	Carbon capture, utilisation, and storage
CEM I 52.5N	Ordinary Portland cement (strength class 52.5, normal early strength)
DJ	Dispersed jute fibres
DTG	Derivative thermogravimetry
ECC	Fibre-reinforced concrete
EJ	Epoxy-coated jute yarn
FRC	Fibre-reinforced concrete
FTIR	Fourier-transform infrared spectroscopy
GGBS	Ground granulated blast-furnace slag
IPA	Isopropanol
ITZ	Interfacial transition zone
LOI	Loss on ignition
MAS NMR	Magic-angle spinning nuclear magnetic resonance
MS	Mass spectrometry
N	Nylon yarn
ODJ	Oven-dried jute yarn
ODMJ	Oven-dried, cement-slurry-coated jute yarn
OPC	Ordinary Portland cement
QXRD	Quantitative X-ray diffraction
REF	Plain reference (fibre-free) system
RH	Relative humidity
ROI	Region of interest
SEM	Scanning electron microscopy
SJ	Saturated jute yarn
SMJ	Saturated, cement-slurry-coated jute yarn
TGA	Thermogravimetric analysis
TRM	Textile reinforced mortars
XRD	X-ray diffraction
XRF	X-ray fluorescence

Chapter 1 Introduction

1.1. Background

Despite the relatively low embodied energy and carbon footprint of concrete compared with other structural materials, its enormous global production volume results in substantial greenhouse gas emissions. Cement production contributes approximately 5–8 % of global anthropogenic CO_2 emissions (Miller et al., 2024; IEA, 2021), arising primarily from limestone calcination during clinker manufacture (~60 %) and fossil fuel combustion (~40 %). Although cementitious materials partially reabsorb CO_2 through natural and service-life carbonation, the sequestration rate remains insufficient to offset sector-wide emissions. Recent estimates indicate that 0.84–0.93 Gt CO_2 was absorbed globally in 2023 through carbonation of concrete, mortar, cement paste, and industrial cementitious wastes (Wu et al., 2024; Niu et al., 2025), with cumulative reabsorption since the 1930s estimated at 21.3–23.9 Gt CO_2 (Wu et al., 2024; Guo et al., 2021). These values highlight the significant, yet underutilised, potential of CO_2 mineralisation in cementitious systems, particularly when combined with low-clinker formulations and enforced carbonation strategies (Driver et al., 2024; Pamenter & Myers, 2021).

Carbonation in cement-based materials proceeds through gaseous diffusion of CO_2 into the pore network, dissolution into pore solution, and subsequent reaction with calcium-bearing phases. Dissolved CO_2 destabilises hydrate phases and precipitates calcium carbonate alongside a silica-rich phase (Zajac et al., 2022). As carbonation progresses, carbonate precipitation fills pore space and increases local pore saturation, progressively restricting further CO_2 ingress and impeding gas transport (Steiner et al., 2020; Jang & Lee, 2016). Carbonation efficiency is therefore governed by the coupled effects of reaction kinetics and transport, which depend on curing conditions (CO_2 concentration, pressure, temperature, and relative humidity) as well as material porosity and mix design(Liu & Meng, 2021; von Greve-Dierfeld et al., 2020; Rostami et al., 2012). Although elevated CO_2 concentrations and pressures increase carbonation rate and degree (Zhang, Ghouleh & Shao, 2017), the energy-intensive separation and purification of CO_2

partly counteract the emissions-reduction benefit and increase cost (Chu et al., 2022). For this reason, carbonation under ambient pressure and temperature is therefore attractive for implementation. Flue-gas carbonation, using CO_2 concentrations of approximately 20 vol.%, has been demonstrated as a feasible approach (He et al., 2020; Xian, Zhang & Shao, 2021), but CO_2 uptake in dense precast products remains limited under such conditions, often requiring extended curing durations for up to two weeks (Yoshioka et al., 2013).

Reported CO_2 uptake values under flue-gas-level carbonation vary widely across materials, specimen sizes, and curing systems. Portland cement pastes ($20 \times 20 \times 20$ mm³) cured for 24 hours under 20 vol.% CO_2 absorbed approximately 8 wt.% CO_2 (Chen & Gao, 2019), while cyclic closed-circulation curing achieved 6.84 wt.% uptake within 12 h for $50 \times 50 \times 50$ mm³ paste cubes (Xian, Zhang & Shao, 2021). In dry-mix precast concrete, an average uptake of 8.93 wt.% was reported after 1 h using a flow-through reactor with 20 vol.% CO_2 (Kashef-Haghighi & Ghoshal, 2010). Despite these advances, commercial carbonation curing remains largely confined to porous, non-reinforced products such as blocks, pipes, and pervious pavements (Chen & Gao, 2020; Shi, He & Wu, 2012; Xian, Mahoutian & Shao, 2023; Ellingboe, Arehart & Srubar, 2019). Interconnected voids in these materials facilitate deeper CO_2 penetration (Shi et al., 2017; Adresi et al., 2023), whereas conventional reinforced concrete elements exhibit denser microstructures that limit gas transport (Jang & Lee, 2016; Rostami et al., 2012). In addition, carbonation reduces pore solution alkalinity, raising concerns regarding steel depassivation and corrosion in reinforced systems (Parrott, 1994; Belda Revert et al., 2018), which further constrains application (Xian et al., 2022; Zhang & Shao, 2019, 2016). As a result, CO_2 uptake in dense cement-based products is often limited to 20–50 % of the theoretical capacity (Liu & Meng, 2021), with reported values typically ranging from 7 to 20 wt.% (Jang et al., 2016).

Comparison of carbonation performance across studies is further complicated by inconsistencies in CO_2 quantification methods and their underlying assumptions (He, Shi & Poon, 2018). Mass-change methods (He, Shi & Poon, 2018; Phung et al., 2015; Zhan, Poon & Shi, 2013) assume homogeneous carbonation and report average uptake over entire specimens, without resolving depth-dependent reaction gradients or accounting for specimen geometry (Zhang & Shao, 2016). Thermogravimetric analysis (TGA) relies on small samples extracted from different depths, raising concerns regarding

representativeness, while other techniques such as gamma densitometry, infrared analysis, and coulometric analysis face similar limitations (He, Shi & Poon, 2018; Villain, Thiery & Platret, 2007; Lo & Lee, 2002). Phenolphthalein indicator testing is widely used to visualise carbonation depth, and when combined with image analysis (Choi et al., 2017; Giulietti et al., 2021), provides a rapid means of assessing carbonation profiles based on pH reduction. However, existing image-based approaches typically rely on manual threshold selection in HSV or RGB colour spaces (Choi et al., 2017; Giulietti et al., 2021; Hubler, Wendner & Bažant, 2015), introducing subjectivity due to specimen heterogeneity, illumination variability, and differences in stain intensity. A standardised and objective image analysis procedure is therefore required to enable reliable assessment of heterogeneous carbonation behaviour and its relation to CO_2 uptake.

In industry, enforced carbonation curing is mainly applied to factory-produced concrete products such as precast elements, masonry units, and paving blocks (Zhang, Ghouleh & Shao, 2017; El-Hassan, Shao & Ghouleh, 2013; Sidhu et al., 2023), where curing conditions can be controlled. These products are typically manufactured with low water-to-cement ratios and high compaction to achieve early strength and durability, resulting in dense pore structures that limit CO_2 ingress beyond the near-surface region and restrict overall uptake. Industrial application therefore requires careful control of carbonation extent, as excessive carbonation can reduce mechanical performance through extensive formation of carbonation products that disrupt the cement matrix (Li & Wu, 2022), while inappropriate carbonation in reinforced systems may compromise the alkaline environment required for steel passivation and increase the risk of carbonation-induced corrosion (Xian et al., 2022). In-situ approaches, including the use of carbonated water as a mixing agent, have been explored and shown potential in specific cases such as recycled aggregate concrete (Suescum-Morales, Fernández-Rodríguez & Jiménez, 2022). However, such approaches remain uncommon due to practical constraints, including the need for specialised equipment and the difficulty of achieving uniform and effective CO_2 exposure under site conditions (Kim et al., 2024). At the scale of practical concrete products, size effects further exacerbate carbonation non-uniformity, making complete reaction difficult to achieve in larger or denser specimens (Wang, Xiao & Duan, 2022; Zajac et al., 2022). This has motivated interest in approaches that modify internal transport behaviour rather than relying solely on external exposure conditions. Natural fibres have therefore been explored as a means of modifying internal transport behaviour in cement-based materials.

The incorporation of natural fibres in cementitious materials has traditionally focused on mechanical reinforcement and crack control (Farooqi & Ali, 2023; Saini, Matsagar & Kodur, 2024), using either short, randomly distributed fibres in fibre-reinforced concrete (Balea et al., 2021; Mukhopadhyay & Khatana, 2015) or woven and non-woven fabrics in textile-reinforced mortars (Raupach & Morales Cruz, 2016; Ventura et al., 2022). When assembled into continuous, placed yarns, natural fibres can promote moisture transport along fibres and inter-fibre voids (Alatawna et al., 2022; Pourasee, Peled & Weiss, 2011), suggesting a potential route to influence carbonation beyond near-surface regions. Cellulose-based fibres are compatible with the hydrophilic cement matrix (Balea et al., 2021), but are susceptible to alkaline degradation, leading to fibre dissolution and deterioration of the fibre–matrix interface (Ramakrishna & Sundararajan, 2005; Almeida et al., 2013; Onuaguluchi & Banthia, 2016; Lin et al., 2023). Enforced carbonation at early age has been shown to mitigate these effects by reducing alkalinity and densifying interfacial transition zones, thereby preserving natural fibres(Balea et al., 2021; Ramakrishna & Sundararajan, 2005; Tonoli et al., 2016, 2010; Filomeno et al., 2023; Pizzol et al., 2014), with reported enhancements in tensile, flexural, and fatigue performance in engineered cementitious composites (Santos et al., 2015; Hu et al., 2023). Nevertheless, studies employing dispersed fibres generally report only modest increases in CO_2 uptake (Hu et al., 2023; Hay, Krishnan & Celik, 2024), with carbonation typically confined to near-surface regions due to the lack of connectivity between individual fibres.

While dispersed short fibres can locally influence pore structure and moisture distribution, their discontinuous and randomly distributed nature limits the formation of connected transport pathways and does not overcome transport constraints at greater depths. Spun natural fibre yarns therefore offer a structurally continuous alternative in cementitious composites (El Mogahzy, 2009). By aggregating individual filaments into aligned bundles, natural fibre yarns introduce internal lumens and inter-fibre voids that can modify moisture distribution and interfacial transport within the cement matrix. Compared with randomly distributed fibres, yarn-based reinforcements allow controlled placement and continuity, enabling the formation of connected internal pathways. *Figure 1.1* summarises the conceptual differences in internal CO_2 transport continuity between fibre-free matrices, systems reinforced with dispersed short fibres, and composites containing placed fibre yarns.

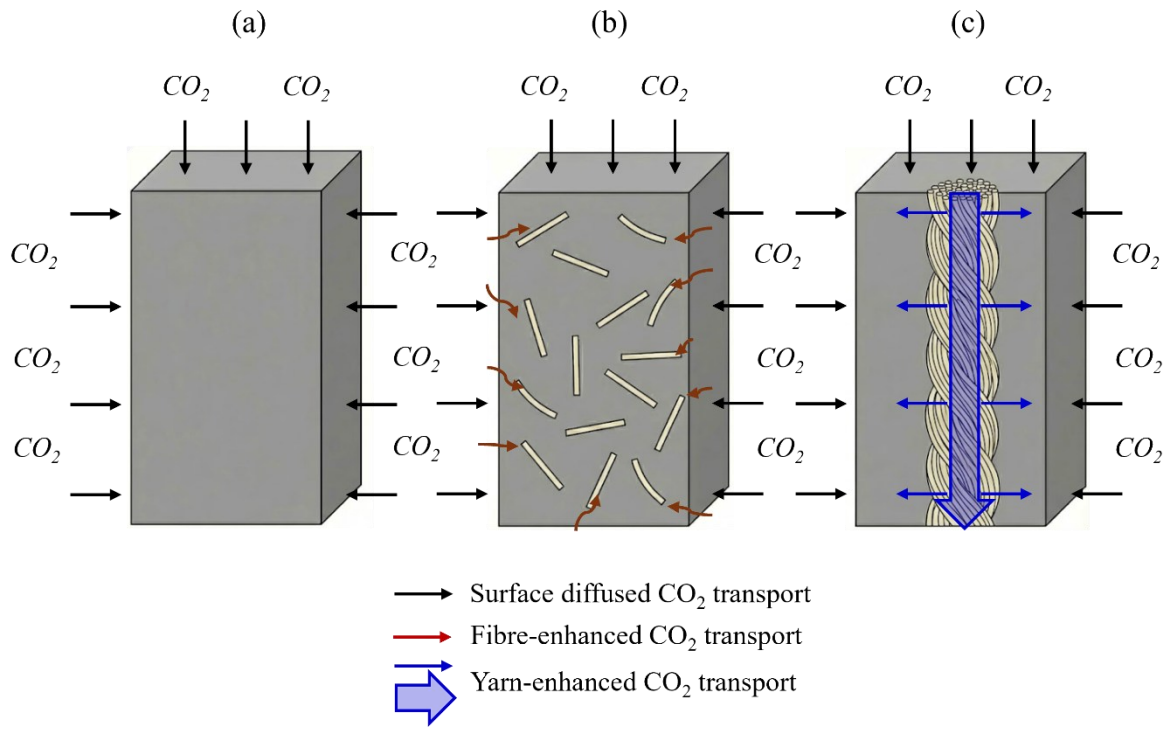


Figure 1.1 Conceptual comparison of internal CO_2 transport pathways in cement-based materials: (a) fibre-free matrix with surface-limited CO_2 ingress; (b) matrix with short, randomly dispersed fibres showing localised, discontinuous transport paths; and (c) matrix containing a placed fibre yarn, introducing a continuous internal pathway.

Despite this conceptual advantage, the role of spun natural fibre yarns as internal transport modifiers under carbonation curing remains insufficiently explored. In particular, the influence of yarn architecture, moisture state, interfacial pore structure, and surface condition on CO_2 transport and carbonation front development has not been systematically isolated. Moreover, the interaction between yarn-assisted carbonation and early-age hydration under enforced carbonation curing conditions remains poorly characterised. Addressing these gaps is essential for evaluating the feasibility of yarn-based transport modification as a strategy for enhancing CO_2 uptake in dense cement-based materials.

1.2. Aims and objectives

Motivated by transport limitations in the carbonation curing of dense cement-based materials, this thesis evaluates yarn-enhanced carbonation across multiple length scales, progressing from single-yarn feasibility studies through the effects of yarn treatment and moisture state to mesh-based reinforcement and performance assessment at the mortar scale. The aim of this thesis is to determine whether natural fibre yarns can be used as

placed internal transport modifiers to enhance CO_2 transport, carbonation extent, and CO_2 uptake in cement-based materials under enforced carbonation curing, while maintaining acceptable compressive strength.

The objectives of this thesis are to:

- Develop and validate depth-resolved experimental and phenolphthalein-based image analysis methods to quantify heterogeneous carbonation and CO_2 uptake in fibre-containing cementitious systems.
- Determine whether embedded natural fibre yarns enhance carbonation extent and CO_2 uptake relative to fibre-free reference systems, and assess differences between natural fibre types.
- Investigate how yarn properties, including moisture state, internal porosity, and surface treatment, govern CO_2 transport, effective carbonation radius, and local hydration–carbonation interactions.
- Quantify effective carbonation radii and establish suitable yarn spacing and mesh configurations that balance carbonation enhancement with fibre-induced heterogeneity.
- Evaluate the influence of yarn architecture, fibre volume fraction, curing sequence, and post-carbonation moisture exposure on compressive strength and moisture transport at paste and mortar scales.

1.3. Thesis outline

This thesis is organised into eight chapters. Following this introduction, Chapter 2 presents a critical review of carbonation in cement-based materials and natural fibre reinforcement. The review summarises current understanding of carbonation mechanisms, CO_2 transport, and moisture effects, and identifies limitations in existing studies, particularly with respect to organised fibre architectures and their interaction with carbonation curing. Chapter 3 describes the materials, specimen preparation procedures, curing regimes, and characterisation methods used throughout the thesis. An overview of the experimental programme is first presented, followed by detailed descriptions of yarn conditioning, cement paste and mortar fabrication, carbonation curing, and data analysis procedures adopted to ensure consistency across the experimental chapters.

Chapters 4 – 7 present the experimental results of the thesis. Chapter 4 introduces an image-based carbonation analysis method based on phenolphthalein indicator testing, which provides a quantitative basis for analysing heterogeneous carbonation patterns in yarn-reinforced systems. Chapter 5 examines the feasibility of using natural fibre yarns to enhance carbonation in cement paste, establishing baseline effects and fibre-type dependence. Chapter 6 investigates the influence of yarn properties, including moisture state and surface condition, on carbonation and hydration behaviour. Chapter 7 extends the analysis to mechanical performance, evaluating compressive strength in yarn-reinforced cement pastes and mortars under different mesh configurations and curing sequences.

Finally, Chapter 8 concludes the thesis by summarising the main findings and discussing their implications for the design of carbonation-compatible, yarn-reinforced cementitious composites. The limitations of the present work are identified, and directions for future research are proposed.

Chapter 2 Literature review

2.1.Carbon capture, utilisation and storage and mineral carbonation

Numerous strategies have been proposed to mitigate climate change, among which carbon capture, utilisation, and storage (CCUS) is recognised as one of the primary technological pathways for reducing anthropogenic CO_2 emissions (Yan & Zhang, 2019; Vega et al., 2020; Zhang et al., 2020; IPCC, 2021). In a typical CCUS process, CO_2 is first captured from industrial exhaust streams and subsequently purified for either long-term sequestration or utilisation. Currently adopted CO_2 storage routes include ocean storage, geological storage in depleted oil and gas reservoirs, and industrial fixation of CO_2 into solid carbonates (IPCC, 2005; Wilberforce et al., 2021). In parallel, captured CO_2 can also be valorised through commercial pathways such as food and beverage processing, enhanced oil or gas recovery, enhanced coalbed methane recovery, and mineralisation-based applications (Al-Mamoori et al., 2017).

While ocean and geological storage offer large theoretical storage capacities, they are associated with potential environmental risks, including CO_2 leakage, ecological disturbance, and groundwater contamination (Rahman et al., 2017). In contrast, mineral carbonation provides a permanent and leakage-free storage route, in which CO_2 reacts with alkaline materials to form thermodynamically stable carbonate phases (Seifritz, 1990; Lackner et al., 1995). This approach allows CO_2 to be utilised across a wide range of solid feedstocks, including natural minerals, industrial by-products, and cement-based materials. Four principal mineralisation routes have been identified in the literature (Zhang et al., 2020; Osman et al., 2021; Rafiee et al., 2018) are (i) direct carbonation of solid minerals or alkaline solutions (Ji & Yu, 2018), (ii) indirect carbonation involving prior extraction of metal ions (Zevenhoven & Fagerlund, 2010), (iii) electrochemical mineralisation using electrochemical cells (Giddey et al., 2012), and (iv) carbonation curing, in which CO_2 is applied directly during the curing of cement-based materials.

Among these routes, carbonation curing of cement-based materials has attracted increasing attention, as it directly integrates CO_2 sequestration with construction material production. Cementitious systems are particularly suitable for mineral carbonation due to their high calcium content and alkaline pore solution, making them effective hosts for material-based CO_2 utilisation within CCUS frameworks.

2.2. Carbonation of cement-based materials under enforced conditions

2.2.1. Carbonation mechanisms in cement-based materials

The fundamental mechanisms of CO_2 mineralisation in cement-based materials involve gaseous CO_2 diffusion through the pore network, dissolution into the pore solution, and subsequent reaction with calcium-bearing solid phases (Vagelis G. Papadakis, 1991; Li & Wu, 2022; Chen & Gao, 2019). The dominant reaction products are calcium carbonates and silica-rich phases, while the overall extent of carbonation is governed primarily by the availability and accessibility of carbonatable calcium-containing phases (Shah et al., 2018).

Carbonation may involve both hydration products and anhydrous clinker phases, depending on the degree of hydration and exposure conditions. *Reactions 2.1 – 2.3* describe carbonation of the principal hydration products, whereas *Reactions 2.4 – 2.5* represent direct carbonation of anhydrous calcium silicates. Among hydration products, carbonation of portlandite ($Ca(OH)_2$) is thermodynamically favoured and kinetically dominant in ordinary Portland cement systems. This reaction, expressed by *Reaction 2.1*, proceeds spontaneously with a negative Gibbs free energy change under ambient conditions (Van den Heede, De Schepper & De Belie, 2019). The preferential carbonation of portlandite is attributed to its high solubility and rapid dissolution kinetics relative to calcium (alumino)silicate hydrate (C–(A)–S–H) in alkaline pore solutions (Phung, 2015).

$$Ca(OH)_2 + CO_2 \rightarrow CaCO_3 + H_2O \quad (2.1)$$

Once portlandite is locally depleted, or in binders with low initial portlandite content, carbonation increasingly involves the principal binding phase, C–(A)–S–H. This reaction is expressed schematically in *Reaction 2.2*. Carbonation of C–(A)–S–H proceeds through progressive decalcification of the silicate structure, releasing calcium ions that precipitate as $CaCO_3$ and leaving a silica-rich, amorphous or polymerised residue (Groves, Rodway

& Richardson, 1990; Phung, 2015; Saillio et al., 2021). This reaction is inherently non-stoichiometric, reflecting the compositional variability of C–(A)–S–H, with Ca/Si ratios typically ranging from 1.2–2.0 in OPC systems and from approximately 0.8–1.4 in silica-rich blended binders (Liu et al., 2020).

$$C-(A)-S-H+xCO_2 \rightarrow CaCO_3+SiO_2\cdot nH_2O\,(+Al\text{-}bearing\ gel) \tag{2.2}$$

Aluminate-bearing hydrates can also participate in carbonation. *Reaction 2.3* represents carbonation of AFt-type assemblages, which may yield $CaCO_3$ alongside sulphate- and aluminium-bearing phases, with aluminium frequently redistributed into amorphous aluminosilicate or calcium–aluminate hydrates rather than forming well-crystallised products. Calcium-containing phases including C–(A)–S–H, AFm, and AFt all contribute to CO_2 fixation, although carbonation of these phases is often incomplete.

$$3CaO\cdot Al_2O_3\cdot 3CaSO_4\cdot 32H_2O+3CO_2 \rightarrow 3CaCO_3+3(CaSO_4\cdot 2H_2O)+Al(OH)_3\cdot xH_2O+(26-x)H_2O \tag{2.3}$$

Under enforced carbonation conditions, carbonation is not limited to hydration products. Unhydrated clinker phases can also react directly with CO_2, particularly at early ages when hydration is incomplete. In these reactions, CO_2 competes with water, enabling direct conversion of alite and belite to $CaCO_3$ and silica gel without prior hydration (*Reactions 2.4* and *2.5*). Such pathways are favoured under high CO_2 concentrations and conditions of limited water availability, where direct carbonation can compete with hydration.

$$3CaO\cdot SiO_2+3CO_2+nH_2O \rightarrow SiO_2\cdot nH_2O+3CaCO_3 \tag{2.4}$$

$$2CaO\cdot SiO_2+2CO_2+nH_2O \rightarrow SiO_2\cdot nH_2O+2CaCO_3 \tag{2.5}$$

Calcium carbonate precipitates in cementitious matrices as several polymorphs, including calcite, aragonite, vaterite, and amorphous calcium carbonate. Polymorph distribution reflects both carbonation conditions and the calcium source. Portlandite carbonation preferentially yields calcite, whereas carbonation of C–(A)–S–H and aluminate phases promotes formation of metastable polymorphs such as vaterite and aragonite, particularly under high supersaturation and rapid precipitation conditions typical of enforced

carbonation (Liu et al., 2020; Saillio et al., 2021). Subsequent transformation to calcite may occur if sufficient moisture and time are available (Saillio et al., 2021; Charitha et al., 2022).

Overall, carbonation proceeds from preferential portlandite carbonation to progressive decalcification of C–(A)–S–H and aluminate-bearing hydrates as buffering capacity diminishes, accompanied by redistribution of calcium and aluminium into carbonate and amorphous aluminosilicate phases (Saillio et al., 2021; Morandeau, Thiéry & Dangla, 2014). In aluminium- and alkali-rich systems, secondary phases such as monocarbonates or alkali carbonates may form, further modifying phase assemblage and pore-solution chemistry (Bernal et al., 2012; Charitha et al., 2022).

2.2.2. Enforced carbonation and governing parameters

Enforced carbonation is an active curing and treatment process in which CO_2 is deliberately introduced into cement-based materials under controlled environmental conditions. Unlike natural atmospheric carbonation, which proceeds slowly and is typically considered a durability concern, enforced carbonation is designed to promote rapid CO_2 uptake and controlled formation of carbonate phases within practical timescales. Early feasibility of this approach was demonstrated in the 1970s (Berger, Young & Leung, 1972), with renewed interest driven by its potential role in carbon capture, utilisation, and storage.

Under enforced conditions, carbonation is applied using elevated CO_2 concentrations in combination with regulated temperature and humidity, enabling reactions to proceed over hours to days rather than years. As elucidated in Section 2.2.1, such conditions activate multiple carbonation pathways, including reactions involving hydration products and, at early ages, direct carbonation of unhydrated clinker phases. The resulting phase assemblage therefore differs from that formed under hydration alone, positioning enforced carbonation as a curing strategy rather than an accelerated analogue of long-term natural exposure (Lippiatt, Ling & Pan, 2020; Liu & Meng, 2021). From a practical perspective, the short timescales associated with enforced carbonation are compatible with industrial curing processes, particularly in precast and factory-controlled applications (Zhang, Ghouleh & Shao, 2017).

In experimental and industrial practice, enforced carbonation is commonly implemented using CO_2 concentrations in the range of approximately 10–100% (Liu et al., 2023a; Frías et al., 2018; Wawrzyńczak et al., 2022; Liu & Meng, 2021). Under such conditions, carbonation behaviour does not vary linearly with CO_2 concentration or exposure duration. Changes in reaction balance, depletion of buffering phases, and evolving transport constraints introduce non-linear responses that limit direct extrapolation between different enforced carbonation regimes (Chen, Gao & Qin, 2019). Comparative analyses of fly ash–rich concretes show that increasing CO_2 concentration from atmospheric levels to 1–10 % alters the governing carbonation regime, with reported carbonation depth–time relationships deviating from the classical square-root-of-time law and exhibiting concentration-dependent rate exponents (You et al., 2022; AL-Ameeri et al., 2021). These observations demonstrate that carbonation behaviour under enforced conditions cannot be extrapolated reliably from low-CO_2 tests by simple concentration scaling.

Binder composition exerts a strong influence on carbonation behaviour under enforced conditions. Supplementary cementitious materials consume portlandite through pozzolanic or hydraulic reactions during hydration, reducing the buffering capacity of the system and promoting earlier involvement of C–(A)–S–H and aluminate-bearing hydrates in carbonation reactions (Van den Heede, De Schepper & De Belie, 2019). As a result, slag- and fly ash–rich binders often exhibit greater apparent carbonation depths in phenolphthalein tests (Younsi et al., 2013), reflecting earlier loss of alkalinity rather than intrinsically faster carbonation kinetics (Appendix 1, *Table A1.1*).

The efficiency and extent of CO_2 uptake during enforced carbonation are governed by a coupled set of exposure parameters and material characteristics. Key exposure parameters include CO_2 concentration and pressure, temperature, relative humidity, and moisture state, while material-related parameters include curing age at the onset of carbonation, binder composition, water-to-binder ratio, and pore structure (Rostami et al., 2012; von Greve-Dierfeld et al., 2020; Liu & Meng, 2021). While the relative importance of individual parameters varies with mix design and curing protocol, reported directional trends in carbonation rate and extent are broadly consistent across studies and are summarised in Appendix 1, *Table A1.2*. Among these parameters, moisture state and moisture transport exert a dominant control on carbonation rate (Saetta, Schrefler & Vitaliani, 1993). Maximum carbonation rates are typically reported at intermediate relative humidity levels of approximately 50–80%, which balance gaseous CO_2 ingress

with aqueous-phase dissolution and ionic mobility (Chen, Gao & Qin, 2019; Wang et al., 2025). High humidity restricts gas-phase CO_2 transport, whereas low humidity limits aqueous-phase reaction kinetics.

In addition, carbonation reactions generate water, and under high CO_2 fluxes this reaction water can accumulate locally, further restricting gas transport. Bernal et al. (2012) showed that increasing CO_2 concentration from natural levels (~0.04%) to accelerated regimes (1–7%) fundamentally alters pore solution chemistry, promoting a transition from carbonate-dominated to bicarbonate-dominated systems, increasing the prevalence of metastable $CaCO_3$ polymorphs (vaterite and aragonite), and reducing pore solution pH by nearly two units. These chemically more aggressive conditions enhance reaction progress but modify pore blocking and transport behaviour, reinforcing that enforced carbonation represents a distinct reaction–transport regime rather than a simple acceleration of natural carbonation.

2.2.3. Effect of carbonation on phase evolution and composite performance

Building on the mechanisms and governing parameters outlined in Sections 2.2.1 and 2.2.2, enforced carbonation alters phase assemblage evolution by introducing carbonation reactions alongside ongoing hydration. When appropriately controlled, this process can enhance early-age mechanical performance by promoting rapid carbonate precipitation, matrix densification, and accelerated strength development (Jang et al., 2016; Qiu, 2020). These effects support the use of enforced carbonation as both a curing strategy, and also a CO_2 sequestration pathway.

In Portland cement–based systems, enforced carbonation has been shown to densify the near-surface microstructure by filling capillary pores with $CaCO_3$ and reducing average pore size. Using a superimposed carbonation strategy combining slag pretreatment and paste carbonation at 30 bar CO_2, Li, Chen & Gao (2023), reported that total CO_2 sequestration more than doubled compared with either carbonation curing or slag pretreatment alone, while 28-day compressive strength increased by 9.8–16.1%, depending on slag content and curing duration. Mercury intrusion porosimetry showed a reduction in total porosity of up to 7.1% and a shift of the dominant pore diameter from approximately 80–95 nm to 45–57 nm after short-duration carbonation curing, confirming that strength enhancement was associated with pore refinement. Similar

matrix densification effects have been reported in alternative binders and composites, including construction and demolition waste–derived aggregates (Liang et al., 2020), steel slag aggregates for infrastructure and marine applications (Song et al., 2021; Li et al., 2022b), magnesium phosphate cements via formation of magnesium carbonates (Jeon, Qudoos & Kim, 2021). In biochar-blended cement mortars subjected to carbonation curing, Yang & Wang (2021) observed compressive strength increases of approximately 12–18% relative to non-carbonated references, accompanied by a marked increase in electrical resistivity and a reduction in chloride diffusion coefficients by up to 35%. These improvements were attributed to carbonate precipitation within biochar-modified pore networks and partial blockage of connected capillary pores, demonstrating that carbonation-induced densification can synergise with pore-modifying additives to enhance transport resistance. In blended cement systems, Frías et al. (2018) reported compressive strength increases concurrent with pore refinement after enforced carbonation, with OPC reaching 85.2 MPa and a cement containing 20% activated coal waste reaching 77.2 MPa after 7 days of exposure to 100% CO_2.

These benefits are spatially dependent because carbonation remains transport-limited. Under diffusion-controlled conditions, carbonate precipitation and pore refinement are concentrated near the exposed surface, whereas deeper regions may remain partially carbonated or hydration-dominated (Phung, 2015). This contrast leads to non-uniform mechanical profiles, in which surface densification contributes disproportionately to measured strength. Such heterogeneity can complicate interpretation of bulk performance indicators, as carbonated mortars have been shown to exhibit reductions in total porosity from ~40% to ~29% and decreases in intrinsic permeability by nearly one order of magnitude, alongside lower sorptivity, even though measured carbonation depths remained limited to the outer ~5–10 mm of specimens 40 mm thick (Ren et al., 2025). This distinction becomes increasingly important with increasing specimen size, where near-surface densification can contribute disproportionately to measured performance while the interior remains comparatively unmodified.

At the pore scale, enforced carbonation typically redistributes pore size populations rather than simply reducing porosity. Studies commonly report a reduction in larger capillary pores together with an increase in finer pores, including pores in the approximately 2–7 nm range (Li, Chen & Gao, 2023; Wawrzyńczak et al., 2022). Two coupled mechanisms contribute to this behaviour. Carbonation of portlandite forms $CaCO_3$ with a greater solid

molar volume than the original $Ca(OH)_2$, allowing carbonate precipitation to fill or narrow existing capillary voids. In parallel, decalcification of C–S–H produces a more polymerised silica-rich phase and reorganises the gel-scale pore structure, contributing finer-scale porosity. The apparent shift from coarse to fine pores therefore reflects simultaneous pore filling by carbonate products and restructuring of the hydrate assemblage rather than uniform pore closure. At advanced carbonation, however, extensive C–S–H decalcification and associated shrinkage may promote pore coarsening or microcracking, so the net microstructural response depends on the phases reacting and the extent of carbonation. This mechanistic interpretation is consistent with previous observations that $CaCO_3$ formation can reduce total porosity while carbonation of C–S–H increases the fraction of pores in the nanometre range (Wawrzyńczak et al., 2022).

The resulting pore refinement can reduce permeability and alter moisture transport, but these changes do not necessarily translate into improved long-term durability (Liang et al., 2024). The loss of alkalinity associated with carbonation has been recognised for several decades and forms the basis of classical durability assessments of reinforced concrete (Tuutti, 1982; Vagelis G. Papadakis, 1991; Parrott, 1994). Carbonation consumes portlandite and other alkaline buffering phases, progressively lowering the initially high pore-solution pH (>12.5); in extensively carbonated regions, values approaching approximately 8–9 have been reported (Dudi & Bishnoi, 2024). As steel passivation requires pH values above approximately 11.5–12.0, this alkalinity loss presents a clear risk of reinforcement depassivation and corrosion in reinforced systems (Belda Revert et al., 2018; Zhang & Shao, 2019). In addition, early-age carbonation competes directly with hydration for available calcium and water. While short-duration carbonation can accelerate setting and early strength, excessive or poorly timed CO_2 exposure may suppress later hydration and reduce long-term strength potential (Charitha et al., 2022; Zhang, Cai & Jaworska, 2020; Jeon, Qudoos & Kim, 2021; Zajac et al., 2022). These trade-offs underscore the need to control both carbonation extent and internal transport processes when carbonation is used as a curing strategy.

2.2.4. Current application in industry

Despite its demonstrated potential, carbonation curing technology remains at a limited stage of industrial deployment, with most applications confined to pilot-scale or niche precast production. While several studies have highlighted its capacity to reduce cement-

related emissions and enhance early-age performance, further development is required to address challenges associated with process control, curing uniformity, and integration into large-scale manufacturing workflows (Chen & Gao, 2020; Zhang et al., 2024b; Li et al., 2022a).

Current commercial implementation is largely restricted to factory-controlled precast applications, where environmental conditions and curing duration can be tightly regulated. CarbonCure Technologies injects purified CO_2 into fresh concrete at atmospheric pressure and ambient temperature, enabling in-mixer mineralisation without dedicated carbonation chambers (Monkman & MacDonald, 2017; Monkman et al., 2016). In contrast, CO_2-SUICOM employs flue gas–based carbonation, curing concrete products for approximately 14 days under CO_2 concentrations of 15–20 vol.% at 40 °C. This approach has been applied in infrastructure projects such as the Fukuyama Photovoltaic Power Station, demonstrating the feasibility of extended-duration carbonation under moderate-temperature flue-gas conditions (Yoshioka et al., 2013; Higuchi et al., 2014). Solidia Technologies similarly utilises flue gas at ambient pressure and moderate temperatures (~30 °C), with reported curing durations ranging from 0.5 to 145 hours, achieving near-full compressive strength within 24 hours and enabling just-in-time manufacturing with reduced inventory requirements (Ashraf, Olek & Atakan, 2016; Meyer et al., 2018).

By contrast, in-situ (cast-in-place) carbonation remains uncommon due to the difficulty of achieving controlled CO_2 exposure and uniform reaction under site conditions. Limited studies have explored alternative strategies to introduce CO_2 during or after casting. For example, incorporating 12 wt.% CO_2-impregnated faujasite into CEM I mortars increased $CaCO_3$ content by 1.9 wt.% after 28 days(Luo et al., 2023) , while wollastonite-blended systems achieved mineral carbonation via CO_2-enriched mixing, with 20 wt.% wollastonite replacement yielding approximately 22.5 wt.% $CaCO_3$ (Pae, Kim & Moon, 2024). In steel slag–based artificial lightweight aggregates, the addition of 3 wt.% biochar increased CO_2 uptake by 24.3% and improved crushing resistance to 5.7 MPa, attributed to enhanced internal diffusion pathways and CO_2 retention within the biochar structure (Xu et al., 2023). In extrusion-based 3D-printed calcium silicate binders, filament-scale architectures combined with in-line CO_2 exposure increased the degree of carbonation by up to 8.9 times relative to cast specimens, rising to 12.9 times with in-situ carbonation during printing, and resulted in flexural strength increases of up to 16.5 times (Ralston, Gupta & Moini, 2024).

Despite these advances, application of carbonation curing to reinforced concrete remains contentious, particularly at early ages, due to unresolved concerns regarding alkalinity loss, steel depassivation, and long-term durability (Sidhu et al., 2023). More broadly, large-scale deployment is constrained by practical challenges related to environmental control, curing uniformity, process integration, and production throughput within existing manufacturing lines (Zhang & Shao, 2016; Zhang, Ghouleh & Shao, 2017). These limitations underscore the need for strategies that enhance internal CO_2 transport and carbonation uniformity without relying on prolonged curing durations or tightly controlled external environments.

2.3. Carbonation assessment methods

2.3.1. Overview and classification of assessment techniques

Efforts to standardise carbonation assessment began in the 1980s through RILEM recommendations, which established phenolphthalein spray testing as the reference method for measuring carbonation depth in concrete. In the RILEM CPC-18 method (1988), a 1% phenolphthalein solution in 70% ethanol is applied to a freshly fractured surface; the transition from pink (pH $\gtrsim$ 9–10) to colourless (pH $\lesssim$ 9) is used to define carbonation depth. These protocols were developed primarily for ordinary Portland cement (OPC) systems, where high portlandite content and strongly alkaline pore solutions (typically pH > 13) produce a clear colour contrast at the carbonation front (Yue et al., 2023).

Subsequent research has shown that this pH-based depth approach is not universally applicable, particularly for binders with lower initial alkalinity or altered hydrate assemblages. Since approximately 2015, studies have increasingly focused on alternative systems, including calcium aluminate cement (CAC), calcium sulfoaluminate (CSA), and alkali-activated binders, in which uncarbonated pore solution pH may lie in the range of approximately 9–11 (Zhang et al., 2025; Dixit, Du & Pang, 2021). In such systems, phenolphthalein may exhibit limited or no colour change despite substantial CO_2 uptake. For example, comparative studies across OPC, CAC, CSA, and alkali-activated fly ash binders have reported bound CO_2 contents of approximately 5–15 wt.% in specimens showing similar or negligible phenolphthalein-indicated carbonation depths (Alapati &

Kurtis, 2018), highlighting the inconsistency between pH reduction and carbonate formation in these materials.

Recognition of these discrepancies has led to increasing reliance on mass- and phase-based techniques for quantifying CO_2 uptake (Mo, Zhang & Deng, 2016; Praneeth et al., 2020). Direct methods include bulk mass-gain measurements, cumulative mass monitoring of the carbonation set-up, thermogravimetric analysis, quantitative X-ray diffraction (QXRD), gamma densitometry, and coulometric titration (Charitha et al., 2022; Liu et al., 2023b; He, Shi & Poon, 2018). Each technique captures different components of the carbonation process and operates over different spatial and temporal scales; reported CO_2 sequestration capacities nevertheless vary widely across the literature, reflecting differences in assessment techniques and their underlying assumptions (He, Shi & Poon, 2018). Bulk mass-change approaches typically assume a uniform degree of carbonation and report an average uptake over the entire specimen (He, Shi & Poon, 2018; Phung et al., 2015; Zhan, Poon & Shi, 2013). While straightforward, this assumption obscures carbonation gradients from the exposed surface and complicates comparisons across specimens with different sizes and surface-area-to-volume ratios (Zhang & Shao, 2016). On the other hand, TGA provides phase-specific information but is typically limited to powder samples of less than 10–100 mg, raising concerns about representativeness in heterogeneous or fibre-reinforced systems.

Comparative studies demonstrate that different methods can yield uptake values that differ by several percentage points even for the same specimen. For Portland limestone cement pastes, CO_2 contents determined by infrared-based carbon analysis exceeded those calculated from mass gain by up to 6 wt.% due to differences in reference mass and treatment of evaporable and non-evaporable water (Shao et al., 2013). QXRD, while capable of distinguishing calcite, vaterite, and aragonite, systematically underestimates total CO_2 uptake because amorphous and poorly crystalline carbonates are not detected; in 4-bar carbonation tests, QXRD accounted for only ~16–21 wt.% calcite, whereas TGA and ignition methods indicated total carbonate contents exceeding 30 wt.% (Tu et al., 2016).

Taken together, these findings show that carbonation is a spatially graded and phase-diverse process that cannot be fully characterised by a single metric. Depth-based indicators such as phenolphthalein provide rapid visualisation of alkalinity loss but

systematically under-represent partial carbonation and total CO_2 uptake, while bulk and micro-analytical techniques trade spatial resolution for chemical specificity.

2.3.2. Carbonation depth and CO_2 uptake quantification

While Section 2.3.1 distinguishes carbonation assessment techniques according to their physical and chemical basis, an equally important distinction lies in the metric used to describe carbonation progress. In practice, carbonation is most commonly reported either as a single penetration depth or as a total amount of CO_2 bound within the material. These two descriptors capture fundamentally different aspects of the carbonation process and are not directly interchangeable.

Carbonation depth, typically expressed in millimetres, denotes the distance from the exposed surface at which a specified pH or chemical threshold is reached and is most often inferred from phenolphthalein indicator testing (Chang & Chen, 2006). Meanwhile, total CO_2 uptake, which is usually reported as a mass fraction of binder or as mass of CO_2 per unit volume, quantifies the cumulative amount of chemically bound CO_2, irrespective of its spatial distribution within the specimen (Teune et al., 2023; von Greve-Dierfeld et al., 2020). As a result, materials exhibiting similar carbonation depths may differ substantially in their actual degree of carbonation and CO_2 storage capacity.

To bridge this disconnection, profile-resolved approaches have been developed to characterise carbonation as a spatially graded process rather than a discrete front. Using confocal Raman microscopy in combination with TGA, XRD, FTIR, and backscattered electron imaging, Zhang et al. (2024a) showed that carbonation depths derived from phase-sensitive techniques consistently exceed those indicated by phenolphthalein spray tests. For CEM I, 30% pulverised fuel ash (PFA), and 50% GGBS pastes, discrepancies of approximately 1.5–3.0 mm were reported, depending on binder composition and water-to-binder ratio. These differences arise because profile-based techniques detect the onset of $CaCO_3$ formation within partially carbonated regions, whereas phenolphthalein primarily reflects the pH drop associated with near-complete portlandite depletion.

Depth-resolved chemical measurements further confirm that significant carbonation can occur beyond the visually defined carbonation front. Combined modelling and experimental profiling have shown bound CO_2 concentrations of approximately 0.5–1.0 $mol \cdot L^{-1}$ at depths classified as uncarbonated by phenolphthalein, with discrepancies

increasing in denser concretes and at later exposure times (Thiery et al., 2007). Similarly, thermogravimetric analysis has detected continued carbonate formation beyond ~9 mm in specimens for which phenolphthalein indicated no further carbonation, demonstrating that alkalinity loss and carbonate precipitation are not spatially coincident processes (Phung et al., 2015).

Consequently, the relationship between carbonation depth and total CO_2 uptake is non-linear and strongly dependent on binder composition and phase assemblage. Materials exhibiting similar phenolphthalein-measured carbonation depths can bind substantially different amounts of CO_2. In high-volume fly ash systems, the amount of bound CO_2 per unit carbonation depth has been reported to be up to 40% higher than in OPC pastes, reflecting enhanced carbonation of C–(A)–S–H rather than increased penetration alone (Van den Heede, De Schepper & De Belie, 2019). In light of these considerations, these findings demonstrate that carbonation depth and carbonation degree represent related but non-equivalent descriptors. Depth-based measurements remain useful for durability-related assessments tied to alkalinity thresholds, but are insufficient for evaluating reaction extent, phase evolution, or CO_2 utilisation efficiency. For such purposes, profile-resolved and uptake-based approaches are required, particularly in heterogeneous or non-OPC systems.

2.3.3. Phenolphthalein-based image analysis methods

Phenolphthalein staining remains widely used for rapid carbonation assessment due to its low cost, simplicity, and compatibility with standard laboratory practice. However, manual interpretation of the colour boundary is inherently subjective and sensitive to operator judgement, specimen moisture state, illumination conditions, and surface roughness. Digital image analysis has therefore been introduced to reduce operator dependence and to convert stained cross-sections into reproducible, specimen-scale descriptors of carbonation geometry, extending assessment beyond single-point depth measurements.

Most phenolphthalein-based image analysis workflows follow three main steps: (i) controlled image acquisition using fixed lighting conditions, camera settings, and colour references; (ii) colour-based segmentation of stained and unstained regions using RGB or alternative colour spaces, typically combined with thresholding and basic morphological

filtering; and (iii) extraction of quantitative metrics, such as average carbonation depth along a defined reference line, carbonated area fraction, front roughness, or spatial statistics describing non-uniformity (Lee et al., 2016; Giulietti et al., 2021; Choi et al., 2017). Silveira & Isaia (2022) demonstrated that automated segmentation reduced the coefficient of variation in measured carbonation depth from approximately 18–22% (manual interpretation) to below 10% across replicate specimens, provided that image acquisition conditions were strictly controlled. However, their results also showed that threshold selection remained sensitive to local staining intensity and surface moisture, particularly near partially carbonated regions, limiting transferability across specimens without recalibration.

More recent studies have explored machine-learning-based segmentation to further reduce sensitivity to illumination gradients, uneven staining, and local colour variability. While these methods can improve robustness in heterogeneous specimens, their performance is strongly dependent on training dataset quality, consistent sample preparation, and careful validation against manually annotated or independently measured references (Madera, 2018). Researchers have also attempted to extract continuous information from phenolphthalein intensity rather than binary classification (Silveira & Isaia, 2022), where greyscale intensity profiling were adopted to approximate gradual pH transitions; however, the obtained intensity–depth relationships varied significantly with dye concentration and surface reflectance, requiring specimen-specific calibration. As a result, such methods were still considered semi-quantitative and unsuitable for direct comparison across different binders or exposure histories without independent validation.

Fundamentally, phenolphthalein-based image analysis remains constrained by the indicator's pH response range and does not directly resolve carbonate formation. High-resolution optical pH imaging provides an independent reference for this limitation. Using luminescent sensor foils, Müller et al. (2018) resolved continuous pH gradients from pH ~ 12.5 to below 8.5 across carbonated concrete cross-sections, recording gradients of up to 1.5 pH units per millimetre and spatial resolutions down to 35 μm. Their measurements showed that substantial pH reduction extends well beyond the phenolphthalein colour boundary and proceeds gradually rather than as a sharp front, confirming that phenolphthalein delineates only a threshold crossing rather than the full alkalinity profile.

Within these constraints, phenolphthalein-based image analysis is most effective as a high-throughput, comparative tool for assessing carbonation geometry and heterogeneity. When paired with depth-resolved mass or phase measurements (e.g. TGA or XRD at selected locations), it provides a practical link between spatial carbonation patterns and CO_2 uptake trends while maintaining experimental efficiency.

2.4. Fibre reinforced cementitious composites

2.4.1. Fibre reinforcement in cement-based materials

Cement-based materials exhibit high compressive strength but low tensile strength and strain capacity, leading to brittle crack localisation under tensile or flexural loading. Fibre reinforcement modifies this behaviour by bridging cracks and redistributing stresses, thereby increasing fracture energy, post-cracking load capacity, and deformation tolerance (Curosu et al., 2021). The effectiveness of this mechanism depends on fibre stiffness, geometry, volume fraction, orientation, and fibre–matrix bond characteristics (Balea et al., 2021). Short, discontinuous fibres are most commonly used in fibre-reinforced concrete (FRC) for pavements, impact-resistant structures, seismic elements, and offshore applications (Lee, Choi & Kim, 2023; Nascimento et al., 2023). Fibre systems employed in cementitious composites can be broadly classified into metallic, polymeric, mineral, and natural fibres (*Figure 2.1*), each exhibiting distinct mechanical efficiency and durability constraints.

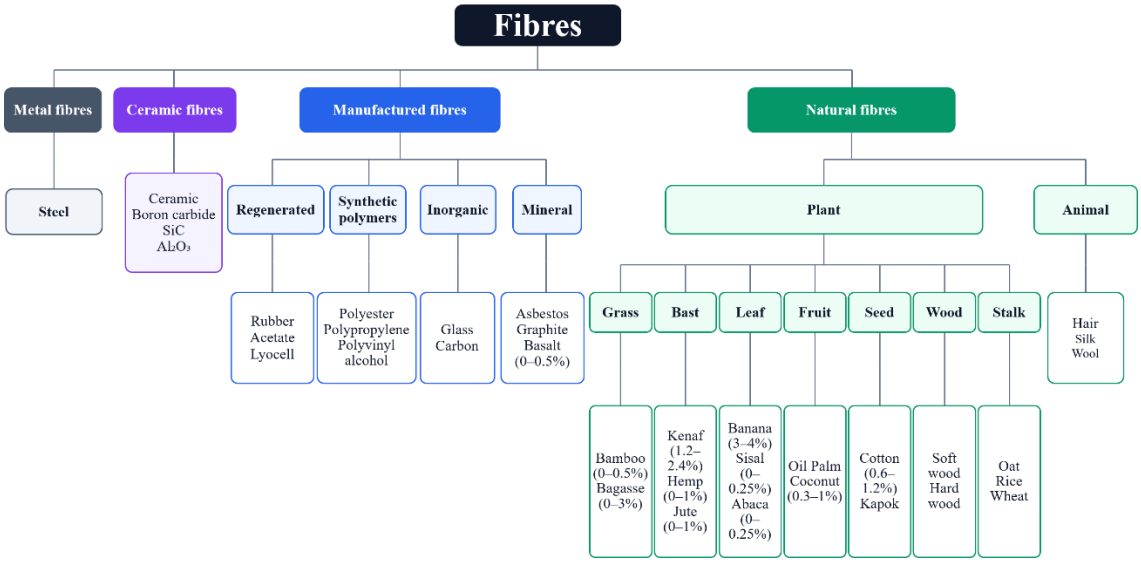


Figure 2.1. Classification of fibres and optimum replacement percentage by volume (vol.%) of some natural fibres in cement composites (Abdalla et al., 2023).

Steel fibres remain the most efficient crack-bridging reinforcement due to their high elastic modulus (~200 GPa) and tensile strength. Pull-out tests showed peak pull-out loads exceeding 1 kN and energy absorption capacities above 1000 N·mm for hooked or deformed steel fibres, substantially higher than polymeric fibres (Ravichandran et al., 2022). Crack-bridging efficiency scales with fibre aspect ratio and anchorage geometry, enabling significant improvements in flexural toughness and post-peak load retention at dosages of ~1.0–2.0 vol.% in conventional concrete and ~2.0 vol.% in UHPC. However, steel fibres are susceptible to corrosion once exposed through cracking or carbonation-induced alkalinity loss, particularly in chloride-rich environments, leading to section loss and bond degradation (Liew & Akbar, 2020).

Synthetic polymer fibres, including polypropylene (PP) and polyvinyl alcohol (PVA), provide corrosion resistance and improved workability relative to steel fibres. PVA fibres, with elastic moduli of ~40 GPa (Lan, Zhou & Xu, 2021), form strong chemical and hydrogen bonds with cement hydrates, enabling multiple microcracking and strain-hardening behaviour in engineered cementitious composites at fibre contents of 1–2 vol.% Hou & Li (2023). Ravichandran et al. (2022) report tensile strains of ~2–3% with crack widths below 50 μm in PVA-based systems. In contrast, PP fibres (modulus ~3–5 GPa) contribute mainly to plastic shrinkage control and impact resistance, with limited load-carrying capacity unless used at higher dosages (>1.5 vol.%).

Glass fibres, particularly alkali-resistant formulations containing ≥16 wt.% ZrO_2, exhibit tensile strengths of 1700–3500 MPa and moduli of 70–80 GPa. Despite improved durability compared with conventional E-glass, long-term exposure to alkaline pore solutions still results in gradual strength loss and embrittlement, limiting their structural application (Shafei et al., 2021). Carbon fibres offer superior stiffness and strength but remain restricted to niche uses due to cost and brittle pull-out behaviour (Monazami & Gupta, 2022).

Natural fibres such as jute, flax, sisal, and bamboo have gained attention as low-carbon alternatives derived from renewable resources (Bhattacharyya, Subasinghe & Kim, 2015; Hamada et al., 2023; Onuaguluchi & Banthia, 2016). Reductions of up to 40–60% have been reported in embodied energy compared with steel fibres (Balea et al., 2021). However, natural fibres exhibit high variability in geometry and mechanical properties, moisture sensitivity, and susceptibility to alkaline degradation, resulting in fibre

mineralisation, lumen collapse, and interfacial weakening over time (Tolêdo Romildo D. et al., 2003). These issues are discussed in detail in Section 2.5.

Fibre performance is strongly governed by dosage and dispersion quality. Typical effective volume fractions range from 0.5–2.5 vol.% depending on fibre type and target behaviour (Ragalwar et al., 2020; Naaman, 2000). At fibre contents above ~2 vol.%, reported compressive strength reduces 5–15% when dispersion is inadequate (Balea et al., 2021). de Felice et al. (2020) reported coefficients of variation of 15–40% in tensile strength for fibre-reinforced composites, highlighting the sensitivity of mechanical performance to manufacturing consistency.

From a practical perspective, fibre addition increases yield stress and plastic viscosity, with severity controlled by fibre aspect ratio, surface roughness, and volume fraction. Conventional mixing becomes unreliable above ~1.5–2.0 vol.% for most fibre types without specialised procedures (Wu et al., 2023c). Inadequate dispersion promotes fibre balling and local defects, which act as preferential transport pathways and compromise durability (Booya et al., 2019). These limitations motivate alternative reinforcement strategies with controlled fibre placement and continuity, discussed in Section 2.4.4.

2.4.2. Fibre–matrix interfaces and interfacial porosity

The fibre–matrix interfacial transition zone (ITZ) is a critical microstructural region governing stress transfer, crack initiation, and durability in fibre reinforced cementitious composites. Compared with the aggregate–paste ITZ, the fibre ITZ is more sensitive to fibre surface chemistry, geometry, and wetting behaviour, owing to the high surface area–to–volume ratio of fibres and local disturbance of particle packing during casting.

Experimental characterisation consistently shows that the fibre ITZ extends approximately 10–50 μm from the fibre surface and exhibits elevated porosity, preferential portlandite accumulation, and reduced C–S–H density relative to the bulk paste (Zhou, Fan & Chen, 2016). Using X-ray computed tomography and SEM-based segmentation, Tao, Hadigheh & Wang (2024) reported ITZ porosities 15–25% higher than the surrounding matrix, with pore size distributions skewed toward larger capillary pores within the first 20 μm from the fibre surface. This porosity gradient was attributed to wall effects, local water enrichment, and hindered cement particle packing. The effect

intensified for smaller-diameter fibres due to increased curvature, leading to higher local water-to-cement ratios and weaker interfacial zones.

Fibre surface chemistry strongly modulates ITZ quality. Hydrophobic and chemically inert fibres (e.g. carbon and polypropylene) exhibit poorer wetting and greater air entrapment, resulting in more porous and discontinuous ITZs compared with hydrophilic fibres or alkali-reactive glass fibres (Shafei et al., 2021). SEM observations show that poor wetting correlates with interfacial gaps and reduced hydration product coverage, which lowers interfacial shear resistance and promotes premature debonding. Elevated ITZ porosity, on the other hand, directly reduces fibre–matrix bond strength and shifts failure toward interfacial slip rather than fibre rupture. Incorporation of supplementary cementitious materials has been shown to partially mitigate this weakness. Pozzolanic reactions consume portlandite and refine pore structure within the ITZ, increasing C–S–H density and improving mechanical interlock. In silica fume– and slag-modified matrices, a transition from clean fibre pull-out to roughened, partially ruptured fibre surfaces were observed, which is consistent with enhanced interfacial bonding (Lin et al., 2023).

Fibre geometry and surface modification provide additional control over interfacial behaviour. Twisted or deformed fibres increase effective contact area and induce non-uniform stress fields that raise frictional resistance, with interfacial shear strength increases sufficient to shift failure from debonding to fibre rupture in carbon fibre bundles (Pei et al., 2021). Surface treatments further enhance bonding: silica-based coatings have been shown to increase interfacial shear strength by up to ~40%, with micro-silica coatings densifying the ITZ through combined physical filling and pozzolanic reaction, whereas coarser coatings primarily enhance mechanical interlocking but may introduce local stress concentrations (Lv, Pei & Zhu, 2025).

Fibre ITZ porosity arises primarily from wall effects and wetting limitations, with severity governed by fibre diameter, surface chemistry, and matrix composition. These interfacial features not only control mechanical load transfer but also act as preferential transport pathways for CO_2 and chlorides. While such characteristics are common to all fibre reinforced cementitious systems, natural fibres introduce additional moisture-driven and chemical effects, which are addressed separately in Section 2.5.

2.4.3. Effects of fibres on cracking control and transport-related durability

Beyond their contribution to strength and ductility, fibres influence durability primarily through their effect on crack topology. Crack width, spacing, and connectivity govern the formation of continuous transport pathways, linking mechanical response directly to permeability and ingress of aggressive agents (Mechtcherine & Lieboldt, 2011).

Under tensile or flexural loading, fibres limit crack opening and promote the formation of multiple fine cracks rather than a small number of wide cracks. In hybrid PVA–PP systems, crack widths were limited to approximately 50 μm at tensile strains of ~2%, reflecting strong fibre–matrix interaction for crack initiation control combined with distributed cracking at higher strains (Hou & Li, 2023). Such crack patterns reduce the connectivity of preferential flow paths compared with unreinforced or poorly reinforced matrices.

The effectiveness of crack control depends on reinforcement scale. In textile-reinforced cementitious composites, the addition of microfibres increased crack density while reducing individual crack widths, with an optimum reported for 6 mm PVA microfibres at 0.7 vol.% (Gielis et al., 2024). In these systems, macro-scale reinforcement governs crack spacing, while micro-scale reinforcement suppresses crack coalescence. This division of roles is consistent with broader observations that microfibres primarily control early microcracking, whereas macrofibres act after crack localisation (Balea et al., 2021).

Reductions in crack width generally translate into reduced transport, but the relationship is not linear. Fibre-reinforced concretes exhibit 30–50% lower water permeability than unreinforced controls when crack widths are maintained below approximately 100 μm under comparable loading(Zeng et al., 2024; Su et al., 2021). As a result, permeability often exhibits a non-monotonic dependence on fibre volume fraction: low contents (<0.5 vol.%) provide insufficient crack-bridging density, intermediate contents (~0.5–2.0 vol.%) minimise permeability, and higher contents (>2.0 vol.%) increase transport due to workability loss, fibre agglomeration, and incomplete consolidation.

In some fibre systems, transport is influenced not only by cracking but also by fibre-related interfacial effects. Increased permeability has been reported in pulp fibre–reinforced concretes, attributed to porous fibre–matrix interfaces and moisture retention

associated with cellulosic fibres (Jamshaid et al., 2022; Feng et al., 2023). Surface functionalisation can partially mitigate these effects by modifying interfacial chemistry and limiting ion availability, extending the role of fibres beyond purely mechanical crack control (Lv, Pei & Zhu, 2025). Long-term durability therefore depends on the stability of crack control mechanisms over time. Degradation of fibres or fibre–matrix interfaces reduces crack-bridging efficiency and can progressively increase transport at later ages, even if early-age performance is favourable. Durability assessment of fibre-reinforced cementitious composites must therefore consider not only initial crack geometry but also the evolution of fibre performance and transport pathways under service conditions.

2.4.4. Textile-reinforced mortars and structured fibre systems

While Sections 2.4.1–2.4.3 addressed fibre reinforcement primarily in the context of short, randomly dispersed fibres, textile-reinforced mortars (TRM), also referred to as textile-reinforced concrete or fabric-reinforced cementitious matrix composites, employ continuous fibres arranged in predefined architectures prior to matrix impregnation. The use of woven fibre architectures in cementitious matrices was already being investigated experimentally in the 1990s, with early studies demonstrating the importance of textile geometry and matrix penetration for composite behaviour (Peled, Bentur & Yankelevsky, 1994). Common configurations include orthogonal grids, woven or knitted fabrics, and three-dimensional (3D) textiles in *Figure 2.2* (Peled, Mobasher & Bentur, 2017; Nahum, Peled & Gal, 2020; Koutas et al., 2019).

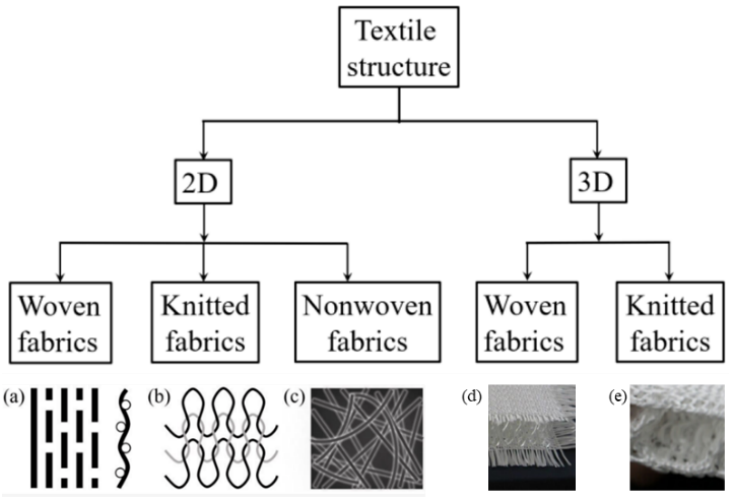


Figure 2.2. Textile category and structure.

TRM/FRCM systems typically consist of one or more textile layers embedded within a fine-grained cementitious or lime-based mortar. The textiles are composed of continuous fibre rovings in warp and weft directions and are manufactured from materials such as carbon, alkali-resistant glass, basalt, steel, aramid, and PBO, offering a wide range of stiffness and tensile capacity (De Santis et al., 2017; Koutas et al., 2019). Compared with dispersed short fibres, predefined fibre alignment enables more efficient mobilisation of fibre tensile strength. Direct tensile tests show that aligned textiles can activate 60–90% of fibre tensile capacity, whereas randomly oriented short fibres typically mobilise less than 30–40% under similar loading (Sadrolodabaee et al., 2021).

The tensile response of TRM systems is characterised by a multi-stage behaviour: an initial elastic stage governed by the matrix, followed by a multiple-cracking regime with progressively reduced stiffness, and a post-cracking stage in which load is carried primarily by the textile until fibre rupture or pull-out occurs (Wu et al., 2023). The onset of multiple cracking typically occurs at matrix cracking stresses of 2–4 MPa, while ultimate tensile strengths of 800–2000 MPa at the fibre level have been reported depending on textile material and architecture (Sadrolodabaee et al., 2021). Bond quality and matrix penetration into textile yarns strongly control crack spacing and stress redistribution, distinguishing TRM behaviour from that of short fibre reinforced concretes.

Textile architecture governs bond–slip behaviour and failure mode. Two-dimensional (2D) textiles rely primarily on frictional and chemical bonding at the textile–matrix interface, which often results in progressive debonding and pull-out (Gielis et al., 2024; Aybar, 2025). By contrast, 3D textiles incorporating through-thickness fibres provide mechanical anchorage that suppresses interlayer delamination and increases energy dissipation. Comparative tests show that 3D TRC systems exhibit 20–40% higher post-cracking stiffness and reduced sensitivity to debonding relative to 2D configurations (Ventura et al., 2022). Twisted yarns and surface coatings further enhance bond by improving mortar penetration and increasing effective contact area, shifting failure modes from interfacial slip toward fibre rupture (Ghiassi, 2019).

Despite their mechanical efficiency, TRM systems exhibit significant scatter in measured properties. A RILEM round-robin programme covering 28 FRCM composites reported coefficients of variation of 15–40% in tensile strength and 20–50% in cracking stress, attributed to sensitivity to specimen preparation, curing conditions, gripping systems, and

the quasi-brittle nature of textile–matrix interaction (De Santis & De Felice, 2015; de Felice et al., 2020). This variability exceeds that typically reported for short fibre reinforced concretes and highlights the need for improved standardisation and quality control.

From a practical perspective, structured fibre systems allow high effective fibre volume fractions—typically 3–8% within textile layers—without the workability loss and fibre agglomeration that limit dispersed fibre systems to approximately 1–2% by volume (Wu et al., 2023). Controlled fibre alignment reduces orientation-related scatter and enables thin sections and complex geometries. Hybrid systems combining textiles with short fibres further allow reinforcement roles to be separated by scale, with textiles providing primary load-bearing capacity and short fibres enhancing matrix crack control (Alma'aitah, Ghiassi & Dalalbashi, 2021; Raupach & Morales Cruz, 2016).

TRM and FRCM systems have been successfully applied in strengthening and lightweight construction, particularly where thin sections and high tensile efficiency are required (Zhang & Deng, 2022). However, broader adoption remains constrained by the absence of harmonised design models, standardised durability assessment methods, and long-term performance data under combined mechanical loading and environmental exposure. Addressing these limitations is essential for the reliable integration of structured fibre systems into cementitious construction.

2.5. Natural fibre reinforced cementitious composites

2.5.1. Properties of natural fibres

Natural fibres are hierarchical biocomposites composed primarily of cellulose, hemicellulose, and lignin, whose relative proportions govern mechanical performance, moisture sensitivity, and durability in cementitious environments (Lv et al., 2023; Wei & Meyer, 2015). Cellulose forms semi-crystalline microfibrils that provide tensile strength and stiffness, while hemicellulose and lignin constitute an amorphous matrix controlling moisture affinity, viscoelastic response, and dimensional stability (Pacheco-Torgal & Jalali, 2011). The microfibril angle (MFA) is the angle between the cellulose microfibrils in the secondary cell wall and the longitudinal axis of the elementary fibre. A smaller MFA indicates greater alignment with the fibre axis and generally produces higher

longitudinal stiffness and strength. Fibres with MFAs below ~10° exhibit moduli up to three times higher than those with MFAs exceeding ~30° (Wu et al., 2023b).

Biochemical composition varies widely across fibre species and correlates directly with tensile performance. High-cellulose fibres such as cotton (~90% cellulose) and flax (~70–96%) exhibit high tensile strength and stiffness, with flax strengths of 800–1500 MPa and moduli of 27.6–80.0 GPa (Schiavon & Andrade, 2023; Miyauchi, 2023). Fibres with higher lignin content, such as coir, show lower strength (~300–500 MPa) but higher elongation capacity. Sisal fibres, with intermediate composition (~68% cellulose, 12–14% lignin), typically exhibit strengths around 500–700 MPa and moduli of 4–6 GPa (Silva et al., 2010; Thomas & Jose, 2022). Reduced tensile efficiency in lignin-rich fibres is associated with higher MFA and lower cellulose crystallinity (Wu et al., 2023b).

A defining morphological feature of natural fibres is the lumen, the hollow internal cavity extending longitudinally through the elementary fibre cell. Its size and continuity influence fibre density, internal water storage and capillary transport. Reported lumen diameters range from 5–10 μm in flax to 15–25 μm in sisal, corresponding to void fractions of approximately 10–30% of the fibre cross-section (Liu & Lv, 2021; Liu et al., 2024b). Combined with abundant hydroxyl groups in cellulose and hemicellulose, this structure confers pronounced hydrophilicity. Under high relative humidity, moisture uptake values of 60–80% are typical for bast and leaf fibres, while highly porous fibres may exceed 300–500%, depending on lumen continuity and cell-wall porosity (Addis, Sendekie & Satheesh, 2022; Lv et al., 2023). Water absorption is initially governed by capillary filling of the lumen, followed by slower diffusion and polymer-chain swelling in the amorphous cell-wall regions (Li et al., 2021; Addis, Sendekie & Satheesh, 2022).

When incorporated into cementitious matrices, the low intrinsic density of natural fibres (~1.2–1.5 $g \cdot cm^{-3}$) and entrapped air reduce composite density by approximately 5–15%, but this is commonly accompanied by increased open porosity and water absorption (Yeh, Wu & Yang, 2024). Review data show that natural-fibre-reinforced mortars frequently exhibit 20–60% higher water absorption and one to two orders of magnitude higher sorptivity than fibre-free references when fibre treatment and dispersion are not optimised (Wu et al., 2023b). These effects are attributed to fibre swelling, interfacial voids, and lumen connectivity.

Natural fibres exhibit substantial variability in tensile properties due to inter-species differences and intra-species heterogeneity arising from growth conditions and extraction processes. Reported tensile strengths typically span 300–1000 MPa, with elastic moduli between 4 and 30 GPa, and elongation at break ranging from 1–2% for stiff bast fibres to >10–15% for compliant leaf fibres (Camargo et al., 2020). For untreated fibres embedded in Portland cement matrices, interfacial shear strengths are commonly reported in the range of 0.5–1.5 MPa, significantly lower than for synthetic fibres, due to poor chemical compatibility and progressive alkaline degradation (Mejia-Ballesteros et al., 2025). As a result, relatively long embedment lengths are required to mobilise fibre tensile capacity, and pull-out rather than fibre rupture often governs failure in short-fibre systems.

In practice, natural fibres are frequently processed into spun yarns, in which elementary fibres are aligned and twisted into continuous bundles. Textile processing improves handling and tensile coherence but introduces internal porosity and hierarchical transport pathways within the yarn (El Mogahzy, 2009; Signorini et al., 2024). In cement-based materials, spun natural fibre yarns have been used predominantly in textile-reinforced mortars and fabric-reinforced cementitious composites, where yarns are arranged in woven or grid-based architectures to provide directional reinforcement (Zhang & Deng, 2022; Orlowsky, Beßling & Kryzhanovskyi, 2023). By contrast, their use as discrete reinforcement and internal transport modifiers in conventional mortars or concretes remains sparsely explored.

2.5.2. Natural fibres in cement composites

Natural fibres have been investigated as reinforcement in cementitious materials for several decades (Aziz, Paramasivam & Lee, 1981), with renewed interest driven by the potential to reduce reliance on synthetic reinforcement, lower material density and utilise renewable feedstocks. More recent studies have examined their performance in a wider range of cementitious systems and processing conditions (Kurpińska et al., 2022). Experimental studies consistently show that low-volume incorporation of plant fibres can improve flexural toughness and post-cracking behaviour, although strength benefits are highly fibre- and processing-dependent (Abdalla et al., 2023). Incorporation of plant fibres including pinecone, malva, coconut, and date palm below 1.0 vol.% improve flexural strength by 10–35%, while reduction of 5–20% were observed in compressive strength due to increased porosity and fibre-induced defects (Labib, 2022).

Most reported natural fibre cement composites employ short, dispersed fibres, for which fibre distribution is a primary determinant of performance. Industrial fibre–cement products therefore rely on controlled manufacturing routes such as the Hatschek process, extrusion, or slurry vacuum dewatering, which promote fibre alignment and limit agglomeration (Chen et al., 2023; Wu et al., 2023b). While these methods improve fibre distribution, they rely on dedicated equipment and increase production cost. Conventional casting and cast-in-place mixing are more accessible but typically result in greater variability in fibre dispersion and composite quality (Wu et al., 2023b).

To overcome these constraints, structured and aligned natural fibre systems have been explored, drawing on concepts from textile-reinforced mortars (Section 2.4.4). Codispoti et al. (2015) demonstrated that flax- and hemp-based textiles embedded in lime- and cement-based mortars achieved stable multiple cracking and tensile strain capacities of 0.4–0.6%, significantly exceeding those of short-fibre composites at comparable fibre contents. Similar improvements have been reported for jute- and hemp-based TRM systems used in masonry strengthening, where controlled fibre orientation enabled efficient stress transfer and reduced scatter relative to randomly reinforced matrices (Muzyczek, 2020; Sen & Jagannatha Reddy, 2013).

Beyond reinforcement geometry, the physical and chemical characteristics of natural fibres strongly influence composite behaviour. Irregular fibre surfaces and lumen-driven roughness enhance mechanical interlocking, contributing to improved bond strength compared with smooth synthetic fibres of similar stiffness (da Silva et al., 2023). The porous structure of cellulosic fibres has also motivated their use as internal moisture agents (Choi, 2022): abaca, hemp, and jute fibres absorbed 200–300% of their dry mass in water and reduced autogenous shrinkage by up to 40% at 7 days when used at 0.5 wt.% of cement, although early hydration was delayed by 2–5 h due to interactions between fibre constituents and cement pore solution chemistry and fibre-dependent (Siqueira, Filho & Koenders, 2015; Oinam et al., 2023).

Despite these benefits, durability remains the dominant barrier to widespread application. High moisture uptake induces repeated swelling–shrinkage cycles, weakening the fibre–matrix interface and increasing variability in mechanical response (Wu et al., 2023b). In addition, fibre mineralisation driven by precipitation of $Ca(OH)_2$ within fibre lumens and

cell walls leads to progressive embrittlement and loss of crack-bridging capacity (Tolêdo Filho et al., 2000). Microstructural studies report near-complete lumen filling within months of exposure in Portland cement matrices, accompanied by reductions in fibre tensile capacity exceeding 50% (Lv et al., 2023; Addis, Sendekie & Satheesh, 2022). Reported mitigation strategies include partial replacement of OPC with supplementary cementitious materials to reduce portlandite availability (Pacheco-Torgal & Jalali, 2011), and carbonation curing to convert $Ca(OH)_2$ to $CaCO_3$, which has been shown to stabilise fibre–matrix interfaces and improve post-cracking performance and applying carbonation curing to convert $Ca(OH)_2$ to $CaCO_3$, which resulted in improved fibre-matrix adhesion and mechanical performance (Addis, Sendekie & Satheesh, 2022).

2.5.3. Fibre conditioning and pre-treatment

To mitigate moisture sensitivity and durability limitations, surface conditioning and pre-treatment are widely applied to natural fibres prior to incorporation into cementitious matrices (Zhou, Fan & Chen, 2016). Chemical and physical pre-treatments aim to modify fibre surface chemistry, internal structure, and moisture response, thereby improving compatibility with cementitious matrices. Among the reported approaches, alkalinisation, silane treatment, and hornification are the most extensively investigated (Li et al., 2021).

Alkali treatment using sodium hydroxide (NaOH) is the most widely applied chemical conditioning method. It selectively removes hemicellulose and partially degrades lignin, increasing cellulose exposure, surface roughness, and fibrillation, which improves mechanical interlocking at the fibre–matrix interface (Prabhu et al., 2021; Geremew et al., 2021). Typical protocols employ 5–10 wt.% NaOH for 1–24 hours at ambient to moderate temperatures (20–60 °C). Across multiple fibre types, moderate alkalinisation increased fibre tensile strength by 10–30% and interfacial shear strength by approximately 40–55%, translating into flexural strength gains of 15–35% in cementitious composites (Yeh, Wu & Yang, 2024; Camargo et al., 2020). However, exceeding this processing window leads to cellulose chain scission and microfibril damage, with reported reductions in fibre modulus of up to 25% under aggressive treatment conditions (Li et al., 2021; Addis, Sendekie & Satheesh, 2022).

Silane treatment provides an alternative conditioning route based on covalent coupling and surface hydrophobisation. Organosilane agents react with fibre hydroxyl groups to

form stable siloxane networks, reducing water affinity while improving interfacial adhesion with cement hydrates (Xie et al., 2010). Treatments typically involve 1–5 vol.% silane solutions (Tonoli et al., 2013), under mildly acidic conditions for short exposure times. Reported outcomes include reductions in fibre water uptake of 40–70% and increases in fibre–matrix bond strength of 20–45%, alongside improved dimensional stability under wet–dry cycling (Addis, Sendekie & Satheesh, 2022). Contact angle measurements commonly increase from ~30–40° for untreated fibres to >90°, indicating a transition from hydrophilic to moderately hydrophobic behaviour.

Hornification offers a chemical-free conditioning approach based on repeated wetting–drying cycles. During drying, irreversible hydrogen bonding between adjacent cellulose microfibrils densifies the cell wall, reduces lumen accessibility, and limits fibre swelling (Mo et al., 2022). Typical protocols involving 5–10 cycles with drying temperatures of 60–80 °C have been shown to reduce fibre water absorption by 30–60% and increase fibre stiffness by approximately 10–20% (Mantovani et al., 2025). In cementitious composites, hornified fibres exhibit improved fibre–matrix adhesion and reduced interfacial porosity, leading to enhanced crack-bridging stability under cyclic moisture exposure (Liu & Lv, 2021). Other surface modifications, including oxalic acid treatment and crystallisation-based methods, have also been reported to enhance bond strength while influencing carbonation behaviour and pore structure (Schiavon & Andrade, 2023; Liang et al., 2025)

2.5.4. Internal curing and moisture regulation via natural fibres

Beyond their role as reinforcement, natural fibres have been investigated as internal curing agents due to their intrinsic porous structure and high-water absorption capacity. Plant fibres contain longitudinal lumens and cell-wall micropores that can absorb several times their own mass in water and subsequently release this moisture during cement hydration, partially compensating for self-desiccation in low water-to-cement ratio systems (Li et al., 2023).

Experimental evidence confirms a direct link between fibre moisture absorption capacity and shrinkage mitigation. Using abaca, hemp, and jute fibres at 0.5 wt.% of cement, Choi (2022) measured moisture absorption values of approximately 213–291% by mass, with corresponding reductions in 7-day autogenous shrinkage of 37–52% relative to plain mortar. Linear correlations ($R^2 > 0.98$) were reported between fibre absorption capacity

and shrinkage compensation at 1, 2, and 7 days, indicating that internal curing efficiency is governed primarily by fibre pore structure rather than fibre type alone. These results align with the mechanistic framework proposed by Jongvisuttisun, Leisen & Kurtis (2018), who demonstrated that effective internal curing by natural fibres requires (i) sufficient water uptake during mixing, (ii) timely desorption driven by capillary tension and osmotic gradients, and (iii) hydraulic connectivity between fibre pores and the surrounding cement paste.

Internal curing by natural fibres also influences hydration kinetics and microstructure development. Isothermal calorimetry and ultrasonic pulse velocity measurements reported by Gwon, Choi & Shin (2021) showed delayed early hydration peaks (by 2–5 h) due to fibre-derived sugars, followed by increased cumulative heat release and higher $Ca(OH)_2$ contents at 28 days (up to 12.3% vs. 9.7% in plain paste), attributed to prolonged hydration enabled by gradual moisture release. SEM observations confirmed dense secondary hydration products forming around fibres, indicating localised hydration enhancement in fibre-adjacent regions. Similar observations were reported, where lumen-mediated capillary flow was identified as the dominant early-age release mechanism, with diffusion through cell walls governing longer-term moisture supply (Jongvisuttisun, Leisen & Kurtis, 2018).

The internal curing effect is nevertheless time-dependent and sensitive to fibre stability. Progressive alkaline degradation and fibre mineralisation reduce lumen accessibility and moisture release efficiency, diminishing shrinkage mitigation at later ages. In addition, high fibre water uptake alters fresh-state rheology and effective water availability, requiring careful adjustment of mixing water to avoid unintended porosity increases. Consequently, the use of natural fibres as internal curing agents has been most effective at low fibre contents ($\leq$ 0.5 wt.%) and in systems where early-age shrinkage control is prioritised over long-term crack-bridging performance (Islam & Ahmed, 2018; Gwon, Choi & Shin, 2021; Choi, 2022).

2.6. Fibre-enhanced carbonation behaviour and practical implications

Although the chemical pathways governing carbonation in cement-based materials are well established (Section 2.2), practical CO_2 uptake in dense matrices is often restricted by gas and moisture transport rather than reaction kinetics. This limitation has prompted

increasing interest in approaches that modify internal transport characteristics instead of relying solely on surface exposure or elevated CO_2 concentration (Fernández Bertos et al., 2004; Mechtcherine & Lieboldt, 2011). In fibre-reinforced cementitious systems, fibres introduce additional interfaces, local porosity gradients, and moisture reservoirs that can measurably alter carbonation transport and reaction patterns (Schiavon & Andrade, 2023; Wu et al., 2023b; Onuaguluchi & Banthia, 2016).

Experimental studies demonstrate that fibres can actively influence carbonation behaviour rather than acting as mechanically inert inclusions. In fibre–cement composites containing bleached eucalyptus pulp, Urrea-Ceferino et al. (2017) reported a 17 % increase in matrix densification and a 43 % increase in modulus of rupture after carbonation curing, attributed to $CaCO_3$ precipitation within fibre-adjacent pore regions. In hemp fibre-reinforced alkali-activated mortars, accelerated carbonation reduced water absorption by approximately 30 % while increasing compressive and flexural strength, although partial fibre embrittlement was observed at advanced carbonation stages (Merta et al., 2022).

Clear evidence for transport-controlled enhancement is provided by Wu & Qiu (2022), where 2 vol.% hollow sisal fibres into reactive magnesia cement. Under 10 % CO_2 curing, carbonation depth increased by a factor of 2–3 compared with fibre-free and PVA-fibre controls, while 14-day compressive strength increased from 20.9 MPa to 39.3 MPa. Depth-resolved FTIR and XPS analyses showed sustained carbonation to depths exceeding 15 mm, whereas solid PVA fibres produced only marginal changes. The authors attributed this effect directly to lumen-mediated CO_2 transport, noting that lumen openings (1–10 μm) are orders of magnitude larger than capillary pores and exceed the mean free path of CO_2 molecules, enabling efficient diffusion

A commonly proposed mechanism for fibre-induced carbonation enhancement is the development of preferential CO_2 pathways along the fibre–matrix interfacial transition zone (ITZ). As discussed in Section 2.4.2, ITZs surrounding natural fibres typically exhibit porosities of 25–35 %, compared with 15–20 % in bulk paste, forming partially connected void networks along fibre lengths (Ma, Yan & Kasal, 2025; Schiavon & Andrade, 2023). Fernández Bertos et al. (2004) similarly reported that interfacial porosity and moisture accumulation at fibre surfaces promote local CO_2 dissolution and reaction,

particularly under intermediate relative humidity. These features can increase effective carbonation depth even when bulk permeability remains low.

However, fibre effects on carbonation are not universally accelerating. Schiavon & Andrade (2023; Mejia-Ballesteros et al., 2025) showed that mortars containing 2 vol.% oxalic-acid-treated coir fibres exhibited slower carbonation rates than untreated systems. Image analysis and MIP indicated reduced ITZ porosity and disrupted interfacial connectivity, demonstrating that improved fibre–matrix bonding can offset transport benefits. The net influence of fibres on carbonation therefore reflects a balance between transport enhancement via porous interfaces and permeability reduction through crack control and interfacial densification.

As discussed in Section 2.2.3, the reduction in cement-paste alkalinity caused by carbonation is a long-established consequence of consumption of alkaline buffering phases. In natural-fibre composites, this reduction can be beneficial because highly alkaline Portland cement environments promote hydrolysis and mineralisation of cellulosic fibres (Tolêdo Filho et al., 2000; Wei & Meyer, 2015; Addis, Sendekie & Satheesh, 2022). Sisal fibres that lost nearly all tensile capacity after prolonged exposure to $Ca(OH)_2$ solutions retained 60–70 % of their original strength when embedded in carbonated matrices, accompanied by reported increases in composite toughness of up to 80 % (Addis, Sendekie & Satheesh, 2022; Wei & Meyer, 2015).

In parallel, $CaCO_3$ precipitation at the fibre–matrix interface refines ITZ porosity and enhances load transfer. Short-term carbonation curing ($\leqslant$ 7 days) has been shown to increase compressive and flexural strength by 15–30 %, alongside substantial improvements in fracture toughness, reflecting both reduced fibre embrittlement and stronger interfacial bonding (Santos et al., 2015; Bui et al., 2021). These benefits are, however, system-dependent. As illustrated in previous section (Section 2.2.3), excessive carbonation can compromise steel passivation in reinforced systems and may overly densify the matrix, restricting moisture transport and increasing susceptibility to freeze–thaw damage in cold climates (Addis, Sendekie & Satheesh, 2022). These considerations highlight both the opportunity and the need for targeted carbonation strategies when applied to natural fibre–reinforced cementitious composites.

For an internal transport-modification strategy, effectiveness cannot be assessed solely from near-surface carbonation or a single specimen-average value. A transport modifier may have limited influence on the already highly carbonated exposed surface but a much larger influence at depths where the reference material remains transport-limited. Its significance should therefore be evaluated using both the magnitude and spatial distribution of the response, including depth-resolved CO_2 uptake, carbonation geometry and the distance over which the internal pathway remains active. These material-scale indicators establish whether the transport mechanism is effective, but they do not by themselves quantify whole-product CO_2 storage, gas utilisation efficiency or net environmental benefit.

2.7. Summary

Enforced carbonation has been widely investigated as a means of enhancing early-age mechanical performance in cement-based materials while enabling permanent CO_2 sequestration through mineralisation. Existing studies show that carbonation curing can promote matrix densification and carbonate precipitation within practical curing timescales. However, in dense cementitious systems, carbonation extent is consistently constrained by CO_2 transport rather than reaction kinetics alone. This limitation indicates that further improvements in carbonation efficiency depend on strategies that modify internal transport and moisture conditions, rather than relying solely on surface exposure, elevated CO_2 concentration, or extended curing duration.

Fibre-reinforced cementitious composites are well established for crack control and toughness enhancement, yet their interaction with carbonation processes remains insufficiently understood. Most reported systems employ short, randomly dispersed fibres, which are inherently limited by dispersion challenges, discontinuous interfaces, and variability in fibre–matrix interaction. For natural fibres, these limitations are compounded by high moisture uptake, alkaline degradation, and fibre mineralisation, which affect durability and mechanical reliability. As a result, the potential for fibres to influence CO_2 transport, carbonation geometry, and depth-dependent reaction behaviour has not been systematically examined.

Organised fibre systems, including textile- and yarn-based reinforcements, provide an alternative reinforcement approach by enabling controlled fibre placement, continuity,

and geometry. In particular, spun natural fibre yarns combine aligned fibre bundles with internal porosity and inter-fibre voids, altering moisture distribution and interfacial transport relative to conventional short-fibre composites. These characteristics suggest that yarns may function not only as mechanical reinforcement but also as placed internal modifiers of CO_2 and moisture transport under enforced carbonation curing.

The literature further indicates that fibres can influence carbonation through competing mechanisms. Porous fibre–matrix interfaces may facilitate preferential CO_2 ingress, while effective crack control, interfacial densification, and matrix refinement can restrict transport. Carbonation itself can mitigate alkaline degradation of natural fibres by lowering pore-solution alkalinity and densifying the fibre–matrix interface, improving fibre preservation and load transfer. However, the balance between transport enhancement, fibre durability, and mechanical performance remains unresolved, particularly in systems employing organised natural fibre reinforcement and controlled carbonation regimes.

Interpretation of existing studies is also limited by carbonation assessment methods. Phenolphthalein testing provides rapid visualisation of carbonation fronts but does not quantify CO_2 uptake or partially carbonated regions, while mass- and phase-based techniques capture total uptake without resolving spatial heterogeneity. This highlights the need for depth-resolved approaches that directly link carbonation geometry, reaction extent, and CO_2 sequestration efficiency in fibre-containing systems.

Taken together, the literature reveals a clear gap in understanding how organised natural fibre yarns influence internal CO_2 transport, carbonation mechanisms, and performance under enforced carbonation curing. The work presented in this thesis is hence designed to address these needs and to evaluate the feasibility of yarn-assisted carbonation as a transport-modifying strategy for enhancing CO_2 uptake in dense cement-based materials.

Chapter 3 Materials and methods

3.1. Research design and scope

This thesis employs a staged experimental design to develop cementitious composites reinforced with spun natural fibre yarns under enforced carbonation curing. Given the limited prior work within this field, the experimental programme was structured to progress from feasibility assessment to optimisation and performance evaluation (*Figure 3.1*).

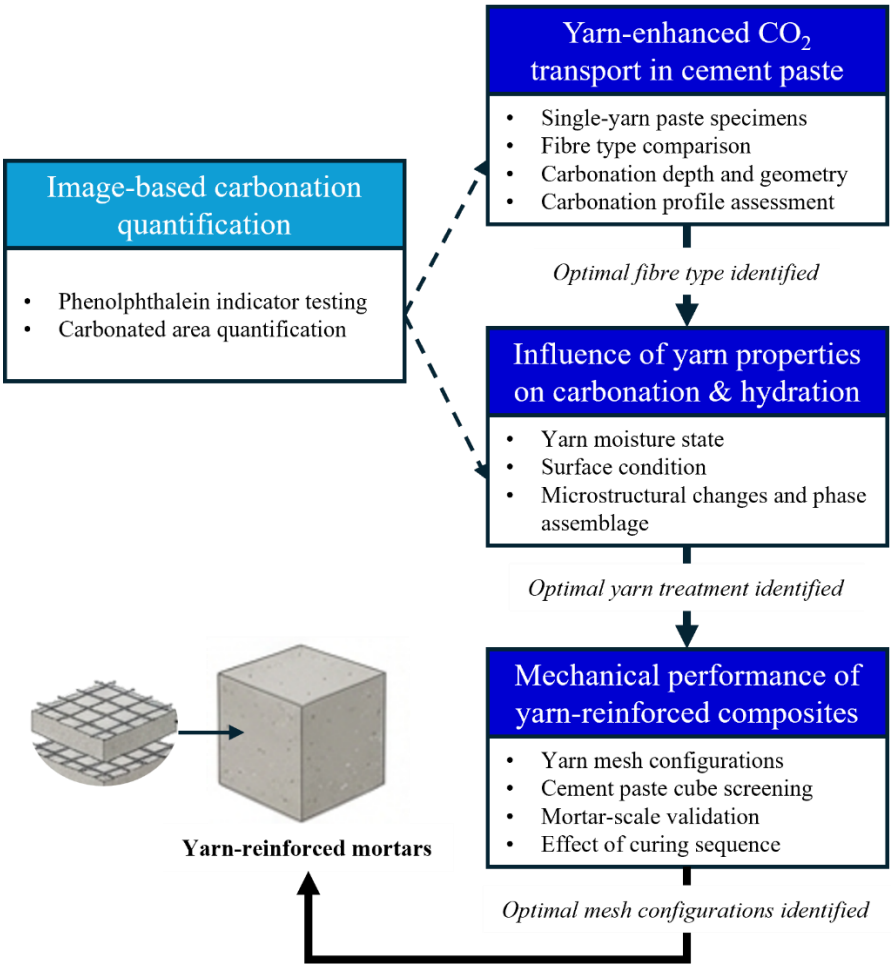


Figure 3.1. Schematic overview of the experimental sequence adopted in this thesis.

To enable rapid and reproducible quantification of heterogeneous carbonation in yarn-reinforced systems, an image-based analysis method based on phenolphthalein indicator testing was first developed. This method, presented in Chapter 4, establishes a consistent analytical framework for all subsequent image-based carbonation assessments reported in this thesis.

Regarding the material selection, the study first screens multiple natural fibre yarns to assess their ability to promote CO_2 transport and carbonation development in cement paste systems, enabling identification of a suitable yarn type for further study. The selected yarn was then examined to evaluate the influence of yarn condition and pre-treatment on carbonation behaviour, with emphasis on fibre–matrix interaction, moisture retention, and interfacial transport. Finally, the optimised yarn type and conditioning strategies were applied to cement paste and mortar specimens to examine the effect of yarn spatial configuration on compressive strength under different curing sequences.

3.2. Materials

A range of commercially available spun natural fibre yarns, synthetic yarns, and untwisted jute fibres were used in this study. The materials were selected to represent fibres with contrasting chemical composition, internal structure, hygroscopicity, and yarn architecture, while remaining compatible with cementitious composites. Spun natural fibre yarns with diameters ranging from 0.29 to 4.38 mm and ply counts between 2 and 7 were sourced from Tenn Well, Eco, and MacCulloch & Wallis.

All natural fibre yarns underwent industrial pre-treatment prior to purchase. For jute, hemp, and cotton, this included removal of pectin, waxes, and hemicellulose, while wool yarns were scoured to remove lanolin. Selected cotton yarns were mercerised. These industrial processes ensured consistent surface quality and fibre cleanliness, allowing the yarns to be used as received without further laboratory processing. Representative appearances of the natural fibre yarns are shown in *Figure 3.2(a)–(g)*, and their basic properties are summarised in *Table 3.1*.

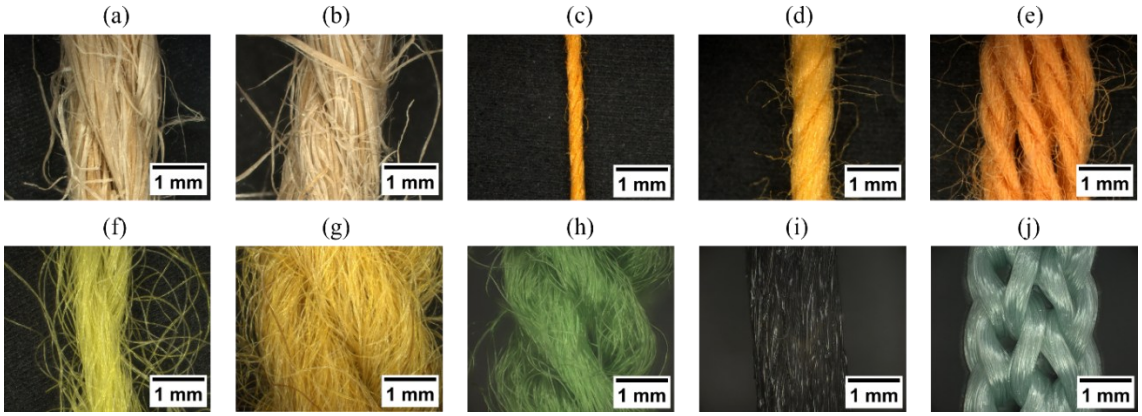


Figure 3.2. Selection of natural fibre yarns; (a) jute, (b) hemp, (c) cotton (super slim), (d) cotton (slim), (e) cotton (thick), (f) wool (slim), (g) wool (thick), (h) Acrylic, (i) Nylon, (j) Polypropylene.

Table 3.1. Basic properties of selected natural and synthetic fibre yarns.

	Fibre Type	Ply count	Average diameter – original (mm)	Average diameter – manually tightened (mm)	Water absorption (%) – 24h	Compactness of fibres (%)
J	Jute	3	1.99	1.52	68.9%	68.7%
H	Hemp	3	2.51	1.65	64.8%	90.4%
CSS	Cotton	3	0.292	0.272	47.6%	44.8%
CS	Cotton	3	0.960	0.656	49.9%	52.0%
CT	Cotton	7	2.23	0.981	48.7%	39.3%
WS	Wool	2	2.18	0.528	28.3%	49.0%
WT	Wool	3	4.38	1.09	39.0%	43.5%
AC	Acrylic	3	2.78	0.994	13.6%	27.9%
N	Nylon	3	1.76	1.76	72.4%	39.5%
P	Polypropylene	3	2.50	2.03	45.7%	19.3%

Jute and hemp yarns were included as representative bast fibres with relatively high cellulose contents, reported as 61–71% for jute and 70–74% for hemp (Bhattacharyya, Subasinghe & Kim, 2015). Jute fibres possess a porous internal structure that contributes to high moisture uptake (Cottrell et al., 2023), while the cellular morphology of hemp fibres has been reported to influence transport processes within cementitious matrices (Manaia, Manaia & Rodriges, 2019). The yarns used in this study were produced using conventional industrial routes, which typically involve retting, softening, bleaching, and spinning for jute (Sanyal, 2017), and retting, scutching, and spinning for hemp, with additional softening steps to accommodate its coarser fibre structure (Muzyczek, 2020). Both jute and hemp yarns were bleached to a beige colour. In addition, jute staple fibres

were included in selected experiments to enable direct comparison between yarn-based and dispersed fibre reinforcement.

Cotton yarns were included to represent a plant-based fibre with very high cellulose content (approximately 95%) and a distinct morphology characterised by a hollow central lumen (Abdalla et al., 2023). Cotton fibres were processed through blowing, carding, combing, roving, and spinning, and were dyed orange. Wool yarns were included as protein-based fibres with a morphology fundamentally different from plant-derived fibres. Wool fibres are hygroscopic and exhibit a crimped structure, which has been reported to influence fibre–matrix interaction in cementitious composites (Jóźwiak-Niedźwiedzka & Fantilli, 2020; Alyousef et al., 2020). Wool yarns were spun from scoured sheep wool and dyed brownish-yellow.

Three synthetic yarns were included as reference materials to separate the effects of fibre chemistry and moisture uptake from those associated with yarn geometry and packing (*Figure 3.2, h–j*), with their properties summarised at *Table 3.1*. Acrylic yarn (Sirdar Double Knitting, green) was selected as a staple-spun fibre with limited chemical reactivity in alkaline cement pore solutions (Pereira-De-Oliveira, Castro-Gomes & Nepomuceno, 2012). Its capacity to retain water is attributed primarily to capillary storage within the yarn bundle rather than absorption into the polymer. Nylon yarn (Tonifu, black) was selected as a multifilament polyamide with moderate polarity and water uptake associated with amide functional groups, while remaining chemically stable in cementitious environments (Spadea et al., 2015). Polypropylene yarn (Sensy, sage) was used as a non-polar, hydrophobic comparator; its chemical inertness and low surface energy provide a reference system with minimal interfacial interaction (Rahbar et al., 2006).

All yarns studied exhibit internal porosity arising either from twist-induced voids between staple fibres, as in jute, cotton, wool, and acrylic yarns, or from interstitial capillaries between filaments in multifilament yarns such as nylon and polypropylene (Tausif, Cassidy & Butcher, 2018; Rahbar et al., 2006). Fibre compactness was determined from epoxy-impregnated transverse cross-sections using image analysis, as described in Section 3.6.1. Yarn diameters were measured in two conditions: the original diameter, representing the relaxed state, and the tightened diameter, measured under light pretension to simulate placement during casting. Measurements were taken at 30

positions along each yarn to account for local variability arising from twist and surface hairiness. Water absorption over 24 hours was measured using the procedure described in Section 3.8.1.

All cementitious specimens were prepared using CEM I 52.5 N Portland cement supplied by Breedon. Two production batches of the same cement type were used over the course of the experimental programme. The chemical compositions of both batches, determined by X-ray fluorescence (Section 3.5.4), are reported in *Table 3.2*, with loss on ignition values of 1.72 wt.% and 2.01 wt.%, respectively. The initial CO_2 content of each cement batch was measured by thermogravimetric analysis (1.52 ± 0.35 wt.%). This initial carbonate content was accounted for in subsequent calculations of CO_2 uptake following carbonation curing. A constant water-to-cement mass ratio of 0.40 was used for all cement paste and mortar specimens.

Table 3.2. Chemical composition of the CEM I 52.5N Portland cement (wt.%). Loss on ignition was 1.72 wt.% for cement 1 and 2.01 wt.% for cement 2.

	SiO_2	Al_2O_3	Fe_2O_3	CaO	SO_3	MgO	Na_2O	K_2O	Cl^-
Batch 1	19.4	5.64	2.75	64.8	3.96	0.881	0.210	0.599	0.077
Batch 2	19.2	5.44	2.63	63.6	3.30	0.910	0.210	0.530	0.060

For mortar preparation, standard graded siliceous sand sourced from Builder Depot was used. The sand was oven-dried at 105 ± 5 °C to constant mass prior to mixing to eliminate the influence of variable moisture content. Particle size distribution was characterised by sieve analysis, as shown in *Figure 3.3*, confirming a continuous grading with a maximum particle size of 4 mm, consistent with standard mortar testing requirements. The grading curve indicates that approximately 80–85 wt.% of particles pass 1 mm, with a gradual transition across the fine and medium sand fractions.

The sand exhibited a water absorption of 0.8 wt.%, measured in accordance with ASTM C128-22 (ASTM International, 2022), and this value was accounted for in mix proportioning to maintain a consistent effective water-to-cement ratio across all mortar specimens. A constant sand-to-binder mass ratio of 2:1 was used for all mortar mixes. All mixing and curing water used in this study was laboratory tap water at ambient temperature.

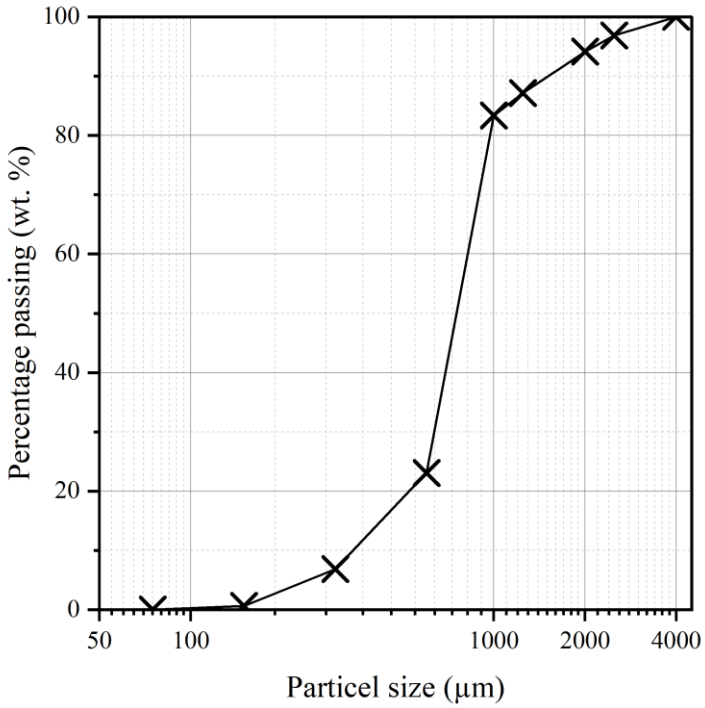


Figure 3.3. Sieve analysis of siliceous sand.

3.3. Sample preparation

Two types of specimens were prepared in this study to address different experimental objectives. Cylindrical cement paste specimens containing a single fibre yarn were prepared primarily for carbonation assessment and microstructural characterisation, and were subsequently sectioned into discs at defined depths for different tests. Cubic specimens, including cement paste cubes and mortar cubes reinforced with yarn meshes, were prepared to evaluate mechanical performance.

Single-yarn cylindrical cement paste specimens were cast using 15 mL polyethylene centrifuge tubes as moulds. Prior to casting, the yarn was aligned along the central axis of the tube by threading it through pre-drilled holes at the top and bottom of the mould and securing it with waterproof duct tape. This arrangement ensured consistent yarn positioning along the specimen length. Cement paste was prepared using a Silverson L5T high-shear mixer for 2 min, until a visually homogeneous paste was obtained. Fresh cement paste was then poured into the tube, which was subsequently capped and sealed. After casting, the yarn was manually tightened in the longitudinal direction to remove slack and ensure axial alignment. This tightening resulted in a reduction in the average yarn diameter relative to the relaxed state, as reported in *Table 3.1*. Following casting, the

filled tubes were subjected to external vibration for approximately 45 s until no further air bubbles were observed escaping along the tube walls. The specimens were cured within the centrifuge tubes for the first 24 hours (*Figure 3.4a*). After this initial curing period, the upper portion of each tube was removed using a Buehler IsoMet 1000 precision cutter with water as the cooling agent, exposing the paste surface for subsequent curing and testing illustrated in (*Figure 3.4b*).

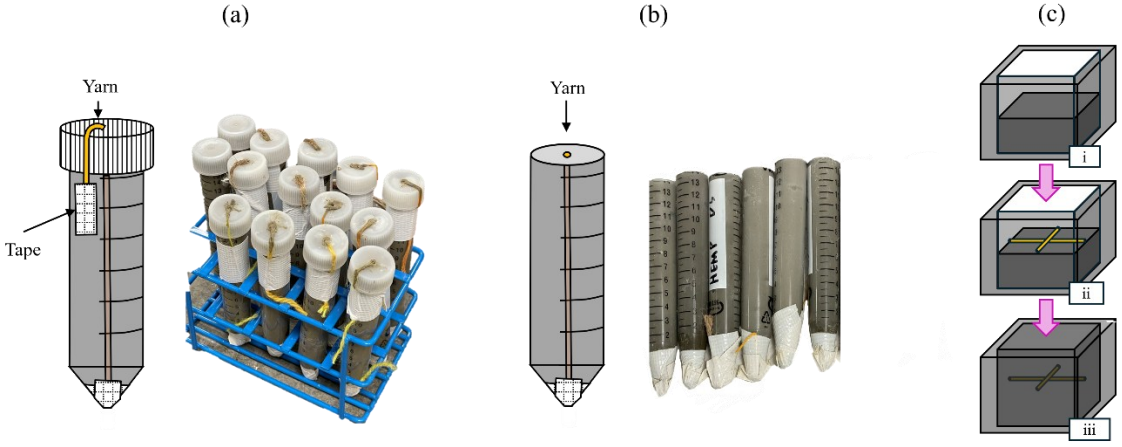


Figure 3.4. Preparation of specimens. (a–b) Cylindrical (centrifuge-tube-cast) single-yarn cement paste specimens showing curing within the tubes for the first 24 hours and subsequent removal of the tube cap and upper section to expose the paste surface. (c) Cement paste and mortar cubes reinforced with yarn meshes prepared using a layer-by-layer casting approach.

In addition to single-yarn cylindrical specimens, cubic specimens were prepared to examine the influence of yarn mesh configuration at the material scale. Cement paste cubes (20 × 20 × 20 mm³) and mortar cubes (50 × 50 × 50 mm³) were cast. For both specimen types, a layer-by-layer casting approach was adopted (Peled, Mobasher & Bentur, 2017; Preinstorfer et al., 2024). Unlike the single yarns used in the cylindrical specimens, the yarn meshes were positioned without longitudinal tension, as uniform tensioning of the two-dimensional mesh was not practicable during casting. The yarns in the mesh specimens therefore remained closer to their relaxed geometry. Mortars were prepared in accordance with BS EN 196-1:2016 (British Standards Institution, 2016). Cement and water were first mixed using a paddle mixer (CONTROLS, USA) at low speed for 30 seconds, after which sand was steadily added over the subsequent 30 seconds. Mixing was then paused for 90 seconds, during which material adhering to the wall of the mixing bowl was scraped down and returned to the centre. The mortar was subsequently mixed at high speed for a further 60 seconds. Immediately after mixing, the fresh mortar

was placed into cubic steel moulds and compacted on a vibration table for 2 minutes to ensure adequate consolidation.

As illustrated schematically in *Figure 3.4c* (i–iii), yarns were manually positioned within the mould at prescribed locations, followed by the addition of fresh paste or mortar to embed the yarns. This sequence was repeated according to the specified mesh configuration until the mould was completely filled. The same casting procedure was used for cement paste and mortar specimens, with the matrix composition being the only difference.

Specimens are identified using the notation X–R–DY(–Z), which is applied consistently to both cement paste and mortar specimens. Here, *X* denotes the fibre yarn type, *R* indicates the curing regime, with A representing air curing and C representing enforced carbonation curing, and *DY* denotes the curing duration in days. For bulk specimens, the depth term is omitted, while for sectioned specimens used for depth-resolved measurements, *Z* is included to indicate the depth in millimetres from the CO_2-exposed surface. For example, a specimen labelled H–C–D7–20 corresponds to a hemp-yarn-reinforced specimen subjected to 7 days of carbonation curing, with measurements taken at a depth of 20 mm from the exposed surface, whereas a specimen labelled J–C–D7 corresponds to a jute-yarn-reinforced specimen subjected to 7 days of carbonation curing. Where applicable, the specimen type (cement paste or mortar) is specified in the accompanying text, figure captions, or table headings.

3.4. Curing regimes

3.4.1. Enforced carbonation curing

After removal of the upper portion of the centrifuge caps and exposure of a freshly cut paste surface (*Figure 3.4b*), the cylindrical cement paste specimens were conditioned prior to carbonation curing to remove free surface water. For these specimens, an electric fan providing a wind speed of 1.11 m s^{-1} was used to fan-dry the exposed surface at room temperature (21 ± 2 °C) and ambient relative humidity (approximately 55%) for 30 minutes.

Following surface drying, the centrifuge-cast cylindrical specimens were placed vertically on a perforated support within the carbonation chamber, such that only the top

surface was directly exposed to CO_2. Cement paste cubes and mortar cubes were placed on an open rack that allowed gas ingress from all exposed faces. The specimens were not sealed or taped during carbonation curing. The experimental setup is visualised in *Figure 3.5a*.

Enforced carbonation curing was conducted in a Panasonic MCO-230AIC CO_2 incubator. The carbonation conditions were selected to approximate cement plant flue gas, with a temperature of 25 ± 0.5 °C, atmospheric pressure, and a CO_2 concentration of 19.9 ± 0.1 vol.%, achieved by mixing compressed air with carbon dioxide gas of 99.8% purity (BOC Ltd). The relative humidity within the carbonation chamber was maintained at 64 ± 2% using a saturated sodium nitrite ($NaNO_2$) solution (Anstice, Page & Page, 2005).

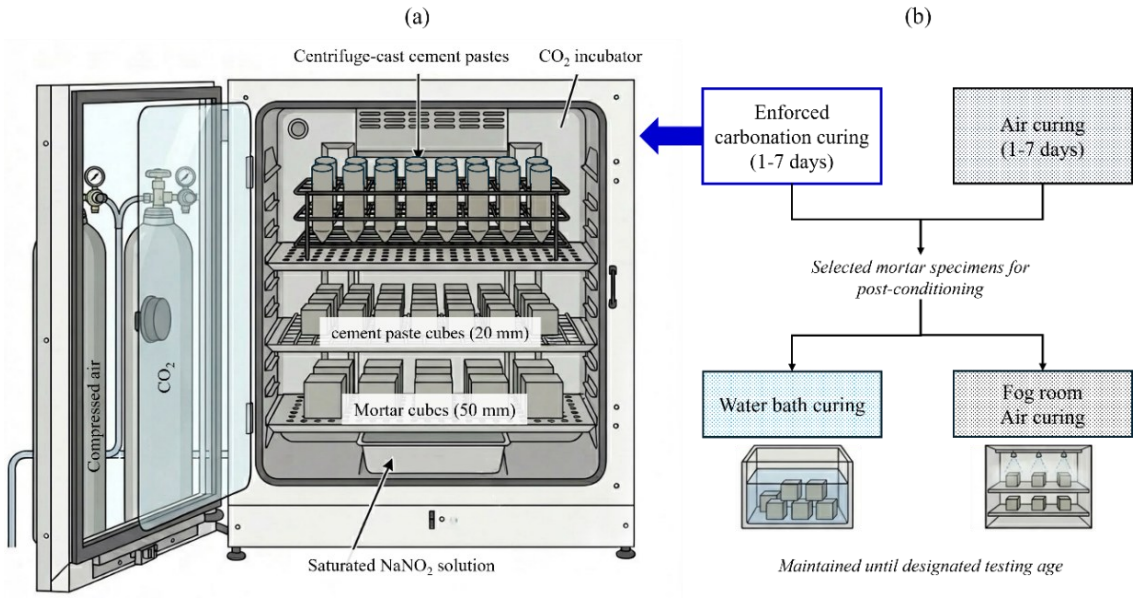


Figure 3.5. Schematic illustration of curing regimes applied in this study: (a) enforced carbonation curing of centrifuge-cast cement paste specimens and cement paste and mortar cubes in a controlled CO_2 incubator; and (b) alternative curing and post-conditioning regimes, including air curing for comparison and post-conditioning by water bath curing or air curing in a fog room, depending on the experimental programme adopted in each result chapter.

Specimens were subjected to enforced carbonation curing for 1, 3, 5, and 7 days. At each curing duration, samples were retrieved in batches and sectioned at predefined depths using a Buehler IsoMet 1000 precision cutter with water cooling to minimise thermal or mechanical damage.

3.4.2. Air-curing

To provide a direct baseline for comparison with enforced carbonation curing, a parallel group of specimens was subjected to air curing under controlled environmental conditions. Following demoulding or surface preparation, specimens assigned to air curing were placed in a sealed climate chamber maintained at 25 ± 0.5 °C and 64 ± 2% relative humidity, matching the temperature and humidity conditions used for carbonation curing.

Air-cured specimens were exposed for durations of 1, 3, 5, and 7 days, corresponding exactly to the enforced carbonation curing periods (*Figure 3.5b*). During air curing, specimens were maintained under atmospheric CO_2 conditions. All other handling procedures were identical to those used for carbonation-cured specimens.

3.4.3. Post-conditioning

Following the initial curing period under enforced carbonation or air curing, selected mortar specimens were subjected to post-conditioning to examine the influence of subsequent moisture exposure on material behaviour. Two post-conditioning regimes were applied: water curing and high-humidity air curing in a fog room (*Figure 3.5b)*.

For water curing, specimens were immersed in a water bath at ambient temperature. For air post-conditioning, specimens were transferred to a fog room maintained at > 96% relative humidity and ambient temperature. Specimens remained under these post-conditioning environments until the designated testing age.

The choice of post-conditioning regime and its duration depended on the specific experimental programme and specimen type. Details of the post-conditioning sequences applied to mechanical testing specimens, including curing timelines and combinations with prior carbonation or air curing, are provided in Chapter 7 (Section 7.2.3).

3.5. Characterisation tests

Except for isothermal calorimetry and X-ray fluorescence analysis, cylindrical cement paste specimens were used for the characterisation tests described in this section. After curing, the cylindrical specimens were sectioned at designated positions along the depth

into discs for sampling. For thermogravimetric analysis (Section 3.5.2), X-ray diffraction (Section 3.5.3), and Fourier-transform infrared spectroscopy (Section 3.5.5), specimens were cut into 1 mm-thick discs at locations of interest. Thicker bulk discs (typically 9–10 mm) were prepared for scanning electron microscopy (Section 3.5.6). The nominal depth assigned to each sample was based on the predefined cutter position. Small uncertainty in the represented depth interval may arise from cutter positioning, blade kerf, and material loss during sectioning, particularly where steep carbonation gradients occur.

Hydration was halted using solvent exchange with isopropanol (IPA, 99% purity, Sigma Aldrich), a method shown to suppress ion transport and preserve hydrate assemblages more effectively than direct thermal or vacuum drying (Scrivener, Snellings & Lothenbach, 2018). Bulk disc specimens, including those prepared for SEM, were immersed in excess IPA for 5 days to replace free and capillary pore water. The specimens were then oven-dried at 40 °C to constant mass, a temperature selected to avoid dehydration of metastable hydrates and stored under low vacuum (~0.2 bar) prior to further preparation.

For powder-based analyses (TGA, XRD, and FTIR), a rapid solvent exchange protocol was applied. Powdered cement paste samples were soaked in IPA for 15 minutes at a solid-to-solvent ratio of 3 g per 100 mL, followed by rinsing with diethyl ether (99.0%, VWR Chemicals) on a Büchner funnel under vacuum. The ether rinse facilitated rapid removal of residual IPA and limited rehydration during drying. The rinsed powders were dried in an oven at 40 °C for 8 minutes, in accordance with RILEM technical committee recommendations (Snellings et al., 2018). After drying, all samples were sealed in airtight bags and stored in a desiccator containing soda lime and silica gel to minimise moisture uptake and unintended carbonation prior to testing. Samples were analysed at the earliest practicable time.

3.5.1. Isothermal calorimetry

Isothermal calorimetry was used to monitor the hydration behaviour of cement paste in the presence of embedded fibre yarns. The test was conducted in accordance with the general principles outlined in BS EN 196-11:2018 (British Standards Institution, 2019), with modifications to accommodate fibre inclusion. Measurements were performed using a TAM Air isothermal calorimeter operated at 20 °C.

Cement paste samples were prepared at a constant water-to-cement ratio of 0.40. For each measurement, approximately 10 g of fresh paste was placed into a sealed calorimeter ampoule. A 30 mm segment of fibre yarn was embedded into the paste, oriented perpendicular to the paste surface, such that a consistent fibre–matrix contact length was achieved across all samples. Reference measurements were conducted on paste samples without fibres prepared under identical conditions. Heat flow was recorded continuously for 168 h (7 days), enabling assessment of early hydration reactions and subsequent hydration development under the different fibre conditions. Selected measurements were repeated three times to confirm reproducibility.

3.5.2. Thermogravimetric analysis

Thermogravimetric analysis (TGA) was used to quantify the extent of carbonation in cement paste specimens. Following hydration stoppage and storage as described in Section 3.5, the preserved material was crushed and ground to a homogeneous powder with a particle size smaller than 125 μm prior to analysis.

TGA measurements were performed using a Netzsch STA 449 F5 thermal analyser. Approximately 55 ± 0.2 mg of powdered sample was heated from 30 °C to 1050 °C at a heating rate of 10 °C min^{-1} under a constant nitrogen flow of 50 mL min^{-1}. To aid identification and quantification of portlandite and calcium carbonate decomposition, TGA was coupled with mass spectrometry (TGA–MS) for selected representative samples. A QMS 403 Aëolos Quadro mass spectrometer was connected via a heated quartz capillary (300 °C) to detect the evolution of H_2O (m/z = 18) and CO_2 (m/z = 44), corresponding to the decomposition of hydration products and carbonates. Mass losses associated with the decomposition of portlandite and calcium carbonate were determined using the tangential method, with decomposition ranges of 420–520 °C for portlandite and 550–850 °C for calcium carbonate (Scrivener, Snellings & Lothenbach, 2018).

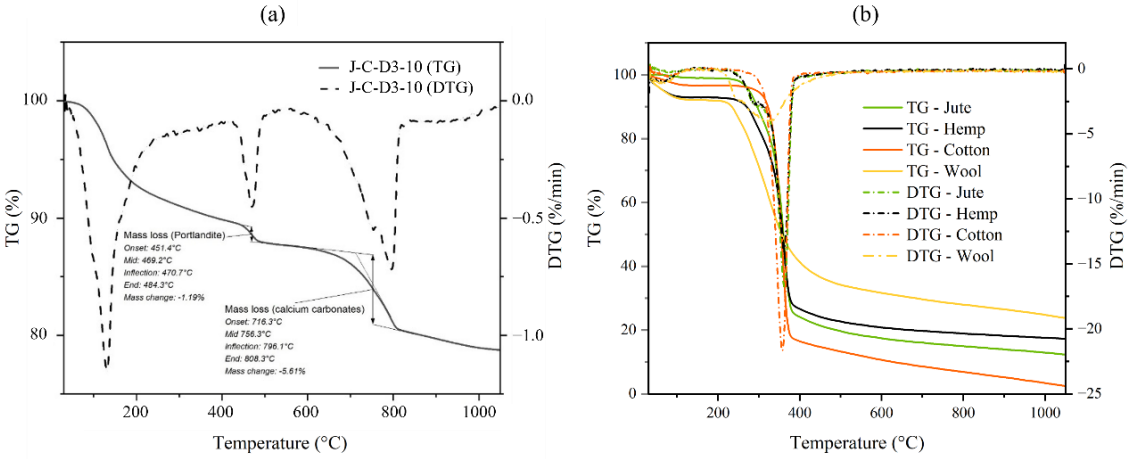


Figure 3.6 (a) Example of using tangential method to determine the mass loss (in wt.%) due to portlandite and calcium carbonate decomposition. (b) TG-DTG curves of raw jute, hemp, cotton and wool fibres. All chosen natural fibres experienced decomposition between 300 °C and 400 °C, culminating in a weight reduction to roughly 0% - 25% of their original weights at 1050 °C.

An example of the application of the tangential method to TG–DTG curves is shown in *Figure 3.6a*. Tangents were drawn on the points of TG curve, where the rate of change begins to increase significantly (i.e. corresponding to the beginning of DTG peaks). Similarly, tangents are placed at points where the rate of change decreases back to baseline (i.e. ending of the DTG peaks). The percentages of weight loss observed between these start and end points were quantified to calculate the amount of phases that had decomposed.

The CO_2 uptake ($CO_{2\,uptake}$, wt.%) was calculated as the percentage of CO_2 absorbed during enforced carbonation relative to the initial mass of cement (M_{cement}, g). To account for amorphous calcium carbonates, which could decompose before 600 ºC, M_{cement} is calculated by adding the mass loss from decomposition of $CaCO_3$ in the initial cement and the residual mass of the sample after heating to 1050 °C, i.e., the anhydrous and CO_2-free mass of cement (M_{1050}, g) (*Equation 3.1*), assuming that the initial cement is dry.

$$M_{cement} = \frac{M_{1050}}{1 - \frac{CO_{2\,initial}}{100}} \tag{3.1}$$

Where $CO_{2\,initial}$ (%) denotes the percentage of CO_2 initially present in the cement (i.e., CEM I powder), and is determined via TGA. Based on the initial mass of cement, CO_2 sequestration during enforced carbonation of a sample can be derived from the total mass lost due to $CaCO_3$ decomposition excluding the mass of CO_2 initially in the sample. The CO_2 uptake can hence be quantified as follows (He, Shi & Poon, 2018; Liu & Meng, 2021) (*Equation. 3.2*).

$$CO_{2\,uptake} = \frac{WL_{CaCO_3} - CO_{2\,initial} \times M_{cement}}{M_{cement}} \times 100 \tag{3.2}$$

Where, WL_{CaCO_3} (g) represents the mass loss attributed to the decomposition of $CaCO_3$.

In addition, TG–DTG analysis was performed on the natural fibre yarns to characterise their thermal decomposition behaviour. Representative TG–DTG curves for jute, hemp, cotton, and wool fibres are shown in *Figure 3.6b*. This analysis was used to identify the temperature ranges over which fibre decomposition occurs and to ensure separation from the decomposition ranges of cement hydration and carbonation products. All selected natural fibres experienced significant decomposition between 300 °C to 400 °C, which leads to substantial weight losses. By 1050 °C, the natural fibres were reduced to 0% - 25% of their original weights. Unlike jute, hemp and cotton fibres, which have sharp DTG peaks around 360 °C to 370 °C, wool fibres decompose at a lower temperature (~ 200 °C) and gradually degrade over a wider temperature range until 500 °C. This is likely due to the presence of keratin and other proteins in wool fibres that decompose at lower temperatures compared to cellulose (Fantilli, Sicardi & Dotti, 2017).

3.5.3. X-ray diffraction

X-ray diffraction (XRD) was used to identify and quantify crystalline phases in cement paste specimens, complementing carbonation assessment by thermogravimetric analysis. Measurements were performed using a Bruker AXS D8 Advance diffractometer with Cu Kα radiation operated at 45 kV and 40 mA.

After hydration stoppage, samples were crushed, homogenised, and sieved to <63 μm. Quantitative phase analysis was conducted using the internal standard method, with

samples mixed with high-purity corundum (Al_2O_3) at a 4:1 mass ratio (sample:corundum) and ground in an agate mortar. Diffraction patterns were collected over a 2θ range of 5–80°, with a step size of 0.02° and a scanning speed of 0.02° s^{-1}. Phase identification and quantification were carried out by Rietveld refinement using HighScore Plus software, with reference patterns obtained from the ICDD PDF-4+/Web (2023) database. Refinement parameters included background fitting, scale factors, unit-cell parameters, peak shape functions, and preferred orientation where necessary.

The degree of hydration (DoH, %) was estimated by comparing the total content of unhydrated clinker phases (alite, belite, aluminate, and ferrite) remaining in the hydrated sample with that of the raw cement, as expressed in *Equation 3.3*:

$$DoH = (1 - \frac{\sum w_{cement,sample}}{\sum w_{cement,raw}}) \times 100 \quad (3.3)$$

Where $\sum w_{cement,sample}$ (wt.%) is the total clinker phases remaining in the sample, $\sum w_{cement,raw}$ (wt.%) is the total clinker content in raw cement. For carbonated specimens, this calculation may overestimate the degree of hydration, as carbonation reactions also consume clinker phases. The DoH values derived for carbonated samples were therefore interpreted qualitatively and used primarily for comparative assessment between curing conditions rather than as absolute hydration metrics.

3.5.4. X-ray fluorescence

The chemical composition of the cement used in this study was determined by X-ray fluorescence (XRF) using a Malvern Panalytical Zetium spectrometer. Samples were prepared as fused glass discs using a lithium borate fusion method. Approximately 0.9 g of cement powder was mixed with 9 g of lithium borate flux in a platinum crucible and homogenised thoroughly. To improve fusion behaviour, ten drops of lithium iodide were added. The mixture was fused at 1050 °C in a LeNeo fusion furnace, and the resulting melt was cooled to form a homogeneous glass disc. Elemental compositions were quantified using SuperQ Spectra software.

Loss on ignition (LOI) was determined separately by heating cement powder to 1050 °C until constant mass was achieved. LOI was calculated as the percentage mass loss relative to the initial dry mass of the cement and was used to account for volatile components in the reported oxide compositions.

3.5.5. Fourier-transform infrared spectroscopy

Fourier-transform infrared spectroscopy (FTIR) was used to examine chemical bonding in powdered samples. Measurements were performed in attenuated total reflection (ATR) mode using a Thermo Fisher Scientific Nicolet iS50 FT-IR spectrometer. In ATR mode, infrared radiation is transmitted through a diamond crystal and internally reflected at the crystal–sample interface, with the resulting absorbance recorded by the detector.

FTIR–ATR measurements were conducted on the same powdered samples used for thermogravimetric analysis. Each sample was analysed three times, with 64 scans collected per measurement at a spectral resolution of 4 cm^{-1} over a wavenumber range of 400–4000 cm^{-1}.

3.5.6. Scanning electron microscopy

Scanning electron microscopy (SEM) was used to examine the microstructure of natural fibre yarn–cement composites. Imaging was performed using a Zeiss Sigma 500VP field-emission scanning electron microscope (FE-SEM) equipped with a five-quadrant high-definition backscattered electron (BSE) detector.

For SEM samples, the preparation steps are summarised schematically in *Figure 3.7*. The discs were impregnated with a low-viscosity epoxy resin–hardener mixture at a mass ratio of 22:3 and cast in plastic moulds. Impregnation was performed under vacuum to remove entrapped air and ensure penetration of the pore structure, after which the samples were cured for 24 hours to allow full resin hardening. The cured specimens were then ground sequentially using 220, 500, and 1200 mesh abrasive papers, followed by polishing with 3 μm, 1 μm, and 0.25 μm diamond suspensions to obtain a smooth surface suitable for electron microscopy. Acetone was used intermittently during grinding and polishing to remove debris and polishing residues. Following polishing, samples were placed in a desiccator for at least 48 h to allow complete evaporation of residual acetone and moisture.

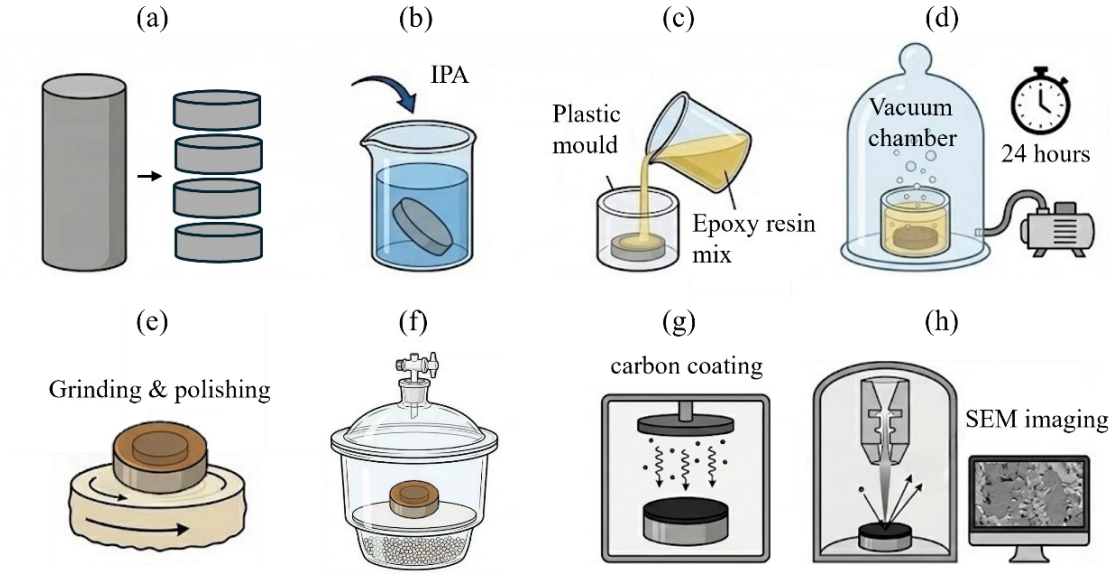


Figure 3.7. Schematic overview of SEM sample preparation. (a) Sectioning of cylindrical specimens into discs; (b) hydration stoppage by solvent exchange; (c) epoxy resin impregnation in plastic moulds; (d) vacuum-assisted air removal and curing; (e) sequential grinding and polishing with intermittent acetone cleaning; (f) storage in a desiccator for ⩾48 hours to remove residual acetone and moisture prior to coating; and (g) carbon coating before BSE-SEM imaging (h).

Prior to imaging, the samples were carbon coated to a thickness of approximately 15 nm under a vacuum of 7×10^{-2} mbar using an Emitech K550X sputter coater. Backscattered electron (BSE) images were acquired at a resolution of 3072 × 2304 pixels, using an accelerating voltage of 12.5 kV and a working distance of 8.5 mm.

3.6. Image analysis

3.6.1. Yarn compactness

Yarn compactness was quantified using a resin-impregnation and image-analysis method developed in this study. This approach was developed specifically for this thesis because spun yarns are porous assemblies of individual fibres, containing inter-fibre voids that cannot be resolved or quantified reliably once embedded within the cement matrix.

Fibre yarns were first oven-dried at 50 °C to remove free moisture. After drying, each yarn was placed in a 15 ml polyethylene centrifuge tube and manually tightened at both ends following the procedure described in Section 3.3. A fluorescent epoxy resin was then poured into the tube and allowed to cure for 24 hours at room temperature (23 ± 2 °C). After curing, a 10 mm-thick cross-sectional disc containing the yarn centrally embedded

in the resin was sectioned using the Buehler IsoMet 1000 precision cutter, with water as the cooling agent, followed by drying, grinding and polishing

Polished cross-sectional images of the resin-impregnated yarns were acquired using a Zeiss Axio Imager Z2m digital microscope operated in fluorescence mode. Image analysis was performed using ImageJ software. For each image, the fibre phase, which appears dark under fluorescence illumination, was segmented by applying a greyscale threshold. The total fibre area (A_{fibre} , mm^2) was calculated as the sum of the segmented fibre cross-sectional areas. The total yarn area (A_{yarn} , mm^2) was defined as the convex area enclosing the outer boundary of the yarn bundle, corresponding to the convex hull of the yarn cross-section, which was manually delineated. Yarn compactness (%) was calculated as:

$$Yarn\ compactness = \frac{A_{fibre}}{A_{yarn}} \times 100 \tag{3.4}$$

To obtain representative values, compactness was determined from three independent transverse cross-sections per yarn, and the reported compactness corresponds to the average of these three measurements. An illustrative example of the compactness determination is provided in *Figure 3.8*.

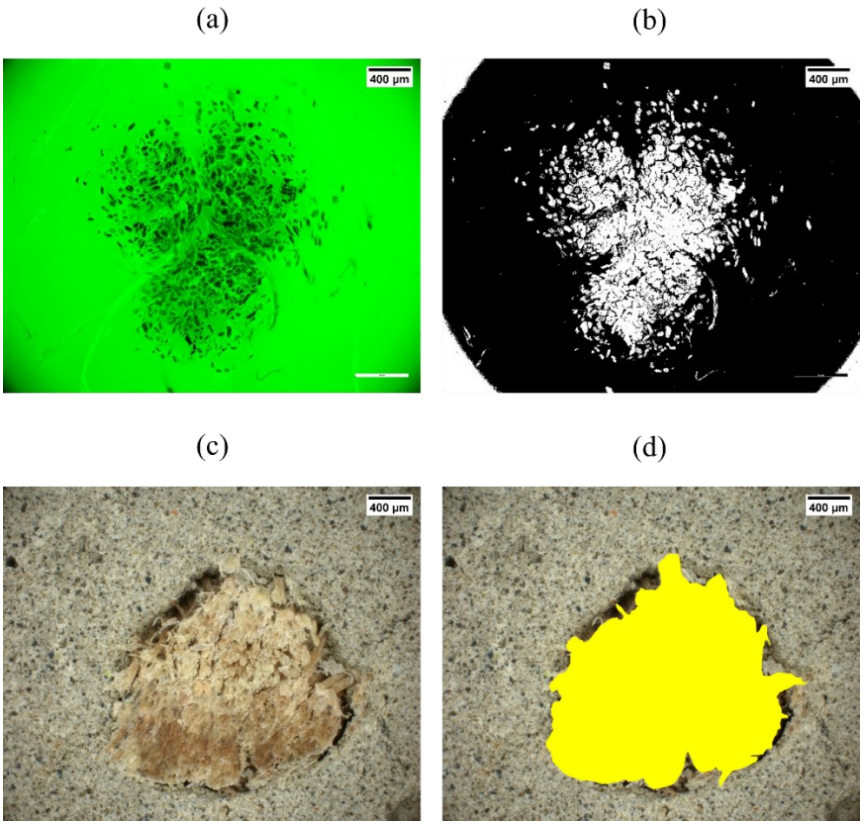


Figure 3.8. Yarn compactness determination: (a) fluorescence micrograph of a resin-impregnated hemp yarn cross-section; (b) threshold image showing segmented fibre filaments; (c) hemp yarn cross-section embedded in cement paste; and (d) manually defined convex area of the yarn bundle.

3.6.2. Phenolphthalein indicator test

Carbonation of cementitious materials involves a neutralisation reaction that reduces the pore solution pH from approximately 13 to below 9. Changes in alkalinity associated with carbonation were assessed using a phenolphthalein indicator test, which provides a rapid visual indication of carbonated and uncarbonated regions.

After curing, specimens were sectioned at designated depths from the exposed surface to obtain transverse cross-sections in the form of discs, typically at 10 mm intervals, to examine carbonation penetration and geometry. Sectioning was performed using a precision cutter with water as the cooling agent. As residual surface water could influence the phenolphthalein colour response, the freshly cut surfaces were immediately wiped with tissue paper and briefly fan-dried for ~ 10 minutes before indicator application. This controlled cutting procedure was necessary because the small cylindrical specimens required reproducible planar cross-sections at prescribed depths, which could not be achieved reliably by splitting. The freshly cut disc surfaces were sprayed evenly with a

phenolphthalein solution prepared by dissolving 10 g of phenolphthalein in 1 L of a 50% ethanol–water solution, in accordance with BS EN 12390-12:2020 (British Standards Institution, 2020). Regions with a pH greater than 9 developed a reddish-purple colour, indicating uncarbonated material, while carbonated regions with a pH below 9 remained colourless.

A dedicated image-analysis method was developed to enable quantitative assessment of heterogeneous carbonation patterns from yarn-embedded phenolphthalein-stained cement paste discs. The development and validation of this approach are presented separately in Chapter 4.

3.6.3. Porosity quantification

Porosity was quantified from SEM-BSE images acquired under the imaging conditions described in Section 3.5.6, using the overflow segmentation method (Wong, Head & Buenfeld, 2006). Images used for porosity quantification were acquired at 500× magnification with a resolution of 1024 × 728 pixels and a pixel size of 0.182 μm/pixel, corresponding to a field of view of approximately 186 × 132 μm. For each image, the pixel-intensity histogram was analysed by fitting two linear shoulders corresponding to the solid matrix and pore phases. The intersection of these two lines was taken as the upper intensity threshold for pore segmentation, allowing pores (dark regions) to be distinguished from the solid matrix.

The pore area fraction (μ_p) was calculated as:

$$\mu_p = \frac{A_{pores}}{A_{ROI}} \times 100 \tag{3.5}$$

where A_{pores} (mm^2) is the total area of pores identified by image segmentation and A_{ROI} (mm^2) is the total area of the region of interest (i.e. the total area of the analysed image). For each region of interest, 30 BSE images were analysed under identical brightness and contrast conditions, and the resulting pore area fractions were averaged to obtain representative porosity values.

3.7. Compressive strength test

Compressive strength testing was conducted on both cement paste and mortar cube specimens using load-controlled compression machines appropriate to specimen size.
For cement paste cubes (20 × 20 × 20 mm³), compressive strength was measured using an Instron 6800 series universal testing machine equipped with Bluehill Universal software for load control and data acquisition. Testing was carried out under displacement control at a constant crosshead displacement rate of 0.5 mm min^{-1} until failure. For each curing regime and yarn configuration, three replicate cubes were tested and the mean compressive strength was reported.

For mortar cubes (50 × 50 × 50 mm³), compressive strength testing was performed using a Controls Automax 5 compression testing machine. Tests were conducted under load control at a loading rate of 0.3 MPa s^{-1}, in accordance with BS EN 196-1 (British Standards Institution, 2016). At each testing age, three cubes per mix were tested and the average compressive strength was calculated.

3.8. Transport and absorption measurements

3.8.1. Yarn water absorption test

Water absorption of fibre yarns was measured following a protocol modified from BS EN ISO 62:1999 (The British Standards Institution, 1999). The yarns were initially oven-dried at 50 °C and cooled to room temperature inside a desiccator conditioned by silica gel, before being prepared to 100 mg ± 0.1 mg. The process was reiterated until the specimens had reached a consistent mass. Following that, the yarns were submerged in de-ionised water at room temperature (23 °C ± 2 °C) for 24 hours. After the designated period, the specimens were removed from the water bath, with excessive surface water blotted up by a clean, dry cotton cloth. These were then immediately weighed within 1 minute to the nearest 0.1 mg. The water absorption (%) of the fibres was then computed by Equation 3.6:

$$Water\ absorption = \frac{w_a - w_b}{w_b} \times 100 \tag{3.6}$$

Where w_b represents weight before immersion (mg), w_a is weight after immersion (mg).

3.8.2. Sorptivity test

Sorptivity testing was used to characterise capillary water uptake in hardened cementitious materials. Tests were conducted in accordance with ASTM C1585 (ASTM International, 2020), with minor adaptations to accommodate cube specimens, as illustrated in *Figure 3.9*. Cubic specimens with dimensions of 50 × 50 × 50 mm³ were used. After completion of the prescribed curing regime, specimens were removed from the curing environment, gently blotted to a surface-dry condition, and conditioned to achieve a controlled internal moisture state. Conditioning consisted of oven storage at 40 °C (RH ~ 80%) for 7 days, followed by storage in a sealed container for a further 15 days to allow internal moisture equilibration. After conditioning, specimens were weighed and placed on support stands in a shallow water tray such that only the bottom surface was exposed to water. The water level was maintained at approximately 2–3 mm above the specimen base. Mass measurements were recorded at 1, 5, 10, 20, 30, 60, 120, 180, 300, and 360 min after initial contact with water on the first day, and subsequently once per day up to 7 days. Capillary water absorption was calculated from the measured mass increase at each time point and expressed as a function of the square root of time.

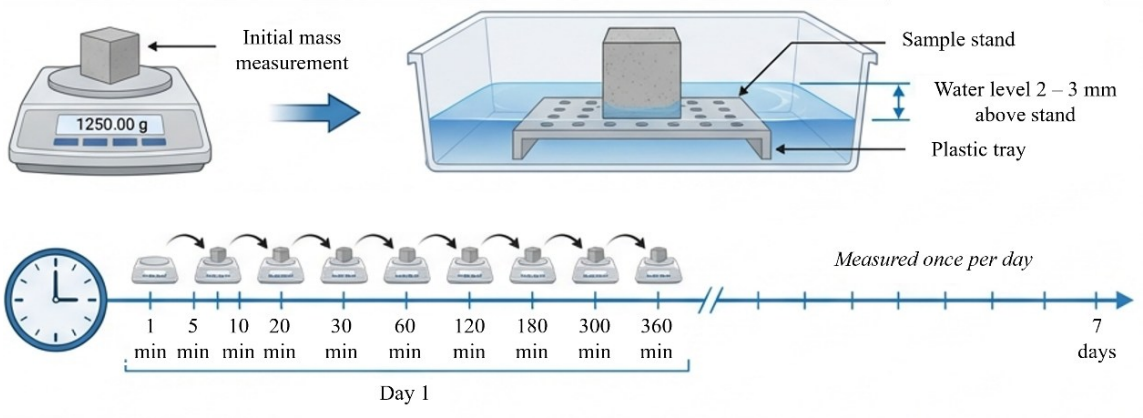


Figure 3.9. Sorptivity test setup and mass measurement schedule.

Chapter 4 Development of a phenolphthalein-based image analysis method

This chapter presents an image-analysis workflow developed using a dedicated dataset of phenolphthalein-stained cement paste discs. The workflow was progressively refined and tested through two related studies: (1) *Natural fibre-enhanced CO_2 transport and uptake in cement pastes subjected to enforced carbonation* (Journal of CO_2 Utilization, 90 (2024) 102983), and (2) *Influence of fibre treatments on early-age carbonation in yarn–cement composites under enforced carbonation* (Cement and Concrete Composites, 173 (2026) 106737). The final workflow established here forms the methodological basis for all subsequent image-based quantification of carbonation in this thesis.

4.1. Introduction

Phenolphthalein staining is widely used to indicate carbonation in cement-based materials, as the colour change corresponds to the drop in pore solution pH associated with portlandite depletion and calcium carbonate formation (British Standards Institution, 2020; Chang & Chen, 2006). To make use of this staining in a quantitative framework, an image-analysis method is required that can extract consistent and comparable measurements from the stained specimens.

Most published phenolphthalein-based image-analysis methods have been developed for specimens sectioned parallel to the direction of CO_2 ingress, where carbonation progresses predominantly in one dimension. Under these conditions, carbonation fronts can often be approximated as planar, and segmentation is typically achieved using simple thresholding or edge-detection approaches. In the present study, however, specimens were sectioned perpendicular to the direction of CO_2 ingress, producing transverse disc surfaces parallel to the original CO_2-exposed surface, at defined depths. This sampling strategy captures the lateral distribution of the phenolphthalein response at each depth

and preserves spatial heterogeneity across the cross-section, but it also introduces image-analysis challenges that are not encountered in larger specimens or longitudinal sections.

As discussed in detail in Chapter 2 (Section 2.3), phenolphthalein-defined carbonation boundaries are inherently diffuse, reflecting the gradual reduction in pore solution pH associated with overlapping stages of portlandite depletion, early calcium carbonate formation, and partial decalcification of C–S–H. Under enforced carbonation conditions, particularly at elevated CO_2 concentrations, these gradual transitions are further broadened due to rapid near-surface reactions and evolving transport constraints (Section 2.2.2). In the small disc specimens examined here, this intrinsic diffuseness is accentuated by the limited specimen size and by the sensitivity of high-resolution optical imaging to local variations in surface texture and illumination.

Preliminary analysis showed that these factors strongly affect segmentation reliability in the present dataset. Simple thresholding of RGB or HSV colour channels did not consistently identify carbonation boundaries. Even the green channel, which typically provides the highest contrast for phenolphthalein staining, was highly sensitive to shadows, surface roughness, stray fibres, and non-uniform illumination. Systematic trials using established thresholding methods and published image-analysis procedures (Appendix 2, Section 2A1) showed substantial variation between techniques, confirming that existing workflows cannot be applied directly to these specimens.

Quantitative analysis of phenolphthalein-stained discs therefore requires an image-processing approach capable of isolating the phenolphthalein response from the cement paste under variable imaging conditions, accommodating common artefacts, and excluding non-paste regions from area calculations. This chapter presents an image-analysis workflow developed using reference and fibre-embedded cement paste samples sectioned at known depths. Carbonated area fractions derived from processed images are evaluated against independent measurements from thermogravimetric analysis, quantitative X-ray diffraction, and Fourier-transform infrared spectroscopy. The objective of this chapter is to establish a reliable and reproducible image-analysis method for quantifying carbonation in phenolphthalein-stained cement paste disc specimens.

4.2. Materials and imaging setup

4.2.1. Sample preparation

Jute-embedded and reference (plain) cement paste cylinders were prepared using CEM I 52.5N at a constant water-to-cement ratio of 0.40. Specimen casting, yarn placement, initial curing, and conditioning procedures followed the protocols described in Section 3.3. After 24 hours of initial hydration, the specimens were subjected to enforced carbonation curing for durations of 1, 3, 5, or 7 days under the controlled conditions described in Section 3.4.1. At the end of each curing period, the cylindrical specimens were sectioned perpendicular to the direction of CO_2 ingress to obtain depth-resolved discs for image analysis and complementary chemical characterisation. The sectioning strategy and sampling layout are illustrated in *Figure 4.1*a.

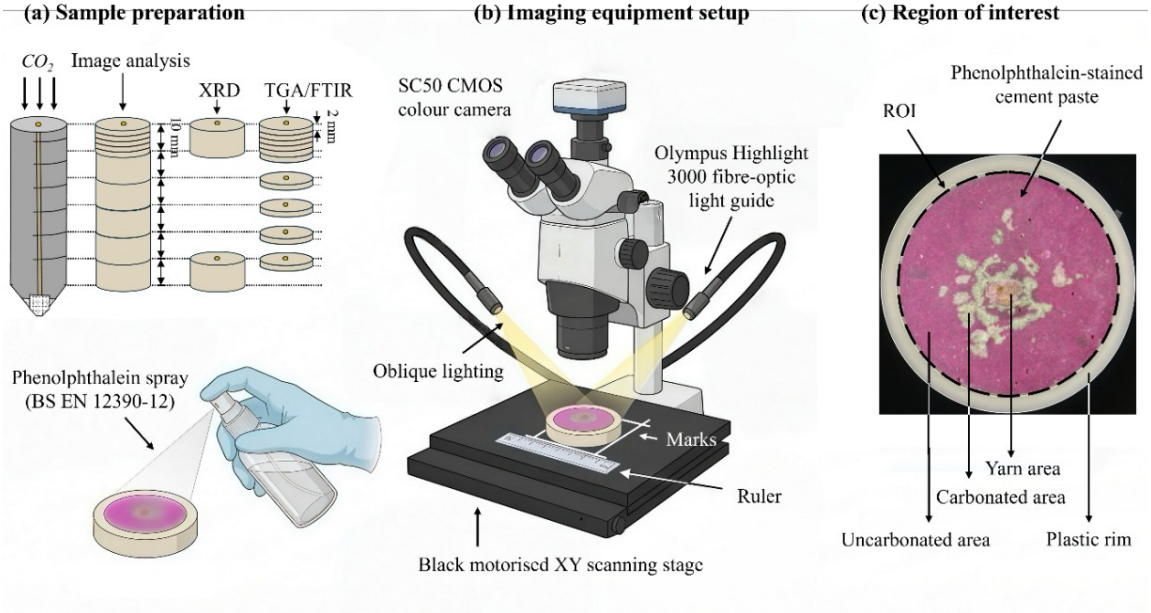


Figure 4.1. Experimental setup for phenolphthalein-stained discs. (a) Preparation of cement paste cylinders and depth-resolved sectioning for image analysis, XRD and TGA/FTIR sampling, followed by phenolphthalein spraying. (b) Microscope setup with controlled oblique lighting and calibrated XY stage. (c) Region of interest showing cement paste, yarn area, carbonated zone, and exclusion of the plastic rim.

For image analysis, discs were cut at nominal depths of 0, 2, 4, 6, 8, 10, 20, 30, 40, and 50 mm from the CO_2-exposed surface. After cutting, the freshly exposed surfaces were wiped, briefly fan-dried for less than 10 min, and then sprayed with phenolphthalein solution in accordance with BS EN 12390-12 (Section 3.6.2). Parallel specimens from the same cylinders were prepared for thermogravimetric analysis (TGA), quantitative X-ray diffraction (QXRD), and Fourier-transform infrared spectroscopy (FTIR) to support

validation of the image-based carbonation measurements. Hydration stoppage, sample storage, and general preparation protocols followed the procedures described in Section 3.5, with analytical details provided in Sections 3.5.2–3.5.5.

For QXRD, powders were collected from two depth intervals (0–10 mm and 50–60 mm) to capture mineralogical differences between highly carbonated and minimally carbonated regions. FTIR samples were taken at discrete depths of 0, 10, 20, 30, 40, and 50 mm to provide qualitative information on carbonation evolution with depth. For TGA, finer depth resolution was adopted to enable direct comparison with image-derived carbonation profiles: the region from 0–10 mm was sampled at 2 mm intervals, followed by continued sampling at 2 mm intervals to a depth of approximately 50 mm.

The QXRD, TGA, and FTIR datasets provide complementary validation of the image-analysis method. TGA was used to calculate CO_2 uptake at each depth for direct comparison with the carbonated area fractions obtained from image analysis, while FTIR was used to confirm qualitative carbonation trends and QXRD to distinguish mineralogical differences between highly and minimally carbonated zones.

4.2.2. Imaging setup

For image analysis, each phenolphthalein-stained disc was imaged using an Olympus SZX10 stereomicroscope equipped with an SC50 CMOS camera (*Figure 4.1b*). Oblique illumination was provided by two Olympus Highlight 3000 fibre-optic light guides to improve contrast between stained and unstained regions. The discs were placed on a black motorised XY scanning stage, where fixed reference marks enabled consistent positioning and ensured that the paste region remained centred in the field of view. This alignment was required for automation of the ROI step described in Section 4.2.3.

All imaging parameters were kept constant (light intensity, brightness level 3.5, exposure time 199 ms) to minimise variation between sessions. A ruler positioned at the focal plane provided a calibration scale for converting between pixel units and physical dimensions.

Images were processed in ImageJ (Version 1.54h). As shown in *Figure 4.1c*, each disc contained a bright plastic rim from the centrifuge tube, which needed to be removed before segmentation. A region of interest (ROI) was therefore applied to isolate the

cement paste only. Fixed positional marks on the motorised XY stage ensured that every disc was placed in a repeatable position, keeping the paste centred in the image and enabling automation of the cropping step.

4.2.3. Region of interest

As the centrifuge tubes used in this study are slightly tapered, the internal cross-sectional area of the cement paste decreases with depth. To account for this geometry, the paste area at each depth between 0 and 50 mm was determined from calibrated images of 10 representative tubes by manually outlining the internal paste boundary in ImageJ. The measured areas were converted to equivalent circular radii using $r = \sqrt{A/\pi}$. The resulting radii decreased systematically from 7.22 mm at the exposed surface to 6.88 mm at 50 mm depth.

An ImageJ macro was then used to apply the corresponding circular region of interest (ROI) automatically to each image (*Figure 4.1*c; *Figure 4.2*a). Depth information embedded in the file names allowed the macro to assign the appropriate radius and draw the ROI at a fixed centre coordinate. This procedure standardised the cropping step, eliminated user-dependent variation, and ensured that only the cement paste region was retained for subsequent segmentation and analysis. The same pixel-to-length calibration was applied to all images.

4.3. Method development

4.3.1. Background subtraction

Microscope images of phenolphthalein-stained discs commonly exhibit low-frequency illumination gradients as well as local artefacts arising from surface roughness, pores, and cement paste texture (*Figure 4.2a*). These features introduce unwanted intensity variations that can obscure the colour contrast associated with carbonation. To reduce these effects, each image was converted to RGB format and processed using a rolling-ball background subtraction with a radius of 100 pixels (*Figure 4.2b*).

The chosen radius exceeds the characteristic scale of local texture features while remaining smaller than the disc diameter, allowing broad illumination gradients to be removed without eroding genuine stain features. Smaller radii (<50 pixels) tended to

suppress parts of the carbonation boundary, whereas larger radii (>150 pixels) were insufficient to correct edge-related gradients. A radius of 100 pixels provided consistent correction across the full dataset and was therefore adopted for all subsequent analysis.

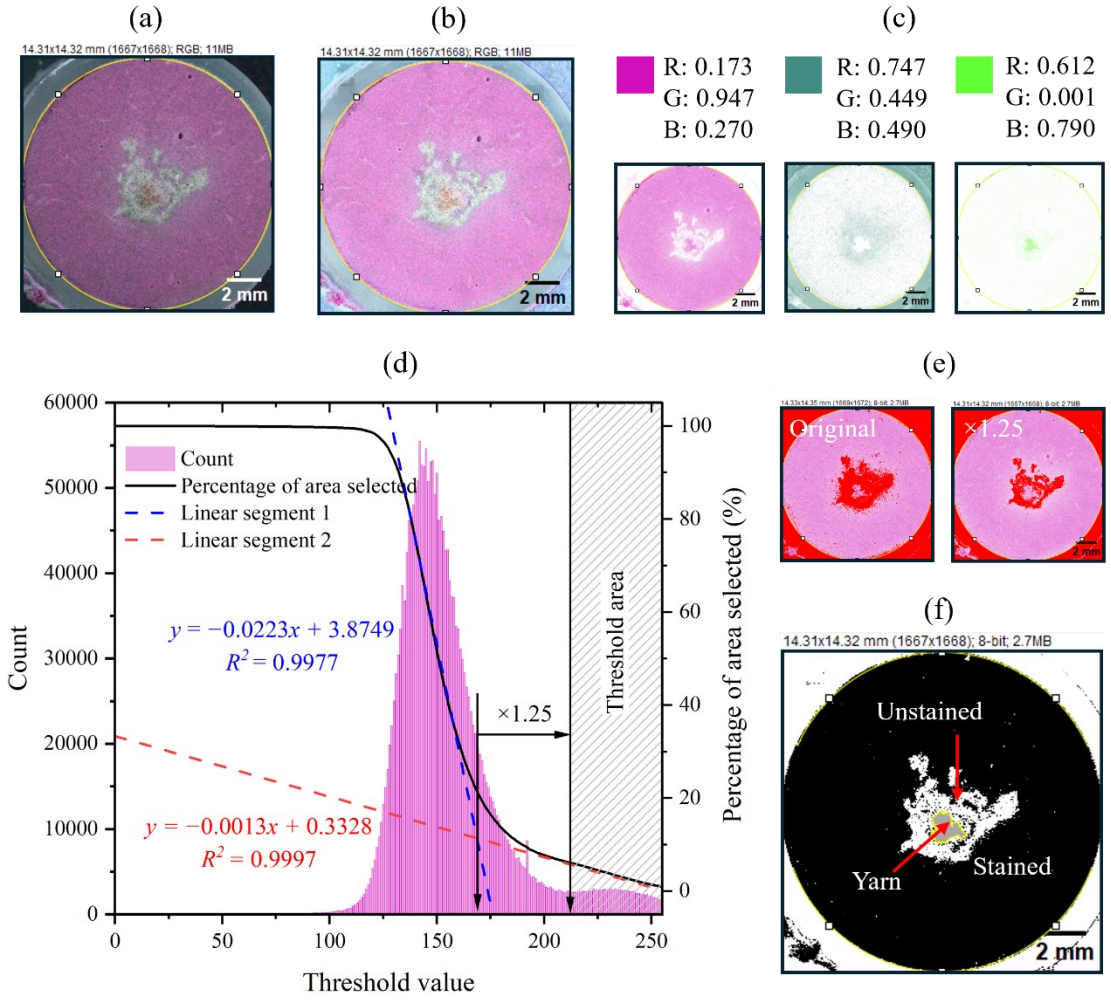


Figure 4.2. Image processing workflow for a representative phenolphthalein-stained disc (J-C-D7). (a) Raw RGB image with ROI defined. (b) Rolling-ball background subtraction at 100 pixels. (c) Colour deconvolution using standardised vectors: (c-1) phenolphthalein stain; (c-2) cement matrix paste; and (c-3) residual colour. (d) Threshold determination using the overflow segmentation method. (e) Binary mask of carbonated area before and after the correction factor (×1.25) applied. (f) Schematic illustration of carbonated area fraction.

4.3.2. Colour deconvolution

Colour deconvolution was used to separate overlapping colour contributions in phenolphthalein-stained images (Ruifrok & Johnston, 2001), where the images were decomposed according to 2 - 3 user-specified sets of colour vectors. For phenolphthalein-sprayed samples, two distinctive colours can be identified: (1) yellowish-grey from the

unstained carbonated areas (pH < 9) and (2) reddish-purple from the uncarbonated areas (pH > 9).

To determine the values of these, the mean colour vectors pertaining to the carbonated and uncarbonated zones across all samples (240 discs) were measured and normalized from an RGB scale of 0-255 to a unitary scale of 0-1. Using these vectors, each background-corrected RGB image was decomposed into three 8-bit channels (*Figure 4.2*c): a stain channel, a cement matrix channel, and a residual channel. The first two channels showed the absorbance along the defined vectors, while the residual channel captured any remaining colours. The very small residual signal within the ROI confirmed that the selected vectors described the phenolphthalein response and paste colour accurately.

The residual channel also revealed features not represented by the stain or matrix vectors. The fibre yarns consistently appeared in this channel because their colour differed from both phenolphthalein stain and cement paste. This separation ensured that fibres did not affect the histogram used for threshold selection (Section 4.3.3) and allowed their area to be identified cleanly in the masking step that followed. The stain channel showed the clearest tonal separation and was therefore used for segmentation.

4.3.3. Threshold and segmentation

The overflow segmentation method (Wong, Head & Buenfeld, 2006), originally developed for pore detection in backscattered electron images, was adapted to this channel to identify the carbonation boundary. The method determines the threshold from the inflection point of a cumulative intensity histogram and is therefore suited to situations where pixel intensity distributions overlap and transitions between regions are gradual rather than sharply defined.

An objective threshold was first obtained by constructing a cumulative histogram of stain-channel intensities, in which the segmented area fraction (%) was plotted against pixel value (0–255). Two linear segments were fitted to the cumulative curve, and their intersection was taken as the lower threshold bound, corresponding to the transition between pixel populations associated with stained and unstained paste (*Figure 4.2d*). The upper threshold bound was fixed at 255.

Because overflow segmentation is known to slightly overestimate the segmented region, the calculated lower threshold was multiplied by a correction factor, f. This factor accounts for the gradual nature of the colour transition and suppresses spurious segmentation near the specimen edge. The value of f was selected by comparison with visual interpretation of representative discs, ensuring close agreement between the corrected segmentation boundary and visual assessment (*Figure 4.2e*). The determination and sensitivity of this parameter are described in detail in Section 4.4.

Fibre yarns did not influence the segmentation step because they are not represented in the stain channel. Their area was identified separately using the residual channel (Channel 3), in which fibre pixels are isolated following colour deconvolution. Applying a full-range threshold (0–255) to this channel extracted the fibre region, allowing its area to be excluded from the region of interest during subsequent area calculations.

With these procedures, segmentation was applied consistently across all 240 discs analysed. The resulting binary masks were used for fibre exclusion and for calculation of the carbonated area fraction.

4.3.4. Quantification of carbonated area fraction

Following segmentation and thresholding, the carbonated area fraction (%) was calculated using the areas of each region (*Figure 4.2f*). The carbonated area fraction ($f_{carbonated}$, %) was defined as:

$$f_{carbonated} = \frac{A_c}{A_{ROI} - A_f} \times 100 \tag{4.1}$$

where, A_c is the area of the segmented carbonated zone (mm^2), A_f is the area of the yarn bundle, and A_{ROI} is the area of region of interest (mm^2).

Subtracting the fibre area from the denominator ensured that only cement paste contributed to the final measurement, allowing carbonation to be quantified consistently across all discs regardless of fibre type or bundle size.

4.4. Sensitivity analysis

A subset of 20 discs was selected for validation, comprising jute-reinforced specimens at 1, 3, 5 and 7 days of carbonation and depths of 0, 10, 20, 30 and 40 mm from the exposed surface. For each disc, two observers (the author and a colleague) manually delineated the carbonation boundary on the phenolphthalein stain-channel image (*Figure 4.3c*). The same region of interest and fibre exclusion rules as in the automated workflow were used (Section 4.3). Small, unwanted carbonated regions surrounding the outer edge of the specimen, caused by CO_2 ingress through the narrow gap between the disc and centrifuge tube during curing, were manually removed at this stage. Manual carbonated area fractions were averaged across both observers; the underlying data are given in Appendix 2 (*Table A2.2*).

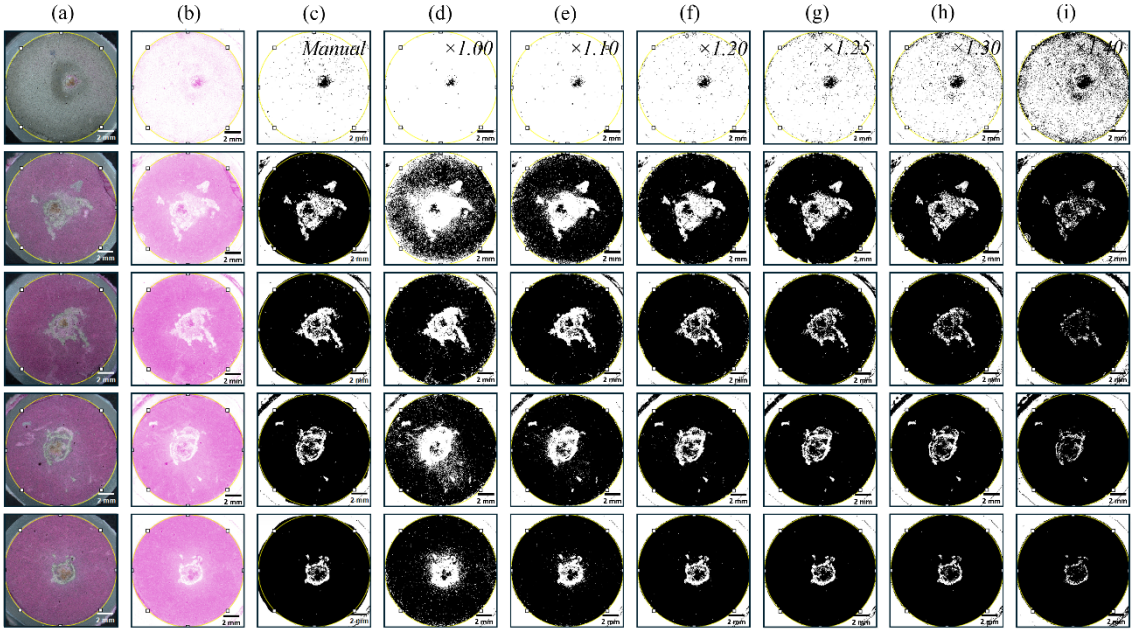


Figure 4.3. Representative phenolphthalein-stained cross-sections of J-C-D7 specimens at increasing depths from the CO_2-exposed surface (0–40 mm, top to bottom). (a) Original images. (b) Corresponding colour-deconvoluted binary images. (c) Manual segmentation based on visual interpretation of the phenolphthalein boundary. (d–i) Automated segmentation using the overflow-based thresholding method with correction factors of 1.00 (original threshold), 1.10, 1.20, 1.25, 1.30, and 1.40, respectively.

Automated segmentation was then repeated on the same discs for correction factors f =1.00, 1.10, 1.20, 1.25, 1.30 and 1.40. *Figure 4.3* compares, for specimen J-C-D7, the original colour images, the stain-channel binary images, the manual threshold, and the automated segmentations for each correction factor applied. At the original calculated

threshold by overflow segmentation (f =1.00), the segmented region is clearly too extensive, with scattered pixels and a bright rim near the specimen edge. Increasing f suppresses this spurious rim and progressively sharpens the carbonation front. Visual agreement with the manually segmented boundary is best for f between 1.20 and 1.25, whereas higher factors (f =1.30–1.40) truncate the outer part of the carbonated zone.

For each disc and each value of f , the calculated carbonated area fraction was compared with the manual threshold reference. Bias, mean absolute error, standard error of the error (i.e. difference from manual threshold $f_{carbonated}$), and the coefficient of determination (R^2) from linear regression were calculated (*Table 4.1*, *Figure 4.4*). Mean absolute error decreased from 10.8 % area at f =1.00 to a minimum of 1.0 % area at f =1.25, with a small increase at f =1.30 and a marked increase at 1.40. Standard error followed the same trend. R^2 increased from 0.94 at f =1.00, to 0.99–1.00 for f values of 1.2 – 1.3, with the regression line for f =1.25 lying closest to the 1:1 line in *Figure 4.4*. Thus, both visual inspection (*Figure 4.3*) and the error metrics (*Table 4.1*) indicate that a correction factor of 1.25 gives the best overall agreement with manual observation and threshold, while lower factors retain unwanted peripheral carbonation and higher factors begin to under-segment the carbonated region.

Table 4.1. Validation of overflow-based image segmentation against manual segmentation for different threshold scaling factors. Agreement is quantified for the carbonated area fraction using mean absolute error, standard error, and coefficient of determination. Threshold values correspond to the lower and upper bounds applied to the deconvoluted binary images.

f	Threshold value		Carbonated area fraction		
	lower bound	upper bound	mean absolute error (% area)	Standard error (% area)	R^2
1.00	168	255	10.8	2.2	0.937
1.10	185	255	4.1	0.8	0.991
1.20	201	255	1.3	0.3	0.998
1.25	**210**	**255**	**1.0**	**0.2**	**0.999**
1.30	218	255	1.6	0.4	0.999
1.40	235	255	6.1	1.7	0.995

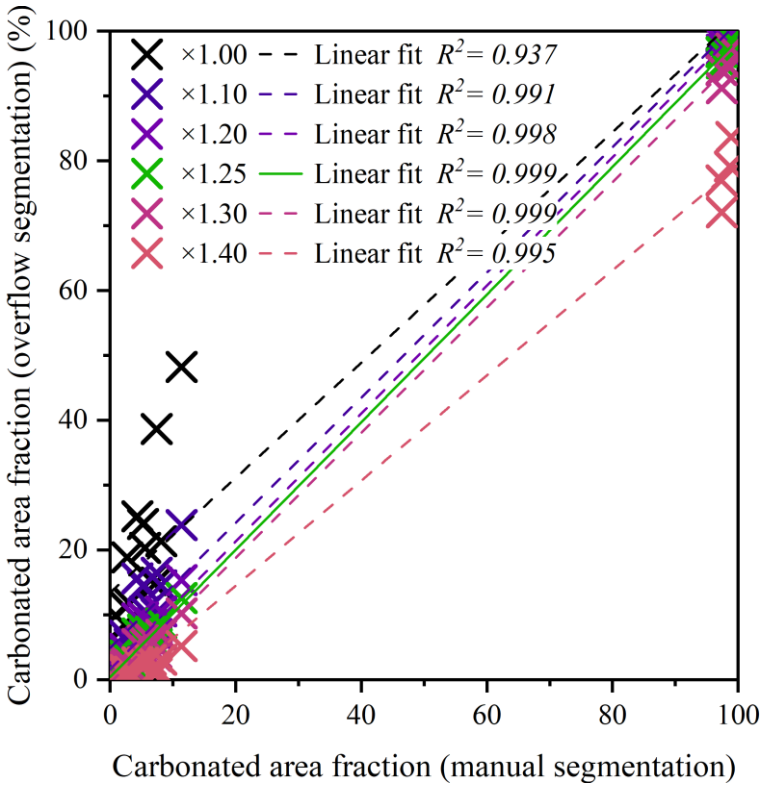


Figure 4.4. Correlation between carbonated area fraction determined by manual segmentation and by overflow segmentation method. Coefficient of determination (R^2) is obtained from linear regression.

The variation in mean absolute error and standard error across f also provides a direct measure of sensitivity to the threshold correction factor. Within the range f = 1.20–1.30, both MAE (1.0–1.6 % area) and SE (0.2–0.4 % area) remain very low and R^2 remains ≥ 0.998, indicating that the segmentation outcome is robust to moderate changes in f around the selected value. By contrast, more extreme values (f = 1.00 and f = 1.40) lead to substantially larger errors and lower R^2, confirming that the threshold correction factor is important outside this stable range. On this basis, the correction factor of 1.25 was adopted for subsequent image analyses (*Figure 4.2*).

4.5. Validation of the method

4.5.1. Carbonated area fraction derived from image analysis

Carbonated area fraction profiles derived from phenolphthalein-stained disc images are used to assess the consistency and depth sensitivity of the proposed image-analysis method. *Figure 4.5* presents the evolution of the image-derived carbonated area fraction with depth for the reference paste and jute-embedded composites after 1, 3, 5, and 7 days of enforced carbonation.

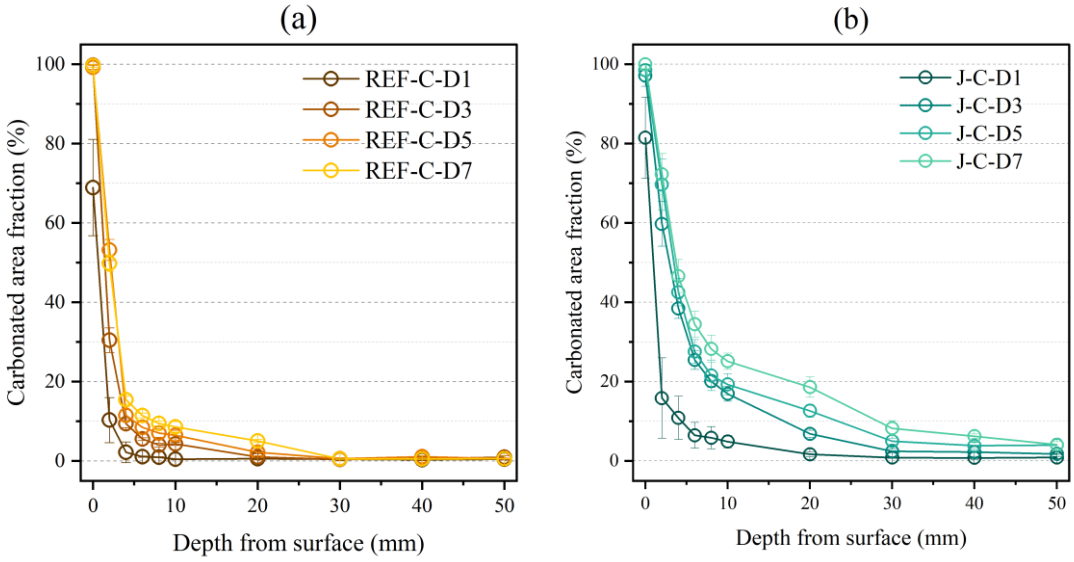


Figure 4.5. Carbonated area fraction profiles for (a) reference paste and (b) jute-embedded composites after 1, 3, 5, and 7 days of enforced carbonation.

In the reference paste (*Figure 4.5a*), the image-derived carbonated area fraction is highest at the CO_2-exposed surface and decreases rapidly with increasing depth. Elevated values are detected at the surface after 1 day of carbonation; however, at all curing durations the carbonated area fraction drops sharply within the first few millimetres and remains close to zero beyond approximately 10 mm. Increasing the carbonation duration from 3 to 7 days results in only minor changes in the depth profiles, indicating that the phenolphthalein response identified by the image-analysis method remains strongly localised near the exposed surface for the reference system.

In contrast, the jute-embedded specimens exhibit higher image-derived carbonated area fractions at all depths and a more gradual decrease with distance from the exposed surface (*Figure 4.5b*). At the exposed surface, the carbonated area fraction increases from 81.5% after 1 day to 97.1% after 3 days, with only small further changes at 5 and 7 days. The most pronounced temporal changes occur between 1 and 3 days, particularly within the near-surface region. For example, at a depth of 2 mm, the carbonated area fraction increases from 15.8% to 59.8% over this period, while at 10 mm it increases from 4.88% to 16.9%.

Across all carbonation durations, the carbonated area fraction decreases with depth, with the steepest gradients consistently observed within the upper 10 mm from the exposed surface. Beyond this region, the decline with depth becomes more gradual. Importantly,

the image-analysis method resolves small but non-zero phenolphthalein responses at greater depths. At 50 mm, a measurable carbonated area fraction is detected after 3 days (1.77%), with further increases at longer carbonation durations (4.00% after 5 days and 4.11% after 7 days). At intermediate depths, progressive increases with carbonation time are also resolved; for instance, at 20 mm the carbonated area fraction rises from 6.83% at 3 days to 12.7% at 5 days and 18.6% at 7 days.

Extending carbonation beyond 3 days does not produce abrupt changes at individual depths. Instead, the image-derived profiles show a smooth broadening of the phenolphthalein-defined region with both time and depth. This gradual evolution indicates that the method is sensitive to incremental changes in the phenolphthalein response across the full section rather than being limited to near-surface detection. On the other hand, the larger scatter observed in carbonated area fraction within the upper 10 mm, particularly at early carbonation ages, likely reflects the combined influence of surface roughness, local heterogeneity, and the sensitivity of the phenolphthalein indicator near its pH transition range. At greater depths, variability decreases as the measured carbonated area fractions approach uniformly low values.

Overall, these profiles demonstrate that the image-analysis method captures systematic, depth-resolved trends in phenolphthalein response that are consistent across specimens and carbonation durations.

4.5.2. Thermogravimetric analysis

Thermogravimetric analysis was used to examine the depth- and time-dependent evolution of carbonation products and to assess whether the trends obtained from phenolphthalein-based image analysis are reflected in calcium carbonate formation. Representative TG–DTG curves for surface, partially carbonated, and bottom discs are shown in *Figure 4.6*, while depth-resolved CO_2 uptake profiles calculated from TG data are presented in *Figure 4.7*.

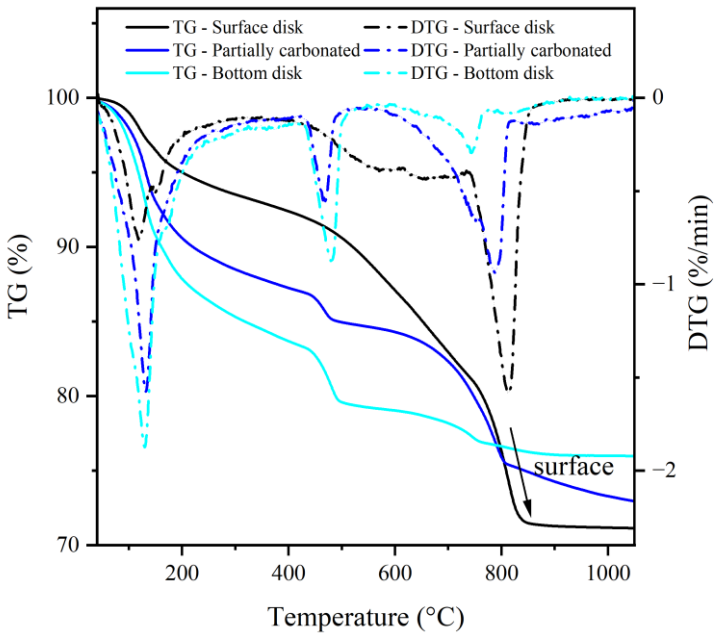


Figure 4.6. Representative TG–DTG curves for surface, partially carbonated, and bottom discs

In the low-temperature region below approximately 200 °C, mass loss associated with dehydration of AFt- and C–S–H-type hydrates decreases progressively from bottom to surface discs. This systematic variation indicates modification of the hydrate assemblage with increasing carbonation severity and proximity to the CO_2-exposed surface. Concurrently, the portlandite decomposition peak in the range of approximately 400–500 °C diminishes markedly towards the exposed surface, confirming progressive consumption of portlandite with increasing carbonation duration and decreasing depth. Carbonate-related mass losses dominate the higher-temperature region of the DTG curves. Surface discs exhibit a broad decomposition feature extending from approximately 400 to 750 °C, together with a more pronounced peak between 750 and 850 °C. The breadth of this signal indicates the presence of carbonate phases decomposing over a wide temperature range (Xian, Zhang & Shao, 2021; Thiery et al., 2007). In contrast, bottom discs show substantially weaker carbonate-related features, consistent with the very low carbonated area fractions identified by image analysis at these depths.

The depth profiles of CO_2 uptake calculated from TG data (*Figure 4.7*) show trends that closely correspond to those obtained from image-derived carbonated area fractions. For both the reference paste and the jute-embedded composites, CO_2 uptake is highest at the exposed surface and decreases rapidly within the first 10 mm, followed by a more gradual decline with depth. With increasing carbonation duration, CO_2 uptake increases at all depths, with the most pronounced changes occurring between 1 and 3 days, particularly

near the exposed surface. Beyond this period, further increases in uptake are more gradual, consistent with the image-derived profiles that show progressive broadening of the phenolphthalein-defined region rather than abrupt inward advancement.

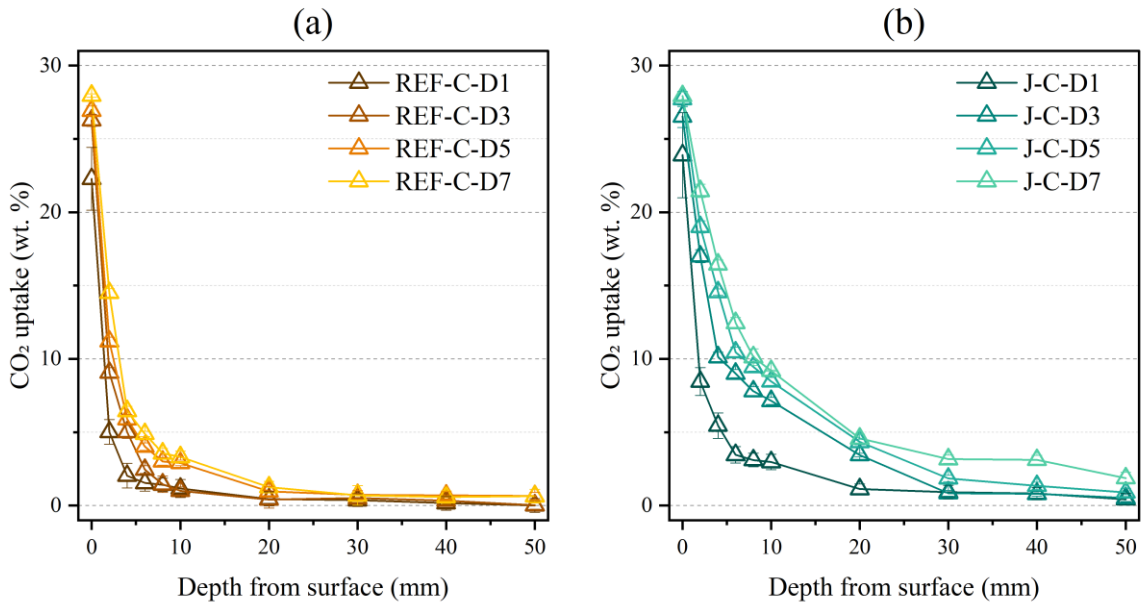


Figure 4.7. CO_2 uptake (wt.%) calculated from TG curves for (a) reference paste and (b) jute-embedded composites after 1, 3, 5, and 7 days of enforced carbonation.

4.5.3. X-ray diffraction

X-ray diffraction was used to identify crystalline carbonation products and to cross-check depth-dependent trends indicated by image analysis and thermogravimetric measurements. Representative diffraction patterns for uncarbonated, partially carbonated, and mostly carbonated discs are shown in *Figure 4.8a*.

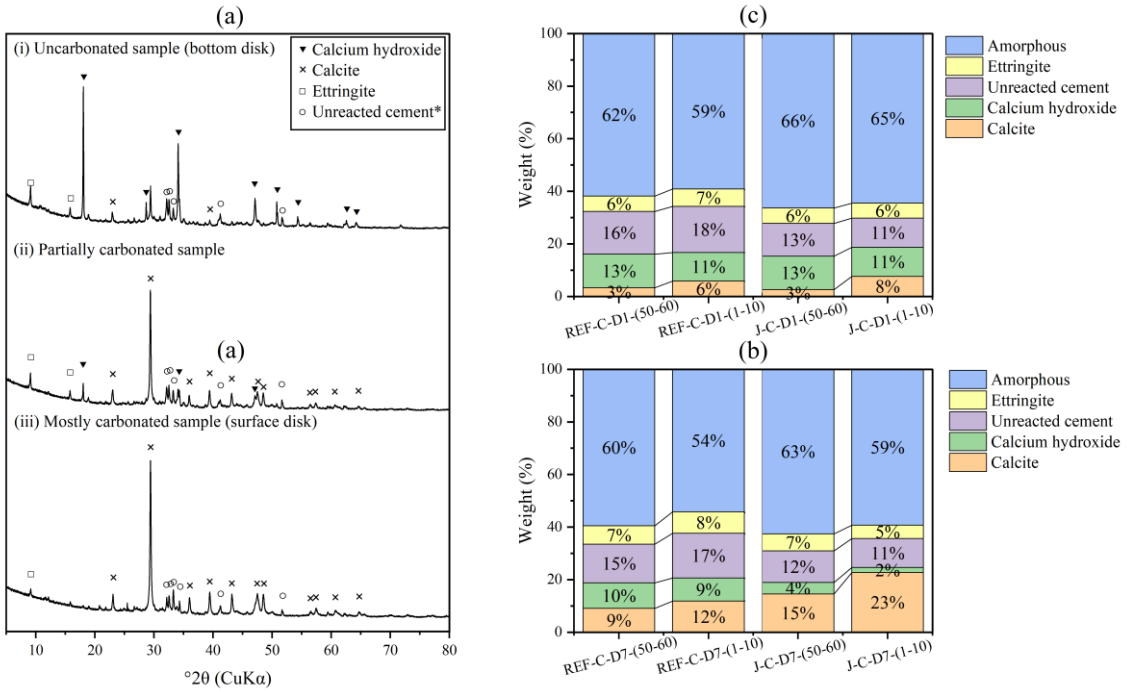


Figure 4.8. (a) XRD patterns of (i) uncarbonated bottom disc, (ii) partially carbonated disc, (iii) mostly carbonated sample (surface disc). *Unreacted cement phases include C_3S, C_2S, C_3A and C_4AF. Phase compositions of (b) top (1 – 10 mm) and (c) bottom (50-60 mm) reference and jute-embedded samples carbonation cured for 1 and 7 days.

The diffraction patterns show calcium hydroxide, calcite, and ettringite as the main crystalline hydration- and carbonation-related phases, together with residual anhydrous cement phases (C_3S, C_2S, C_3A, and C_4AF). With increasing carbonation severity from bottom to surface discs, portlandite reflections decrease while calcite reflections increase, confirming progressive carbonation with decreasing depth. Calcite was the only crystalline calcium carbonate polymorph detected; no aragonite or vaterite reflections were observed. Near the exposed surface, portlandite peaks are strongly reduced or absent, accompanied by diminished ettringite and clinker reflections. This indicates that carbonation affects both hydration products and residual cement phases. AFm reflections were not detected, which is consistent with their low crystallinity and the relatively early hydration age of the specimens.

Quantitative phase analysis (*Figure 4.8b–c*) shows that calcite content increases with carbonation duration at both investigated depths. At equivalent depths and curing times, calcite contents are consistently higher in jute-embedded samples than in the reference paste. After 7 days of carbonation, calcite content in the 1–10 mm region reaches approximately 23 wt.% in jute-embedded samples, compared with around 12 wt.% in the

reference paste. Calcite was also detected in the 50–60 mm region and increased with carbonation duration.

4.5.4. Fourier-transform infrared spectroscopy

Fourier-transform infrared spectroscopy (FTIR) was used to provide complementary, phase-sensitive information on carbonation products that are not fully resolved by XRD, particularly poorly crystalline or amorphous calcium carbonates and changes to C–S–H.

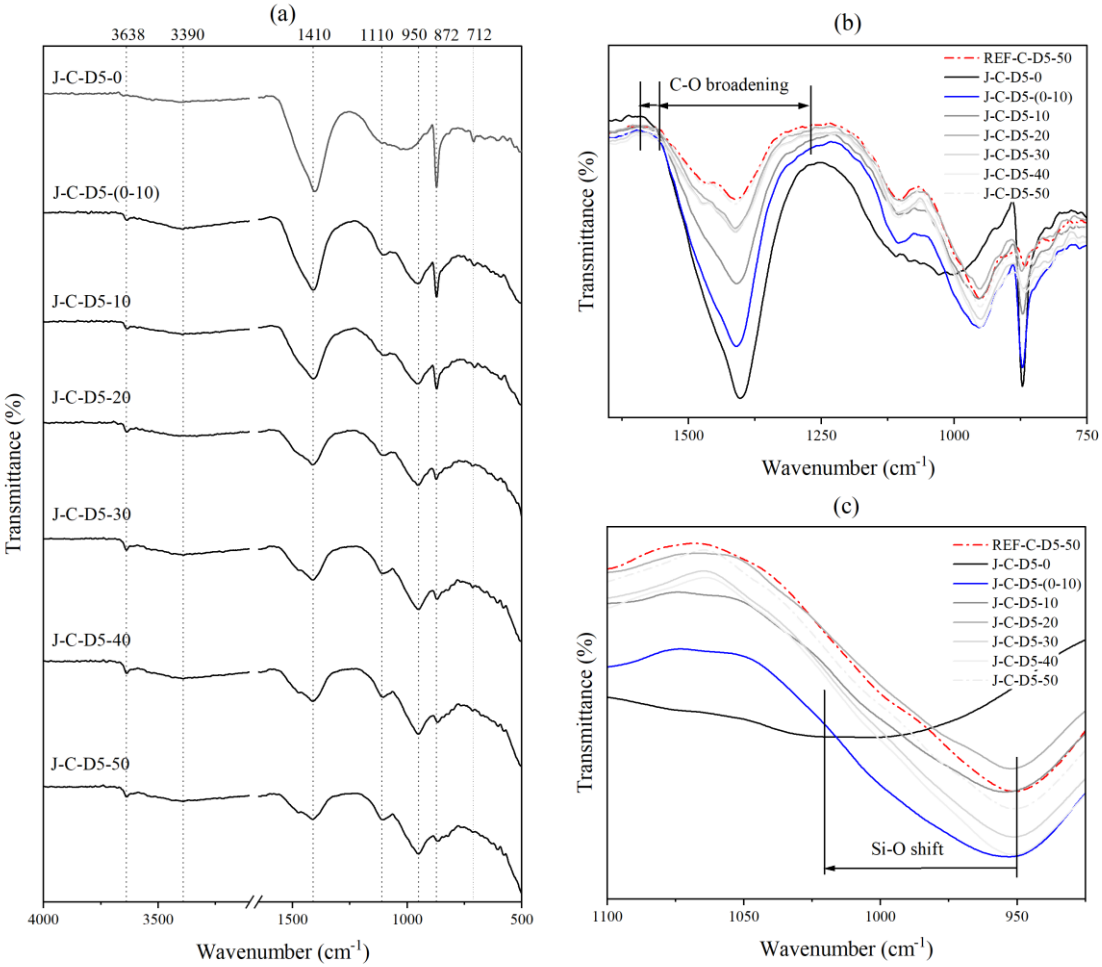


Figure 4.9. Evolution of the FTIR spectra of jute-embedded discs (J-C-D5) subjected to 5 days of enforced carbonation; (a) stacked overview; (b) position and broadening of C-O bonds; (c) position and shifting of Si-O bonds.

Figure 4.9a shows FTIR spectra for jute-embedded samples after 5 days of carbonation curing, which are representative of the trends observed across all carbonation durations. The region between 800 and 1200 cm^{-1} is dominated by Si–O stretching vibrations associated with C–S–H (Zajac et al., 2020). In the least carbonated regions, a band centred at approximately 950 cm^{-1} is observed, corresponding to Q^1 silicate units in C–S–H (Xian,

Zhang & Shao, 2021). Towards the exposed surface, this band shifts and broadens towards higher wavenumbers, approaching the Si–O–Si stretching region near 1100–1120 cm^{-1} (Bhat & Debnath, 2011) (*Figure 4.9c*). This shift indicates progressive decalcification and structural reorganisation of C–S–H associated with carbonation. At greater depths, where carbonation is limited, the position of the Si–O band remains largely unchanged.

Carbonation near the exposed surface is further confirmed by the development of characteristic carbonate absorption bands. Strong asymmetric C–O stretching bands appear at approximately 1410–1470 cm^{-1}, together with out-of-plane and in-plane bending modes at around 872 cm^{-1} and 712 cm^{-1}, respectively (*Figure 4.9b*). The intensity of these bands decreases progressively with depth from the exposed surface, providing a qualitative indication of the carbonation gradient that is consistent with image-derived and TGA-derived depth profiles. In addition, the depletion of portlandite in highly carbonated regions is reflected by the disappearance of the O–H stretching band at approximately 3640 cm^{-1}, while a reduction in broad water-related bands between 3600 and 3000 cm^{-1} is consistent with carbonation of hydrate phases (Xian, Zhang & Shao, 2021).

In the most carbonated surface discs, the asymmetric carbonate stretching region exhibits band broadening and weak shoulders at higher wavenumbers (*Figure 4.9b*). Such features have been reported in the literature to be associated with poorly crystalline or amorphous calcium carbonate, and in some cases with minor contributions from metastable polymorphs (Rodriguez-Blanco, Shaw & Benning, 2011). However, due to the overlap of carbonate absorption bands and the limited ability of FTIR to distinguish between carbonate polymorphs, these phases cannot be identified unambiguously by FTIR alone.

4.6. Discussion

4.6.1. Comparison between image analysis and mass- and phase-based characterisation results

The carbonated area fractions obtained from phenolphthalein-based image analysis were compared with TGA, QXRD, and FTIR results to determine whether the image-derived metric provides a consistent representation of carbonation severity across methods with different analytical bases.

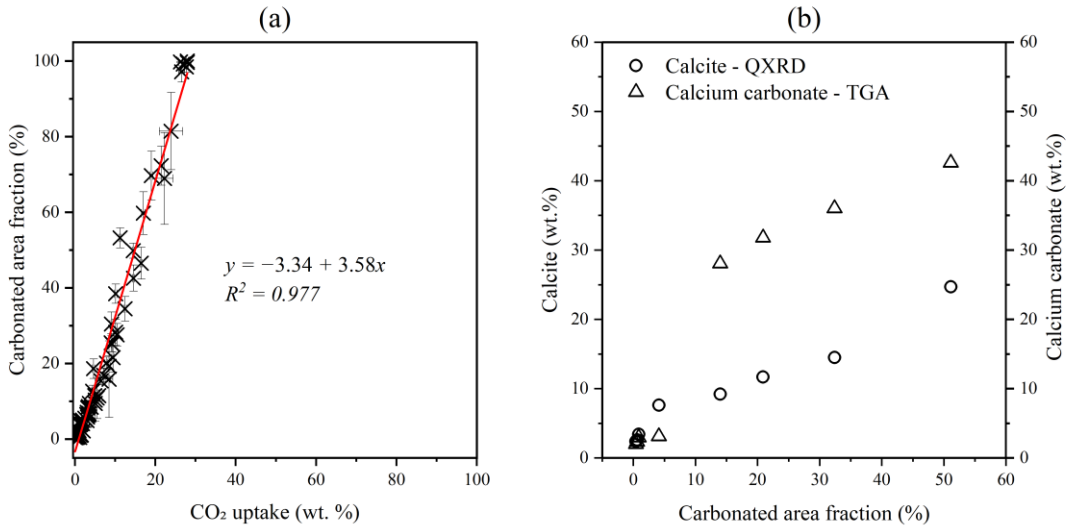


Figure 4.10. (a) Relationship between carbonated area fraction (image analysis) and CO_2 uptake from TGA. (b) Comparison of calcite contents from quantitative XRD and calcium carbonate contents from TGA plotted against carbonated area fraction.

The strong relationship between carbonated area fraction and TGA-derived CO_2 uptake (R^2=0.977, *Figure 4.10a*) provides the clearest evidence of consistency between the image- and mass-based measurements. Phenolphthalein identifies the proportion of paste below its pH transition range, whereas TGA quantifies carbonate within a homogenised powder sample. Their agreement therefore indicates that carbonated area fraction tracks the relative progression of carbonation, but does not imply that it can be converted directly into CO_2 uptake. The fitted relationship is specific to the specimen geometry, sampling scheme, and image-processing procedure. The small intercept may reflect carbonate formation detected by TGA in partially carbonated material that has not undergone sufficient alkalinity loss to cross the phenolphthalein transition threshold.

The QXRD comparison provides a complementary phase-based check (*Figure 4.10b*). Calcite, the only crystalline calcium carbonate polymorph detected, increased with carbonated area fraction but remained below the total carbonate content determined by TGA. This is consistent with TGA detecting both crystalline and poorly crystalline carbonate species, whereas QXRD quantifies only detectable crystalline phases. The difference between the two measurements therefore indicates a carbonate fraction that was not fully resolved by QXRD. FTIR provides complementary evidence through the development of carbonate bands and changes in the Si–O stretching region, although overlapping bands prevent quantitative identification of individual carbonate species.

The evolution of the carbonate decomposition response is best interpreted as a progressive change in the phase assemblage participating in carbonation. Portlandite provides the principal early alkaline buffer and is preferentially carbonated, favouring formation of relatively well-crystallised calcite. As portlandite is depleted, carbonation increasingly involves other Ca-bearing phases, particularly C–S–H and ettringite, as well as residual clinker phases under the early-age enforced carbonation conditions. C–S–H decalcification releases Ca for carbonate precipitation while leaving a more polymerised silica-rich residue, whereas ettringite carbonation redistributes Ca, Al and sulphate into carbonate and other secondary products. These reactions can generate finer, structurally disordered, poorly crystalline or amorphous carbonate species that are less thermally stable and therefore contribute to the broader lower-temperature TGA response (*Figure 4.6*). This interpretation is consistent with the surface regions, where XRD showed strong depletion of portlandite together with reduced ettringite and clinker reflections, FTIR showed loss of the portlandite O–H band and a shift of the C–S–H Si–O band towards higher wavenumbers, and TGA measured more total carbonate than the calcite quantified by QXRD. At greater depths, where portlandite and ettringite remained more evident and the C–S–H band changed little, the phase assemblage was less extensively carbonated. The decomposition temperature should nevertheless not be used to assign a unique carbonate precursor, because thermal stability also depends on crystallinity, polymorph, particle size and structural disorder.

The comparison is also affected by spatial resolution and sampling volume. Image analysis retains the lateral distribution of the phenolphthalein response across each disc before reducing it to an area fraction. By contrast, TGA represents homogenised powder from 1-mm-thick discs sampled at nominal 2 mm depth increments, QXRD averages broader 0–10 and 50–60 mm intervals, and FTIR represents homogenised powder collected at selected depths. At the exposed surface, where carbonation was near-uniform across the disc, this difference has little effect. At greater depths, carbonation became increasingly localised around the jute yarn, so powder-based methods necessarily averaged highly carbonated yarn-adjacent paste with surrounding material of lower carbonation extent. A locally highly carbonated region may therefore produce only a moderate bulk chemical response. In addition, phenolphthalein reflects alkalinity loss rather than carbonate formation itself, allowing chemical evidence of carbonation to extend beyond the phenolphthalein-defined carbonated region.

Taken together, these results validate carbonated area fraction as a comparative spatial measure of phenolphthalein-defined carbonation rather than a direct measure of reacted carbonatable phases. Image analysis describes carbonation geometry, TGA quantifies CO_2 uptake, QXRD identifies crystalline phase evolution, and FTIR provides complementary evidence of carbonate formation and silicate modification. The correspondence between these measurements supports the use of carbonated area fraction for resolving heterogeneous carbonation profiles, while their differences reflect the distinct spatial scales and chemical responses of each method.

4.6.2. Strength and limitations

The proposed image-analysis method enables quantification of carbonation profiles from cross-sectional discs, capturing spatial variations in carbonation geometry that cannot be resolved using conventional depth-based metrics. Colour deconvolution provides robust separation of the phenolphthalein response from the cement paste background, reducing sensitivity to illumination gradients, surface texture, and local artefacts. Objective threshold selection based on cumulative histograms ensures consistent segmentation, while automated processing allows large datasets to be analysed without user-dependent adjustment. The cross-method validation in Section 4.6.1 supports the use of carbonated area fraction as a comparative measure of heterogeneous carbonation, while recognising that phenolphthalein reflects alkalinity loss rather than carbonate mass.

Fibre regions are excluded without manual outlining by isolating yarn pixels in the residual channel generated during colour deconvolution, preventing systematic overestimation of carbonation area in fibre-embedded specimens. However, this step relies on sufficient colour contrast between fibres, stain, and paste; where overlap occurs, additional controls such as alternative fibre selection or imaging prior to staining would be required.

Several limitations should be noted. The method depends on a consistent phenolphthalein response, which can be influenced by moisture state and the extent of carbonation, and on calibrated colour vectors that may require reassessment if staining or imaging conditions change. The analysis is inherently two-dimensional and characterises carbonation only within the exposed cross-section; three-dimensional connectivity and continuity of carbonated regions cannot be resolved without complementary techniques.

In addition, severely rough or mechanically damaged surfaces may introduce segmentation artefacts and therefore warrant visual verification of automated outputs.

4.6.3. Implications for future work

The image-analysis workflow established and validated in this chapter provides a flexible framework that can be extended to a wider range of cementitious systems and experimental conditions and would support a more general understanding of natural fibre-enhanced carbonation mechanisms. In addition, the carbonated area fraction calculated from this method provide a suitable foundation for numerical modelling of CO_2 transport and reaction pathways, particularly in systems where fibres modify carbonation front and geometry.

The depth resolution adopted here was chosen to capture rapid near-surface carbonation for validation against TGA; however, the dense sampling in the first 10 mm is not required in all applications. Future studies may adopt coarser or adaptive depth intervals depending on specimen size, exposure conditions, and the spatial resolution required. Application of the method to specimens with different geometries and dimensions would further clarify how carbonated area fraction relates to CO_2 uptake across sample formats. While absolute correlations are expected to remain geometry-specific, systematic comparison may reveal transferable scaling trends.

The unresolved carbonate response identified in the present analyses warrants further phase-specific characterisation. Coupling TGA with evolved gas analysis would allow the origin of these features to be resolved and improve interpretation of early-stage carbonation. Integration with SEM-BSE imaging also offers scope for linking carbonation maps with pore structure and fibre–matrix interfacial zones, providing insight into how fibre-induced microstructural features influence carbonation. Furthermore, extension of the workflow to three-dimensional datasets through serial sectioning or micro-CT would enable analysis of carbonation along fibre length, complementing the cross-sectional approach used here. Beyond phenolphthalein staining, the proposed image analysis method could be adapted to other colour-based indicators, including those used for chloride ingress or pH mapping in alternative binder systems.

4.7. Conclusion

This chapter established and validated a phenolphthalein-based image-analysis workflow for quantifying carbonation in small cement paste disc specimens sectioned perpendicular to the CO_2-exposed surface. The method was developed to address challenges associated with heterogeneous carbonation patterns, diffuse phenolphthalein colour transitions, and sensitivity to imaging artefacts in high-resolution datasets.

By combining background correction, colour deconvolution, objective segmentation, and automated processing, the method enables reproducible quantification of carbonated area fraction across large datasets while avoiding systematic bias from fibre cross-sections. Comparison with thermogravimetric analysis, quantitative X-ray diffraction, and Fourier-transform infrared spectroscopy shows that the image-derived metrics are consistent with independent chemical indicators of carbonation, with differences reflecting the inherent sensitivities of each technique.

Overall, the proposed image-analysis method enables efficient quantification of carbonation geometry from phenolphthalein-stained images and provides the methodological basis for examining fibre-enhanced carbonation behaviour in the chapters that follow.

Chapter 5 Feasibility study on natural fibre-enhanced CO_2 transport and uptake

This chapter is based on the journal article "*Natural fibre-enhanced CO_2 transport and uptake in cement pastes subjected to enforced carbonation*" by Zhuge, Y., Ong, P. B., Wong, H. S., and Myers, R. J., published in the Journal of CO_2 Utilization. The experimental programme, data analysis, and interpretation were led by the author. Pei Boon Ong contributed to the experimental design, assisted with sample preparation, and carried out part of the thermogravimetric analysis. The results are reorganised and discussed here in the context of this thesis, with emphasis on carbonation behaviour and fibre-enhanced CO_2 transport in cement pastes.

5.1. Introduction

Enforced carbonation curing has been proposed as a practical route for increasing CO_2 uptake in cement-based materials. In dense cement pastes, however, carbonation commonly remains confined to regions close to the exposed surface, even under elevated CO_2 concentrations. This behaviour reflects limitations in gas transport within the cement matrix, arising from restricted pore connectivity and progressive pore blocking as carbonation products accumulate (Steiner et al., 2020; Jang & Lee, 2016). As demonstrated in Chapter 4, reference cement paste specimens without fibre addition exhibit strongly surface-localised phenolphthalein responses, with carbonation largely restricted to a shallow near-surface zone (Section 4.5.1).

This limitation motivates the examination of strategies that may redistribute CO_2 ingress beyond the surface region. Spun natural fibre yarns introduce continuous features that extend from the exposed surface into the interior of the paste and therefore differ fundamentally from short, dispersed fibres, whose influence on transport is local and poorly controlled (Hu et al., 2023; Hay, Krishnan & Celik, 2024). When embedded in cement paste, yarns provide connected pathways with defined geometry that may

influence how CO_2 enters and propagates within the material. In addition, natural fibre yarns possess intrinsic porosity arising from both the internal structure of individual fibres and the packing of fibres within the yarn bundle. These characteristics may modify the local pore structure of the surrounding cement paste and increase the interfacial area available for carbonation reactions.

Results presented in Chapter 4 provide initial evidence that the presence of an embedded yarn is associated with altered carbonation patterns relative to plain cement paste. In particular, yarn-containing specimens exhibit more heterogeneous phenolphthalein responses and detectable pH changes at locations further from the exposed surface. While these observations do not in themselves establish governing transport mechanisms, they indicate that the introduction of a single yarn is associated with a redistribution of carbonation geometry beyond surface-controlled carbonation and therefore warrants a systematic investigation.

Hence, the purpose of this chapter is to assess the feasibility of using spun natural fibre yarns to influence CO_2 transport and carbonation behaviour in cement pastes subjected to enforced carbonation. The chapter focuses on the effect of individual yarns and examines how different natural fibre types modify the extent and geometry of carbonation within the cement matrix. Carbonation is characterised using the phenolphthalein-based image analysis framework established in Chapter 4, with thermogravimetric and microstructural measurements used to support interpretation of the results. The findings provide a focused evaluation of single-yarn effects on carbonation behaviour and inform the development of more complex yarn arrangements examined in later chapters.

5.2. Materials and methods

5.2.1. Materials and sample preparation

Spun natural fibre yarns of jute, hemp, cotton, and wool were selected to examine carbonation behaviour at the level of individual yarns. These fibre types represent a range of yarn morphologies, internal porosities, and moisture-related properties, enabling comparison of carbonation behaviour associated with different yarn structures. The yarns were drawn from the material set introduced in Section 3.2, with details of fibre sourcing, industrial pre-treatment, physical properties (including diameter, water absorption, and compactness), and representative appearances provided in *Table 3.1* and *Figure 3.2*.

Cement paste was prepared using CEM I 52.5N Portland cement supplied by Breedon. The cement composition, determined by X-ray fluorescence, and the initial CO_2 content measured by thermogravimetric analysis are reported in *Table 3.2* (Batch 1). All specimens were produced at a constant water-to-cement mass ratio of 0.4.

Cylindrical cement paste specimens containing a single centrally embedded fibre yarn were prepared using the procedure described in Section 3.3 (*Figure 3.4*). For each yarn type, specimens were prepared in triplicate to assess repeatability.

5.2.2. Enforced carbonation curing and sampling

Enforced carbonation curing was conducted under the conditions described in Section 3.4.1. Specimens were carbonated for durations of 1, 3, 5, and 7 days, after which they were sectioned to obtain depth-resolved samples for characterisation. As illustrated in *Figure 5.1*, discs were extracted at depths between 0 and 50 mm below the CO_2-exposed surface at 10 mm intervals to assess cross-sectional carbonation behaviour.

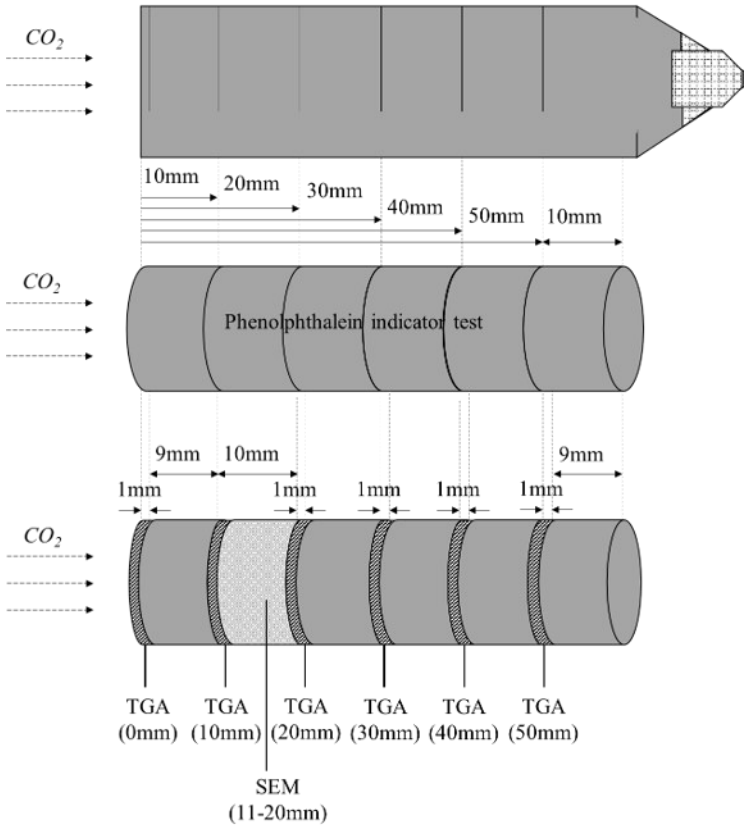


Figure 5.1. Schematic diagram of disc extraction for phenolphthalein indicator testing and complementary characterisation tests.

Immediately after cutting, discs were wiped with tissue paper and briefly fan-dried (less than 10 min) to minimise the influence of excess moisture prior to phenolphthalein indicator test. For complementary characterisation tests, the first 1 mm from the exposed face of each disc was removed and ground for thermogravimetric analysis (TGA). Material from intermediate depths (11–20 mm) was prepared for SEM.

5.2.3. Phenolphthalein indicator test

Carbonation per disc was assessed using phenolphthalein indicator testing following the procedure established in Chapter 4. In this study, phenolphthalein testing was applied to all depth-resolved discs extracted after 1, 3, 5, and 7 days of enforced carbonation. For each carbonation duration and depth (0, 10, 20 ,30, 40, 50 mm), three replicate specimens were analysed to account for variability.

The captured images were analysed using a preliminary version of the phenolphthalein-based image analysis workflow later formalised in Section 4.3. This earlier implementation is illustrated in *Figure 5.2*. Different from the refined workflow, background subtraction was not applied. In specimens containing a centrally embedded yarn, portions of the yarn cross-section were occasionally classified as carbonated due to similarities in colour and texture with carbonated cement paste. To avoid overestimation of carbonation extent, the yarn area was therefore identified manually and excluded explicitly from the analysis. Accordingly, the carbonated area fraction in this chapter was calculated using a modified definition (*Equation 5.1*):

$$Carbonated\ area\ fraction = \frac{A_c - A_y}{A_{ROI} - A_y} \times 100 \tag{5.1}$$

Where, A_c is area of the segmented carbonation zone (mm^2), A_f is the manually selected convex area of the fibre bundle (mm^2), and A_{ROI} is the area of region of interest (mm^2). This formulation reflects the state of the image-analysis workflow at the time these experiments were conducted. The implications of applying this earlier version of the method are discussed in Section 5.4.

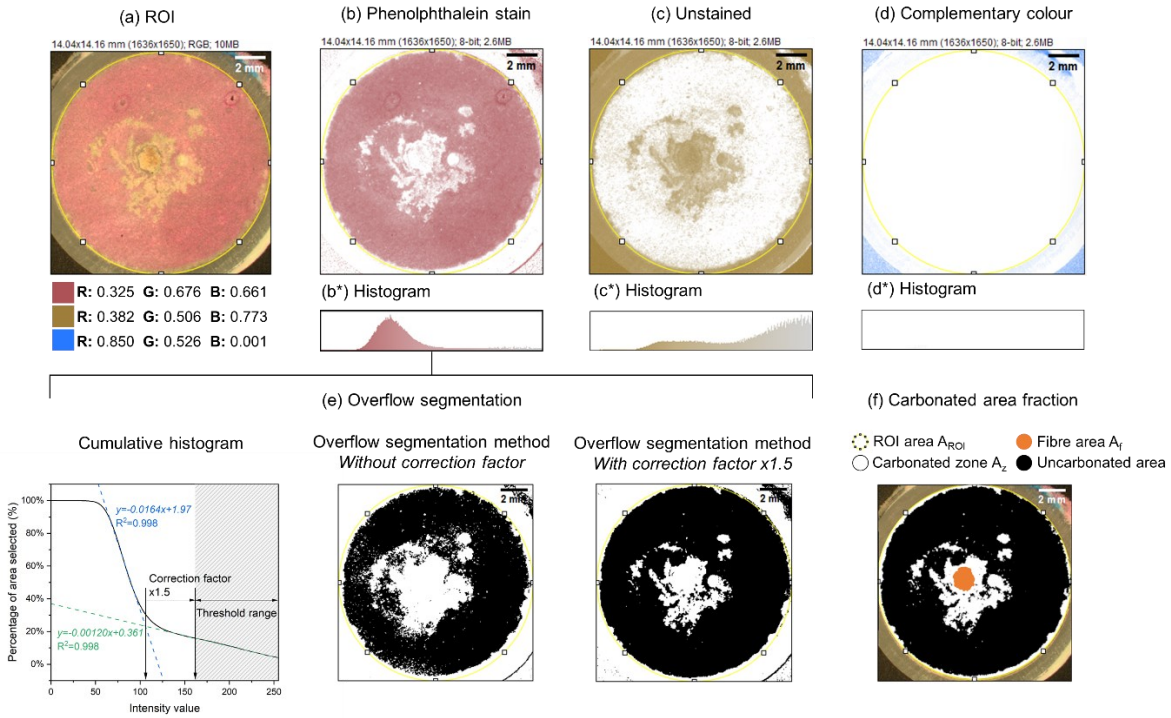


Figure 5.2. (a) Selected region of interest of a carbonated jute yarn sample (J-D7-20); (b-d) colour deconvolution and the corresponding histograms in (b*-d*) using ImageJ; (e) overflow segmentation method to obtain the threshold range of carbonated zone; (f) schematic illustration of carbonated area fraction based on image analysis.

In addition, a set of reference specimens without fibre yarns was sectioned perpendicular to the CO_2-exposed surface to examine the vertical carbonation profile.

5.2.4. Scanning electron microscopy

SEM was used to examine microstructural features associated with carbonation in cement pastes containing natural fibre yarns. Imaging was performed on specimens carbonated for 7 days, using discs extracted from depths of 11–20 mm below the CO_2-exposed surface, corresponding to regions of partial carbonation identified by phenolphthalein testing. Sample preparation and imaging conditions followed the procedures described in *Section 3.5.6*. Backscattered electron (BSE) images were used to assess fibre–matrix interfaces, local porosity, and microstructural changes associated with carbonation.

5.2.5. Thermogravimetric analysis

TGA was used to quantify CO_2 uptake and to enable comparison with image-derived carbonated area fraction. Testing procedures and calculation of CO_2 uptake (*Equation 3.1* and *3.2*) followed the methodology described in Section 3.5.2. For comparisons across

the specimen depth, the reported average CO_2 uptake between 0 and 50 mm was calculated as the arithmetic mean of the TGA-derived uptake values measured at the six sampled depths: 0, 10, 20, 30, 40 and 50 mm. This value is hereafter referred to as the depth-profile-average CO_2 uptake.

To allow direct comparison with image analysis results, the degree of carbonation (DoC, %) for each disc was calculated as the ratio between the measured CO_2 uptake and the theoretical maximum CO_2 uptake of the cement (*Equation 5.2*), providing a normalised metric for comparing carbonation extent with spatial carbonation patterns obtained from image analysis.

The theoretical maximum CO_2 uptake was calculated based on the CaO content of the cement available for carbonation, excluding CaO associated with calcium sulphate phases and pre-existing carbonate in the cement (*Equation 5.3*) (Younsi, Turcry & Aït-Mokhtar, 2022). Cement oxide composition was determined by XRF (*Table 3.2*, Batch 1), while the initial carbonate content was determined by TGA from the uncarbonated cement, corresponding to 1.52 wt.% CO_2. Based on these values, the theoretical maximum CO_2 uptake for the cement paste in this study was 48.6 wt.%.

$$DoC = \frac{CO_{2,uptake}}{CO_{2,theorectical}} \times 100 \tag{5.2}$$

$$CO_{2,theorectical} = \%CaO \times \frac{m_{CO_2}}{m_{CaO}} - \%SO_3 \times \frac{m_{CO_2}}{m_{SO_3}} - CO_{2,initial} \tag{5.3}$$

Thermal decomposition of phenolphthalein and fibre constituents was not resolved in the DTG curves due to their low mass fraction relative to the cement paste and is therefore not discussed further.

5.3. Results and analysis

5.3.1. Image analysis

In image analysis, the carbonated area fractions for fibre-embedded samples were consistently higher than their non-fibre reference counterparts (dotted black line, *Figure 5.3*), confirming that the presence of fibres enhances the transport of CO_2 into the samples. This was also evidenced in the vertical profile carbonation depth tests, where reference

samples (VP-REF) exhibited minimal carbonation, with depths of 0.18 mm, 0.63 mm, 0.80 mm and 0.94 mm respectively.

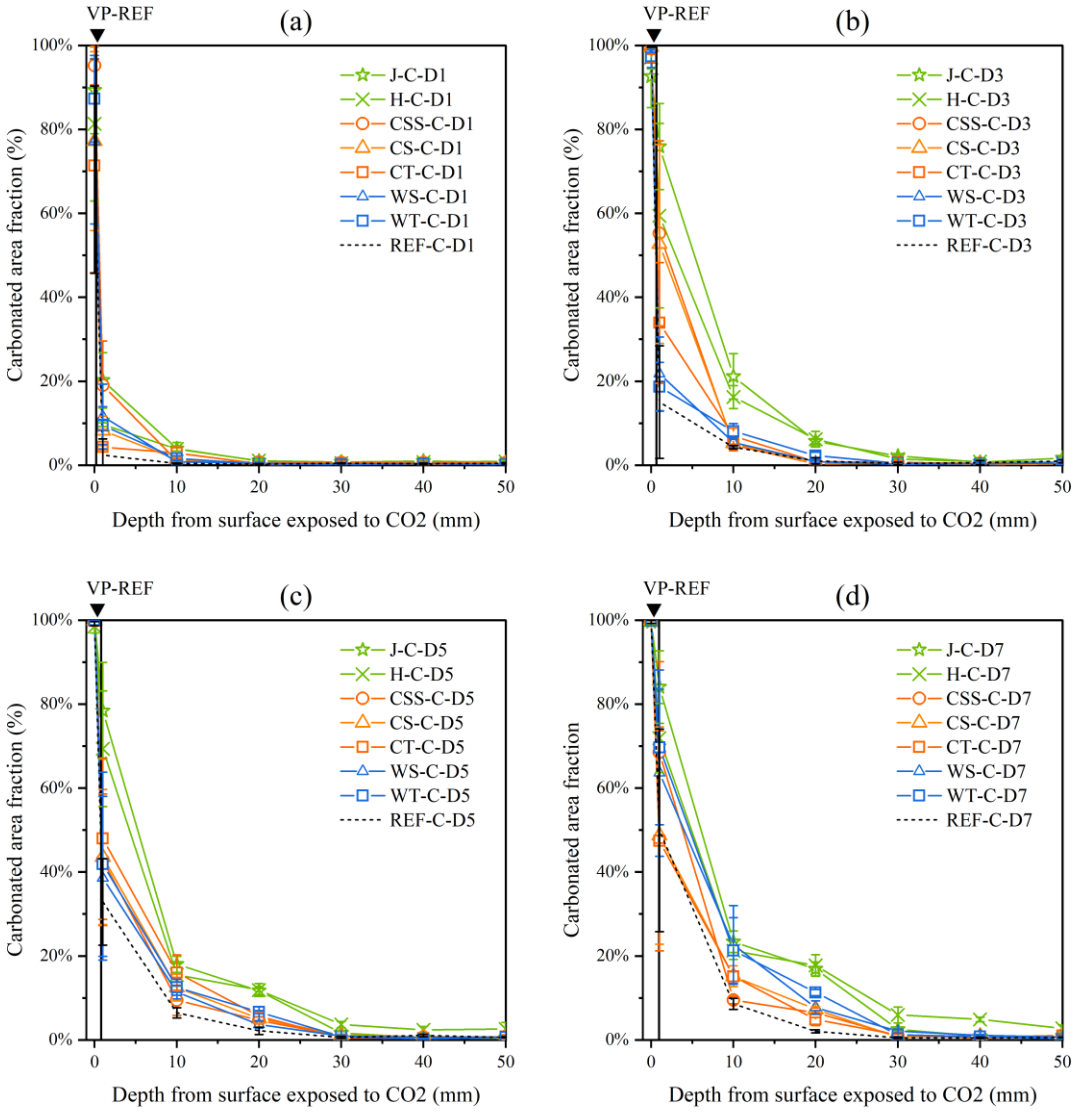


Figure 5.3. Carbonated area fraction in specimens exposed to CO_2 curing; (a) 1-day carbonation curing; (b) 3-day carbonation curing; (c) 5-day carbonation curing; (d) 7-day carbonation curing. VP-REF: vertical carbonation depth of reference samples.

In the first 24 hours of enforced carbonation (*Figure 5.3a*), all samples containing natural fibres exhibited minimal enhancement in carbonation depth. Significant carbonation was localised in the top disc but limited CO_2 penetration beyond 10 mm in depth. The most substantial carbonation occurred between 1 and 3 days (*Figure 5.3b*), particularly in bast cellulose-based fibres such as hemp and jute, which displayed a marked increase in carbonated area. Carbonation progressed more slowly beyond 3 days of curing. After 5 days of enforced carbonation, the increase in carbonated area fraction at depth of 10 mm was less pronounced than that from 1 to 3 days. A reduced rate of carbonation was also

observed between 5 and 7 days of enforced carbonation curing. The results reflected the influence of fibre type and the thickness of fibre yarns on enhancing CO_2 transport into the cement matrix.

Whilst all fibres were effective in enhancing CO_2 transport into greater depth during enforced carbonation, hemp and jute outperformed other type of fibres regardless of thickness or ply count. Jute and hemp-embedded samples showed detectable carbonated area fractions at 50 mm depth after 3 days of curing (0.692% and 1.69%, respectively), whereas cotton and wool demonstrated little to no carbonation beyond 20 mm. Thicker yarns demonstrated slightly increased CO_2 sequestration around the fibres, as implied by the slight increase in unstained areas by the phenolphthalein indicator. Fibre type had a significantly greater effect on carbonated area fraction than yarn thickness.

The geometry of carbonated area also varied among different type of yarns (Appendix 3, *Figure A3.1*). Hemp and jute embedded samples (*Figure 5.4a-b*) displayed an irregular and spread-out carbonation front, demonstrating a more extensive CO_2 transport throughout the matrix. Apart from the colourless carbonation rings around the fibre yarns, patches of carbonated area were also observed in the uncarbonated region. Cotton and wool (*Figure 5.4c,d*), on the other hand, exhibited a more defined and concentrated carbonation front around the yarns, with a clear demarcation between the carbonated and uncarbonated area. The irregular carbonation fronts can be ascribed to the presence of stray fibres (i.e., fibres that diverge from the main yarn bundle). The fibrillation of fibres forms separate CO_2 transport channels and extended carbonated strips from the yarn.

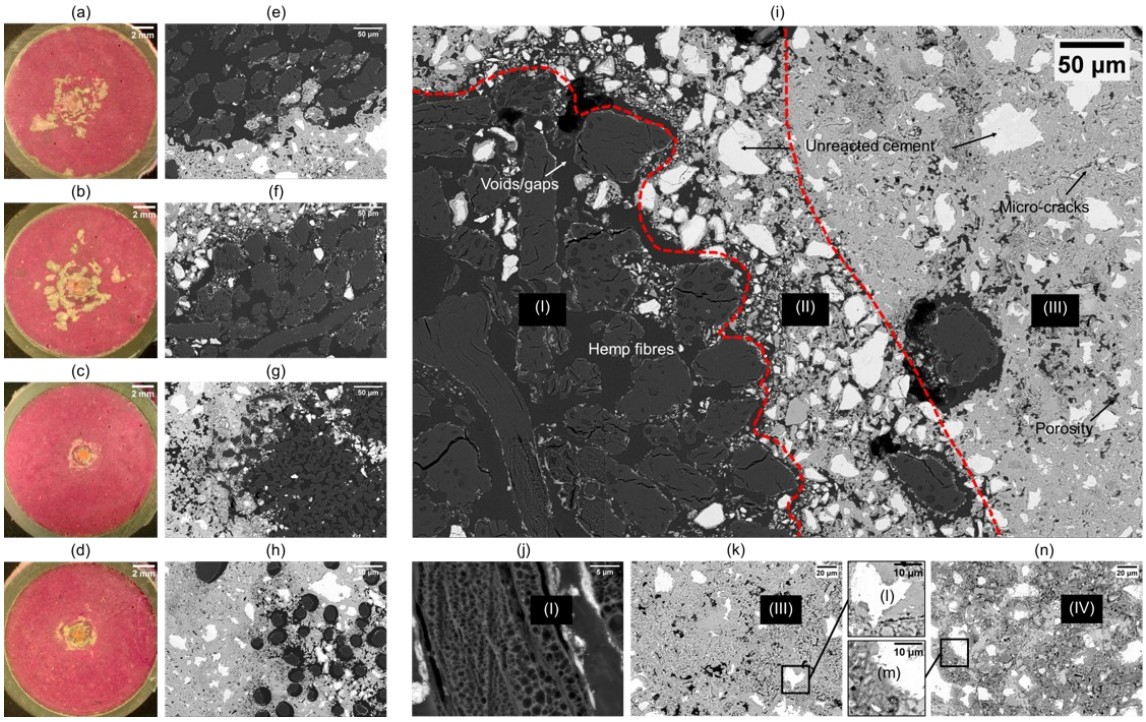


Figure 5.4. Microstructure of carbonated natural fibre cementitious composites. Panels (a-d) show the carbonated areas in samples containing (a) jute (J-C-D7-20), (b) hemp (H-C-D7-20), (c) cotton (CT-C-D7-20), and (d) wool (WT-C-D7-20) yarns. SEM-BSE images (e-h) detailing the paste-fibre interface for (e) jute (J-C-D7-11), (f) hemp (H-C-D7-11), (g) cotton (CT-C-D7-11), and (h) wool yarns (WT-C-D7-11). Images (i-k) further illustrate the microstructural variations in (i) the transition zone featuring the porous hemp yarns adjacent to carbonated cement pastes, (j) internal structure of hemp fibre, (k) a dense calcium-rich carbonated area, and (n) an uncarbonated reference zone. (l) 2-tone inner C-S-H with residual alite observed in carbonated area, (m) inner and outer C-S-H surrounding alite in uncarbonated area. Annotations: (I) natural fibre yarn, (II) porous interfacial transition zone, (III) carbonate-rich zone, (IV) uncarbonated reference zone.

5.3.2. Scanning electron microscopy

SEM-BSE imaging (*Figure 5.4e-n*) further elucidate the interface between natural fibre yarns and the cement matrix, revealing variances in the structural and spatial arrangements of fibres within different yarns.

The bast fibre yarns (*Figure 5.4e-f*) jute and hemp have larger and more internally porous fibre filaments with irregular cross-sections, with hemp fibres (average fibre spacing <10 µm) more compactedly arranged than jute (average fibre spacing <15 µm). Bast fibre yarns demonstrate a clearly defined boundary between the yarn bundles and the cement matrix. Hydration products, carbonation products, and unreacted cement grains only rarely penetrated into the bast fibre yarn convex areas. The edges of individual hemp and jute fibres were surrounded by bright and discrete patches of carbonated hydration

products, aligning with previous research that the surfaces of cellulose-based natural fibres are not inert in early interactions with cement-based materials (Jongvisuttisun, Leisen & Kurtis, 2018).

Cotton fibres, in contrast, possess a distinctive twisted ribbon-like shape (i.e. convolutions) (Chand & Fahim, 2008). Due to the smaller size of cotton fibres, the cotton yarn was made from several threads twisted together. Despite the higher local compactness (average fibre spacing <5 μm), the multi-thread composition of cotton yarns leads to a relatively lower overall compactness as gaps exist between the threads. Cement paste seeped into the voids in between cotton threads (*Figure 5.4g*).

Jute, hemp, and cotton embedded samples showed a gradational interface pattern in transition from the yarn to the cement paste. This pattern is particularly evident in hemp yarn samples (*Figure 5.4i*), where there are three distinct regions: the yarn bundle (I), a porous and carbonated transition zone in the cement paste (II) with higher concentration of unreacted cement grains, and a densified, carbonate-rich region in the cement paste (III). Among the different natural fibres selected in this study, bast fibres have the highest internal porosity (i.e. pores within fibres). Detailed examination of hemp fibres reveals numerous vessels and pores (*Figure 5.4j*). The SEM data show that CO_2 is able to penetrate through the porous transition zone (II) to carbonate more internal regions of the cement paste (III), within which micro carbonation cracks and voids around fibres were observed. There was no clear indication of internal curing effects brought by the yarns (I) (Choi, 2022), as the transition zones (II) did not exhibit increase in hydration products but appeared largely carbonated.

Wool fibres have elliptical or ovate shapes, larger average fibre spacing (>20 μm), and do not form distinctive boundaries between the main fibre bundle and the cement matrix. Partial dissolution of individual wool fibres is observed (Fantilli & Jóźwiak-Niedźwiedzka, 2021), creating voids around the fibres (*Figure 5.4h*). The SEM images for wool containing samples show fewer interactions between fibres and a more homogenous integration in the cement matrix. Carbonated cement paste is present amid the wool fibres.

Carbonated cement paste adjacent to the centre yarn show a more refined and less porous microstructure than the uncarbonated counterpart, with significant transformation of

calcium hydroxide, C-S-H, and unreacted cement into calcium carbonates. The densification of cement matrix, associated with the formation and volumetric expansion of calcium carbonates, likely caused local stress concentrations, resulting in some microcracks, as observed in SEM-BSE images taken near the fibres (Region III). The size of cement grains and hydration products were reduced in the carbonated cement paste (*Figure 5.4k*), and portlandite was absent in the carbonated region (III) but present in the uncarbonated cement paste (*Figure 5.4l*). The low-density outer C-S-H, which was evident in uncarbonated regions (*Figure 5.4n*), transformed into a densified matrix following extensive carbonation. This transformation substantially reduced the porosity of the outer C-S-H. Scattered darker grey areas within this region indicated silica gel formation from enforced carbonation reactions (Skocek, Zajac & Ben Haha, 2020).

Inner C-S-H was not extensively formed due to the early age of the samples. After a prolonged enforced carbonation period (i.e., 7 days), the inner C-S-H remained visible, exhibiting a two-tone appearance (*Figure 5.4m*). As Ca/Si was not measured directly, this BSE contrast is best interpreted as qualitative evidence of local compositional heterogeneity consistent with carbonation-induced decalcification (Famy, Scrivener & Crumbie, 2002). The observations show that while outer C-S-H was more susceptible to carbonation, inner C-S-H remained relatively resistant (Groves, Rodway & Richardson, 1990; Morales-Florez, Findling & Brunet, 2012; Šavija & Luković, 2016). Additionally, volume shrinkage, characterised by shell-like boundaries, was observed around some inner C-S-H rims after carbonation (*Figure 5.4m*). SEM-BSE imaging thus indicates reaction of C-S-H with CO_2 and localised decalcification of C-S-H in regions adjacent to the natural fibre yarns, although the magnitude of any Ca/Si change cannot be determined from BSE imaging alone.

In addition, SEM results suggested that hydrated cement paste might have penetrated the yarns, hence, the convex area measured likely contained a fraction of carbonated cement paste, which leads to potential underestimation of the carbonated area fraction in *Figure 5.3*.

5.3.3. Thermogravimetric analysis

Figure 5.5a-b shows TGA-MS analysis of representative discs extracted from the surface and deeper sections of the samples. The TGA results showed three main features (Tonoli

et al., 2016; Jang et al., 2023; Zajac et al., 2022): (1) the early dehydration of C-S-H gels and ettringite (30-200 °C), dehydroxylation of $Ca(OH)_2$ (420-520 °C), and decarbonation of calcium carbonate (550-850 °C). In TGA-MS, two major water releases were observed: the initial release between 50 °C and 200 °C, attributed to incomplete dehydration of C-S-H gels and ettringite, and a later release between 420 °C and 520 °C, corresponding to $Ca(OH)_2$ (CH) dehydroxylation. The results are consistent with literature asserting that C-S-H gradually decomposes until 600°C (Villagrán-Zaccardi et al., 2017; Chu et al., 2021). The reduced mass loss between 30 °C and 200 °C for the surface disc compared to the other deeper discs *(Figure 5.5d*) is caused by smaller amounts of ettringite (AFt) and/or C-S-H due to their decomposition upon reacting with CO_2.

In mostly carbonated discs (*Figure 5.5a*), two types of calcium carbonates (CC) peaks were identified: a broad and relatively flat DTG peak spanning from 450 °C to 740 °C, and a subsequent more pronounced decomposition extending from 740 °C to 850 °C. This suggests the coexistence of amorphous/poorly crystalline calcium carbonates (which decomposes at lower temperature) and well-crystallised carbonates (i.e. calcite polymorph) (Guan et al., 2024; Liu et al., 2021; Villain, Thiery & Platret, 2007; Zajac et al., 2022). In partially carbonated samples (*Figure 5.5b*), CC decomposition initiated at higher temperatures, typically 550 °C to 850°C. Amorphous or poorly crystalline calcium carbonates decomposed before 740 °C, in alignment with literature findings (Rostami et al., 2012; Thiery et al., 2007; Qiu, 2020; Kim, Siddique & Jang, 2022).

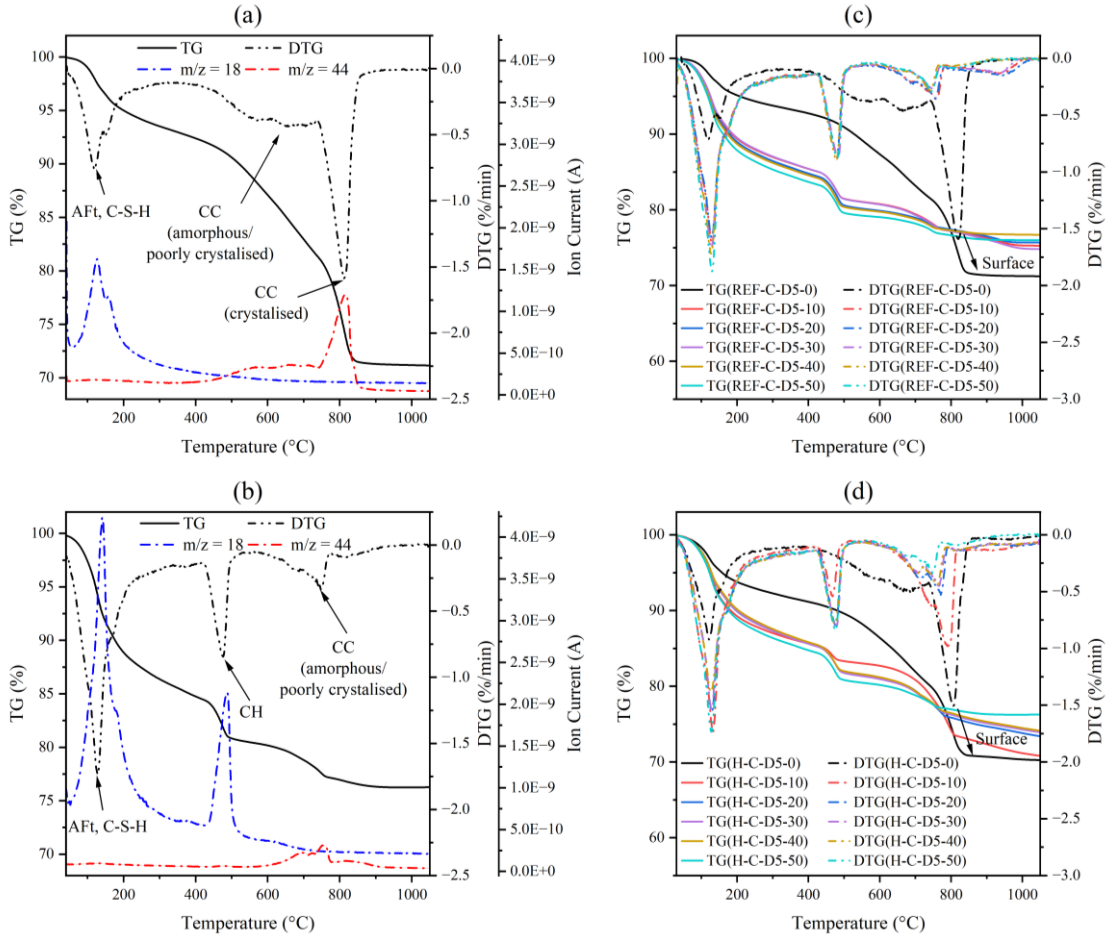


Figure 5.5. TGA-MS analysis of selected (a) mostly carbonated disc (H-C-D7-0) at surface and (b) partially carbonated disc (H-C-D7-50) at bottom. TGA-DTG curves of (c) reference and (d) hemp-embedded samples at different depths after 5-day enforced carbonation.

Figure 5.5c-d presents the TG-DTG curves from 0-50 mm of both reference and hemp-embedded samples subjected to 5 days of CO_2 curing. Irrespective of fibre inclusion, the topmost discs (0-1 mm) were mostly carbonated and had very little remaining hydration products, as identified by their lower chemically bound water. Portlandite is preferentially carbonated over other cement hydrates here, which is consistent with literature (Šavija & Luković, 2016; Rostami et al., 2012; Zajac et al., 2022; Zhang & Shao, 2016), followed by the consumption of calcium silicate hydrate (C-S-H) gel and ettringite. The content of chemically bound water was similar in discs extracted from deeper sections (10 - 50 mm), regardless of fibre addition.

The incorporation of hemp yarn greatly enhanced the mass loss between 550 °C and 850 °C, as shown by the size of DTG peaks across the depth range for samples subjected to enforced carbonation (*Figure 5.5d*). Similar enhancement of mass loss between 550 °C and 850 °C was observed for hemp fibre samples cured using enforced carbonation for 1,

3, and 7 days (Appendix 3, *Figure A3.2*). In contrast, the TG-DTG curves largely overlapped (10 – 40 mm) for reference samples; other than the top discs, the remaining discs demonstrated similar level of mass loss between 550 °C and 850 °C (*Figure 5.5c*), which can be ascribed to the decomposition of limestone originally present in the cement.

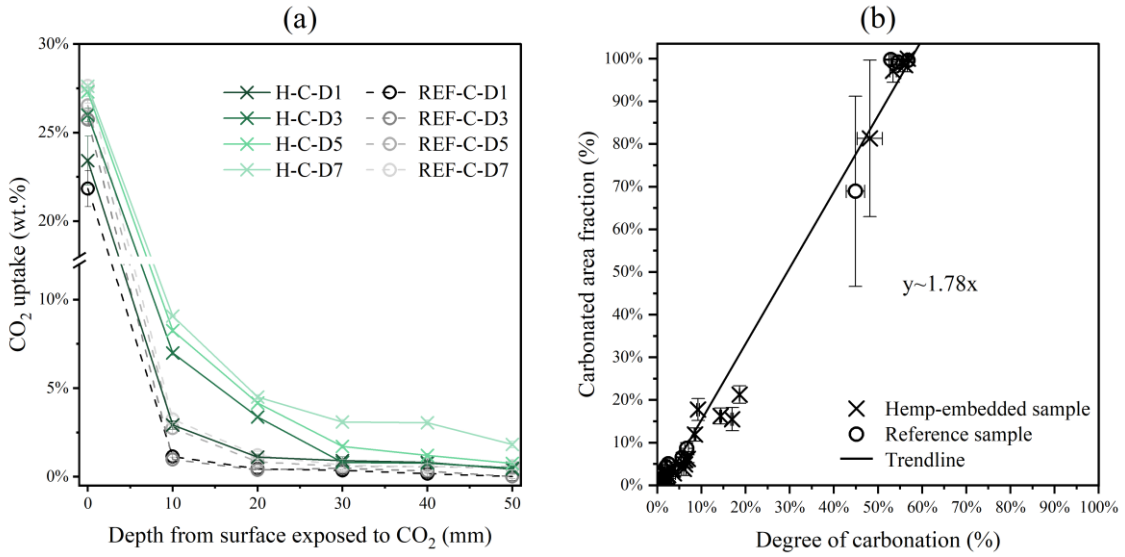


Figure 5.6. (a) CO_2 uptake by wt.% for reference (REF-D1, REF-D3, REF-D5, REF-D7) and hemp-embedded (H-D1, H-D3, H-D5, H-D7) samples subjected to carbonation curing of 1, 3, 5, and 7 days, determined by *Equation 3.2*. (b) Comparison between the carbonated area fraction obtained by image analysis against the degree of carbonation measured by TGA.

The quantitative assessment of CO_2 uptake in the samples derived from TGA results indicates a distinct enhancement in CO_2 uptake for the hemp samples across all measured depths and time intervals, as evidenced by the increased calcium carbonate content across various depths and curing duration (*Figure 5.6a*, Appendix 3 – *Figure A3.3*). This corroborates the image analysis findings presented in *Figure 5.3*.

For hemp-embedded samples subjected to 1, 3, 5, and 7 days of carbonation curing, the depth-profile averaged CO_2 uptake (0 to 50 mm depth) was 4.92 wt.%, 6.40 wt.%, 7.23 wt.%, and 8.19 wt.%, marking 23.4%, 37.7%, 36.6%, and 45.1% increases compared to the respective reference samples. The CO_2 uptake decreased exponentially across the 50 mm profile from the exposure surface, with the highest absorption in the top 10 mm. CO_2 uptake in the top discs of each sample was relatively consistent. Initially, for reference and hemp-embedded discs, the 1-day CO_2 uptake at 0-1 mm was between 21 wt.% to 23 wt.%, which then increased to between 26 wt.% and 28 wt.% from days 3 to 7. The sample depth where there was the greatest increase in CO_2 uptake from the addition of hemp

fibres was observed at the 10 mm depth and after 3 days of carbonation curing, with CO_2 uptake rising from 0.969 wt.% to 6.98 wt.%. At deeper depths from 20 mm to 50mm, even with 7 days of enforced carbonation, the reference discs showed minimal CO_2 uptake ranging from 1.21 wt.% to 0.594 wt.%, whereas the addition of hemp yarns increased the variance in carbonation profile from 4.49 wt.% to 1.81 wt.%. This increase primarily arose from greater CO_2 uptake within the specimen interior, whereas the uptake values near the exposed surface were comparatively similar between the reference and hemp-containing specimens.

Figure 5.6b shows that there is a positive linear relationship between the carbonated area fraction determined by image analysis and degree of carbonation determined by TGA. The calculated carbonated area fraction went as high as up to ~100% for the topmost discs, while the highest degree of carbonation obtained was 56.8%. These results show that the carbonated area fraction based on phenolphthalein indicator determined was approximately 1.78 times the degree of carbonation determined from TGA. Hence this study contrasts statements reported in the literature that phenolphthalein underestimates carbonation depths in concrete materials (Lo & Lee, 2002; Chang & Chen, 2006; Villain, Thiery & Platret, 2007).

5.4. Discussion

5.4.1. Natural-fibre induced modifications in carbonation mechanisms

This chapter elucidates the influence of natural fibres on carbonation rate and extent in cement paste samples. The phenolphthalein indicator test revealed two types of carbonation profiles. (1) in the reference cement paste without fibre addition, carbonation was slower and was largely confined to the sample surface. This was evidenced in the vertical profile carbonation depth tests, where reference samples were carbonated to depths of <1 mm after 7 days. (2) Accelerated carbonation was observed in all samples embedded with natural fibres, where CO_2 was transported along the channels made by the yarns to deeper sections of the cement paste, significantly surpassing the carbonated area fraction and CO_2 uptake recorded by the reference samples. The TGA results indicated that the CO_2 penetration was deeper and faster than that indicated by image analysis, and within 24 hours of enforced carbonation they showed that the CO_2 uptake at 50 mm depth was increased from 0.010 wt.% to 0.423 wt.% with hemp yarns. *Figure*

5.7a provides a schematic illustration of how natural fibre affects carbonation of cement paste.

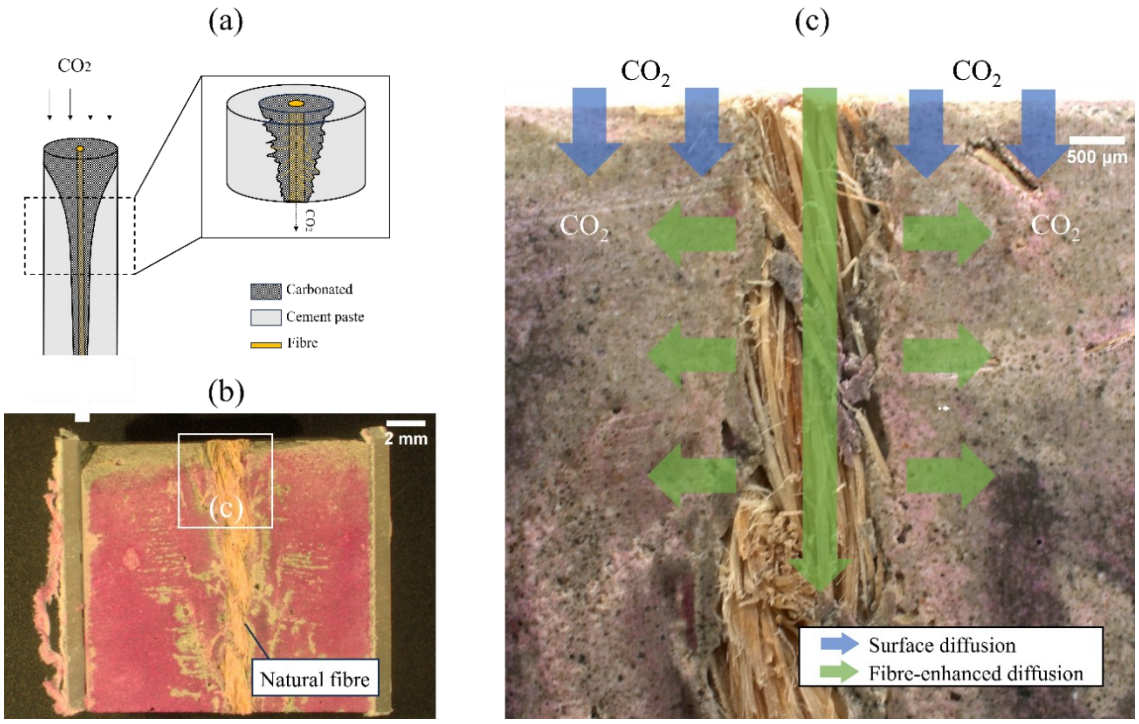


Figure 5.7. (a) Schematic illustration of fibre-enhanced carbonation mechanism; (b) Vertical carbonation profile (0-15 mm) of a hemp-embedded sample subjected to 5 days of enforced carbonation (c) CO_2 transport pathways in natural fibre (hemp) embedded cement paste (5× magnification, darkfield, light intensity 50.2%).

The results collectively demonstrated the feasibility of embedding natural fibre yarns in cement pastes to direct CO_2 transport along designated paths, resulting in funnel-shaped carbonated areas. The phenolphthalein-indicated carbonated areas are concentric around the yarns (*Figure 5.7b*), showing that the natural fibres act as bulk channels from which carbonation propagates into the cement paste samples. Overall, the geometries of the fibre-modified carbonation fronts observed here are similar to that caused by short dispersed natural fibres (Shah et al., 2018), where thread-like uncarbonated areas were observed along the fibre/cement interface. Hence carbonation initiates at the exposed cement paste surface, CO_2 transports through the bulk channels caused by the natural fibres, and its uptake in the cement paste radically narrows with increasing distance from the surface. The carbonation observed in these samples represents a combination of surface-diffused carbonation and transport-enhanced carbonation along the bulk channels created by the natural fibres (*Figure 5.7c*).

The properties of different fibres also impacted the carbonation rate due to variations in internal porosity and water absorption. By creating CO_2 pathways, the natural fibres also influenced moisture distribution in the surrounding cement matrix. As fibres released absorbed water, they altered local moisture conditions, which may have facilitated CO_2 dissolution and enhanced carbonation near the fibre-matrix interface. This could have led to increased calcium carbonate formation, densifying the microstructure around the fibres. SEM observations (*Figure 5.4*) suggested densified zones and indicated carbonated areas around the natural fibre yarns.

A notable gradient in CO_2 uptake of the cement pastes was observed, with a higher degree of carbonation near the yarns and little to no degree of carbonation further away from the yarn channels. This gradient likely results from the natural fibres acting as conduits, concentrating CO_2 transport through the yarns and leading to accelerated carbonation in their immediate vicinity. The higher degree of carbonation near the fibres can result in denser precipitation of calcium carbonate, which could enhance the bond between the fibre and the matrix. However, the areas further from the yarns, where little to no carbonation occurs, experience fewer benefits in terms of densification or mechanical improvements. This spatial variation highlights the importance of fibre selection and placement in composite design, to maximise carbonation without compromising the composite's overall integrity. Moreover, wool and cotton yarns, which exhibit better fibre–cement bonding, resulted in shallower CO_2 penetration. In contrast, jute and hemp yarns, which created larger gaps and more porous interfacial transition zones, enabled deeper carbonation but may adversely affect mechanical performance. Therefore, the result suggests that selecting and placing the appropriate natural fibre type requires balancing CO_2 sequestration benefits with the mechanical and durability requirements of the intended application.

Overall, the natural fibre properties and the CO_2 transport pathways created by the natural fibre yarns actively modify carbonation mechanisms by altering the spatial distribution and precipitation of carbonation products within the cement pastes. These modifications significantly affect CO_2 transport, microstructure, and CO_2 uptake, which we explore further in the following sections.

5.4.2. Effect of natural fibre properties on CO_2 transport and carbonation rate

The diffusion of CO_2 into cement pastes, modified by the addition of natural fibre yarns, is primarily governed by the internal porosity of fibres, the porosity of yarns (i.e. the spatial arrangement of fibres within yarns), and the interconnected pores throughout the system.

In terms of internal fibre porosity, both SEM-BSE imaging and the resin-impregnated sample analysis (Appendix 3, *Figure A3.4*) reveals that hemp and jute possess the most internal porosity among the fibres examined, including hollow centres (i.e., lumens) (*Figure 5.4e-f*) that offer additional channels for CO_2 transport. Cotton and wool fibre bundles have less internal porosity (*Figure 5.4g-h*). The different internal pore characteristics of the natural fibre yarns (hemp, jute, cotton, wool) contribute to variations in moisture absorption and water retention capabilities, which in turn created different gaps between the fibres and matrix. SEM observations showed that some natural fibre yarns contracted as they released moisture into the matrix, particularly hemp and jute (*Figure 5.4d-g*), forming larger gaps at the fibre-matrix interface. This observation is consistent with the high water absorption values of jute and hemp in the first 24 hours (*Table 3.1*), while cotton absorbed less water. Wool fibres, being protein-based, experienced partial dissolution in the alkaline cement paste. These variations in internal porosity influence the CO_2 transport pathways available within the fibres, and also at the interface with the cement matrix. The more porous the natural fibres, the faster the carbonation rate.

The spatial arrangement of fibres within the yarns was quantified as the compactness of fibres and visually analysed by SEM-BSE imaging. *Table 3.1* shows that hemp yarns were the most compact (90.4%), followed by jute (68.7%), cotton (39.3-52.0%) and wool (43.5-49.0%). The two diameter measurements provide complementary information on yarn geometry: the original diameter describes the relaxed yarn envelope, whereas the manually tightened diameter indicates how much this envelope contracts under light tension. Compactness instead describes the proportion of the yarn cross-section occupied by fibres and is therefore not directly related to diameter because yarn twist, surface hairiness and bundle deformability also influence the measured envelope. Wool yarns had the largest spacing between fibres (typically > 20 μm) which resulted in filling of the spaces with cement paste, obstructing CO_2 transport deeper into the samples. On the other hand, the smaller size of individual cotton fibres resulted in greater local compactness, which narrows the bulk channel for CO_2 transport. Compactness therefore influences the

geometry and continuity of internal transport pathways, whereas yarn diameter mainly describes the overall bundle size. Neither very open nor very tightly packed structures are necessarily favourable; therefore, a balance could be made to achieve an optimum spatial arrangement of fibres within the yarn.

While the bulk yarn bundle is the major network for CO_2 diffusion, the pore distribution within the cement paste is also affected by the morphology of the natural fibres. This is because 'fluffy' yarn surfaces, especially bast fibres, can stretch out horizontally into the cement paste, creating additional pathways for CO_2 diffusion and thus enhancing the carbonation rate. Cotton and wool yarns, with their smoother surfaces, offer fewer connected pores for CO_2 transport, resulting in more concentrated carbonation patterns as observed in *Figure 5.4c-d*. These observations indicate that yarns with higher internal fibre porosity and moderate inter-fibre spacing are more effective at promoting interconnected pore networks within the cement paste, resulting in deeper CO_2 penetration and faster development of carbonation compared with yarns with smoother, more compact structures.

5.4.3. Natural fibre yarn composites under enforced carbonation conditions

While fibre properties significantly influenced early-stage carbonation, their impact diminished over prolonged curing durations, as evidenced by the plateau in both carbonated area fraction and CO_2 uptake at 7 days of enforced carbonation with 20 vol.% CO_2 at ambient pressure and temperature. This could be due to limitations in CO_2 transport into the carbonated cement paste or within the fibre structure, e.g., by pore space filling by carbonation products.

In past experiments under similar carbonation curing conditions (20 vol.% CO_2 and 8 hours of in-mould curing), the 1 day CO_2 uptake for 20 mm cement paste cubes (w/c = 0.35) was found to be 7.98 wt.% (Chen & Gao, 2019), with CO_2 diffusing from around the samples. This value closely aligns with the average 1 day CO_2 uptake of 7.80 wt.% found here in the first 20 mm of reference samples. The inclusion of hemp yarn enhanced this uptake by 15%, to achieve a CO_2 uptake of 9.14 wt.%. Comparatively, after 1 day of curing under 99.8 vol.% CO_2 at 5 bar pressure, dispersed short-sisal-fibre engineered cementitious composites showed an average CO_2 uptake of 8.99 wt.% along a 50-mm depth (Shah et al., 2018), surpassing the uptake in hemp-embedded samples (4.92 wt.%)

which were carbonated at ambient pressure. The results hence suggest that the carbonation extent of fibre embedded samples to be enhanced at elevated pressure. We note that despite the higher overall CO_2 uptake in carbonated dispersed natural fibre samples, there was no carbonation at sample depths greater than 30-35 mm, while the hemp samples presented a gradual, yet consistent carbonation from the surface to 50 mm depth.

These results demonstrate a substantial transport-mediated effect at cement-paste scale. Natural fibre yarns reduced the surface-controlled nature of carbonation by extending measurable CO_2 uptake into deeper regions. However, the effect remained spatially graded and did not result in complete carbonation. The reported values summarise discrete depth-resolved TGA measurements and do not represent direct whole-specimen or product-scale uptake.

The results demonstrate the laboratory-scale effectiveness of placed natural fibre yarns in altering both the extent and spatial distribution of carbonation in cement pastes under enforced carbonation. However, the presence of unreacted cement clinker observed in SEM–BSE images across all specimens indicates that the carbonation process was not fully optimised. This highlights the importance of curing regime design, including in-mould curing duration, pre-carbonation moisture conditioning, CO_2 exposure parameters, and post-carbonation curing to promote continued hydration of unreacted cement phases. In addition, although not directly resolved in the present study, the potential role of yarns in redistributing internal moisture may influence carbonation kinetics and warrants further investigation.

This study provides a basis for employing more complex natural fibre yarn arrangements in future research. Unlike conventional ECC, which involves the random distribution of fibres, the concept proposed in this study can be utilised as organised placement of fibre yarns in cement-based materials, akin to textile-reinforced mortars (Choi, 2022; Liu et al., 2021), where fibres are systematically organised into woven or stitched meshes across at least two orthogonal directions. The results confirm the practicality of creating natural textile-reinforced mortars under enforced carbonation conditions, and established a fundamental understanding for controlled CO_2 transport and uptake within these composites.

5.4.4. Carbonation profile assessments

A clear linear relationship was observed between the carbonated area fraction obtained from image analysis and the degree of carbonation determined by TGA (*Figure 5.6b*). In this chapter, this relationship is used to interpret depth-resolved carbonation behaviour in yarn-containing cement pastes. Notably, this correspondence is observed despite the use of a preliminary image analysis workflow that did not include background subtraction or automated fibre exclusion.

Across the investigated depths, data points cluster toward low and high degrees of carbonation, indicating a strong spatial contrast in carbonation extent within the specimens. The relatively uniform scatter along the linear trend indicates that the image-derived carbonated area fraction captures systematic variations in carbonation extent that are consistent with changes in CO_2 uptake. A modest increase in variability is observed at higher degrees of carbonation, which is attributed primarily to uncertainties associated with depth-resolved disc preparation, including small deviations in cutting position and material loss during sectioning, particularly in regions where carbonation gradients are steep.

The persistence of a strong correlation with TGA, despite the absence of several refinement steps introduced later, indicates that the core image-based metric is robust for comparative analysis within this chapter. However, the large number of phenolphthalein-stained images generated in this study (504 discs), together with the need to manually identify fibre regions, highlights the limitations of manual processing and motivates the development of automated background correction and fibre exclusion implemented in Chapter 4. Viewed in this context, the results presented here provide independent support for the validity of the final workflow, while also illustrating the necessity of the more advanced and automated workflow developed subsequently for broader and more heterogeneous datasets.

The depth-profile mean should be interpreted as a comparative summary of the six sampled depths rather than as a direct measure of whole-specimen CO_2 uptake. Carbonation was concentrated near the exposed surface, and the material between the sampled depths was not analysed. The arithmetic mean therefore cannot be converted directly into a mass- or volume-weighted uptake for the complete specimen. Nevertheless,

the increase in the profile mean indicates a substantial change in the carbonation distribution, particularly because the largest differences between the reference and hemp-containing specimens occurred below the exposed surface. For each sampled disc, TGA was conducted on powder homogenised across the full cross-section, combining the highly carbonated yarn-adjacent region with the surrounding paste of lower carbonation extent. The resulting disc-level value therefore averages, and likely understates, the local increase in carbonation around the yarn. The local yarn-assisted transport effect may consequently be greater than suggested by the cross-sectionally averaged TGA values.

5.5. Conclusion

Under enforced carbonation (20 vol.% CO_2) at ambient temperature and pressure, it was found that all types of natural fibres, but especially bast fibres (i.e. jute and hemp), increased CO_2 uptake. Distinct carbonation fronts were observed around different natural fibres. Bast yarns exhibited irregular and wider carbonation fronts, whereas cotton and wool yarns showed concentrated patterns.

The controlled diffusion of CO_2 is influenced by the internal porosity of fibres, the spatial arrangement within yarns, and the interconnected pores within the system. Porous natural fibres yarns create additional CO_2 diffusion pathways into the cement paste, as evidenced here by the continuous increase in carbonated area fraction and CO_2 uptake along the yarns relative to the bulk material. This indicates effective CO_2 transport through the interconnected pore networks formed by the yarns.

Hemp yarns were the most effective in enhancing CO_2 uptake of the natural fibres studied here. In the first day of carbonation, hemp-embedded samples achieved significant CO_2 uptake throughout the entire sample depth including at 50 mm (0.432 wt.%). The most pronounced increase in CO_2 uptake occurred within three days of curing, with hemp-embedded samples showing a 37.7% increase in depth-profile averaged CO_2 uptake compared to non-fibre samples. Over a 7-day enforced carbonation period, hemp addition increased the CO_2 uptake from 5.64 wt.% to 8.19 wt.%.

Taken together, this chapter demonstrated the feasibility and potential of natural fibre yarns to enhance CO_2 transport and uptake in cement paste, offering a new strategy to improve carbonation sequestration efficiency in cementitious materials. This provides a

foundation for examining more complex fibre systems, where interactions between multiple yarns, spatial arrangement, and composite architecture may further influence carbonation behaviour. These aspects should be examined in the following chapters, which extends the analysis to more complex yarn configurations and system-level responses under enforced carbonation.

Chapter 6 Influence of fibre treatments on carbonation and hydration in yarn-cement composites

This chapter is based on the journal article "*Influence of fibre treatments on early-age carbonation in yarn–cement composites under enforced carbonation*" by Zhuge, Y., Wong, H. S., and Myers, R. J., published in Cement and Concrete Composites. The experimental programme, data analysis, and interpretation were led by the author. The results are reorganised and discussed here in the context of this thesis, with emphasis on the effects of fibre moisture state and surface condition on carbonation geometry, phase evolution, and microstructural development in yarn–cement composites. Results related to hardened properties are presented separately in Chapter 7.

6.1. Introduction

Previous chapters have shown that embedded natural fibre yarns can modify CO_2 transport and carbonation behaviour in cement pastes subjected to enforced carbonation curing. Compared with cotton or wool, bast yarns such as jute and hemp generally produce deeper carbonation fronts and higher CO_2 uptake, which has been linked to their porous architecture and moderate compactness. These characteristics influence local moisture distribution and internal gas transport pathways within the cement matrix, allowing carbonation to extend beyond the near-surface region. While such observations demonstrate the potential of yarns to modify carbonation behaviour, the mechanisms governing this effect are not yet fully understood.

As outlined in Section 2.2.2, carbonation in cementitious materials is governed by the coupled transport of CO_2 and pore water and is therefore highly sensitive to local moisture conditions (Liu & Meng, 2021; Zhang, Ghouleh & Shao, 2017). Natural fibres can act as internal moisture reservoirs by absorbing and gradually releasing water into the surrounding matrix (Jongvisuttisun, Negrello & Kurtis, 2013; Jongvisuttisun, Leisen & Kurtis, 2018). Cellulose-based fibres such as flax, hemp, and sisal can absorb 30–40 wt.%

of their dry mass in water, with 10–30 wt.% retained as bound water that is released slowly under ambient exposure (Miyauchi, 2023; Baltazar-y-Jimenez & Bismarck, 2007). This moisture-buffering behaviour has been shown to increase hydration heat and reduce early pore connectivity in cement pastes (Liu et al., 2024a; Feng et al., 2023). In the context of carbonated natural fibre reinforced cement composites, the hollow lumens within fibres form internal pathways that can facilitate gas transport when sufficient pore water is present (Hu et al., 2023). The balance between moisture retention and gas accessibility is therefore expected to play a key role in controlling carbonation front development under enforced carbonation curing, which has received limited attention to date.

Surface condition and interfacial characteristics further modify yarn transport behaviour (Section 2.5.3). Surface treatments commonly applied to improve fibre–matrix bonding can substantially reduce fibre hygroscopicity and alter interfacial pore structure. Alkali treatment, silane treatment, and acetylation have been reported to reduce water uptake in cellulose-based fibres by 15–70 %, depending on fibre type and treatment severity (Ernest & Peter, 2022; Fei et al., 2024; Yeh, Wu & Yang, 2024). Although such treatments are widely studied in relation to mechanical performance, their implications for carbonation curing remain poorly understood. Reductions in moisture uptake or changes in interfacial permeability may limit the ability of yarns to sustain carbonation reactions under conditions where both CO_2 transport and water availability are required.

Despite the evidence that yarns can modify carbonation behaviour, the influence of spun yarn architecture, moisture state, and surface condition on carbonation performance remains unresolved. The work in the previous chapter using multiple natural fibres showed clear differences in carbonation depth and CO_2 uptake (Zhuge et al., 2024), but it did not isolate the individual roles of saturation condition, interfacial transport, and yarn–matrix interaction. Moreover, the interaction between fibre-induced carbonation and early-age hydration was not assessed. These gaps motivate a controlled investigation in which moisture state and surface condition are varied systematically while yarn architecture is kept consistent.

To address this need, jute yarn is selected as a representative bast fibre system in which moisture state and surface condition can be modified without altering the underlying yarn architecture. Its relatively open structure and moderate compactness provide a suitable

platform for isolating the effects of internal moisture buffering and interfacial transport on carbonation and hydration behaviour. Synthetic yarns are included as non-hygroscopic controls to separate effects of surface chemistry, polarity and moisture uptake typically associated with natural lignocellulosic fibres (Pereira-De-Oliveira, Castro-Gomes & Nepomuceno, 2012; Spadea et al., 2015; Rahbar et al., 2006).

This chapter aims to investigate how fibre moisture state, interfacial pore architecture, and surface treatment influence carbonation and hydration processes in yarn–cement composites exposed to enforced carbonation curing. Building on previous findings regarding bast fibres in Chapter 5, the focus is placed on clarifying how controlled modifications to fibre condition affect CO_2 transport, carbonation extent, and early-age phase evolution. The findings provide mechanistic insight into fibre-assisted carbonation and inform the design of yarn-based systems examined in subsequent chapters.

6.2. Materials and methods

6.2.1. Materials

Jute yarns were used as the primary fibre system in this chapter to examine the influence of moisture state and surface condition on carbonation and hydration behaviour. The baseline properties and industrial pre-treatment of as-received jute yarns has been described in detail in Chapter 3 (Section 3.2). Five jute variants were prepared, as illustrated in *Figure 6.1*, to provide controlled variation in internal moisture content and interfacial permeability. Oven-dried jute (ODJ) was conditioned at 60 °C for 24 hours to remove free and loosely bound water. To represent a moisture-rich transport environment, saturated jute (SJ) was prepared by immersing yarns in deionised water for 24 hours, followed by surface blotting to remove external water while retaining internal saturation. Two slurry-coated variants were produced by dip-coating ODJ and SJ in fresh cement slurry (w/c = 0.8). These treatments yielded oven-dried, slurry-coated jute (ODMJ) and saturated, slurry-coated jute (SMJ), respectively, introducing a calcium-rich, high-pH interfacial zone intended to promote hydrate formation and local carbonation. Epoxy-coated jute (EJ) was prepared by applying a continuous epoxy layer (resin/hardener ratio 22:3 by mass) to restrict moisture and gas exchange, serving as a wall-effect control to isolate the influence of surface fibre geometry (Masoodi & Pillai, 2012).

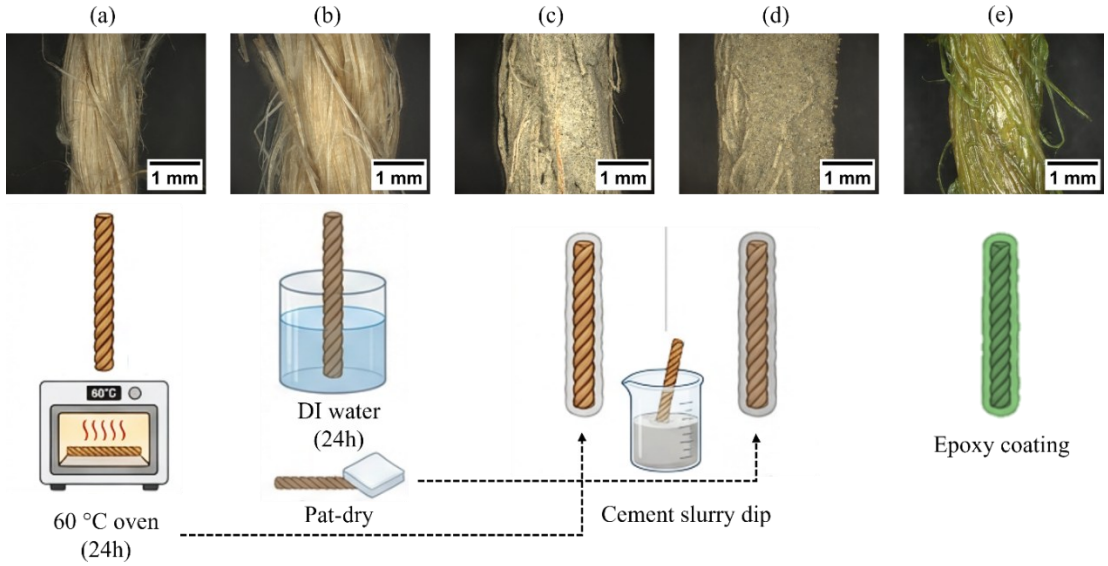


Figure 6.1. Representative morphology and schematic illustration of the treated jute yarns. (a) oven-dried jute (ODJ), (b) water-saturated jute (SJ), (c) oven-dried slurry-coated jute (ODMJ), (d) saturated slurry-coated jute (SMJ), (e) epoxy-coated jute (EJ). All micrographs were acquired at 10× magnification and 46.1% brightness.

Synthetic yarns (acrylic, nylon, and polypropylene) were included as non-hygroscopic reference materials (*Figure 3.2, h-j*), with detailed properties provided in *Table 3.1*. The properties of the treated jute yarn variants examined in this chapter are summarised in *Table 6.1*. Yarn compactness, diameter, and water absorption were characterised using the methods described in Section 3.6.1 and 3.8.1. Coated jute variants were excluded from compactness analysis, as the coatings obscure intrinsic fibre geometry.

Table 6.1. Properties of the treated jute yarn variants.

	Treatment	Average diameter original (mm)	Average diameter tightened (mm)	Compactness of fibres (%)	Water absorption (%)
ODJ	Oven-dried	1.55 ± 0.0380	1.19 ± 0.0544	48.4	89.6
SJ	Saturated	2.43 ± 0.0445	2.04 ± 0.0407	39.1	102
ODMJ	Oven-dried with cement slurry coated	2.27 ± 0.0152	2.16 ± 0.0268	/	56.0
SMJ	Saturated with cement-slurry coated	2.37 ± 0.0293	2.24 ± 0.0351	/	76.0
EJ	Epoxy-coated	1.84 ± 0.0342	/	/	7.72

Yarn-cement composites were produced using CEM I 52.5 N Portland cement (Breedon). The chemical composition of the cement, determined by X-ray fluorescence (XRF), is

reported in *Table 3.2* (Batch 2). A water-to-cement mass ratio of 0.4 was maintained throughout.

6.2.2. Sample preparation

Cylindrical single-yarn cement-paste specimens were prepared for carbonation and microstructural characterisation using the centrifuge-tube casting method described in Section 3.3 (*Figure 3.4*). In total, 216 specimens were produced across all yarn conditions and exposure durations. Following sealed curing for 24 hours, carbonation curing was applied for durations of 1, 3, 5, or 7 days using the controlled CO_2 curing protocol described in Section 3.4.1. To enable direct comparison, a parallel set of specimens was prepared and air-cured for identical durations under the same temperature and relative humidity conditions, as specified in Section 3.4.2. Identical samples were prepared in three separate casting batches to ensure repeatability across all measurements.

After curing, all cylindrical specimens were sectioned for characterisation (*Figure 6.2*). From each 10 mm-thick disc, the uppermost 1 mm was allocated for phase analysis (TGA and XRD), while the remaining 9 mm was used for phenolphthalein-based image analysis and subsequent SEM observation. Sample processing and conditioning followed the procedures described in Section 3.5 (Snellings et al., 2018).

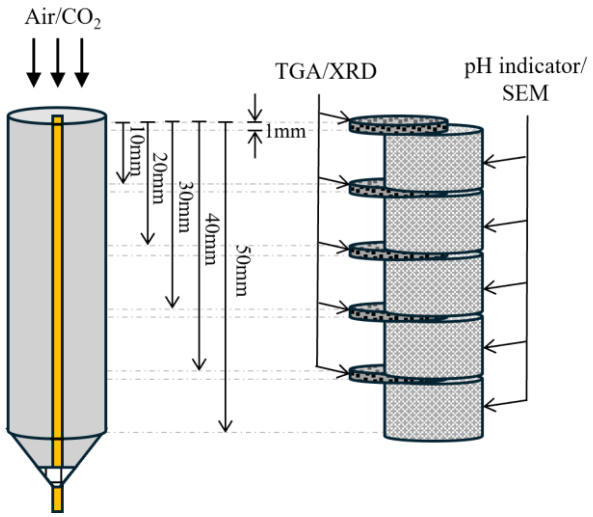


Figure 6.2. Schematic diagram of cylindrical specimen geometry and sectioning strategy for depth-resolved carbonation and microstructural analysis.

6.2.3. Phenolphthalein indicator test

Carbonation fronts on cross-sectional discs were revealed using a phenolphthalein indicator solution, with image acquisition and processing carried out following the validated workflow established in Chapter 4 and described in Section 4.3. Quantification of the carbonated area fraction was performed using *Equation 4.1*, in which the unstained paste area within the region of interest is normalised by the total paste area, excluding the yarn bundle area. Automated background correction, colour deconvolution, threshold selection, and fibre exclusion were applied consistently across all specimens.

To account for variations in sample size and yarn cross-section, an effective carbonation radius ($r_{carbonated}$, mm) was additionally calculated (*Equation 6.1*). This metric represents the equivalent radial penetration depth of carbonation and allows comparison across samples with different fibre sizes or disc diameters. Together with carbonated area fraction, these image-derived metrics were used to quantify carbonation development and to select representative specimens for further characterisation.

$$r_{carbonated} = \sqrt{\frac{A_c}{\pi}} - \sqrt{\frac{A_f}{\pi}} \tag{6.1}$$

Where A_c represents the threshold carbonated area (mm^2), A_f is the yarn area (mm^2) (*Figure 4.2f*).

6.2.4. Scanning electron microscopy

SEM was used to investigate the microstructural evolution and porosity characteristics of selected fibre reinforced cement pastes following 7 days of either air or carbonation curing. Sample preparation and imaging conditions followed the methods described in Section 3.5.6. Backscattered electron (BSE) imaging was used to provide contrast between pores and the solid matrix. The extracted discs were imaged at 1 mm, 11 mm, 21 mm, 31 mm, and 41 mm depths (*Figure 6.2*).

Porosity quantification was performed using the overflow segmentation method (Wong, Head & Buenfeld, 2006), as detailed in Section 3.6.3. Pore area fractions (μ_p) were calculated as the ratio of segmented pore area to total image area (*Equation 3.5*). Each imaged cross-section was categorised into four regions of interest: (i) the yarn cross-

section, (ii) the interfacial transition zone (ITZ) adjacent to the yarn, (iii) the intermediate matrix region, and (iv) matrix at the edge of the samples. For each region, porosity values were obtained by averaging results from 30 BSE images, providing representative measures of local porosity.

6.2.5. Characterisation test

To support interpretation of carbonation and hydration behaviour, isothermal conductivity calorimetry, thermogravimetric analysis (TGA), and quantitative X-ray diffraction (QXRD) were performed on selected specimens.

Isothermal calorimetry was conducted on selected paste samples to assess the influence of fibre type and moisture state on hydration kinetics, following the procedure outlined in Section 3.5.1. To isolate the contribution of yarn-introduced moisture conditions to early hydration behaviour, isothermal conductivity calorimetry was performed on cement paste samples containing oven-dried yarns (ODJ, ODA, ODN, ODP) and their pre-saturated counterparts (SJ, SA, SN, SP), with the reference paste-only control included as benchmark.

TGA was used to quantify carbonation- and hydration-related phase changes in selected yarn–cement composites. As shown in *Figure 6.2*, 1-mm-thick discs were collected at 10 mm intervals from the exposed surface. TGA sample preparation, heating programme, atmosphere, and data processing followed the procedures described in Section 3.5.2. Portlandite consumption and calcium carbonate formation were quantified using the tangential method, with decomposition intervals defined based on prior TGA–MS analysis of carbonated yarn–cement composites *(Figure 5.4*). CO_2 uptake was calculated following *Equation 3.1* and *3.2*, using air-cured specimens analysed at identical curing durations as a reference to isolate carbonation-induced changes.

QXRD was used to complement TGA by enabling phase-specific identification of crystalline hydration, carbonation, and residual clinker phases. Powdered samples were obtained from defined depth intervals (0–1 mm, 10–11 mm, 20–21 mm, 30–31 mm, and 40–41 mm from the exposed surface; *Figure 6.2*), homogenised, and sieved to <63 μm prior to analysis. Measurement conditions, quantitative phase analysis by Rietveld refinement, use of an internal corundum standard, and data processing followed the

procedures described in Section 3.5.3. In this chapter, phase assemblages were quantified to assess the relative contributions of hydration and carbonation reactions across depth.

The degree of hydration (DoH) was calculated based on the residual clinker content using *Equation 3.3*. As carbonation reactions also consume clinker phases, DoH values obtained from carbonated specimens may overestimate the extent of hydration when considered in isolation. To quantify the relationship between hydration and carbonation, a carbonation-to-hydration ratio was introduced (*Equation 6.2*):

$$Carbonation\ to\ hydration\ ratio = \frac{w_{CaCO_3}}{w_{CaCO_3} + w_{Ca(OH)_2}} \tag{6.2}$$

Where w_{CaCO_3} and $w_{Ca(OH)_2}$ are the fractions (wt.%) of calcium carbonates and portlandite obtained from Rietveld refinement, where initial $CaCO_3$ in raw cement was excluded from calculation to isolate carbonation-derived phases. A higher carbonation to hydration ratio indicates that carbonation has outpaced hydration in the local phase assemblage.

6.3. Results and analysis

6.3.1. Carbonated area fraction and CO_2 uptake

The stereomicrographs in *Figure 6.3a–h* present cross-sections of phenolphthalein-stained specimens that have been carbonation-cured for 7 days and extracted at a depth of 20 mm from the exposed surface. These images highlight the variability in carbonation front geometry due to differences in fibre type and surface treatment, which was observed in all samples. Among the jute-based composites, uncoated jute yarns (ODJ and SJ) and cement slurry-coated yarns (ODMJ and SMJ) induce irregular, asymmetric carbonation belts encircling the centre. These belt-shaped carbonation regions are characteristic of bast yarn–cement composites (*Figure 5.3*, Section 5.3.1), where the porous, twisted yarn geometry promotes localised gas–liquid interaction.

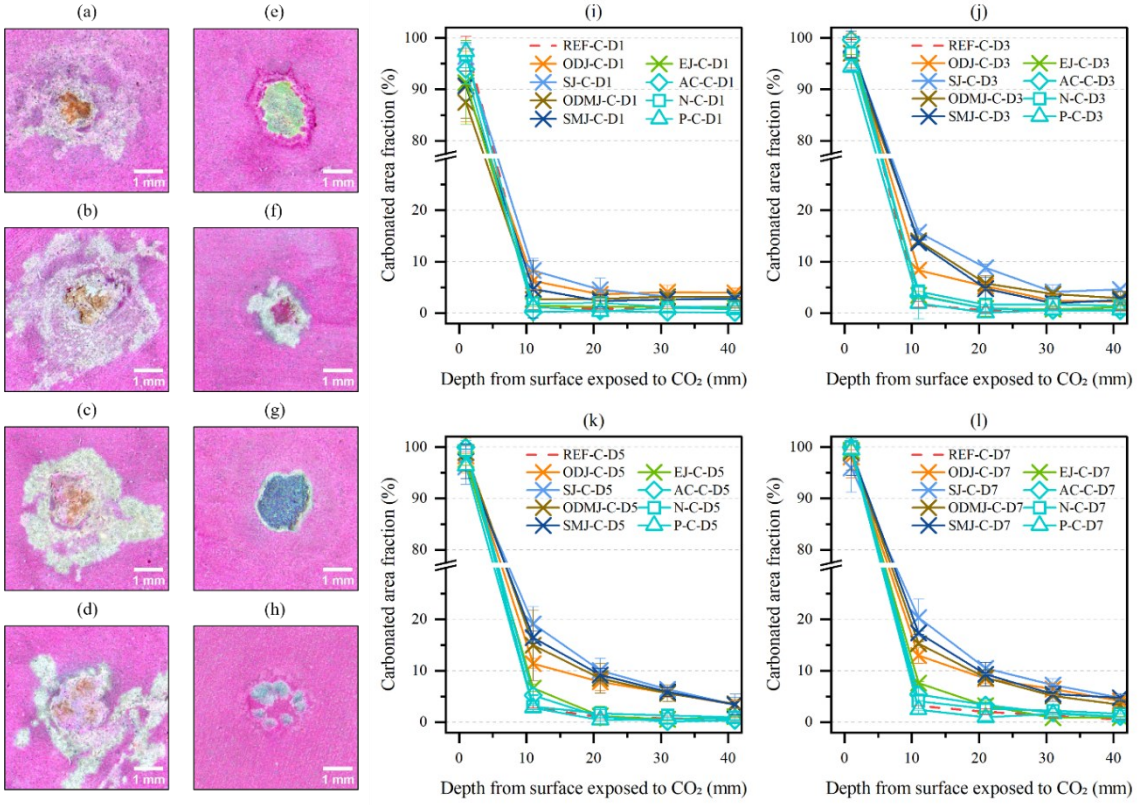


Figure 6.3. Carbonation front geometry and quantitative carbonation assessments. (a–h) Stereomicrographs of phenolphthalein-stained disc cross-sections at 20 mm depth after 7 days enforced carbonation: (a) ODJ, (b) SJ, (c) ODMJ, (d) SMJ, (e) EJ, (f) acrylic, (g) nylon and (h) polypropylene. (i–l) Carbonated area fractions from 0 to 40 mm depth measured at different curing durations: (i) 1 day, (j) 3 days, (k) 5 days, and (l) 7 days.

The saturated jute (SJ) composite (*Figure 6.3b*) displays a broader carbonation belt than oven-dried jute (ODJ) (*Figure 6.3a*), whereas slurry-coated jute composites *Figure 6.3c–d*) showed sharper and more confined fronts. This indicates that the cement slurry coating restricted lateral spread while creating a locally alkaline region that favoured carbonation close to the yarn. By contrast, epoxy-coated jute (EJ) composite (*Figure 6.3e*)showed no visible carbonation belt at this depth, indicating that the epoxy barrier inhibits moisture and CO_2 exchange across the fibre-cement paste interface. The hydrophobic epoxy surface may also have reduced wetting by the fresh pore solution, further limiting interfacial hydration and carbonation reactions.

Synthetic yarns composites (*Figure 6.3f–h*) showed much smaller carbonation fronts, largely confined to the immediate yarn vicinity. This behaviour is consistent with their lower water sorption (*Table 3.1*) and weaker influence on local moisture distribution. Acrylic (*Figure 6.3f*) produced a modest, localised rim, likely due to capillary retention within its staple-spun bundle, while nylon (*Figure 6.3g*) showed a smaller, compact rim

consistent with its dense multifilament structure. Polypropylene (*Figure 6.3h*) produced no observable carbonation belt, in line with its hydrophobic and non-polar surface.

The carbonated area fraction profiles in *Figure 6.3* (i)–(l) shows that carbonation progressed rapidly during the first 3 days and then approached a transport-limited regime. At Day 1, carbonation was mainly confined to the near-surface region (< 15 mm). By Day 3, the carbonated area fraction at 11 mm reached ~16 % for saturated jute and ~14 % for slurry-coated jute, compared with ~8 % for oven-dried jute. Further exposure from 5 to 7 days produced only minor increases (< 2 %). Across all depths, saturated jute consistently showed the largest carbonated area, followed by slurry-coated and oven-dried jute, whereas epoxy-coated and synthetic-yarn composites remained weakly carbonated (< 8 %). These results indicate that moisture-retentive yarns promote deeper and more extensive carbonation than low-moisture or moisture-blocked yarn systems.

Overall, jute-based composites showed substantially higher carbonation extents than synthetic-yarn composites under the present curing conditions. Carbonated area fractions in jute systems were typically 3-5 times higher than those in acrylic, nylon, or polypropylene composites, consistent with their higher water absorption and more open, moisture-retentive yarn structures. The close agreement between carbonated area fraction and 24-hour water absorption (*Table 3.1*) indicates that yarns capable of retaining more moisture sustained CO_2 dissolution and carbonation reactions in the adjacent matrix more effectively.

6.3.2. Heat of hydration and phase assemblages

Figure A4.1 (Appendix 4) the normalised heat flow and cumulative heat release profiles for pastes containing oven-dried and pre-saturated yarns. All samples exhibited a single dominant hydration peak between 6 and 10 h, typical of C3S hydration. Minor variations were observed: saturated jute (SJ) and saturated acrylic (SA) produced slightly broader and delayed peaks, with marginally higher cumulative heat (~304 J/g) than their oven-dried counterparts (~295 J/g). However, these differences were within 3 %, indicating that fibre type and moisture state had only a minor influence on bulk hydration kinetics over 7 days. Therefore, the enhanced carbonation observed in natural-fibre cement paste composites cannot be attributed to accelerated bulk hydration. Under the applied CO2 concentration and curing humidity, hydration was likely limited relative to sealed or high-

humidity curing; differences in carbonation behaviour are more plausibly associated with local moisture distribution and yarn-adjacent pore structure.

Representative TG–DTG curves for the 7-day carbonation-cured saturated jute (SJ) composite are shown in *Figure 6.4a*. As established in Chapter 5 (Section 5.3.3), carbonation is characterised by progressive portlandite depletion and carbonate formation, including the appearance of carbonate decomposition at lower temperatures near the CO_2-exposed surface. Distinct reductions in portlandite decomposition (420–520 °C) were consistent with increasing mass losses between 550 and 850 °C, confirming extensive carbonation. The DTG curves exhibit a distinctive double-shoulder feature: the first shoulder (~550–770 °C) is attributed to poorly crystalline and metastable carbonate phases, including vaterite or aragonite, amorphous CaCO3, as well as carbonates formed through C–S–H decalcification and carbonation. These carbonates may be finely dispersed within the decalcified silicate gel and therefore decompose at lower temperatures than well-crystallised calcite (Huang, Chen & Yu, 2025). The sharper peak between 770 and 850 °C corresponds to well-crystallised calcite, the dominant carbonation product. At the surface directly exposed to CO2, decomposition onset is visible as early as 400–450 °C, suggesting the presence of amorphous or highly disordered CaCO3, potentially associated with carbonated C–S–H or finely dispersed amorphous CaCO3(Mehdizadeh & Ling, 2025).

This multi-peak behaviour reflects the coexistence of metastable and stable carbonate phases formed under varying local conditions of pH and CO2 concentration. Such phase diversity is consistent with literature that all three polymorphs can form when the ambient relative humidity ranges between 20 % and 80 % (Chen et al., 2024). Full TG–DTG curves for air- and carbonation-cured specimens at 1 and 7 days are provided in Appendix 4 (*Figure A4.2*).

Quantified $CaCO_3$ and $Ca(OH)_2$ contents obtained from TGA for the reference paste, ODJ- and SJ- embedded systems after 7 days of carbonation curing are shown in *Figure 6.4b–c*. Carbonation curing led to marked portlandite depletion across all depths, accompanied by proportional carbonate accumulation. Saturated jute composites recorded the highest $CaCO_3$ contents throughout the profile, followed by oven-dried jute, while reference paste exhibited limited carbonation. These trends confirm that the extent of carbonation scales with fibre moisture-retention capacity, consistent with results from

image analysis. A strong linear correlation was observed between CO_2 uptake and effective carbonation radius for the selected reference paste, ODJ, and SJ specimens after 7 days of carbonation curing across the analysed depths ($R^2 = 0.962$, *Figure 6.4d*). This indicates that, although phenolphthalein staining is pH-based, the effective carbonation radius provides a useful comparative indicator of carbonation extent for the tested systems. For yarn systems where TGA was not performed, CO_2 uptake was estimated from this linear relationship using the corresponding image-derived effective carbonation radius and is shown as filled blue markers in *Figure 6.4d* At 10 mm depth, the effective carbonation radius around individual yarns was approximately 2–3 mm, which can be used to define the minimum yarn spacing in mesh arrangements to avoid overlapping carbonation zones.

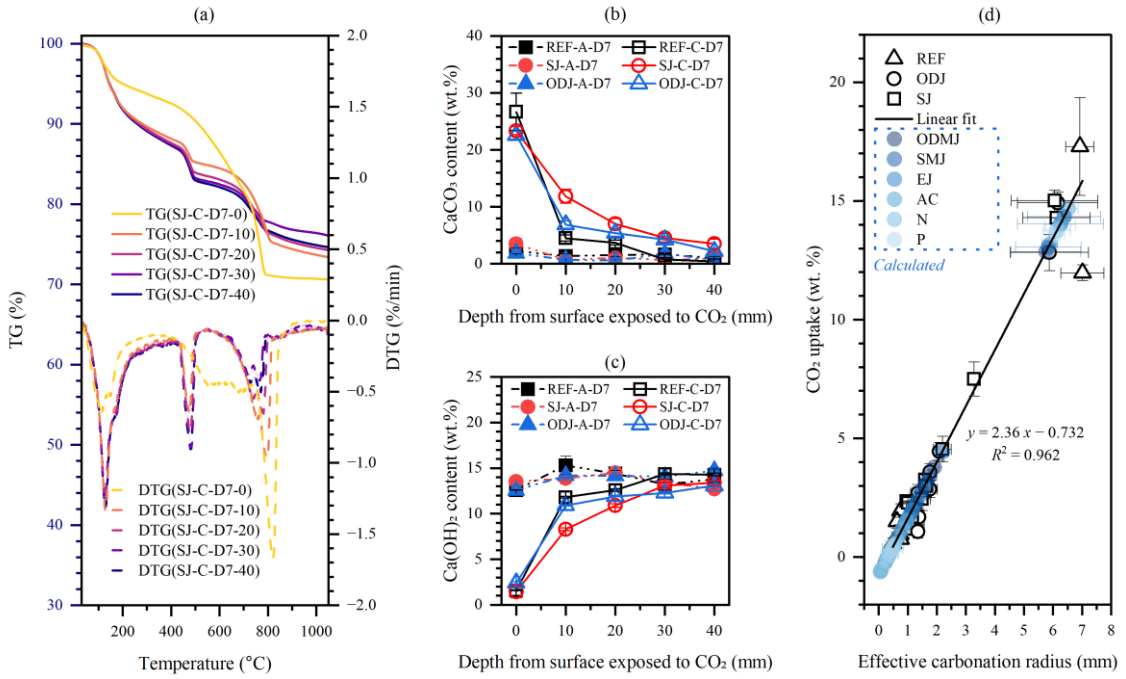


Figure 6.4. Thermogravimetric analysis of yarn–cement composites. (a) TG–DTG curves of saturated jute (SJ) after 7 days of carbonation. (b-c): Depth profiles of (b) $CaCO_3$ contents after 7 days; (c) corresponding $Ca(OH)_2$ contents. (d) Linear correlation between CO_2 uptake and effective carbonation radius.

To complement the thermogravimetric results, quantitative XRD was conducted to assess the relative progression of carbonation and hydration reactions (*Figure 6.5*). As shown in *Figure 6.5a*, the XRD patterns of the saturated jute composite after 7 days of enforced carbonation reveal the presence of portlandite (CH), ettringite, calcite, vaterite, and residual unhydrated clinker phases such as alite (C_3S) and belite (C_2S). Calcite dominated the crystalline carbonate phases, while vaterite was present only in small quantities.

Therefore, the low-temperature shoulders in the DTG curves (*Figure 6.4a*) cannot be attributed in solely to crystalline vaterite (Mehdizadeh & Ling, 2025). They are also likely to include amorphous or poorly crystalline carbonate species formed during C–S–H decalcification, which are not resolved by XRD. This interpretation is consistent with the broad DTG response at lower temperature and the limited crystalline vaterite detected by XRD.

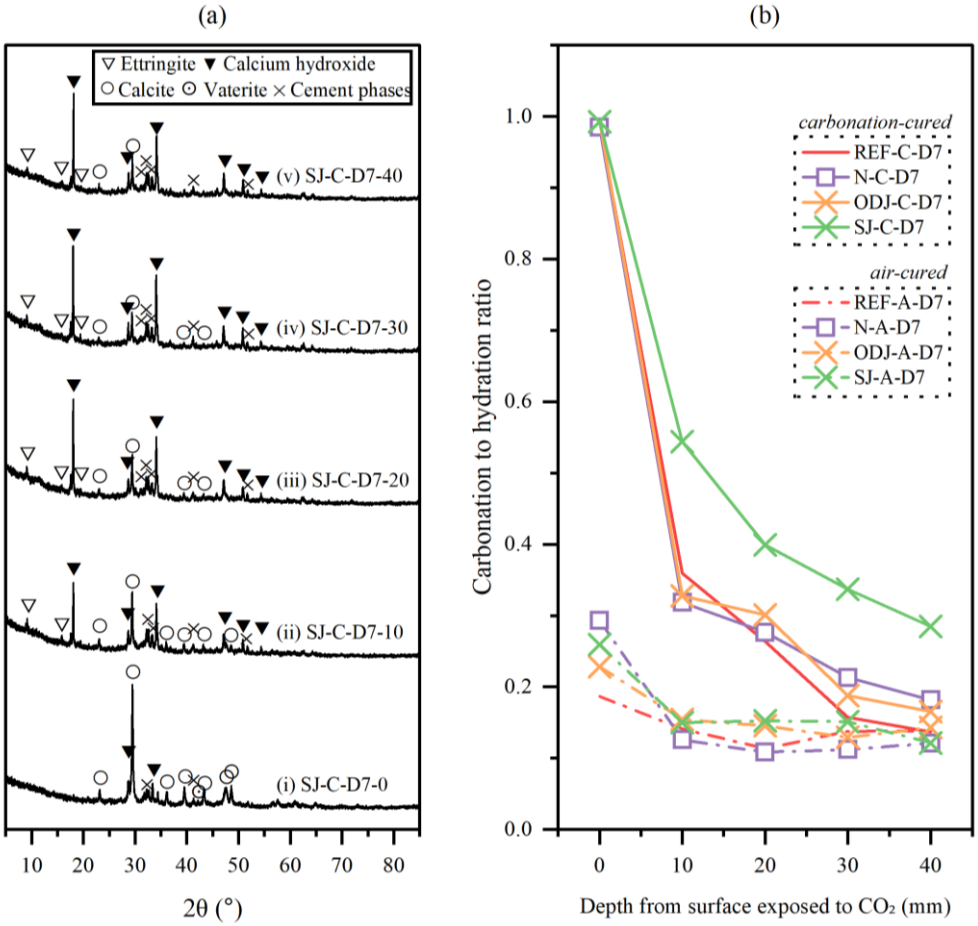


Figure 6.5. (a) XRD patterns of saturated jute–cement discs after 7 days of enforced carbonation, sampled from 0–40 mm depths; cement phases include alite, belite, tricalcium aluminate, and tetracalcium aluminoferrite. (b) Carbonation-to-hydration ratios of yarn–cement discs after 7 days of curing.

At the exposed surface (0–1 mm), all carbonation-cured samples exhibit carbonation-to-hydration ratios approaching unity (*Figure 6.5b*), indicating extensive portlandite depletion and carbonation formation near the CO2-exposed surface. With increasing depth, the index decreased progressively, reflecting the transition from carbonation-dominated to hydration- dominated phase assemblages. The decline was slower in saturated jute (SJ), which maintained a higher index at 10 mm than ODJ, nylon, and the reference paste.. This indicates that moisture retained in SJ sustained carbonation

reactions beyond the near-surface zone at early ages. At greater depths (> 20 mm), all carbonation-cured systems converged towards similar low index values (~ 0.2), consistent with the effective carbonation radius derived from image analysis. thereby validating the consistency between phase and microstructural indicators. Detailed phase assemblages are provided in *Figure A4.3* (Appendix 4). These results corroborate the thermogravimetric analysis, confirming that moisture-retentive natural fibres promote greater portlandite consumption and carbonate formation within the carbonated zone.

6.3.3. Microstructure of yarn-cement composites

Backscattered SEM imaging reveals that fibre inclusion produces distinct, radially graded microstructures in yarn–cement composites, comprising four recurring zones: (I) the yarn body, (II) the interfacial transition zone (ITZ), (III) a porous middle rim, and (IV) the outer unmodified matrix. Among these, the ITZ structure, porous rim morphology, and extent of modified region were the most evident of yarn-related effects. Detailed porosity profiles and radial schematics for each system are provided in *Figure A4.4* (Appendix 4), highlighting interfacial and depth-dependent trends across fibre types.

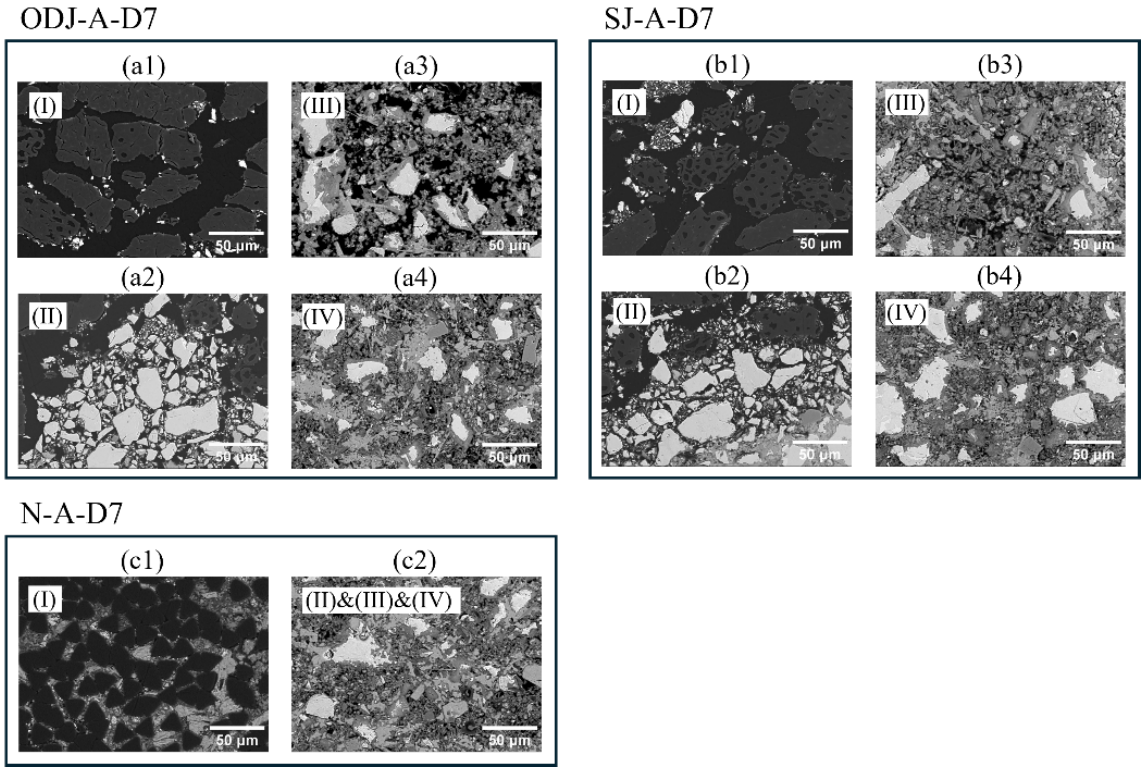


Figure 6.6. SEM-BSE micrographs of air-cured yarn–cement composites after 7 days of sealed curing at 20 mm depth. Four distinct zones are identified: (I) yarn cross-section, (II) interfacial transition zone (ITZ), (III) porous matrix region, and (IV) outer

unmodified matrix. Panels (a1–a4) correspond to oven-dried jute (ODJ-A-D7), (b1–b4) to saturated jute (SJ-A-D7), and (c1–c2) to nylon (N-A-D7).

In air-cured samples (*Figure 6.6*), interfacial transition zones (ITZs) showed the clearest differences between fibre types. Oven-dried jute (ODJ) exhibited a thick, discontinuous ITZ (0.18–0.22 mm) with open interfacial gaps and high local porosity (~ 32 %), consistent with shrinkage of the dried fibres before casting (*Figure 6.6, a1 – a2*). In contrast, saturated jute (SJ) formed a continuous, gel-rich ITZ (0.09–0.11 mm) with fewer unhydrated grains and lower porosity (~ 21 %), indicative of improved bonding and local hydration (*Figure 6.6, b1 – b2*). Nylon composites developed the densest and narrowest ITZs (~ 0.07 mm, μ_p ~ 18 %), showing limited microstructural modification relative to the reference paste (*Figure 6.6, c1*). These findings demonstrate that moisture condition and fibre compactness control ITZ continuity and fibre-matrix bonding quality.

Porous middle rims, consisting of transitional belts between the ITZ and bulk paste, were present in both natural-fibre systems but largely absent in nylon composites. In ODJ, this rim was irregular and moderately thick (0.20–0.74 mm) with extensive porous belts (μ_p ~ 20–23 %), reflecting limited interfacial hydration and local accumulation of unhydrated particles (*Figure 6.6, a3*). SJ displayed a wider but more diffuse porous rim (0.47–0.99 mm) with slightly higher average porosity (~ 19 %), likely associated with local water enrichment from the saturated fibres (*Figure 6.6, b3*). Nylon, by contrast, showed only a single faint porous band near the yarn perimeter, confirming minimal pore reorganisation around synthetic filaments.

The extent of the modified region (zones I–III) was greatest in the jute systems (*Figure A4.4*, Appendix 4). At 20 mm depth, the total affected zone extended to ~1.7 mm in both ODJ and SJ, but only ~1.1 mm in nylon. Despite their differences in ITZ porosity, both jute composites induced deeper microstructural modification, supporting their stronger interaction with the surrounding paste during curing. The outer matrix (zone IV) remained comparable to the reference paste (μ_p ~ 15–16 %) in all systems, confirming that microstructural heterogeneity was confined to the near-fibre region. Collectively, these observations show that under air-cured conditions, natural fibres create a multi-zonal microstructure extending up to ~1.7 mm from the yarn, dominated by a porous rim and a moderately densified ITZ, whereas synthetic fibres maintain a compact, nearly unaltered matrix.

Carbonation curing induced distinct microstructural transformations in all yarn–cement paste systems, most prominently in jute composites. SEM-BSE analysis of 7-day carbonated specimens (*Figure 6.7*, a1,b1) reveals modified zones analogous to those observed under air curing (*Figure 6.6*), but with more clearly defined zone boundaries and densification effects. Four characteristic zones are consistently observed: (I) the yarn cross-section; (II) a densified interfacial transition zone (ITZ); (III) a partially carbonated matrix belt; and (IV) uncarbonated bulk matrix. These match the optical carbonation front geometries in phenolphthalein-stained samples (*Figure 6.3*).

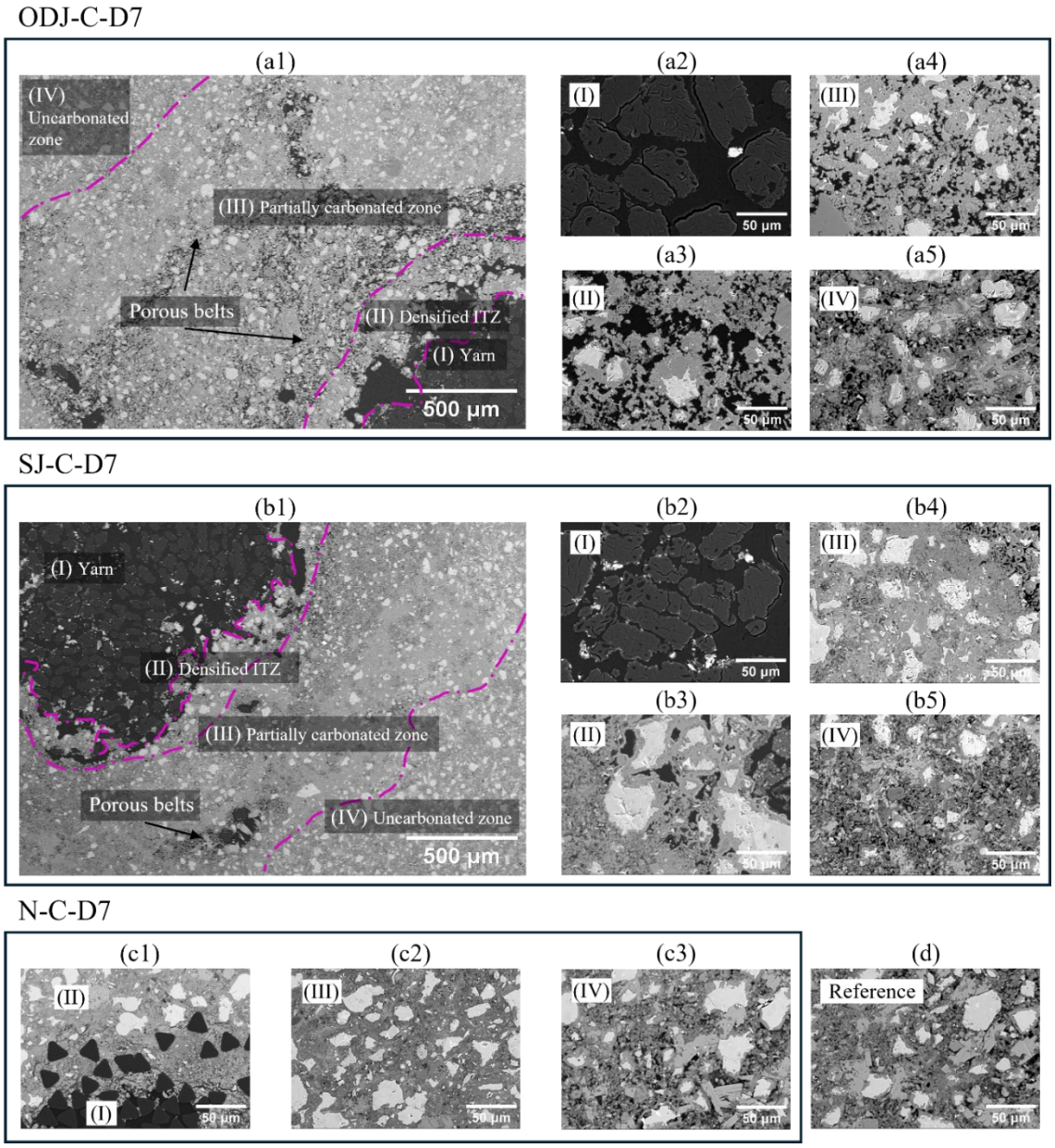


Figure 6.7. SEM-BSE images illustrating the microstructural features of yarn–cement composites after 7 days of enforced carbonation at 20 mm depth. Four characteristic zones are identified: (I) yarn cross-section; (II) interfacial transition zone (ITZ); (III) porous or

partially carbonated matrix; and (IV) uncarbonated matrix. Panels (a1–a5): ODJ-C-D7, showing an (a1) overview at 200× and (a2–a5) corresponding Zones I–IV at 500×. Panels (b1–b5): SJ-C-D7, with (b1) overview and (b2–b5) corresponding Zones I–IV. Panels (c1–c3): N-C-D7, showing Zones I–III. (d) Carbonated reference paste at zone IV.

Within the yarns (Zone I), the internal morphology of the yarns remained stable after 7 days of enforced carbonation. Both oven-dried (*Figure 6.7*, a2) and saturated jute fibres (*Figure 6.7*, b2) showed no visible degradation or delamination. Saturated jute retained well-defined lumens and high porosity (μ_p = 48.6 %), whereas oven-dried jute showed partially collapsed bundles with slightly lower porosity (μ_p = 42.9 %). Nylon bundles (*Figure 6.7*, c1) remained dense and compact (μ_p = 13.1 %), with no observable structural change relative to their air-cured counterparts.

At the fibre–matrix interface (*Figure 6.7*, Zone II), carbonation markedly densified the ITZ in all cement paste composites, with the extent dependent on yarn type and moisture condition. In ODJ-C-D7 (*Figure 6.7*, a3), ITZ porosity decreased from 32.3 % to 15.5 %, a 52 % reduction relative to air curing, accompanied by brighter BSE contrast indicative of CaCO3 precipitation. In SJ-C-D7 (*Figure 6.7*, b3), the ITZ became even denser (μp = 10.5 %), appearing as a carbonate-rich interfacial rim with sharply defined boundaries in the examined cross-sections. Nylon (*Figure 6.7*, c1) exhibited only moderate densification (μ_p = 13.1 %, −26 % relative to air-cured), suggesting more limited microstructural modification.

The porous middle rims surrounding the ITZ (*Figure 6.7*, Zone III) evolved differently depending on fibre type. In ODJ composites (*Figure 6.7*, a4), carbonation slightly reduced porosity from 16.8 % to 14.0 % (−16 %), while rim thickness remained similar (0.74–0.38 mm). SJ composites (*Figure 6.7*, b4) developed a broader and more homogeneous middle rim extending up to 1.20 mm from the yarn, with porosity decreasing to 15–17 % and fewer sharply defined porous belts. This suggests that CO_2 penetration was more spatially uniform around saturated fibres in the examined sections, consistent with moisture-assisted transport near the yarn. Nylon composites (*Figure 6.7*, c2) displayed only minor changes, with the middle rim remaining narrow (~0.7 mm) and porosity largely unchanged (14–16 %).

Across all systems, carbonation effects were mainly confined to the yarn-adjacent region. The outer matrix (*Figure 6.7*, Zone IV) retained baseline porosity (~15–16 %),

comparable to uncarbonated paste. The total modified region extended to approximately 1.2–1.7 mm in jute composites but only ~1.1 mm in nylon, indicating that natural yarns promoted greater local carbonation-induced restructuring of the matrix (*Figure A4.4*, Appendix 4).). No visible degradation of jute fibres was observed after 7 days of enforced carbonation under the curing condition examined.

6.4. Discussion

6.4.1. Hydration and carbonation mechanisms in yarn-cement paste composites

Hydration and carbonation are often treated as competing processes because both depend on pore water and overlapping ionic pathways. Hydration consumes water and generates portlandite and C–S–H, while carbonation proceeds when dissolved CO_2 reacts with Ca^{2+} to form $CaCO_3$. Their relative progression is therefore governed by moisture availability: high pore saturation restricts CO2 diffusion, while insufficient moisture limits CO2 dissolution and ion transport (Vollpracht et al., 2024; von Greve-Dierfeld et al., 2020; Filomeno et al., 2020).

In yarn–cement composites, the fibres moisture state modifies this balance locally. Pre-saturated jute (SJ) retained moisture near the yarn–matrix interface, supporting CO2 ingress, dissolution, and ionic mobility. This does not imply unrestricted hydration under the curing conditions (1–7 days, ~20 % CO2, 64 % RH). Rather, SJ appears to support limited ongoing hydration and clinker dissolution while carbonation remains the dominant reaction, producing progressive CH depletion, $CaCO_3$ accumulation, and local interfacial densification. In contrast, oven-dried jute (ODJ) lacks this moisture-buffering effect; its dry and irregular pore structure may permit gas entry but provides less favourable conditions for CO_2 dissolution, resulting in shallower and less uniform carbonation. Isothermal calorimetry showed only minor differences in bulk hydration kinetics, and XRD confirmed comparable overall hydration extent across fibre types. The carbonation differences therefore arise mainly from local moisture distribution and yarn-adjacent microstructure, rather than accelerated bulk hydration. This is further supported by the molar-based carbonation index, which was higher for SJ (~0.47) than ODJ (~0.27) at 10 mm depth after 7 days.

These findings point to a revised mechanistic framework, building on prior work that emphasised the trade-off between hydration and carbonation under limited or excessive

moisture conditions (Liyew et al., 2024; Liu & Meng, 2021; Zhang, Ghouleh & Shao, 2017). While excessive moisture is known to hinder carbonation, this study shows that localised, retained moisture within embedded yarns can sustain carbonation without blocking gas transport. Although the chamber RH was fixed at 64 %, the yarns created different internal microenvironments. SJ retained and gradually released water along the fibre–matrix interface, maintaining local ion mobility and CO2 solubility. This enabled a locally coupled hydration–carbonation process in which residual hydration and clinker dissolution could supply Ca2+, while carbonate precipitation remained the dominant sink for Ca-bearing species. In addition to portlandite carbonation, partial C–S–H decalcification likely contributed to the broad low-temperature carbonate decomposition observed in DTG, especially near the CO2-exposed surface. Synthetic yarns, although porous at the bundle scale, consist of solid polymer filaments without lumen-type internal porosity. Their lower hygroscopicity and limited water storage made them less effective in sustaining moisture-assisted carbonation. Carbonation performance therefore depends not on porosity alone, but on the scale, accessibility, and water-retention capacity of the pore structure.

The mechanistic interpretation is necessarily bounded by the experimental design, which used a single paste composition (CEM I 52.5 N, w/c = 0.40) and one curing regime (∼20 % CO_2, 64 % RH, 25 °C). Changes in w/c ratio, binder composition, CO_2 concentration, RH, or exposure duration could modify the balance between hydration, carbonation, and transport. The findings should therefore be read as a mechanistic reference for yarn-assisted early-age carbonation under controlled conditions, rather than as a general model for all cementitious systems.

6.4.2. Microstructural and quantitative influence of yarn properties on carbonation

Carbonation curing produced distinctive, radially graded microstructures around embedded yarns. This heterogeneous architecture governs how CO_2 and moisture move through the paste and, consequently, how carbonation progresses. System with higher initial moisture content (i.e. SJ) showed cross-sectional pore arrangements consistent with more favourable moisture retention and CO2 transport near the yarn.

In oven-dried jute (ODJ) composites, the high ITZ porosity observed after air curing should be interpreted partly as an initial mixing-induced feature rather than a consequence of carbonation. During casting, dry jute acts as a local water sink, drawing part of the mixing water from the adjacent fresh paste. This local reduction in effective w/c can hinder particle packing and early hydrate formation near the yarn, while fibre swelling followed by subsequent drying may further open interfacial gaps. The resulting ITZ therefore starts from a more porous and less continuous baseline (~32.3 %) before carbonation begins. Nevertheless, in oven-dried jute (ODJ) composites, carbonation remains shallow and irregular. The dry and irregular pore structure observed around ODJ appears less favourable for sustained CO2 dissolution and transport, showing that visible porosity alone does not guarantee effective carbonation. By contrast, saturated jute (SJ) composites develop a narrower but denser ITZ with fewer unhydrated particles and a well-integrated fibre–matrix interface. The surrounding middle rim, although porous, remains partially saturated due to retained fibre moisture during the curing durations studied. This produces a pore arrangement more favourable for CO2 dissolution and radial carbonation, forming a wider and more spatially uniform carbonated belt than ODJ. Chemical treatments that reduce fibre water uptake, such as alkalisation, silanisation, or hornification, may therefore produce effects similar to oven-dried jute if they reduce internal moisture buffering, making them unsuitable when maximising CO_2 uptake is the primary objective.

Trends in pore area fraction reported here (*Figure A4.4*) should be interpreted in light of the inherent constraints of SEM–BSE image analysis. Measurements are based on two-dimensional sections and do not capture three-dimensional pore connectivity. The SEM–BSE results are used here as comparative, spatially resolved indicators of local microstructural modification in defined yarn-adjacent regions, including the ITZ, middle rim, and outer matrix, rather than as a full pore-network characterisation. Consequently, terms referring to transport or pore accessibility are used here as interpretations based on cross-sectional microstructural evidence, rather than as direct measurements of connected pore networks, while greyscale overlap between fine pores and low-density hydrates is unavoidable, particularly within the ITZ. Variability is highest in this region, with standard errors of approximately 2.0–2.4 % for air-cured ODJ and SJ and up to ~3.3 % for nylon near the exposed surface. By contrast, the outer matrix shows consistently low variability (standard errors < 0.8 %), consistent with minimal microstructural modification away from yarn influence. Despite these constraints, the observed pore

refinement (~15–20 %) is substantially larger than the associated uncertainty. When considered together with the phenolphthalein-stained images, TGA and XRD results, these SEM-BSE data support the reported microstructural trends, although they do not directly prove three-dimensional pore connectivity. Direct confirmation would require three-dimensional methods such as X-ray micro-computed tomography or focused ion beam SEM serial sectioning, although quantifying pore-structure differences across the narrow ITZ and carbonation-induced rim regions would remain challenging because these features span only a few hundred micrometres to millimetres and require high spatial resolution over a representative volume. Similarly, the image-derived carbonation metrics should be interpreted as comparative indicators rather than exact measurements of a sharp carbonation front, since carbonation progresses gradually and partially carbonated regions may not be fully resolved by phenolphthalein staining.

These findings extend our previous work showing that carbonation in natural yarn–cement composites is governed by fibre morphology and water sorption capacity. Natural yarns such as cotton and wool, though inherently hydrophilic, exhibited minimal carbonation due to their compact structure and limited moisture uptake (<50 %). Similarly, synthetic yarns such as acrylic, nylon, and polypropylene formed dense, well-bonded interfaces but lacked the lumen-type internal porosity and moisture associated with sustained carbonation near the yarn. In these systems, carbonation remained confined to a narrow interfacial zone or was entirely absent, confirming that carbonation efficacy is controlled by the physical capacity of the yarn to retain water and restructure the surrounding matrix into a semi-saturated, permeable pore structure favourable for carbonation.

The behaviour of coated yarns provides further insight by selectively modifying interfacial porosity while preserving or suppressing internal moisture. Cement-slurry-coated yarns (ODMJ and SMJ) demonstrate that extensive carbonation can still occur even when macropores at the interface are suppressed, provided internal moisture and some pore access remain. The high water-to-cement ratio (0.8) of the slurry likely promotes a porous inner rim around the coated yarns, allowing limited moisture-assisted CO_2 diffusion. As a result, carbonations front in these systems are more compact and concentric than the belt-shaped fronts observed in uncoated SJ composites, reflecting a shift from open pore-mediated to rim-confined transport. In contrast, the epoxy-coated jute (EJ) system suppress carbonation through both physical and chemical effects. The

continuous coating blocked internal yarn moisture and gas exchange, while the hydrophobic epoxy surface likely reduced wetting by the aqueous pore solution during mixing. This would limit intimate fibre–paste contact, local hydration, and subsequent carbonation reactions at the interface, leading to negligible microstructural development. This confirms that the carbonation-promoting role of natural fibres depends on their ability to sustain a humid, accessibe pore network rather than on interfacial porosity alone.

Phenolphthalein-based image analysis supports these interpretations. At 10 mm depth, pre-saturated jute increased the carbonated area fraction by 32 % relative to the oven-dried jute, consistent with its higher water absorption (*Table 6.1*). Epoxy-coated jute showed a 70–80 % reduction compared with saturated jute, indicating that interface sealing strongly limits carbonation despite the natural-fibre core. Slurry coatings showed a conditional response: they enhanced carbonation by 3–4 % when applied to ODJ, but reduced it by 44 % when applied to SJ, suggesting that a densified interface can hinder CO2 transport in moisture-rich conditions. Across all systems, compact synthetic yarns showed 80–85 % lower carbonated area fraction than porous natural yarns, while fibre diameter showed no systematic influence.

Of the scalar parameters assessed, 24-hour water absorption was the strongest predictor of carbonation performance. When the depth-averaged effective carbonation radius from 10 to 40 mm after 7 days of carbonation curing was plotted against the 24-hour water absorption of the tested yarns, the correlation coefficient reached $R^2 = 0.872$ (*Figure 6.8*). The 95 % confidence band indicates limited scatter around the fitted relationship within the range of yarn absorption values examined, despite the small number of yarn types tested ($n = 8$). This relationship should, however, be interpreted within the scope of the present study. The yarns were tested at relatively low fibre volume fractions and under a single enforced carbonation regime; at higher yarn contents, where carbonation influence zones overlap, or under different curing durations and humidity conditions, the linear relationship with water absorption may weaken or deviate.

As discussed in Section 5.4.2, yarn compactness and diameter influence the geometry of potential transport pathways. However, the present results show that neither parameter provides a consistent predictor of effective carbonation radius when considered independently. Their influence depends on whether the resulting inter-fibre and interfacial pores remain connected, accessible and appropriately moisture-conditioned. In contrast,

24-hour water absorption better captures the combined effects of accessible pore structure and moisture retention. It is also worth noting that the significantly lower variability observed in image-based carbonation area analysis in this study, as compared to results in the previous chapter (Figure 5.6), is largely attributable to improved control over yarn moisture content; in the earlier study, variations in ambient pre-conditioning and fibre saturation introduced large uncertainties in carbonation front delineation.

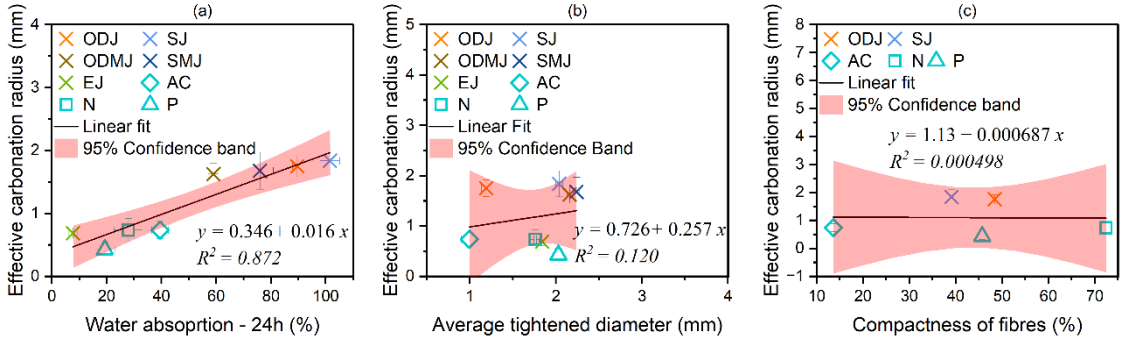


Figure 6.8. Relationship between yarn properties and the depth-averaged effective carbonation radius measured over 10–40 mm after 7 days of enforced carbonation curing: (a) 24 h water absorption, (b) average tightened yarn diameter, and (c) fibre compactness.

Overall, these observations affirm that carbonation is governed not by porosity per se, but by the saturation state and accessible pore network around the yarn. The middle rim zone observed under SEM-BSE plays a pivotal role: when semi-saturated and capillary-connected, it becomes a carbonation corridor; when dry, dense, or sealed, it becomes a barrier.

6.4.3. Practical implications

The results of this study provide guidance for the design of yarn–cement composites intended for CO_2-curable systems, particularly where carbonation efficiency and spatial control are required. For natural yarns such as jute, simple pre-saturation is sufficient to sustain carbonation and promote interfacial densification, whereas complex coatings like cement slurry layers offer only marginal benefit in already saturated systems and can be omitted unless surface protection is required under dry or aggressive conditions. Fibre selection should therefore prioritise high water absorption capacity and moderate compactness when early-age carbonation efficiency and strength development are the primary objectives.

The strong linear relationship between effective carbonation radius derived from image analysis and CO_2 uptake provides a practical tool for estimating carbonation performance without extensive thermogravimetric testing. At a depth of 10 mm, the effective carbonation radius around individual yarns was approximately 2–3 mm (*Figure 6.3; Figure 6.4d*). This characteristic length scale provides an initial basis for informing yarn spacing in mesh or textile arrangements. When adjacent yarns are spaced within approximately twice this radius, carbonation zones are likely to overlap, promoting more continuous carbonation across the cement matrix. At larger spacings, carbonation is expected to remain localised around individual yarns, reducing the overall efficiency of yarn-assisted CO_2 transport. The extent to which these interactions persist in multi-yarn systems, however, requires further investigation.

In the present study, a single yarn was used to isolate yarn-related transport mechanisms; subsequent work must therefore extend this approach to cementitious systems reinforced with multiple yarns to examine the effects of yarn spacing, mesh geometry, and interaction between adjacent carbonation zones. In addition, practical applications will require the inclusion of fine aggregates, which are expected to influence fibre–matrix interactions and CO_2 transport pathways.

6.5. Conclusions

This study demonstrates that under enforced carbonation, the behaviour of yarn–cement composites is controlled not by fibre type alone but by how the fibre modifies pore connectivity, moisture retention, and interfacial transport property. Saturated jute yarns enabled the deepest and most uniform carbonation, its lumina acting as distributed moisture reservoirs that sustained CO_2 dissolution and guided interfacial densification. In contrast, synthetic and epoxy-coated fibres, characterised by compact or sealed architectures, restricted moisture exchange and exhibited negligible carbonation engagement. Pre-saturation alone proved sufficient to activate strong fibre–matrix interaction, while additional surface treatments such as cement slurry coatings provided limited benefit under moist conditions. Across systems, water absorption correlated closely with carbonation depth and uptake, establishing a practical selection metric for CO_2-compatible composites. Overall, fibres that generate semi-saturated, connected pore networks near the interface can convert carbonation from a surface-limited reaction into a matrix-integrated process that enhances CO_2 sequestration efficiency. Nonetheless,

whether these carbonation-related benefits translate into improved mechanical performance requires further investigation.

Chapter 7 Hardened properties of carbonation-cured natural fibre yarn-reinforced cement pastes and mortars

This chapter draws in part on the journal article "*Influence of fibre treatments on early-age carbonation in yarn–cement composites under enforced carbonation*" by Zhuge, Y., Wong, H. S., and Myers, R. J., published in Cement and Concrete Composites. The experimental programme, data analysis, and interpretation of the cement paste results were led by the author. These results are reorganised and extended here in the context of this thesis, with emphasis on the mechanical performance of yarn-reinforced cementitious composites subjected to carbonation curing. Additional mortar-scale experiments are introduced to examine the influence of yarn mesh architecture and curing sequence on hardened properties in more representative composite systems.

7.1. Introduction

Yarn incorporation was found to alter carbonation behaviour by reshaping internal transport pathways and moisture distribution, leading to enhanced CO_2 uptake and preferential carbonation near the yarn–matrix interface (Chapters 5 and 6). The remaining question is whether yarns can be incorporated as organised meshes, and transferred from paste to mortar containing aggregates, without compromising mechanical performance under carbonation curing.

The mechanical response of natural fibre–reinforced cementitious composites depends strongly on fibre form, dosage, arrangement and curing conditions (Chen et al., 2023). For concrete systems tested at 28 days, jute fibre–reinforced mixes with short, dispersed fibres (typically ≤0.3 vol%) and water-to-cement ratios of 0.40–0.50 commonly report compressive strengths in the range of 50–70 MPa (Abdalla et al., 2023; Affan & Ali, 2022), with increases of approximately 6–24% relative to plain concrete when fibres are surface treated, and reductions of around 5–10% at higher fibre contents or with untreated fibres due to increased porosity and air entrainment (Kurpińska et al., 2022; AlMuhanna

et al., 2024; Ahmad et al., 2022). For mortar specimens, usually tested as 40–50 mm cubes at 28 days, reported compressive strengths generally fall between 40 and 65 MPa, with strength changes typically within ±10–20% of reference values depending on fibre dosage and workability control (Chen et al., 2023). Nevertheless, the majority of existing studies focus on short, dispersed fibres, whereas organised fibre architectures such as continuous yarn bundles or meshes remain largely unexplored.

In addition to fibre arrangement, the mechanical outcome of carbonation curing is strongly influenced by post-curing conditions (Liu et al., 2021; Yang et al., 2024). In fibre-free cement pastes and concretes, further water curing after early carbonation has been shown to activate secondary hydration of uncarbonated clinker phases, forming additional C–S–H and ettringite while consuming carbonation-derived calcite during C_3A hydration to produce calcium monocarbonaluminate, leading to pore refinement and continued strength development (He et al., 2016; Li & Ling, 2020). However, these benefits are not universal: Shi & Shui (2023) reported that despite reduced porosity and accelerated hydration during water curing, 28-day strength converges with or falls below that of standard-cured specimens, indicating that microstructural refinement does not necessarily translate into higher later-age strength. In contrast, air curing after carbonation, though less systematically studied, has been shown to produce substantial strength gains in cementitious materials subjected to high-pressure or supercritical CO_2 treatment, with specimens subsequently stored in air at 20 °C and approximately 65 % relative humidity achieving 28-day compressive strengths approaching 98 MPa (Heinz & Urbonas, 2016). Overall, existing evidence demonstrates that post-curing conditions exert a decisive but highly system-dependent influence on strength development after carbonation, yet remains largely confined to fibre-free systems, leaving unresolved how post-curing moisture exposure interacts with fibre-induced heterogeneity and organised transport pathways in yarn-reinforced composites.

This chapter addresses this gap through a staged mechanical assessment of jute yarn–reinforced cementitious composites. Jute was selected based on the favourable moisture-retention and carbonation response identified in the preceding chapters. Yarn mesh configurations are first screened at paste scale to identify arrangements capable of maintaining compressive strength at increasing yarn contents. A selected configuration is then transferred to mortar and compared with a plain reference mortar and mortar containing dispersed jute fibres at an equivalent fibre volume fraction, allowing the effect

of fibre arrangement to be examined independently of fibre content. Carbonation duration and subsequent air or water conditioning are varied to assess their influence on strength development, while sorptivity measurements provide complementary information on moisture transport. This approach evaluates whether the yarn architecture identified from the paste-scale studies remains mechanically compatible with carbonation curing after aggregate addition and under different post-curing conditions.

7.2. Materials and methods

7.2.1. Materials

Based on the findings of Chapter 6, three yarn systems were selected for this study: saturated jute yarns (SJ), oven-dried jute yarns (ODJ), and nylon yarns (N), representing contrasting moisture states and transport characteristics relevant to carbonation behaviour. Saturated jute yarns introduced the highest carbonation extent and CO_2 uptake due to their high water absorption and connected internal pore structure, whereas oven-dried jute yarns provided a moisture-depleted counterpart with reduced carbonation activity. Nylon yarns, with negligible water absorption and a compact filament structure, were included as a synthetic reference to isolate geometric reinforcement effects from fibre chemistry and moisture buffering. All yarns were prepared using the same procedures as described in Section 6.2.1, and nylon yarns were used as received. Representative morphologies of saturated and oven-dried jute yarns are shown in *Figure 6.1a–b*, with their physical properties summarised in *Table 6.1*; nylon yarns are shown in *Figure 3.2i*, with corresponding properties listed in *Table 3.1*.

For comparison with yarn-reinforced systems, dispersed jute fibres were also used. These fibres were obtained by cutting the same continuous jute yarns into short segments with a nominal length of 25 ± 2 mm and were submerged in deionised water for 24 hours prior to mixing to achieve a saturated state. The fibre dosage in mortar specimens was selected to match the volume replacement level of the corresponding yarn-reinforced mixes, enabling mechanical performance to be compared on the basis of fibre arrangement.

All cementitious specimens were prepared using the same ordinary Portland cement as in the preceding chapters to ensure consistency. Cement properties and chemical composition are reported in *Table 3.2* (Batch 2).

7.2.2. Sample preparation

Cement paste cube specimens with dimensions of 20 × 20 × 20 mm³ were prepared for compressive strength testing as a comparative screening study to assess the influence of yarn mesh configuration. A layer-by-layer casting approach was adopted (*Figure 3.4c*, steps i–iii). In each layer, yarns were manually positioned within the mould, followed by the addition of cement paste to embed the yarns. This sequence was repeated according to the prescribed mesh configuration (*Figure 7.1a*) until the mould was completely filled. After casting, the specimens were covered with a plastic membrane and stored at >98% relative humidity for the first 24 hours. The cubes were then demoulded and transferred to either air curing or carbonation curing chambers (Section 3.4).

Six mesh configurations were investigated to evaluate the effect of fibre layout on compressive strength (*Figure 7.1a* (i–vi)). These configurations varied in in-plane yarn spacing (10 mm or 5 mm) and the number of vertical yarn layers (1, 2, or 3 layers). Configurations are denoted using the format X–YL, where X represents the in-plane spacing in millimetres and Y denotes the number of yarn layers (e.g. 10–3L corresponds to three stacked yarn layers with 10 mm spacing). This screening study aimed to identify a mesh configuration that could maintain compressive strength comparable to the reference paste while maximising yarn content. Two additional configurations with an in-plane spacing of 2.5 mm were examined for completeness and are reported in Appendix 5 (*Figure A5.1*); these configurations were not viable due to excessive fibre content, which hindered paste placement and compaction.

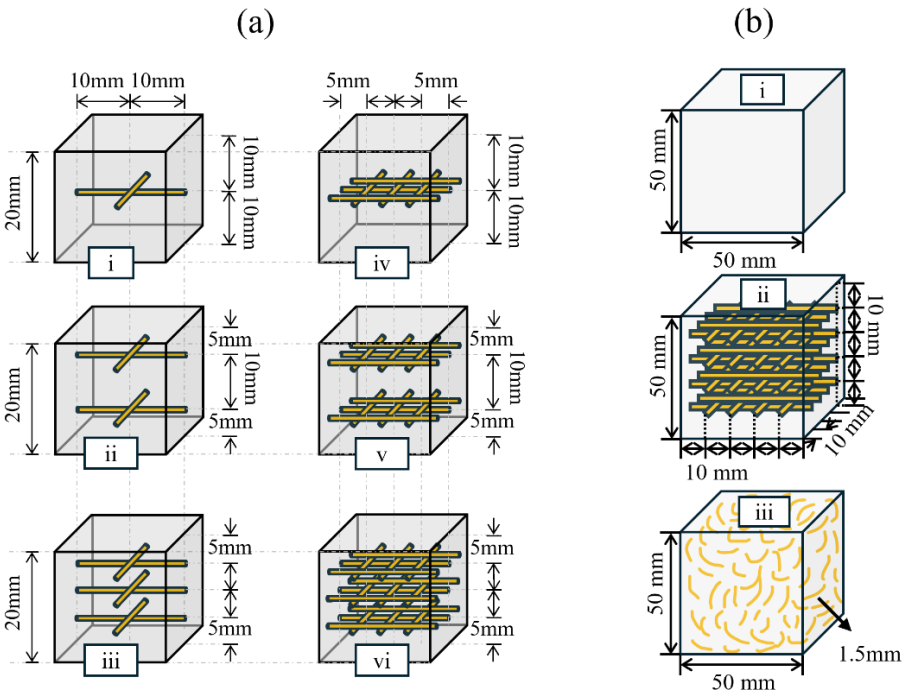


Figure 7.1. Schematic illustration of sample preparation and test configurations. (a) Mesh configurations for cement paste cubes: (i–vi) tested arrangements varying in in-plane yarn spacing (10 or 5 mm) and number of vertical yarn layers (1L to 3L). (b) Mortar specimen types: (i) plain reference mortar, (ii) yarn-reinforced mortar, and (iii) dispersed fibre reinforced mortar.

Based on the paste-scale screening results, a selected mesh configuration was subsequently upscaled to mortar cube specimens (50 × 50 × 50 mm³). This stage served to evaluate whether strength trends observed at paste scale were preserved under more representative composite conditions and to assess the influence of curing sequence and post-carbonation moisture exposure on hardened performance.

Mortars were prepared with a water-to-binder ratio of 0.40 and a sand-to-binder ratio of 2.0, following the general mixing procedures described in Section 3.3. Three types of mortar specimens were cast for comparison (*Figure 7.1b*): (i) a plain Portland cement reference mortar, (ii) a mortar reinforced with saturated jute yarn meshes, and (iii) a mortar reinforced with dispersed saturated jute fibres. Yarn-reinforced mortar specimens were cast using the same layer-by-layer approach (*Figure 3.4c*). For mortars containing dispersed fibres, a dry mixing stage of 5 min was introduced prior to water addition to promote fibre dispersion.

Following casting, all mortar specimens were covered with a plastic membrane and stored at >98% relative humidity in a fog room. After demoulding, specimens were subjected to

the prescribed curing regimes (Section 7.2.3) prior to compressive strength testing and sorptivity measurements.

7.2.3. Curing procedure

For the cement paste screening study, specimens were demoulded after 24 hours and cured either in air (> 96% RH) or under carbonation conditions (20 vol.% CO_2, 25 ± 0.5 °C, 64 ± 2% RH) for 1, 3, or 7 days prior to compressive strength testing. This early age curing window was selected to capture the short-term mechanical response associated with carbonation.

Mortar specimens were subjected to the curing regimes illustrated in *Figure 7.2*. Where applicable, specimens were transferred to the secondary curing environment after an initial curing period of 1, 3, or 7 days. Compressive strength was measured at 1, 3, 7, and 28 days. These curing procedures were designed to assess the combined effects of early carbonation and post-curing moisture exposure on strength development.

To ensure clarity in reporting, a consistent labelling system is used for all mortar specimens to indicate reinforcement type, initial curing regime, carbonation duration, and final curing condition. For example, *SJ-C-D7-28(A)* denotes a saturated jute yarn–reinforced mortar subjected to 7 days of carbonation curing followed by air curing to 28 days, while *(W)* indicates water curing.

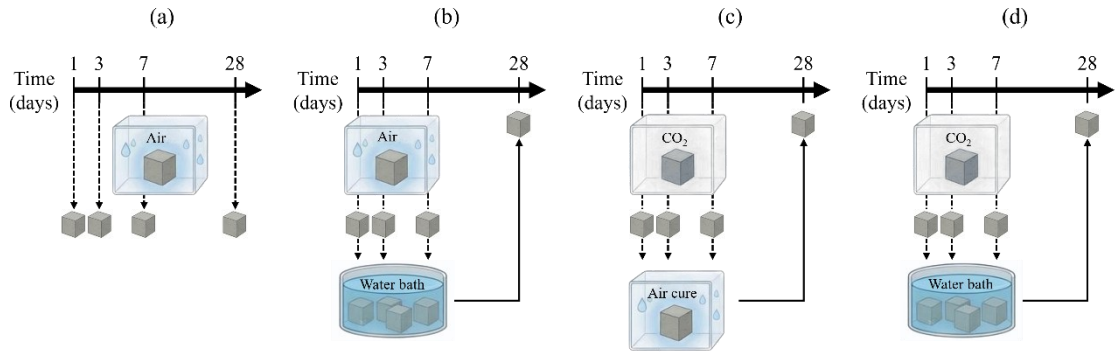


Figure 7.2. Curing procedures applied to mortar specimens. Specimens were subjected to four curing regimes: (a) continuous air curing; (b) initial air curing followed by water curing; (c) initial carbonation curing followed by air curing; and (d) initial carbonation curing followed by water curing. Compressive strength was measured after 1, 3, 7, and 28 days of curing, with specimens transferred to the secondary curing environment after the initial 1, 3, or 7 days where applicable.

7.2.4. Compressive strength test

Testing procedures and equipment calibration followed the standard methods described in Section 3.7. Cement paste cube specimens were tested at the specified curing ages to support screening of yarn mesh configurations. For mortar specimens, compressive strength was measured after completion of the curing regimes illustrated in *Figure 7.2*. Three replicate cubes were tested for each mixture and curing condition, and average values were calculated.

For yarn-reinforced specimens, the fibre volume fraction (replacement level) was defined as the total embedded yarn volume relative to the specimen volume. The embedded yarn volume was calculated from the convex cross-sectional area of the yarn, obtained from image analysis, multiplied by the total yarn length associated with each mesh configuration (Section 3.6.1).

7.2.5. Sorptivity test

Sorptivity tests were conducted to support interpretation of compressive strength results in relation to moisture uptake and transport in mortar specimens. Plain reference mortars, yarn-reinforced mortars, and mortars containing dispersed jute fibres were tested for comparison. Tests were performed on 50 × 50 × 50 mm^3 cube specimens following the procedure described in Section 3.8.2, with the experimental setup visualised in *Figure 3.9.*

7.3. Results and analysis

7.3.1. Screening of mesh configurations using cement paste cubes

Compressive strength increased with curing duration under both air and carbonation regimes (*Figure 7.3a–c*). Carbonation curing produced faster strength gain, particularly between 3 and 7 days, consistent with carbonate formation and matrix densification described in Sections 6.3.1–6.3.3. At 7 days, the magnitude of improvement depended on yarn type and yarn volume fraction (i.e. replacement level).

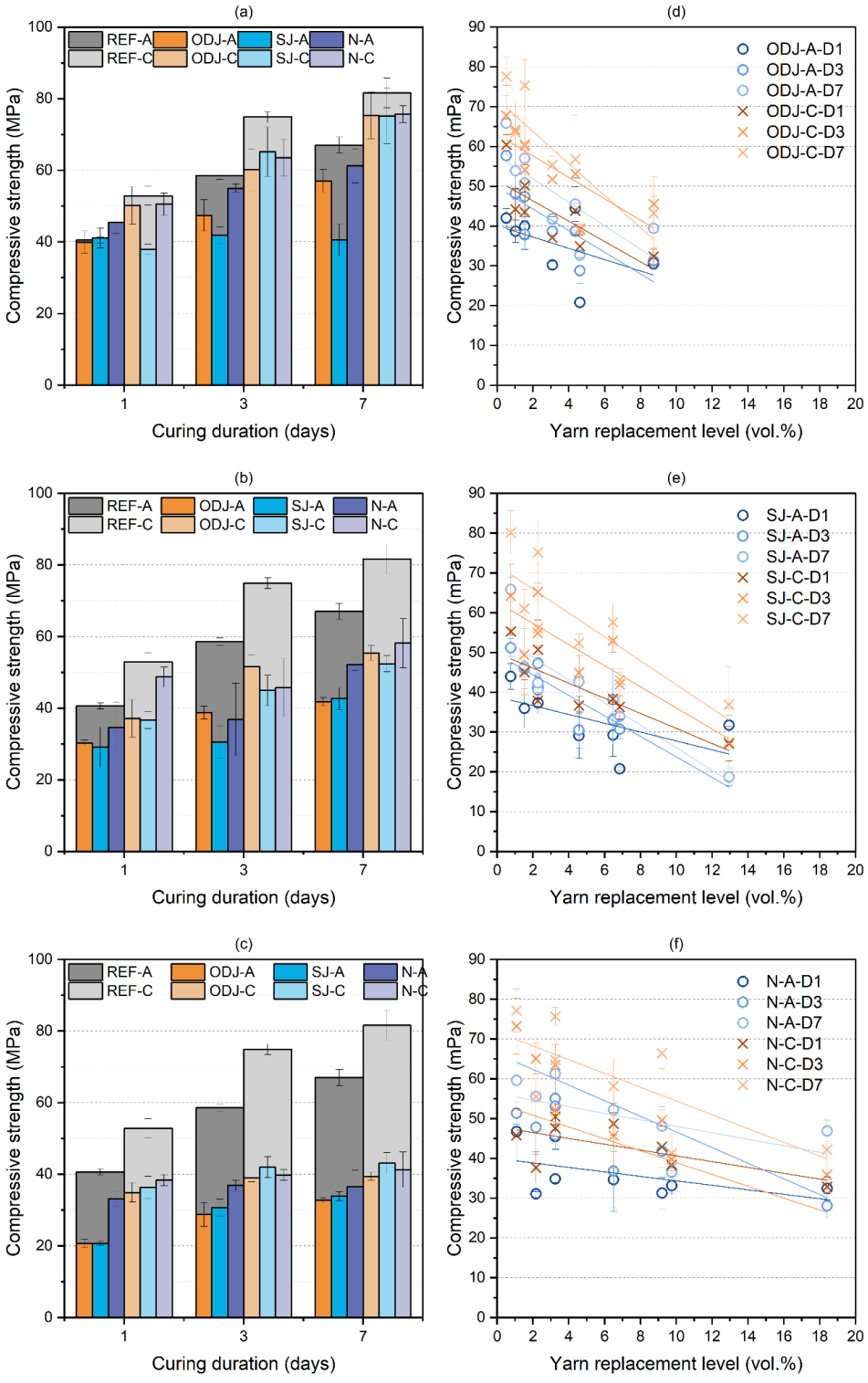


Figure 7.3. Compressive strength of yarn–reinforced cement paste as a function of fibre type, curing regime, curing duration, and fibre volume. (a–c) Strength development at 1, 3, and 7 days for oven-dried jute (ODJ), saturated jute (SJ), and nylon (N) composites under air and carbonation curing, using (a) 5-1L, (b) 5-2L, and (c) 5-3L mesh configurations. The larger grey bars represent the fibre-free reference cement pastes under air curing (REF-A) and carbonation curing (REF-C), included as benchmarks for comparison with the yarn-reinforced specimens. (d–f) Compressive strength variation with fibre volume fraction (replacement level) for (d) ODJ, (e) SJ, and (f) N composites at 1, 3, and 7 days, under both curing regimes. Error bars represent ± standard error of the mean (n = 3). Linear trendlines are included for visual reference.

For SJ cement paste composites, carbonation increased 7-day strength from 46.3 MPa to 61.0 MPa (+32 %) in 10–2L (1.52 vol. %) and from 42.7 MPa to 55.4 MPa (+30 %) in 5–2L (4.57 vol. %). ODJ composites showed smaller but consistent gains, increasing from 53.9 MPa to 63.5 MPa (+18 %) in 10-2L, and from 41.8 MPa to 52.4 MPa (+25 %) in 5 –2L configurations. Nylon exhibited a more variable response, with 7-day carbonation increasing strength by +29.6 % in 10–1L and +23.5 % in 5–1L, but only +5–6 % in 2L meshes. Across fibre types, the largest relative gains under carbonation were therefore observed at low to moderate fibre volumes.

The influence of yarn replacement level, governed by yarn spacing and the number of layers, is shown in *Figure 7.3d–f*. Strength decreased systematically with increasing yarn content under both curing regimes. Under air curing, increasing from 1L to 2L at 5 mm spacing reduced strength by 10–15 MPa, with a further 5–10 MPa loss for 3L meshes. Under carbonation curing, the reduction from 1L to 2L was larger typically 20–30 MPa. At low yarn replacement levels (0.76–2.28 vol. %), SJ 10–1L and SJ 5–1L composites achieved 80.1 MPa and 75.2 MPa, respectively, comparable to the paste control (77.2 MPa) within experimental scatter. Configurations with 2.5 mm spacing showed the lowest strengths and largest scatter, due to excessive yarn content and poor paste continuity (Appendix 5, *Table A5.1*). These mixes also showed the largest scatter, particularly under carbonation curing (e.g. ODJ 2.5–1L: 56.8 ± 11.1 MPa; SJ 2.5–2L: 36.9 ± 9.65 MPa at 7 days). The large standard errors indicate that strength in these configurations is dominated by local defects and poor paste continuity. These configurations were not pursued further, as the measured effective carbonation radius (~2–3 mm; *Figure 6.4d*) indicates that such closely spaced yarns would experience overlapping carbonation zones, providing limited insight into yarn-controlled transport behaviour. Overall, carbonation-induced densification compensated for yarn-induced defects only at low yarn volume fractions; at higher volume fractions, loss of matrix continuity and increased interfacial volume dominated the mechanical response.

Differences in absolute compressive strength among fibre types at a given yarn volume and curing condition were generally modest and often comparable to the associated standard errors, typically $\leqslant 5$ MPa for 1L configurations. Therefore, fibre-type differences should be interpreted cautiously where error bars overlap. Under air curing, ODJ showed slightly higher baseline strength (65.8 MPa in 10–1L) than nylon (59.6 MPa)

and SJ (57.8 MPa). After carbonation, the strengths of SJ, ODJ, and nylon converged to ~75–80 MPa at low yarn volume fractions. At higher yarn volumes, nylon retained marginally higher absolute strength, but its relative carbonation benefit was smaller.

Based on the combined requirements of mechanical performance, controlled fibre volume, and non-overlapping carbonation influence zones, the mesh configuration with 5 mm in-plane spacing and a single yarn layer (5–1L) was selected for subsequent experiments. In the 20 × 20 × 20 mm³ cement paste cubes, this configuration corresponds to a fibre replacement level of 2.28 vol.% for saturated jute yarns. Despite the relatively high fibre content, SJ composites in the 5–1L configuration maintained compressive strength comparable to or exceeding the paste control under carbonation curing, while avoiding the severe strength reductions observed in denser meshes. On this basis, saturated jute yarns were selected for further investigation, as they exhibited the most favourable balance between carbonation-enhanced strength development and fibre-induced strength reduction within the tested configurations. When applied to 50 mm mortar specimens, multiple 5–1L meshes were stacked vertically at 10 mm intervals through the specimen height.

7.3.2. Compressive strength of yarn-reinforced mortars

Figure 7.4 summarises the compressive strength development of plain reference mortars, yarn-reinforced mortars containing saturated jute yarns (SJ), and mortars reinforced with dispersed jute fibres (DJ) under different curing sequences. Across all mixtures, initial carbonation curing for 1–7 days consistently enhanced early-age compressive strength relative to initial air curing.

After 1 day of curing, carbonation increased compressive strength by 6.5 MPa (13.9% increase) for the reference mortar, 6.6 MPa (11.6% increase) for SJ mortars, and 6.1 MPa (13.6% increase) for DJ mortars (*Figure 7.4a,d*). The relative benefit of carbonation was most pronounced after 3 days (*Figure 7.4b,e*), particularly for DJ mortars (+12.1 MPa), which exhibited a 26.0% increase compared with 16.6% for the reference mortar (+8.4 MPa) and 11.6% for SJ mortars (6.6 MPa). At 7 days, carbonation increased strength by 4.6 MPa (7.6%) for the reference and 6.6 MPa (10.7%) for SJ, whereas DJ retained a larger increase of 12.5 MPa (26.3%) (*Figure 7.4c,f*). As highlighted by the red reference

line in *Figure 7.4*, carbonation primarily accelerates early strength development rather than increasing the ultimate strength of the plain reference mortar.

Strength development beyond the initial curing stage depended strongly on the post-curing environment. For specimens initially air cured (*Figure 7.4a–c*), continued air curing generally resulted in higher or comparable 28-day strengths than subsequent water curing for fibre-containing mortars. After 7 days of initial air curing, SJ mortars achieved 64.2 MPa under continued air curing, whereas specimens subsequently water cured reached 55.1 MPa, 9.1 MPa (14.2%) lower than their air-cured counterparts. DJ mortars exhibited a similar effect, reaching 58.2 MPa after continued air curing compared with 49.9 MPa after water curing, marking a drop of 8.3 MPa (–14.2%). In contrast, the reference mortar showed only marginal sensitivity to post-curing environment, with water curing providing limited additional benefit at 28 days.

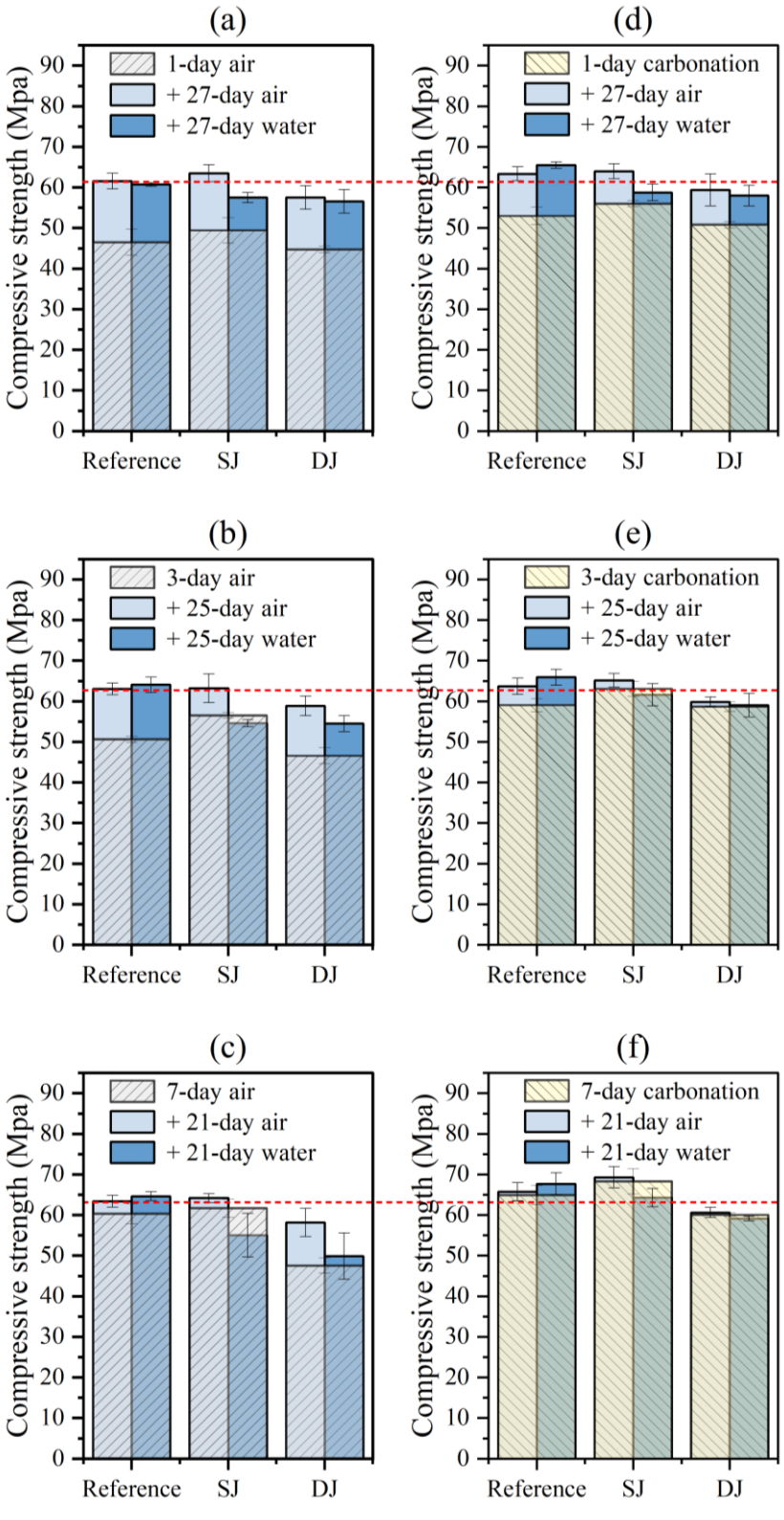


Figure 7.4. Compressive strength development of mortar specimens under different curing sequences. Panels (a–c) show specimens initially air cured for 1, 3, and 7 days, respectively, followed by either continued air curing or water curing to 28 days. Panels (d–f) show specimens initially subjected to carbonation curing for 1, 3, and 7 days, respectively, followed by either air curing or water curing to 28 days. Results are shown for plain reference mortars, yarn-reinforced mortars (SJ), and dispersed fibre reinforced mortars (DJ). The red dotted line indicates the 28-day compressive strength of the plain reference mortar cured continuously in air, shown as a benchmark for comparison.

For specimens initially subjected to carbonation curing (*Figure 7.4d–f*), post-curing effects differed between mixtures. For fibre-containing mortars, higher 28-day strengths were consistently achieved when carbonation curing was followed by air curing rather than water curing. The highest strengths for both SJ and DJ mortars were obtained after 7 days of carbonation followed by air curing, reaching 69.3 MPa and 65.2 MPa, respectively. Subsequent water curing reduced strength in both systems; however, the reductions were smaller than those observed when water curing followed initial air curing, indicating that prior carbonation partially mitigated the adverse effect of moisture exposure. This moderation was most evident for SJ mortars, where strength decreased from 69.3 to 64.3 MPa after water curing. In contrast, the reference mortar benefited modestly from post-carbonation water curing, increasing by approximately 3% after 7 days of carbonation.

Across all curing sequences, SJ mortars consistently outperformed DJ mortars and achieved compressive strengths comparable to or exceeding those of the plain reference system, particularly under carbonation-based curing regimes. Although DJ mortars exhibited the largest relative early-age strength gains from carbonation, their response plateaued after 3 days, with limited benefit from extended carbonation. In contrast, SJ mortars continued to gain strength between 3 and 7 days of carbonation, indicating a greater capacity to convert prolonged carbonation into sustained mechanical improvement. Overall, the most favourable curing sequence for SJ mortars was 7 days of carbonation curing followed by air curing to 28 days, yielding a compressive strength approximately 9% higher than that of the fully air-cured reference mortar.

7.3.3. Sorptivity of yarn-reinforced mortars

Figure 7.5 presents the water absorption behaviour of reference mortars, dispersed fibre reinforced mortars (DJ), and yarn-reinforced mortars (SJ) after different carbonation durations, with selected specimens subsequently air cured or water cured to 28 days. Sorptivity measurements were included to support interpretation of the compressive strength results by examining how carbonation and post-curing moisture exposure influence moisture transport, particularly in fibre-containing systems.

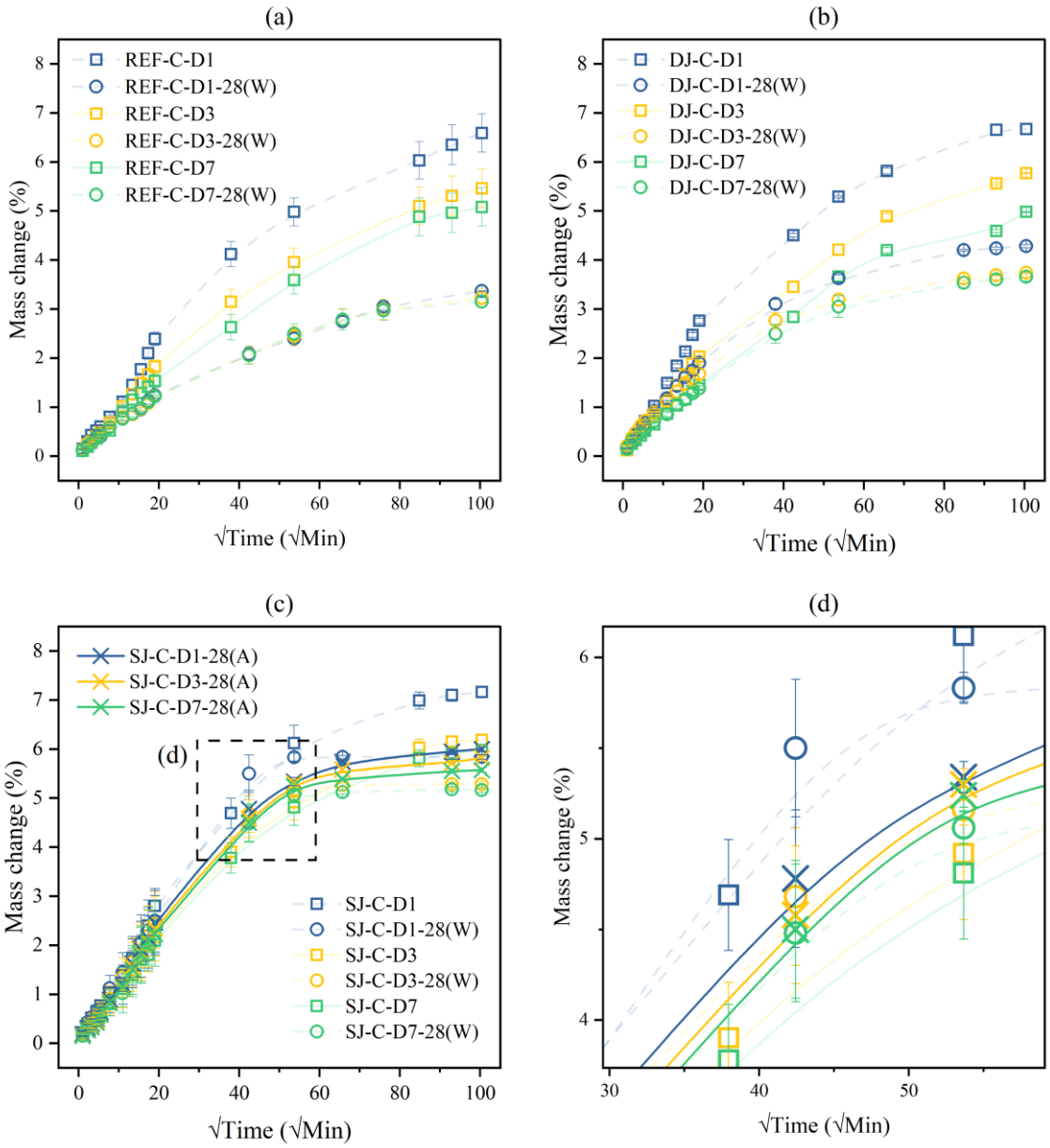


Figure 7.5. Water absorption behaviour of mortar specimens plotted as mass change versus the square root of time. (a) Plain reference mortars and (b) dispersed fibre reinforced mortars (DJ) subjected to carbonation curing for 1, 3, and 7 days, with and without subsequent water curing to 28 days. (c) Yarn-reinforced mortars (SJ) after carbonation curing for 1, 3, and 7 days, including specimens air cured or water cured to 28 days. (d) Enlarged view of the boxed region in (c), highlighting early-stage absorption behaviour.

For the plain reference mortar (*Figure 7.5a*), increasing carbonation duration from 1 to 7 days progressively reduces both the initial absorption rate and total mass uptake. This downward shift indicates increasing pore refinement with longer carbonation exposure. However, after subsequent water curing to 28 days, the sorptivity curves for REF-C-D1-28(W), REF-C-D3-28(W), and REF-C-D7-28(W) converge closely, indicating that early carbonation duration has little influence on 28-day sorptivity once prolonged water

exposure is introduced. This behaviour is consistent with the limited sensitivity of the reference mortar's later-age compressive strength to early carbonation history.

Dispersed fibre–reinforced mortars (DJ) show slightly higher mass uptake than the reference mortar across all carbonation durations (*Figure 7.5b*), although the overall magnitude remains comparable. Carbonation again shifts the curves downward with increasing duration, confirming reduced sorptivity. Compared with the reference system, DJ mortars exhibit a more gradual transition towards saturation, with absorption continuing over a longer √time range. This behaviour suggests that distributed fibre–matrix interfaces maintain moisture-accessible pathways even after carbonation. After water curing to 28 days, the DJ curves also converge, though they remain marginally above the reference, indicating a persistent but moderate increase in transport capacity.

Yarn-reinforced mortars (SJ) display a distinct sorptivity response (*Figure 7.5c*). Despite having the same fibre volume fraction as DJ mortars (2.28 vol.%), SJ specimens exhibit higher mass uptake than both DJ and reference mortars. The sorptivity curves for SJ display a pronounced early uptake followed by a rapid transition towards a plateau, indicating earlier saturation. Notably, the early-stage portions of the SJ curves overlapped closely for different carbonation durations, more so than in the reference and DJ systems. This clustering suggests that early moisture ingress in SJ mortars is dominated by the bulk yarn network, which provides a consistent and repeatable capillary pathway that limits sensitivity to matrix-level changes induced by carbonation. Differences between carbonation durations became more apparent only at later times, once uptake extended beyond the immediate yarn-associated pore system.

The enlarged view in *Figure 7.5d* highlights the early absorption regime of SJ mortars. Specimens air cured after carbonation consistently exhibit higher sorptivity than those subjected to post-carbonation water curing, while remaining below the carbonation-only cases. This indicates that post-carbonation water curing suppresses early capillary uptake more effectively than air curing, despite being detrimental to compressive strength in fibre-containing mortars. The contrasting trends confirm that sorptivity does not correlate directly with compressive strength and that moisture transport alone cannot explain the mechanical response of yarn-reinforced mortars.

7.4. Discussion

7.4.1. Transferability of paste-scale strength trends to mortar systems

The cement paste cube samples were designed as a screening step to isolate the influence of yarn mesh configuration on compressive strength under controlled conditions, independent of aggregate effects. The mechanical response of yarn-reinforced cement paste composites under carbonation curing reflects a balance between carbonation-induced matrix densification and the adverse effects of yarn inclusion. It is therefore governed not simply by carbonation depth, but by whether microstructural refinement can compensate for fibre-induced heterogeneity. This balance depends on fibre morphology, internal moisture availability, and spatial arrangement within the matrix. Porous, twisted natural yarns generate more interfacial complexity than compact synthetic filaments, but also offer greater potential for carbonation-induced densification. At low yarn volumes, densification of the ITZ and adjacent matrix can offset fibre-induced heterogeneity and preserve compressive strength. At higher yarn volumes, the reduced load-bearing paste fraction and cumulative extent of interfacial and porous rim regions dominate, so greater carbonation extent does not translate directly into higher strength (Appendix 5, *Table A5.1*).

The introduction of sand changed the load-bearing structure and reduced the proportion of cement paste, but the principal mechanical trends remained broadly consistent. Carbonation increased the 1-day strength of the reference, SJ, and DJ mortars by approximately 14%. At 3 days, the increase depended on fibre form, ranging from 11.6% for SJ mortar to 26.0% for DJ mortar, while the additional benefit fell below 11% after 7 days. Carbonation therefore accelerated early-age strength development across all mortar systems, although the magnitude and persistence of the increase depended on the reinforcement architecture and curing duration. The selected SJ mortar also maintained higher strength than the DJ mortar at the same fibre volume fraction and achieved strength comparable to or greater than the plain reference under several curing sequences.

These results demonstrate transferability of the mechanical response, but they do not directly demonstrate transferability of the yarn-assisted carbonation mechanism. Carbonation distribution, carbonate content, and CO_2 uptake were not measured in the mortar specimens. It is therefore not possible to determine whether the preferential yarn-adjacent carbonation observed in the single-yarn paste specimens persisted after

aggregate addition or whether the mortar-scale strength differences corresponded to greater CO_2 uptake. The mortar results should instead be interpreted as showing that the selected yarn configuration was mechanically compatible with carbonation curing under the tested conditions.

The comparison between SJ and DJ mortars nevertheless provides evidence that fibre arrangement influenced mechanical performance independently of nominal fibre content and initial moisture condition, because both systems contained the same volume of saturated jute. The placed yarns concentrated the fibres and associated interfaces within defined continuous bundles, leaving larger regions of uninterrupted mortar matrix. By contrast, dispersed fibres introduced a greater number of distributed fibre–matrix interfaces throughout the specimen, increasing the spatial extent of fibre-induced heterogeneity (Hu et al., 2023; Hay, Krishnan & Celik, 2024). This difference provides a plausible explanation for the consistently higher strength of SJ mortars. The yarn architecture may also have localised moisture and carbonation reactions around the bundles, as observed in the single-yarn paste specimens in Chapter 6, although this was not verified directly at mortar scale.

The presence of aggregate may further explain why SJ mortars achieved strengths comparable to or exceeding the plain reference even under air curing, whereas saturated-jute paste specimens showed a clearer fibre-related strength penalty. In mortar, the aggregate skeleton contributes to load transfer and reduces the influence of local paste discontinuities on bulk compressive strength. The mechanical response consequently becomes less sensitive to individual yarn-adjacent regions than in cement paste. However, this interpretation remains indirect because local strain distribution, interfacial damage, and mortar microstructure were not measured.

Transfer from the single-yarn studies in Chapter 6 to the mesh systems in Chapter 7 is also subject to differences in yarn placement. The single yarns were held under light longitudinal tension, whereas the meshes were positioned without equivalent tension. Changes in yarn tension can alter bundle diameter, compactness, internal void volume, and yarn–matrix contact. The single-yarn observations therefore provide a mechanistic basis for interpreting the mesh results, but they do not reproduce the precise yarn geometry present in the paste cubes or mortar specimens.

Overall, the paste screening successfully identified a mechanically viable candidate configuration for mortar-scale assessment. Within the tested paste systems, the most favourable balance was obtained at low yarn volume fractions, with acceptable strength retained up to approximately 2.3 vol.%. This is notably higher than typical fibre contents in engineered cementitious composites systems, where common cellulose dosages range from 0.2 to 1.5 vol% by binder volume (Jamshaid et al., 2022; Siqueira, Filho & Koenders, 2015; Feng et al., 2023). Nevertheless, this value should be treated as an experimental design range rather than a universal threshold. The mortar results confirm mechanical compatibility of the selected 5 mm saturated-jute mesh arrangement but do not establish that it is optimal at mortar scale or that the paste-scale increase in carbonation was retained after aggregate addition.

7.4.2. Effect of carbonation curing and post-curing conditions on strength development

The results demonstrate that carbonation compatibility in natural fibre yarn-reinforced mortars is governed not only by the extent of carbonation, but by whether jute yarn-induced transport pathways remain mechanically stable under post-curing moisture exposure. Carbonation accelerates early-age strength development relative to air curing, while post-curing conditions govern whether the resulting microstructural refinement is retained, augmented by hydration, or degraded by moisture-driven fibre–matrix interactions.

In the plain reference mortar, carbonation curing produced a clear early-age strength enhancement but had a limited effect on 28-day strength. As shown in *Figure 7.4*, carbonation increased 1–7 day compressive strength by up to approximately 17%, while 28-day strengths converged with those of continuously air-cured specimens regardless of post-curing regime. This behaviour reflects carbonation-induced pore refinement and carbonate precipitation accelerating early stiffness development, with later-age strength governed by continued hydration of uncarbonated clinker once moisture is available. Sorptivity results (*Figure 7.5a*) support this interpretation: longer carbonation durations reduced early capillary absorption, but these differences largely disappeared after prolonged water exposure, indicating that transport in the reference system remains matrix-controlled and insensitive to early carbonation history at later ages.

Natural fibre-containing mortars exhibited a fundamentally different response to post-curing moisture exposure. For both yarn-reinforced (SJ) and dispersed fibre reinforced (DJ) mortars, transfer to water curing after either air curing or carbonation curing led to measurable strength reductions by 28 days (*Figure 7.4*). This response diverges from that commonly reported for fibre-free carbonation-cured systems, since the involvement of natural fibres introduces additional moisture that alter how carbonation-derived refinement is retained during subsequent curing.

The sorptivity results provide key insight into this behaviour. In DJ mortars, jute fibre–matrix interfaces remain broadly moisture-accessible even after carbonation, as reflected by gradual absorption curves and delayed saturation (*Figure 7.5b*). Although carbonation reduces overall sorptivity, moisture ingress persists over extended timescales, indicating that transport remains dominated by the capillary pore network. During carbonation curing, this distributed transport structure also limits effective CO_2 penetration into the inner matrix, reducing the localisation of carbonation-induced densification. Consequently, carbonation primarily compensates for fibre-induced strength loss rather than producing a net strength enhancement, and 28-day strengths of DJ mortars remain below those of SJ and reference systems.

Jute yarn-reinforced mortars exhibit a different transport regime compared to the above. Despite having the same fibre volume fraction as DJ mortars, SJ specimens show higher total mass uptake and sorptivity curves characterised by rapid early absorption followed by early saturation (Figure 7.5c). The close overlap of early-stage sorptivity curves across carbonation durations indicates that moisture ingress is governed by the organised yarn network rather than by matrix pore structure. This yarn-scale transport pathway facilitates efficient CO_2 ingress during carbonation curing, promoting preferential carbonation and enhanced early strength development under carbonation-based curing sequences.

However, the same transport efficiency renders SJ mortars particularly sensitive to prolonged water exposure. Submersion activates jute fibre swelling, softening, and interfacial weakening along continuous yarn pathways, effects that are amplified by the bundled fibre geometry (Bhattacharyya, Subasinghe & Kim, 2015; Hamada et al., 2023; Wei & Meyer, 2015; Onuaguluchi & Banthia, 2016). Carbonation densifies the surrounding matrix and stiffens the immediate interface but does not eliminate internal yarn porosity or disrupt yarn continuity as a transport pathway. This is reflected in the

sorptivity response *(Figure 7.5c,d*), where the initial absorption rate of SJ mortars is largely independent of carbonation duration, indicating yarn-controlled early uptake, while total mass uptake is highest yet saturation is reached earlier than in DJ and reference systems. Such behaviour confirms that transport is concentrated within the bulk yarn pathways rather than distributed throughout the matrix.

Prior carbonation reduced, but did not eliminate, the strength loss associated with subsequent water exposure. This suggests that carbonation-induced local densification provided some mechanical stabilisation of the fibre-containing systems, while remaining insufficient to suppress moisture-driven effects associated with the fibres and their interfaces. Air curing after carbonation consistently retained higher strength than water curing for both SJ and DJ mortars. Under these conditions, the carbonated matrix was not subjected to renewed liquid-water transport and the yarns underwent less moisture-induced dimensional change, which may have helped preserve the mechanically favourable state established during carbonation. This interpretation remains provisional because changes in yarn dimensions, interface integrity and mortar phase assemblage were not measured after post-curing.

From a hydration perspective, prolonged water exposure modifies the balance between carbonation products and subsequent hydration. In fibre-free cement pastes and concretes, renewed moisture can promote further hydration of uncarbonated clinker phases, aided by calcite formed during carbonation acting as nucleation sites (Lu et al., 2021; He et al., 2016), In natural fibre–reinforced systems, however, the same water exposure introduces competing fibre-related processes, including swelling, softening, and chemical degradation under alkaline conditions. As a result, additional hydration products formed during post-carbonation water curing contribute less effectively to load-bearing capacity, explaining why reduced sorptivity or apparent pore refinement (*Figure 6.6*) does not translate into higher later-age strength. This interpretation is consistent with observations that post-carbonation hydration can yield neutral or negative strength outcomes in heterogeneous systems despite microstructural refinement (Shi & Shui, 2023).

7.4.3. Practical implications for natural fibre yarn-reinforced cement composites

This study demonstrates that fibre arrangement, together with fibre nature, is a governing design parameter for carbonation-compatible cementitious composites. Compared with

dispersed fibres at the same volume fraction, placed jute yarns concentrated fibre-related porosity within organised pathways rather than distributing interfaces throughout the matrix. Under the selected curing conditions, this architecture retained compressive strength more effectively than dispersed jute fibres. The result demonstrates that yarn-associated porosity does not necessarily preclude high compressive strength when yarn volume and post-curing moisture are controlled.

A key practical outcome is that extended water curing is not required to achieve satisfactory mechanical performance in yarn-reinforced systems. For configurations relevant to thin or slab-like elements, carbonation followed by air curing was sufficient to deliver competitive strength. This is particularly advantageous for natural fibre composites, as prolonged water immersion increases the risk of fibre swelling, softening, and interfacial degradation. Avoiding post-carbonation water curing therefore simplifies processing, as well as preventing moisture-driven deterioration of natural fibres.

Although only a single mesh configuration was examined at mortar scale, the combined paste- and mortar-scale results provide clear guidance for the design and application of natural yarn–cement composites in CO_2-curable systems. Paste screening identified single-layer saturated jute meshes with 5–10 mm spacing and low fibre replacement as offering the most favourable balance between carbonation enhancement and compressive strength, making them a potential candidate for thin-section elements such as façade panels, precast blocks, and modular wall units where reinforcement volume must remain limited (Pidun & Schulze, 2015). Higher-volume configurations, including denser meshes and multi-layer arrangements, while not validated mechanically at mortar scale, are more likely suited to non-structural or repair applications where crack control, deformation tolerance, or durability is prioritised over peak strength (Orlowsky, Beßling & Kryzhanovskyi, 2023). Because the yarns are placed rather than mixed, the concept functions as a reinforcement and transport scaffold, analogous in implementation to textile-reinforced mortars; this approach decouples reinforcement from paste rheology and eliminates the need for high flowability or chemical admixtures. Yarn placement can be achieved using manual positioning, prefabricated meshes, or textile inserts, and is compatible with automated mould-based or robotic assembly processes commonly used in precast manufacturing.

7.4.4. Durability considerations for yarn-reinforced composites

The continuous and porous architecture of natural fibre yarns underpins the enhanced carbonation behaviour and early-age strength development identified in this chapter; however, it also introduces durability considerations that extend beyond the time frame investigated here. As discussed in Section 7.4.2, yarn-centred transport pathways dominate moisture ingress and redistribution in yarn-reinforced mortars. Under service conditions, these pathways may also facilitate the transport of liquid water and dissolved ionic species, shifting durability control from bulk matrix permeability to yarn-associated transport networks.

For natural fibres, transport accessibility directly influences chemical and interfacial stability by facilitating Ca^{2+} ingress into fibre lumens and cell walls, which can promote fibre mineralisation and degradation of fibre–matrix bonding (Addis, Sendekie & Satheesh, 2022; Booya et al., 2019). Carbonation curing may partially mitigate these processes through portlandite consumption and a reduction in pore-solution alkalinity in yarn-adjacent regions (Tonoli et al., 2016). In the previous chapter, no fibre degradation was observed over curing durations of 1–7 days (*Figure 6.7*). However, this early-age stability does not preclude longer-term deterioration under sustained moisture exposure, cyclic wetting and drying, or combined environmental actions. The strength reductions observed following water curing in fibre-containing mortars (*Figure 7.4*) further indicate that moisture exposure remains a critical durability concern.

These mechanisms have direct implications for the design of carbonation-compatible yarn-reinforced cementitious composites. Fibre treatments commonly used to improve durability in natural fibre composites, which typically reduce fibre hydrophilicity (Prabhu et al., 2021), are unsuitable when applied prior to carbonation curing, as they suppress the moisture buffering required to sustain carbonation within the composite interior. For yarn-reinforced systems, durability control must therefore be implemented after carbonation curing, using strategies that restrict transport along yarn-adjacent pore networks while preserving the carbonated microstructure developed during enforced carbonation.

Among post-curing protection strategies, concrete surface treatments, including hydrophobisation, inorganic pore blocking, polymer-modified cementitious coatings, thin recast facing layers, and dense organic barrier coatings (Pan et al., 2017a, 2017b), are

poorly matched to natural fibre yarn systems. These treatments are designed to modify transport within the near-surface cement paste, with protection governed by pore wettability, micro-scale pore filling (Pan et al., 2017a), or the formation of a surface barrier layer, and therefore provide protection that is largely confined to the near-surface cement paste. As a result, their ability to influence the continuous, bulk transport pathways introduced by the yarns, which form millimetre-scale channels through the matrix, is inherently limited. This highlights the need for post-curing strategies that target yarn-induced internal transport pathways rather than the cement paste surface alone.

A potentially effective alternative is near-surface impregnation using low-viscosity organic or organo-silicate systems (e.g. epoxy, polyurethane, or alkoxysilane-based resins) (Batis, Pantazopoulou & Routoulas, 2003; Wu et al., 2023; Zhang et al., 2010), applied after carbonation curing and controlled drying to enable penetration into the connected yarn networks. In practice, the treatment would be directed at composite surfaces where yarn corridors are exposed, allowing the impregnating liquid to be drawn into the yarns and interfacial pore structure by capillary suction, or assisted by mild vacuum or pressure. Subsequent solidification of the impregnant would partially occlude these pathways, forming an internal barrier to liquid and ion transport. The feasibility of this post-curing sequence warrants systematic investigation in future work.

These results identify a central trade-off in the proposed approach. The continuous and moisture-accessible yarn structure that promotes CO_2 transport during curing may remain a preferential pathway for liquid water and dissolved ions during service. The SJ mortars exhibited higher capillary water uptake than the reference and dispersed-fibre systems, and post-carbonation water exposure reduced the strength of the fibre-containing mortars. Carbonation-induced interfacial densification reduced but did not eliminate this sensitivity. Consequently, any practical benefit from increased early carbonation must be evaluated against the possible need for moisture protection, the durability of the natural yarn and the long-term stability of the yarn–matrix interface.

Overall, the findings support a staged carbonation and post-curing protection approach for yarn-reinforced cementitious composites. Carbonation curing can be first used to exploit yarn-enhanced carbonation rates and early-age strength development, after which post-curing interventions can be applied to restrict continued access to yarn-induced transport pathways. Although long-term durability is not evaluated in the present study,

the mechanisms identified here define clear priorities for future work, including extended exposure testing, wet–dry cycling, and assessment of fibre–matrix bond stability following post-curing protection treatments.

7.5. Conclusions

This chapter evaluated the hardened performance of natural fibre yarn–reinforced cementitious composites under carbonation curing, focusing on yarn arrangement and post-curing conditions. Paste-scale screening showed that yarn mesh geometry controls early-age compressive strength by governing fibre-induced heterogeneity, and that carbonation can compensate for this effect only within defined geometric limits. These mechanical trends were preserved when the selected configuration was transferred to mortar, supporting paste-scale screening as an effective method for identifying mechanically viable yarn arrangements.

Among the systems examined, saturated jute yarn reinforcement provided the most favourable mechanical performance under carbonation curing. The selected yarn mesh configuration remained mechanically robust when upscaled to mortar and outperformed mortars containing dispersed jute fibres at the same fibre volume fraction. The highest compressive strength was achieved after 7 days of carbonation curing followed by air curing to 28 days, reaching approximately 69 MPa and exceeding that of the continuously air-cured reference mortar. Compressive strength and sorptivity results further showed that yarn reinforcement altered moisture transport and increased sensitivity to subsequent water exposure. Air curing after carbonation preserved carbonation-induced densification and strength gains, whereas post-carbonation water curing led to strength reductions in fibre-containing mortars.

Overall, the results demonstrate that natural fibre yarn mesh–reinforced composites can be mechanically compatible with carbonation curing when yarn architecture and post-curing conditions are carefully controlled. The selected mesh configuration therefore provides a mechanically feasible basis for further development, but its effect on mortar-scale carbonation and CO_2 uptake remains to be verified directly.

Chapter 8 Conclusions and future work

8.1. Conclusions

This thesis investigated whether placed natural fibre yarns can function as internal transport modifiers to enhance CO_2 transport, carbonation extent, and CO_2 uptake during enforced carbonation curing, while maintaining acceptable hardened mechanical performance. The work addressed a clear gap in existing research, which has largely focused on surface-limited carbonation and short, dispersed fibres, rather than organised yarn architectures that provide continuous and spatially controlled internal transport pathways.

Single-yarn cement paste experiments demonstrated a substantial transport-mediated enhancement of carbonation under enforced curing conditions (~20 vol.% CO_2, 25 ± 0.5 °C, and 64 ± 2% relative humidity). All tested natural fibre yarns increased CO_2 uptake relative to fibre-free paste, with bast fibres showing the strongest effect. Hemp yarn increased the depth-profile averaged CO_2 uptake from 5.64 wt.% in the reference paste to 8.19 wt.% after seven days of carbonation and exhibited measurable uptake at 50 mm depth after only one day (0.432 wt.%). These results show that placed yarns modified the internal carbonation profile and extended CO_2 uptake into regions that remained only weakly carbonated in the fibre-free reference.

Mechanistic investigations using jute-based systems showed that yarn-assisted carbonation was governed by local moisture retention, pore connectivity, and interfacial transport rather than by fibre presence alone. Pre-saturation of yarns increased carbonation extent compared with oven-dried yarns, while epoxy sealing of the yarn–matrix region strongly reduced carbonation. This demonstrates that moisture availability and accessible gas exchange within the yarn–matrix region are both required to sustain the observed transport effect. Across yarn types and treatments, 24-hour water absorption

emerged as the strongest measured predictor of effective carbonation radius, linking yarn moisture-storage capacity with the extent of yarn-adjacent carbonation.

A methodological contribution of this thesis was the development and validation of a depth-resolved phenolphthalein-based image-analysis workflow for heterogeneous yarn-containing specimens. Comparison with TGA, QXRD, and FTIR showed that the image-derived carbonated area fraction captured chemically consistent changes in carbonation extent within the investigated dataset. The method also enabled the lateral influence of individual yarns to be quantified. At 10 mm depth, the effective carbonation radius was approximately 2–3 mm. Together with the observed relationship between effective carbonation radius and CO_2 uptake, this provides an initial quantitative basis for selecting yarn spacing in multi-yarn systems, suggesting that adjacent yarn-affected regions may begin to overlap when the spacing approaches twice the effective radius.

Bulk hydration measurements indicated that yarn inclusion at the investigated volume fractions had only a marginal influence on overall hydration kinetics and bulk phase development. Enhanced carbonation in moisture-retentive yarn systems could therefore not be attributed to accelerated bulk hydration and was instead associated primarily with local moisture redistribution and yarn-centred transport pathways.

Mechanical assessment showed that carbonation curing can be compatible with yarn reinforcement provided that yarn architecture, fibre volume fraction, and interface density are controlled. Paste-scale screening demonstrated that increasing fibre volume fraction generally reduced compressive strength due to fibre-induced heterogeneity and cumulative interfacial effects, with carbonation providing compensation only within a limited range. Guided by both mechanical trends and the effective carbonation radius, a single-layer mesh with 5 mm spacing (5–1L) was selected for upscaling, corresponding to a 2.28 vol.% replacement level in paste specimens.

At the mortar scale, early carbonation increased early-age strength across all mixes, while later-age performance depended strongly on post-curing conditions and fibre form. Saturated jute yarn mesh reinforcement provided the most favourable balance between carbonation response and compressive strength, outperforming dispersed jute fibres at the same replacement level. The most effective curing sequence consisted of seven days of carbonation followed by air curing to 28 days, achieving compressive strength of

approximately 69 MPa and exceeding that of the continuously air-cured reference mortar. In contrast, water curing after carbonation reduced strength in fibre-containing mortars, indicating that carbonation-induced densification is sensitive to post-carbonation moisture exposure.

The same continuous and porous yarn architecture that enhanced carbonation also introduced a potential service-life trade-off. Yarn-centred pore networks may facilitate later transport of liquid water and dissolved ions, while the absence of visible fibre degradation over 1–7 days does not establish long-term fibre or interface stability under sustained or cyclic moisture exposure. Treatments that strongly restrict yarn water uptake or seal the yarn–matrix interface before carbonation are therefore unsuitable when maximising yarn-assisted carbonation is the primary objective. A suitable initial route for evaluation is therefore to use the yarn network to support controlled carbonation during manufacture, followed by a verified protective strategy for service exposure. Proposed methods such as low-viscosity impregnation remain subjects for future testing rather than established protection strategies.

Overall, yarn-assisted carbonation should be regarded as a material-design strategy within controlled carbonation curing rather than as a stand-alone CO_2 sequestration technology. At the depth-profile scale examined in this thesis, the effect was substantial rather than marginal, as the yarns shifted carbonation from a mainly surface-controlled process towards a more distributed internal profile. However, the significance of this effect at product scale remains unquantified because whole-product CO_2 uptake was not measured. Initial product-scale evaluation should focus on controlled manufacturing conditions in which yarn position, moisture state, carbonation exposure and post-curing treatment can be systematically managed. On the evidence available, the material-scale mechanism is effective and mechanically feasible under selected laboratory conditions, but its practical viability remains unproven. Product-scale CO_2 uptake, long-term durability, manufacturing repeatability, process cost and net carbon benefit must be established before practical adoption can be justified.

8.2. Limitations

The scope of this doctoral research was deliberately defined to enable a mechanistic investigation of yarn-assisted carbonation in cementitious materials. While this focus

allowed clear interpretation of transport, reaction, and mechanical effects, it limits the generality and practical transferability of the findings.

The experimental strategy prioritised small-scale specimens and simplified yarn configurations to resolve depth-dependent behaviour with high spatial resolution. In addition, the experimental programme was restricted to a single Portland cement binder (CEM I), with a fixed water-to-cement ratio in paste studies and one mortar mix design at larger scale. This ensured internal consistency and enabled isolation of yarn-related effects, but the conclusions cannot be directly extended to systems with different water contents, aggregate volumes, chemical admixtures, or blended and low-clinker binders, where pore structure and carbonation behaviour may differ. Enforced carbonation curing was studied under a single, controlled regime with fixed CO_2 concentration, temperature, relative humidity under atmospheric pressure. The effects of lower CO_2 concentrations, fluctuating humidity, gas-flow rate, cyclic exposure, specimen preconditioning, and longer carbonation periods were not addressed. The tested condition therefore provides a consistent basis for mechanistic comparison rather than a complete industrial processing window. No coupled transport–reaction model was developed; consequently, the measured relationships remain empirical and cannot yet predict carbonation behaviour under different specimen geometries, material compositions, or exposure conditions.

The image-analysis method developed in Chapter 4 quantified heterogeneous carbonation from two-dimensional phenolphthalein-stained cross-sections and was supported through comparison with TGA, QXRD and FTIR. Because phenolphthalein records a pH transition rather than carbonate formation, the carbonated area fraction is a comparative spatial metric rather than an absolute measure of CO_2 storage. Neither these images nor the SEM–BSE pore-area measurements resolve three-dimensional pore connectivity, capillary continuity or gas transport along the full yarn length. The methods also represent different sampling scales: image masks preserve lateral variation across each disc cross-section, although the area fraction condenses this information into a single value; powder-based methods average material within the sampled disc or depth interval; and SEM–BSE represents selected local fields. Locally extensive carbonation may therefore be diluted in bulk or cross-sectionally averaged measurements. The effective carbonation radius of approximately 2–3 mm, typically determined at a depth of 10 mm, describes the lateral extent of yarn-associated carbonation only under the specimen geometry and curing conditions tested and should not be applied as a general yarn-spacing criterion without

validation across other binders, specimen dimensions, textile arrangements and carbonation regimes. Overall, these limitations restrict the interpretation of the image-derived metrics to comparative spatial assessment within the tested system.

The depth-profile mean reported in Chapter 5 was calculated from TGA measurements at six discrete sampling depths. After 7 days, it increased from 5.64 wt.% CO_2 in the reference paste to 8.19 wt.% in the hemp-containing paste, corresponding to a 45.1% relative increase. This value provides a comparative summary of the measured carbonation profile rather than a mass- or volume-weighted measure of whole-specimen uptake. The material between the sampled depths was not analysed, and equal weighting of the six measurements does not account for the amount of material represented by each location. In addition, each sampled disc was homogenised across its complete cross-section before TGA, combining the highly carbonated yarn-adjacent region with surrounding paste of lower carbonation extent. The disc-level measurements therefore likely understate the local increase around the yarn. Denser depth sampling, local microsampling, and whole-specimen carbonate or reactor mass-balance measurements would be required to quantify total CO_2 uptake and the local yarn-associated contribution more precisely.

Although several natural and synthetic yarns were screened in Chapter 5, the detailed mechanistic investigation in Chapter 6 focused mainly on jute. Natural fibres vary with plant source, growing conditions, extraction, spinning, ply structure, twist, diameter, and surface treatment. These sources of variation were not examined systematically, and only a limited range of yarn moisture states and coatings was tested. The relationships identified between water absorption, interfacial structure, moisture condition, and carbonation radius therefore apply to the investigated yarns rather than to natural fibre yarns in general. Hydration was also assessed mainly using bulk calorimetry and phase analysis. These methods may not fully resolve local hydration and carbonation reactions within narrow yarn-adjacent regions. The SEM–BSE analysis provides comparative two-dimensional pore-area fractions at selected locations rather than a complete pore-size distribution or direct measurement of gas and moisture transport.

The progression from paste to mortar in Chapter 7 was intended as an initial assessment of mechanical compatibility. Several yarn spacings and layer numbers were screened using small paste cubes, but only a single-layer saturated jute mesh with 5 mm in-plane

spacing was transferred to mortar. In addition, the single yarns used in the cylindrical paste specimens were placed under light longitudinal tension, whereas the yarn meshes were not tensioned in the same manner. Differences in yarn diameter, compactness, interfacial contact, and internal void structure may therefore limit direct transfer of the single-yarn transport mechanisms to mesh-reinforced specimens. The highest 28-day compressive strength of the yarn-reinforced mortar was 69.3 MPa after 7 days of carbonation followed by air curing, which exceeded that of the continuously air-cured reference mortar and showed that the selected configuration was mechanically compatible with this curing sequence. However, carbonation distribution, carbonate content, and CO_2 uptake were not measured directly in the mortar cubes. It is therefore not possible to determine whether the paste-scale increase in the depth-profile mean was retained at mortar scale or to calculate the additional CO_2 stored per unit volume of mortar.

Mechanical assessment focused mainly on compressive strength, with sorptivity used to examine capillary water uptake. Flexural and tensile behaviour, fracture energy, crack spacing, yarn pull-out resistance, fibre–matrix bond strength, shrinkage, creep, dimensional stability, and restrained cracking were not measured. The study therefore does not establish whether the yarn meshes provide effective structural reinforcement or crack control. Full-size casting, textile anchorage, curing uniformity, dimensional effects, and element-scale mechanical behaviour were also outside the experimental scope. Consequently, the findings do not establish suitability for façade panels, blocks, wall units, or other full-scale products.

Performance was assessed over relatively short periods. The absence of visible fibre degradation after up to 7 days of carbonation does not demonstrate long-term fibre or interface stability. Fibre-containing mortars were sensitive to post-carbonation water exposure, and yarn-adjacent pore networks may provide preferential pathways for moisture and dissolved ions. Long-term durability under sustained and cyclic environmental exposure, including the stability of the fibres, yarn–matrix interface and associated transport pathways, was not established. Application to systems containing conventional steel reinforcement would also require separate study because carbonation-induced alkalinity loss may conflict with the high-pH conditions required for steel passivation. The results should therefore not be extended directly to steel-reinforced structural elements.

Manufacturing scalability, economic feasibility, and net carbon benefit were not evaluated. Yarn preparation, water saturation, textile placement, dimensional control, carbonation-chamber operation, humidity regulation, cycle time, and any required post-curing protection would introduce additional material, energy, labour, and equipment demands. The study also did not measure production throughput, process cost, yarn supply consistency, gas-phase CO_2 conversion, or losses from the carbonation system. Emissions associated with yarn production and treatment, CO_2 supply, chamber operation, moisture control, and post-curing would need to be included in a full carbon balance or life-cycle assessment.

8.3. Recommendations for future work

Future work should progress from proof of the yarn-assisted transport mechanism towards product-scale validation under controlled manufacturing conditions. The main research question is whether the local increase in carbonation demonstrated in this thesis can produce a measurable whole-product benefit without unacceptable losses in mechanical performance, durability, production efficiency, or net carbon reduction.

A first priority is to establish whether the yarn-assisted transport mechanism remains effective across a wider material and yarn parameter space. Systematic variation of water-to-binder ratio, aggregate content, admixture use and workability should be combined with evaluation of blended and low-clinker binders, where differences in pore solution chemistry, buffering capacity and reaction products may alter carbonation behaviour. Statistically designed studies should separate the effects of fibre source, yarn diameter, compactness, ply count, twist, water absorption, surface condition and placement tension, and determine whether water absorption remains the principal controlling yarn property when geometric and manufacturing variables are considered. Textile development should initially optimise the selected two-dimensional mesh by varying yarn spacing, layer spacing, stacking pattern and through-thickness connections before progressing to more complex three-dimensional systems. The effect of controlled pre-tension should also be examined because tension modifies yarn diameter, compactness, internal void structure and matrix contact. These studies would clarify whether the effective carbonation radius identified for single yarns remains a useful design parameter when multiple yarn-affected regions overlap and when the system is transferred from tensioned single yarns to mesh reinforcement.

The carbonation regime should be expanded from the single controlled condition investigated here to a defined processing window covering CO_2 concentration, relative humidity, temperature, gas flow, exposure duration and curing sequence, including conditions representative of flue-gas carbonation. Particular attention should be given to conditions that sustain CO_2 ingress at depth without excessive near-surface densification. Intermediate moisture adjustment and cyclic carbonation should be examined separately from post-carbonation water curing, which reduced strength in the fibre-containing mortars. These experiments should support development of a coupled moisture–CO_2 transport and reaction model incorporating yarn moisture sorption and release, gas transport through yarn and interfacial regions, CO_2 dissolution and reaction, reaction-water generation, and transport restriction caused by carbonate precipitation. Calibration against depth-resolved TGA and image-analysis data would allow surface ingress and yarn-assisted transport to be separated, while sensitivity analysis could identify the yarn, matrix and exposure parameters controlling whole-element behaviour.

Direct measurement of whole-product CO_2 uptake should form the central next stage of validation. Initial studies should focus on thin, factory-produced, non-steel-reinforced mortar or concrete elements in which yarn placement, moisture conditioning, gas exposure and post-curing storage can be controlled. Complete-specimen carbonate analysis should be combined with inlet–outlet gas monitoring, leakage correction and measurement of chamber losses, and the additional CO_2 retained should be reported as kg CO_2 m^{-3} of product and kg CO_2 t^{-1} of binder together with the absolute and relative difference from equivalent fibre-free controls. Product-scale studies should vary element thickness, exposed surface area, aggregate content, yarn spacing and layer arrangement, gas-flow rate and curing duration. Carbonation distribution and CO_2 uptake should be measured directly rather than inferred from compressive strength, and should be linked to mechanical and transport measurements on equivalent specimens. This would determine whether the paste-scale transport effect is retained following aggregate addition and increases in element size, and how the balance between yarn-assisted ingress, surface carbonation and pore blocking changes with specimen geometry.

Spatial characterisation should also be strengthened to resolve the continuous moisture and gas pathways associated with yarns, particularly in mesh and multilayer systems. Sampling locations should be aligned across image analysis, TGA, XRD, FTIR and

SEM–BSE, with finer depth intervals where steep carbonation gradients occur. Local micro-sampling or chemical mapping should distinguish yarn-adjacent paste from the surrounding matrix rather than homogenising the complete cross-section, allowing local carbonate distribution, phase assemblage and C–S–H composition, including Ca/Si ratio, to be quantified and related to local pore structure. Three-dimensional approaches such as serial sectioning or suitable tomographic methods could further resolve pathway continuity along yarn length. The image-analysis workflow should also be validated using independently prepared specimens, different operators, imaging sessions, binders and staining conditions, with uncertainty reported for segmentation, disc position, sampling volume and analytical resolution. Coupling TGA with evolved gas analysis would additionally help resolve the poorly crystalline or amorphous carbonate response identified near the exposed surface.

Following optimisation of yarn and mesh geometry, mechanical assessment should extend beyond compressive strength to flexural and tensile response, fracture energy, crack spacing and width, yarn pull-out and interfacial shear behaviour. Fresh-state placement, dimensional stability, shrinkage, restrained cracking and element-scale failure should also be assessed using larger specimens and adequate replicate numbers, with appropriate statistical analysis used to distinguish meaningful differences from specimen variability. Relating these properties directly to measured carbonation distributions would establish whether the yarns act primarily as transport modifiers or also provide useful reinforcement.

Durability studies should determine whether yarn-associated regions remain preferential pathways for liquid water and dissolved ions after carbonation curing. Sustained water exposure, wet–dry cycling, chloride ingress and, where relevant, freeze–thaw exposure should be combined with repeated examination of the yarn–matrix interface. Long-term fibre swelling and shrinkage, mineralisation, biological degradation, bond loss and changes in pathway connectivity should be monitored to distinguish carbonation-induced matrix refinement from potentially adverse continued liquid and ionic transport. Systems containing steel reinforcement would require separate assessment of alkalinity loss, steel passivation and corrosion risk. Where persistent yarn-associated transport is confirmed, post-curing protection should be investigated using conventional surface treatments and low-viscosity systems capable of entering yarn-adjacent pore networks. Their penetration depth, effects on water and chloride transport, fibre–matrix bond, vapour transport,

dimensional stability, repairability and recycling should be assessed using untreated carbonated specimens and fibre-free treated controls. Durability performance should be assessed against predefined acceptance criteria based on retention of mechanical performance, control of water and ionic transport, stability of the yarn–matrix interface and, where steel is present, maintenance of adequate passivation and corrosion resistance relative to appropriate fibre-free controls. Treatment quantity, application energy, maintenance frequency and effects on service life should also be recorded for subsequent environmental and economic assessment.

Product development should then progress from whole-specimen laboratory validation to repeated pilot-scale manufacture and long-term exposure of representative elements. Manufacturing trials should quantify yarn displacement, mesh deformation, air entrapment, placement tolerance, compaction quality and differences between nominal and achieved yarn positions, together with cycle time, yarn-conditioning and placement requirements, rejection rate, curing uniformity, process energy, CO_2 consumption and batch-to-batch variability in uptake. This would establish whether the placement and curing control achieved in laboratory specimens can be reproduced during repeated manufacture and whether the resulting product benefit is consistent.

Finally, the system-level value of yarn-assisted carbonation should be assessed using life-cycle assessment and techno-economic analysis. These should account for CO_2 supply and handling, curing-chamber operation, humidity control, cycle time, textile placement, post-curing protection, maintenance and measured service life. The carbon benefit should be reported before and after these inputs are included and should account for gas losses. Performance should be benchmarked against alternative decarbonisation strategies, including conventional carbonation curing, increased use of supplementary cementitious materials and alternative reinforcement approaches. Relevant decision metrics should include net kg CO_2-equivalent reduction per m^3 of product, additional CO_2 retained per tonne of binder, energy and cost per kg of CO_2 retained, production throughput and durability performance. Yarn-assisted carbonation should only be considered technically and environmentally viable if its additional whole-product uptake and service performance outweigh the emissions, costs and durability risks introduced by the yarn and associated processing requirements.

References

Abdalla, J.A., Hawileh, R.A., Bahurudeen, A., Jyothsna, G., Sofi, A., Shanmugam, V. and Thomas, B.S. (2023) A comprehensive review on the use of natural fibers in cement/geopolymer concrete: a step towards sustainability. *Case Studies in Construction Materials*. 19, e02244. https://doi.org/10.1016/j.cscm.2023.e02244.

Addis, L.B., Sendekie, Z.B. and Satheesh, N. (2022) Degradation kinetics and durability enhancement strategies of cellulosic fiber-reinforced geopolymers and cement composites. *Advances in Materials Science and Engineering*. 2022(1), 1981755. https://doi.org/10.1155/2022/1981755.

Adresi, M., Yamani, A., Karimaei Tabarestani, M. and Rooholamini, H. (2023) A comprehensive review on pervious concrete. *Construction and Building Materials*. 407, 133308. https://doi.org/10.1016/j.conbuildmat.2023.133308.

Affan, M. and Ali, M. (2022) Experimental investigation on mechanical properties of jute fiber reinforced concrete under freeze–thaw conditions for pavement applications. *Construction and Building Materials*. 323, 126599. https://doi.org/10.1016/j.conbuildmat.2022.126599.

Ahmad, J., Arbili, M.M., Majdi, A., Althoey, F., Deifalla, A.F. and Rahmawati, C. (2022) Performance of concrete reinforced with jute fibers (natural fibers): a review. *Journal of Engineered Fibers and Fabrics*. 17, 1–17. https://doi.org/10.1177/15589250221121871.

AL-Ameeri, A.S., Rafiq, M.I., Tsioulou, O. and Rybdylova, O. (2021) Impact of climate change on the carbonation in concrete due to carbon dioxide ingress: experimental investigation and modelling. *Journal of Building Engineering*. 44, 102594. https://doi.org/10.1016/j.jobe.2021.102594.

Alapati, P. and Kurtis, K.E. (2018) Carbonation in alternative cementitious materials: implications on durability and mechanical properties. In: *Proceedings of the Sixth International Conference on Durability of Concrete Structures*. Leeds, United Kingdom. 18–20 July 2018. Paper No. ICC02. Leeds: University of Leeds.

Alatawna, A., Nahum, L., Sripada, R., Birenboim, M., Regev, O. and Peled, A. (2022) Textile-reinforced mortar: durability in salty environment. *Cement and Concrete Composites*. 130, 104534. https://doi.org/10.1016/j.cemconcomp.2022.104534.

Alma'aitah, M., Ghiassi, B. and Dalalbashi, A. (2021) Durability of textile reinforced concrete: existing knowledge and current gaps. *Applied Sciences*. 11(6), 2771. https://doi.org/10.3390/app11062771.

Al-Mamoori, A., Krishnamurthy, A., Rownaghi, A.A. and Rezaei, F. (2017) Carbon capture and utilization update. *Energy Technology*. 5(6), pp. 834–849. https://doi.org/10.1002/ente.201600747.

Almeida, A.E.F.S., Tonoli, G.H.D., Santos, S.F. and Savastano, H. (2013) Improved durability of vegetable fiber reinforced cement composite subject to accelerated carbonation at early age. *Cement and Concrete Composites*. 42, pp. 49–58. https://doi.org/10.1016/j.cemconcomp.2013.05.001.

AlMuhanna, M., AlSenan, R., Mustafaraj, E., Luga, E. and Corradi, M. (2024) Fibre reinforcement of cement mortars for reinforcement of masonry buildings: an experimental investigation. *Journal of Building Pathology and Rehabilitation*. 9(2), 142. https://doi.org/10.1007/s41024-024-00498-0.

Alyousef, R., Alabduljabbar, H., Mohammadhosseini, H., Mohamed, A.M., Siddika, A., Alrshoudi, F. and Alaskar, A. (2020) Utilization of sheep wool as potential fibrous materials in the production of concrete composites. *Journal of Building Engineering*. 30, 101216. https://doi.org/10.1016/j.jobe.2020.101216.

Anstice, D.J., Page, C.L. and Page, M.M. (2005) The pore solution phase of carbonated cement pastes. *Cement and Concrete Research*. 35(2), pp. 377–383. https://doi.org/10.1016/j.cemconres.2004.06.041.

Ashraf, W. (2016) Carbonation of cement-based materials: challenges and opportunities. *Construction and Building Materials*. 120, pp. 558–570. https://doi.org/10.1016/j.conbuildmat.2016.05.080.

Ashraf, W., Olek, J. and Atakan, V. (2016) Carbonation reaction kinetics, CO_2 sequestration capacity, and microstructure of hydraulic and non-hydraulic cementitious binders. In: *Proceedings of the Fourth International Conference on Sustainable Construction Materials and Technologies*. Las Vegas, United States. 7 August 2016. pp. 1075–1084. https://doi.org/10.18552/2016/scmt4s303.

ASTM International (2020) *ASTM C1585-20: Standard test method for measurement of rate of absorption of water by hydraulic-cement concretes*. West Conshohocken, PA: ASTM International. https://doi.org/10.1520/C1585-20.

ASTM International (2022) *ASTM C128-22: Standard test method for relative density (specific gravity) and absorption of fine aggregate*. West Conshohocken, PA: ASTM International. https://doi.org/10.1520/C0128-22.

Aybar, K. (2025) Development of a flexible, shape-adaptive and waterproof cementitious composite reinforced with 3D textile. *Brilliant Engineering*. 6(3), pp. 1–8. https://doi.org/10.36937/ben.2025.41049.

Aziz, M.A., Paramasivam, P. and Lee, S.L. (1981) Prospects for natural fibre reinforced concretes in construction. *International Journal of Cement Composites and Lightweight Concrete*. 3(2), 123–132. https://doi.org/10.1016/0262-5075(81)90006-3.

Balea, A., Fuente, E., Monte, M.C., Blanco, Á. and Negro, C. (2021) Fiber reinforced cement based composites. In: *Fiber reinforced composites*. Cambridge: Woodhead Publishing, pp. 597–648. https://doi.org/10.1016/b978-0-12-821090-1.00019-3.

Baltazar-y-Jimenez, A. and Bismarck, A. (2007) Wetting behaviour, moisture uptake and electrokinetic properties of lignocellulosic fibres. *Cellulose*. 14(2), pp. 115–127. https://doi.org/10.1007/s10570-006-9092-x.

Batis, G., Pantazopoulou, P. and Routoulas, A. (2003) Corrosion protection investigation of reinforcement by inorganic coating in the presence of alkanolamine-based inhibitor. *Cement and Concrete Composites*. 25(3), pp. 371–377. https://doi.org/10.1016/s0958-9465(02)00061-6.

Belda Revert, A., De Weerdt, K., Hornbostel, K. and Geiker, M.R. (2018) Carbonation-induced corrosion: investigation of the corrosion onset. *Construction and Building Materials*. 162, pp. 847–856. https://doi.org/10.1016/j.conbuildmat.2017.12.066.

Berger, R.L., Young, J.F. and Leung, K. (1972) Acceleration of hydration of calcium silicates by carbon dioxide treatment. *Nature Physical Science*. 240(97), pp. 16–18. https://doi.org/10.1038/physci240016a0.

Bernal, S.A., Provis, J.L., Brice, D.G., Kilcullen, A., Duxson, P. and van Deventer, J.S.J. (2012) Accelerated carbonation testing of alkali-activated binders significantly underestimates service life: the role of pore solution chemistry. *Cement and Concrete Research*. 42(10), pp. 1317–1326. https://doi.org/10.1016/j.cemconres.2012.07.002.

Bhat, P.A. and Debnath, N.C. (2011) Theoretical and experimental study of structures and properties of cement paste: the nanostructural aspects of C–S–H. *Journal of Physics and Chemistry of Solids*. 72(8), pp. 920–933. https://doi.org/10.1016/j.jpcs.2011.05.001.

Bhattacharyya, D., Subasinghe, A. and Kim, N.K. (2015) Natural fibers: their composites and flammability characterizations. In: *Multifunctionality of polymer composites: challenges and new solutions*. Oxford: William Andrew Publishing, pp. 102–143. https://doi.org/10.1016/b978-0-323-26434-1.00004-0.

Booya, E., Gorospe, K., Ghaednia, H. and Das, S. (2019) Durability properties of engineered pulp fibre reinforced concretes made with and without supplementary cementitious materials. *Composites Part B: Engineering*. 172, pp. 376–386. https://doi.org/10.1016/j.compositesb.2019.05.070.

British Standards Institution (2016) *BS EN 196-1:2016. Methods of testing cement. Determination of strength*. London: BSI. https://doi.org/10.3403/30291447.

British Standards Institution (2019) *BS EN 196-11. Methods of testing cement. Heat of hydration. Isothermal conduction calorimetry method*. London: BSI. https://doi.org/10.3403/30361319u.

British Standards Institution (1999) *BS EN ISO 62. Plastics. Determination of water absorption*. London: BSI. https://doi.org/10.3403/01668657.

British Standards Institution (2020) *BS EN 12390-12:2020. Testing hardened concrete. Determination of the carbonation resistance of concrete. Accelerated carbonation method*. London: BSI.

Bui, H., Boutouil, M., Levacher, D. and Sebaibi, N. (2021) Evaluation of the influence of accelerated carbonation on the microstructure and mechanical characteristics of coconut fibre-reinforced cementitious matrix. *Journal of Building Engineering*. 39, 102269. https://doi.org/10.1016/j.jobe.2021.102269.

Camargo, M.M., Taye, E.A., Roether, J.A., Redda, D.T. and Boccaccini, A.R. (2020) A review on natural fiber-reinforced geopolymer and cement-based composites. *Materials*. 13(20), pp. 1–29. https://doi.org/10.3390/ma13204603.

Castellote, M., Andrade, C., Turrillas, X., Campo, J. and Cuello, G.J. (2008) Accelerated carbonation of cement pastes in situ monitored by neutron diffraction. *Cement and Concrete Research*. 38(12), pp. 1365–1373. https://doi.org/10.1016/j.cemconres.2008.07.002.

Chand, N. and Fahim, M. (2008) Cotton reinforced polymer composites. In: *Tribology of natural fiber polymer composites*. 2nd edn. Duxford: Woodhead Publishing, pp. 129–161. https://doi.org/10.1533/9781845695057.129.

Chang, C.F. and Chen, J.W. (2006) The experimental investigation of concrete carbonation depth. *Cement and Concrete Research*. 36(9), pp. 1760–1767. https://doi.org/10.1016/j.cemconres.2004.07.025.

Charitha, V., Athira, G., Bahurudeen, A. and Shekhar, S. (2022) Carbonation of alkali activated binders and comparison with the performance of ordinary Portland cement and blended cement binders. *Journal of Building Engineering*. 53, 104513. https://doi.org/10.1016/j.jobe.2022.104513.

Chen, L., Chen, Z., Xie, Z., Wei, L., Hua, J., Huang, L. and Yap, P.S. (2023) Recent developments on natural fiber concrete: a review of properties, sustainability, applications, barriers, and opportunities. *Developments in the Built Environment*. 16, 100255. https://doi.org/10.1016/j.dibe.2023.100255.

Chen, T. and Gao, X. (2019) Effect of carbonation curing regime on strength and microstructure of Portland cement paste. *Journal of CO_2 Utilization*. 34, pp. 74–86. https://doi.org/10.1016/j.jcou.2019.05.034.

Chen, T. and Gao, X. (2020) Use of carbonation curing to improve mechanical strength and durability of pervious concrete. *ACS Sustainable Chemistry and Engineering*. 8(9), pp. 3872–3884. https://doi.org/10.1021/acssuschemeng.9b07348.

Chen, T., Gao, X. and Qin, L. (2019) Mathematical modelling of accelerated carbonation curing of Portland cement paste at early age. *Cement and Concrete Research*. 120, pp. 187–197. https://doi.org/10.1016/j.cemconres.2019.03.025.

Chen, X., Li, S., Hu, M., Geng, Y., Meng, S., Jin, L., Hu, Q. and Han, S. (2024) Early age accelerated carbonation of cementitious materials surface in low CO_2 concentration condition. *Construction and Building Materials*. 445, 137975. https://doi.org/10.1016/j.conbuildmat.2024.137975.

Choi, J.I., Lee, Y., Kim, Y.Y. and Lee, B.Y. (2017) Image-processing technique to detect carbonation regions of concrete sprayed with a phenolphthalein solution. *Construction and Building Materials*. 154, pp. 451–461. https://doi.org/10.1016/j.conbuildmat.2017.07.205.

Choi, Y.C. (2022) Hydration and internal curing properties of plant-based natural fiber-reinforced cement composites. *Case Studies in Construction Materials*. 17, e01690. https://doi.org/10.1016/j.cscm.2022.e01690.

Chu, D.C., Kleib, J., Amar, M., Benzerzour, M. and Abriak, N.-E. (2021) Determination of the degree of hydration of Portland cement using three different approaches: scanning electron microscopy (SEM-BSE) and thermogravimetric analysis (TGA). *Case Studies in Construction Materials*. 15, e00754. https://doi.org/10.1016/j.cscm.2021.e00754.

Chu, S., Rashid, R.T., Pan, Y., Wang, X., Zhang, H. and Xiao, R. (2022) The impact of flue gas impurities and concentrations on the photoelectrochemical CO_2 reduction. *Journal of CO_2 Utilization*. 60, 101993. https://doi.org/10.1016/j.jcou.2022.101993.

Codispoti, R., Oliveira, D.V., Olivito, R.S., Lourenço, P.B. and Fangueiro, R. (2015) Mechanical performance of natural fiber-reinforced composites for the strengthening of masonry. *Composites Part B: Engineering*. 77, pp. 74–83. https://doi.org/10.1016/j.compositesb.2015.03.021.

Cottrell, J.A., Ali, M., Tatari, A. and Martinson, D.B. (2023) Effects of fibre moisture content on the mechanical properties of jute reinforced compressed earth composites. *Construction and Building Materials*. 373, 130848. https://doi.org/10.1016/j.conbuildmat.2023.130848.

Curosu, I., Liebscher, M., Burk, S., Li, H., Hempel, S., Raak, N., Rohm, H. and Mechtcherine, V. (2021) Influence of fiber type on the tensile behavior of high-strength strain-hardening cement-based composites (SHCC) at elevated temperatures. *Materials and Design*. 198, 109397. https://doi.org/10.1016/j.matdes.2020.109397.

Dixit, A., Du, H. and Pang, S.D. (2021) Carbon capture in ultra-high performance concrete using pressurized CO_2 curing. *Construction and Building Materials*. 288, 123076. https://doi.org/10.1016/j.conbuildmat.2021.123076.

Driver, J.G., Bernard, E., Patrizio, P., Fennell, P.S., Scrivener, K. and Myers, R.J. (2024) Global decarbonization potential of CO_2 mineralization in concrete materials. *Proceedings of the National Academy of Sciences of the United States of America*. 121(29), e2313475121. https://doi.org/10.1073/pnas.2313475121.

Dudi, L. and Bishnoi, S. (2024) Assessment of carbonation and corrosion in a 50-year-old reinforced concrete building. *Materials and Structures*. 57(9), 203. https://doi.org/10.1617/s11527-024-02487-8.

El-Hassan, H., Shao, Y. and Ghouleh, Z. (2013) Effect of initial curing on carbonation of lightweight concrete masonry units. *ACI Materials Journal*. 110(4), pp. 441–450. https://doi.org/10.14359/51685791.

Ellingboe, E., Arehart, J.H. and Srubar, W.V. (2019) On the theoretical CO_2 sequestration potential of pervious concrete. *Infrastructures*. 4(1), 12. https://doi.org/10.3390/infrastructures4010012.

Ernest, E.M. and Peter, A.C. (2022) Application of selected chemical modification agents on banana fibre for enhanced composite production. *Cleaner Materials*. 5, 100131. https://doi.org/10.1016/j.clema.2022.100131.

Famy, C., Scrivener, K.L. and Crumbie, A.K. (2002) What causes differences of C–S–H gel grey levels in backscattered electron images? *Cement and Concrete Research*. 32(9), pp. 1465–1471. https://doi.org/10.1016/s0008-8846(02)00808-6.

Fantilli, A.P. and Jóźwiak-Niedźwiedzka, D. (2021) Influence of Portland cement alkalinity on wool-reinforced mortar. *Proceedings of the Institution of Civil Engineers: Construction Materials*. 174(3), pp. 172–181. https://doi.org/10.1680/jcoma.20.00003.

Fantilli, A.P., Sicardi, S. and Dotti, F. (2017) The use of wool as fiber-reinforcement in cement-based mortar. *Construction and Building Materials*. 139, pp. 562–569. https://doi.org/10.1016/j.conbuildmat.2016.10.096.

Farooqi, M.U. and Ali, M. (2023) A study on natural fibre reinforced concrete from materials to structural applications. *Arabian Journal for Science and Engineering*. 48(4), pp. 4471–4491. https://doi.org/10.1007/s13369-022-06977-1.

Fei, M., Fu, W., Zheng, X., Chen, Y., Liu, W. and Qiu, R. (2024) Enhancing cement composite interface with waterglass modification on bamboo fiber: a viable and effective approach. *Construction and Building Materials*. 411, 134338. https://doi.org/10.1016/j.conbuildmat.2023.134338.

de Felice, G., D'Antino, T., De Santis, S., Meriggi, P. and Roscini, F. (2020) Lessons learned on the tensile and bond behavior of fabric reinforced cementitious matrix (FRCM) composites. *Frontiers in Built Environment*. 6, 5. https://doi.org/10.3389/fbuil.2020.00005.

Feng, S., Lyu, J., Xiao, H. and Feng, J. (2023) Application of cellulose fibre in ultra-high-performance concrete to mitigate autogenous shrinkage. *Journal of Sustainable Cement-Based Materials*. 12(7), pp. 842–855. https://doi.org/10.1080/21650373.2022.2119618.

Fernández Bertos, M., Simons, S.J.R., Hills, C.D. and Carey, P.J. (2004) A review of accelerated carbonation technology in the treatment of cement-based materials and sequestration of CO_2. *Journal of Hazardous Materials*. 112(3), pp. 193–205. https://doi.org/10.1016/j.jhazmat.2004.04.019.

Filomeno, R.H., Fioroni, C.A., Azevedo, A.G.S. and Savastano, H. (2023) Influence of different curing regimes and accelerated carbonation on the physical, mechanical, and

aging performances of fiber cement. *Journal of Building Engineering*. 78, 107791. https://doi.org/10.1016/j.jobe.2023.107791.

Filomeno, R.H., Rodier, L.B., Ballesteros, J.E.M., Rossignolo, J.A. and Savastano, H. (2020) Optimizing the modified atmosphere parameters in the carbonation process for improved fiber-cement performance. *Journal of Building Engineering*. 32, 101676. https://doi.org/10.1016/j.jobe.2020.101676.

Frías, M., de la Villa, R.V., García, R., Rodríguez, O., Fernández-Carrasco, L. and Martínez-Ramírez, S. (2018) Carbonation-induced mineralogical changes in coal mining waste blended cement pastes and their influence on mechanical and microporosity properties. *Minerals*. 8(4), 169. https://doi.org/10.3390/min8040169.

Geremew, A., De Winne, P., Demissie, T.A. and De Backer, H. (2021) Treatment of natural fiber for application in concrete pavement. *Advances in Civil Engineering*. 2021(1), 6667965. https://doi.org/10.1155/2021/6667965.

Ghiassi, B. (2019) Mechanics and durability of lime-based textile reinforced mortars. *RILEM Technical Letters*. 4, pp. 130–137. https://doi.org/10.21809/rilemtechlett.2019.99.

Giddey, S., Badwal, S.P.S., Kulkarni, A. and Munnings, C. (2012) A comprehensive review of direct carbon fuel cell technology. *Progress in Energy and Combustion Science*. 38(3), pp. 360–399. https://doi.org/10.1016/j.pecs.2012.01.003.

Gielis, C., El Kadi, M., Snoeck, D. and Tysmans, T. (2024) 3D textile reinforced cement (TRC) composites with integrated synthetic microfibres: evaluation of mechanical response and crack formation in bending. *Construction and Building Materials*. 426, 136120. https://doi.org/10.1016/j.conbuildmat.2024.136120.

Giulietti, N., Chiariotti, P., Cosoli, G., Mobili, A., Pandarese, G., Tittarelli, F. and Revel, G.M. (2021) Automated measurement system for detecting carbonation depth: image-processing based technique applied to concrete sprayed with phenolphthalein. *Measurement*. 175, 109142. https://doi.org/10.1016/j.measurement.2021.109142.

von Greve-Dierfeld, S., Lothenbach, B., Vollpracht, A., Wu, B., Huet, B., et al. (2020) Understanding the carbonation of concrete with supplementary cementitious materials: a critical review by RILEM TC 281-CCC. *Materials and Structures*. 53(6), 136. https://doi.org/10.1617/s11527-020-01558-w.

Groves, G.W., Rodway, D.I. and Richardson, I.G. (1990) The carbonation of hardened cement pastes. *Advances in Cement Research*. 3(11), pp. 117–125. https://doi.org/10.1680/adcr.1990.3.11.117.

Guan, Q., Ma, Y., Jin, M., Zeng, H., Gao, C., Tang, J., Liu, J., Han, F., Li, W. and Liu, J. (2024) Carbonation curing of belite-rich cement: the role of fly ash and strengthening mechanism. *Cement and Concrete Composites*. 149, 105530. https://doi.org/10.1016/j.cemconcomp.2024.105530.

Guo, R., Wang, J., Bing, L., Tong, D., Ciais, P., Davis, S.J., Andrew, R.M., Xi, F. and Liu, Z. (2021) Global CO_2 uptake by cement from 1930 to 2019. *Earth System Science Data*. 13(4), pp. 1791–1805. https://doi.org/10.5194/essd-13-1791-2021.

Gwon, S., Choi, Y.C. and Shin, M. (2021) Effect of plant cellulose microfibers on hydration of cement composites. *Construction and Building Materials*. 267, 121734. https://doi.org/10.1016/j.conbuildmat.2020.121734.

Hamada, H.M., Shi, J., Al Jawahery, M.S., Majdi, A., Yousif, S.T. and Kaplan, G. (2023) Application of natural fibres in cement concrete: a critical review. *Materials Today Communications*. 35, 105833. https://doi.org/10.1016/j.mtcomm.2023.105833.

Hay, R., Krishnan, P. and Celik, K. (2024) Influence of natural fibers on hydration and carbonation of reactive magnesium oxide cement (RMC). *Construction and Building Materials*. 411, 134653. https://doi.org/10.1016/j.conbuildmat.2023.134653.

He, P., Shi, C. and Poon, C.S. (2018) Methods for the assessment of carbon dioxide absorbed by cementitious materials. In: *Carbon dioxide sequestration in cementitious construction materials*. Cambridge: Woodhead Publishing, pp. 103–126. https://doi.org/10.1016/b978-0-08-102444-7.00006-x.

He, P., Shi, C., Tu, Z., Poon, C.S. and Zhang, J. (2016) Effect of further water curing on compressive strength and microstructure of CO_2-cured concrete. *Cement and Concrete Composites*. 72, pp. 80–88. https://doi.org/10.1016/j.cemconcomp.2016.05.026.

He, Z., Wang, S., Mahoutian, M. and Shao, Y. (2020) Flue gas carbonation of cement-based building products. *Journal of CO_2 Utilization*. 37, pp. 309–319. https://doi.org/10.1016/j.jcou.2020.01.001.

Van den Heede, P., De Schepper, M. and De Belie, N. (2019) Accelerated and natural carbonation of concrete with high volumes of fly ash: chemical, mineralogical and microstructural effects. *Royal Society Open Science*. 6(1), 181665. https://doi.org/10.1098/rsos.181665.

Heinz, D. and Urbonas, L. (2016) Modification of cementitious building materials by treatment with CO_2. *Chemical Technology*. 67(1), pp. 46–52. https://doi.org/10.5755/j01.ct.67.1.15823.

Higuchi, T., Morioka, M., Yoshioka, I. and Yokozeki, K. (2014) Development of a new ecological concrete with CO_2 emissions below zero. *Construction and Building Materials*. 67(Part C), pp. 338–343. https://doi.org/10.1016/j.conbuildmat.2014.01.029.

Hou, M. and Li, V.C. (2023) Crack width control of LC3-based engineered cementitious composites (ECC) via fiber hybridization: from micromechanics design to macro investigation. *Materials and Design*. 235, 112433. https://doi.org/10.1016/j.matdes.2023.112433.

Hu, W.H., Zhang, D., Ftwi, E., Ellis, B.R. and Li, V.C. (2023) Development of sustainable low carbon engineered cementitious composites with waste polyethylene fiber, sisal fiber and carbonation curing. *Resources, Conservation and Recycling*. 197, 107096. https://doi.org/10.1016/j.resconrec.2023.107096.

Huang, J., Chen, Y. and Yu, Q. (2025) Amorphous calcium carbonate formation from carbonated recycled cement powder: a novel carbonation-activated cementitious material. *Composites Part B: Engineering*. 297, 112336. https://doi.org/10.1016/j.compositesb.2025.112336.

Hubler, M.H., Wendner, R. and Bažant, Z.P. (2015) A comparison of methods for determining carbonation depth in fly ash-blended cement mortars. *ACI Materials Journal*. 112(2), pp. 287–294. https://doi.org/10.14359/51687452.

International Energy Agency (2021) *Cement tracking report*. Available at: https://iea.blob.core.windows.net/assets/cbaa3da1-fd61-4c2a-8719-31538f59b54f/TechnologyRoadmapLowCarbonTransitionintheCementIndustry.pdf (Accessed: 24 February 2024).

Intergovernmental Panel on Climate Change (2005) *IPCC special report on carbon dioxide capture and storage*. Cambridge: Cambridge University Press.

Intergovernmental Panel on Climate Change (2021) *Climate change 2021: mitigation of climate change*. Cambridge: Cambridge University Press. Available at: https://www.ipcc.ch/site/assets/uploads/2018/05/uncertainty-guidance-note.pdf (Accessed: 24 February 2024).

Islam, M.S. and Ahmed, S.J. (2018) Influence of jute fiber on concrete properties. *Construction and Building Materials*. 189, pp. 768–776. https://doi.org/10.1016/j.conbuildmat.2018.09.048.

Jamshaid, H., Mishra, R.K., Raza, A., Hussain, U., Rahman, M.L., Nazari, S., Chandan, V., Muller, M. and Choteborsky, R. (2022) Natural cellulosic fiber reinforced concrete: influence of fiber type and loading percentage on mechanical and water absorption performance. *Materials*. 15(3), 874. https://doi.org/10.3390/ma15030874.

Jang, D., Yoon, H.N., Seo, J., Yang, B., Jang, J.G. and Park, S. (2023) Effect of carbonation curing regime on electric heating performance of CNT/cement composites. *Journal of Building Engineering*. 73, 106815. https://doi.org/10.1016/j.jobe.2023.106815.

Jang, J.G., Kim, G.M., Kim, H.J. and Lee, H.K. (2016) Review on recent advances in CO_2 utilization and sequestration technologies in cement-based materials. *Construction and Building Materials*. 127, pp. 762–773. https://doi.org/10.1016/j.conbuildmat.2016.10.017.

Jang, J.G. and Lee, H.K. (2016) Microstructural densification and CO_2 uptake promoted by the carbonation curing of belite-rich Portland cement. *Cement and Concrete Research*. 82, pp. 50–57. https://doi.org/10.1016/j.cemconres.2016.01.001.

Jeon, I.K., Qudoos, A. and Kim, H.G. (2021) Influence of carbonation curing on hydration and microstructure of magnesium potassium phosphate cement concrete. *Journal of Building Engineering*. 38, 102203. https://doi.org/10.1016/j.jobe.2021.102203.

Ji, L. and Yu, H. (2018) Carbon dioxide sequestration by direct mineralization of fly ash. In: *Carbon dioxide sequestration in cementitious construction materials*. Cambridge: Woodhead Publishing, pp. 13–37. https://doi.org/10.1016/b978-0-08-102444-7.00002-2.

Jongvisuttisun, P., Leisen, J. and Kurtis, K.E. (2018) Key mechanisms controlling internal curing performance of natural fibers. *Cement and Concrete Research*. 107, pp. 206–220. https://doi.org/10.1016/j.cemconres.2018.02.007.

Jongvisuttisun, P., Negrello, C. and Kurtis, K.E. (2013) Effect of processing variables on efficiency of eucalyptus pulps for internal curing. *Cement and Concrete Composites*. 37(1), pp. 126–135. https://doi.org/10.1016/j.cemconcomp.2012.11.006.

Jóźwiak-Niedźwiedzka, D. and Fantilli, A.P. (2020) Wool-reinforced cement based composites. *Materials*. 13(16), 3590. https://doi.org/10.3390/ma13163590.

Kashef-Haghighi, S. and Ghoshal, S. (2010) CO_2 sequestration in concrete through accelerated carbonation curing in a flow-through reactor. *Industrial and Engineering Chemistry Research*. 49(3), pp. 1143–1149. https://doi.org/10.1021/ie900703d.

Kim, H., Siddique, S. and Jang, J.G. (2022) Effect of carbonation curing on the mechanical properties of belite-rich cement mortar exposed to elevated temperatures. *Journal of Building Engineering*. 52, 104453. https://doi.org/10.1016/j.jobe.2022.104453.

Kim, W.K., Lee, J., Park, J. and Moon, J. (2024) Carbon sequestration in cementitious systems through CO_2-rich hydration and chemically enforced CO_2 mineralization. *Journal of CO_2 Utilization*. 84, 102834. https://doi.org/10.1016/j.jcou.2024.102834.

Koutas, L.N., Tetta, Z., Bournas, D.A. and Triantafillou, T.C. (2019) Strengthening of concrete structures with textile reinforced mortars: state-of-the-art review. *Journal of Composites for Construction*. 23(1). https://doi.org/10.1061/(asce)cc.1943-5614.0000882.

Kurpińska, M., Pawelska-Mazur, M., Gu, Y. and Kurpiński, F. (2022) The impact of natural fibers' characteristics on mechanical properties of the cement composites. *Scientific Reports*. 12(1), 20565. https://doi.org/10.1038/s41598-022-25085-6.

Labib, W.A. (2022) Plant-based fibres in cement composites: a conceptual framework. *Journal of Engineered Fibers and Fabrics*. 17, 1–15. https://doi.org/10.1177/15589250221078922.

Lackner, K.S., Wendt, C.H., Butt, D.P., Joyce, E.L. and Sharp, D.H. (1995) Carbon dioxide disposal in carbonate minerals. *Energy*. 20(11), 1153–1170. https://doi.org/10.1016/0360-5442(95)00071-N.

Lan, M., Zhou, J. and Xu, M. (2021) Effect of fibre types on the tensile behaviour of engineered cementitious composites. *Frontiers in Materials*. 8, 775188. https://doi.org/10.3389/fmats.2021.775188.

Lee, B.Y., Song, J.K., Song, K.I., Choi, J.I. and Lee, K.M. (2016) Method for detecting concrete neutralization zone using digital image processing. South Korea Patent KR101848067B1. Available at: https://patents.google.com/patent/kr101848067b1

(Accessed: 21 January 2025).

Lee, H., Choi, M.K. and Kim, B.J. (2023) Structural and functional properties of fiber reinforced concrete composites for construction applications. *Journal of Industrial and Engineering Chemistry*. 125, pp. 38–49. https://doi.org/10.1016/j.jiec.2023.05.019.

Li, J., Wang, C., Song, X., Jin, X., Zhao, S., Qi, Z., Zeng, H., Zhu, S., Jiang, F., Ni, W. and Hitch, M. (2022a) Market stakeholder analysis of the practical implementation of carbonation curing on steel slag for urban sustainable governance. *Energies*. 15(7), 2399. https://doi.org/10.3390/en15072399.

Li, J., Zhao, S., Song, X., Ni, W., Mao, S., Du, H., Zhu, S., Jiang, F., Zeng, H., Deng, X. and Hitch, M. (2022b) Carbonation curing on magnetically separated steel slag for the preparation of artificial reefs. *Materials*. 15(6), 2055. https://doi.org/10.3390/ma15062055.

Li, K., Yang, Z., Yan, X., Xu, L., Briseghella, B. and Marano, G.C. (2023) Effect of modified cow dung fibers on strength and autogenous shrinkage of alkali-activated slag mortar. *Materials*. 16(20), 6808. https://doi.org/10.3390/ma16206808.

Li, L., Chen, T. and Gao, X. (2023) Effects of superimposed carbonation synergy on BOFS cement-based materials. *Cement and Concrete Composites*. 138, 105008. https://doi.org/10.1016/j.cemconcomp.2023.105008.

Li, L. and Wu, M. (2022) An overview of utilizing CO_2 for accelerated carbonation treatment in the concrete industry. *Journal of CO_2 Utilization*. 60, 102000. https://doi.org/10.1016/j.jcou.2022.102000.

Li, Q., Ibrahim, L., Zhou, W., Zhang, M. and Yuan, Z. (2021) Treatment methods for plant fibers for use as reinforcement in cement-based materials. *Cellulose*. 28(9), pp. 5257–5268. https://doi.org/10.1007/s10570-021-03903-w.

Li, X. and Ling, T.C. (2020) Instant CO_2 curing for dry-mix pressed cement pastes: consideration of CO_2 concentrations coupled with further water curing. *Journal of CO_2 Utilization*. 38, pp. 348–354. https://doi.org/10.1016/j.jcou.2020.02.012.

Liang, C., Li, B., Guo, M.Z., Hou, S., Wang, S., Gao, Y. and Wang, X. (2024) Effects of early-age carbonation curing on the properties of cement-based materials: a review. *Journal of Building Engineering*. 84, 108495. https://doi.org/10.1016/j.jobe.2024.108495.

Liang, C., Lu, N., Ma, H., Ma, Z. and Duan, Z. (2020) Carbonation behavior of recycled concrete with CO_2-curing recycled aggregate under various environments. *Journal of CO_2 Utilization*. 39, 101185. https://doi.org/10.1016/j.jcou.2020.101185.

Liang, J., Wang, X., Fu, Z., Li, Z., Liang, L., Luo, Q. and Long, W. (2025) Enhancing the applicability of sisal fibers in cement-based materials through alkali treatment and

penetrating crystallization. *Journal of Cleaner Production*. 490, 144736. https://doi.org/10.1016/j.jclepro.2025.144736.

Liew, K.M. and Akbar, A. (2020) The recent progress of recycled steel fiber reinforced concrete. *Construction and Building Materials*. 232, 117232. https://doi.org/10.1016/j.conbuildmat.2019.117232.

Lin, C., Kanstad, T., Jacobsen, S. and Ji, G. (2023) Bonding property between fiber and cementitious matrix: a critical review. *Construction and Building Materials*. 378, 131169. https://doi.org/10.1016/j.conbuildmat.2023.131169.

Lippiatt, N., Ling, T.C. and Pan, S.Y. (2020) Towards carbon-neutral construction materials: carbonation of cement-based materials and the future perspective. *Journal of Building Engineering*. 28, 101062. https://doi.org/10.1016/j.jobe.2019.101062.

Liu, J. and Lv, C. (2021) Research progress on durability of cellulose fiber-reinforced cement-based composites. *International Journal of Polymer Science*. 2021, 1014531. https://doi.org/10.1155/2021/1014531.

Liu, K., Yu, J., Chen, Y., Zhang, Z., Mei, C., Liu, H., Yang, G. and Zhang, X. (2024a) Preparation of cellulose fibre-sheets and its impact on pore connectivity of cement paste during early hydration. *Construction and Building Materials*. 411, 134535. https://doi.org/10.1016/j.conbuildmat.2023.134535.

Liu, L., Liu, Y., Su, B., Liu, C. and Chen, X. (2023a) Assessing CO_2 uptake of CO_2-cured cement mortar through theoretical modeling and experimental validation. *Construction and Building Materials*. 383, 131393. https://doi.org/10.1016/j.conbuildmat.2023.131393.

Liu, M., Hong, S., Wang, Y., Zhang, J., Hou, D. and Dong, B. (2021) Compositions and microstructures of hardened cement paste with carbonation curing and further water curing. *Construction and Building Materials*. 267, 121724. https://doi.org/10.1016/j.conbuildmat.2020.121724.

Liu, W., Lin, S., Li, Y., Long, W., Dong, Z. and Tang, L. (2020) Slag blended cement paste carbonation under different CO_2 concentrations: controls on mineralogy and morphology of products. *Materials*. 13(15), 3404. https://doi.org/10.3390/ma13153404.

Liu, Y., Li, H., Feng, Z., Ge, L., Li, R. and Liu, S. (2024b) Study on the interfacial bonding properties between alkali-treated bamboo fibers and high-performance seawater sea-sand concrete. *Construction and Building Materials*. 426, 136190. https://doi.org/10.1016/j.conbuildmat.2024.136190.

Liu, Z., Van den Heede, P., Zhang, C., Shi, X., Wang, L., Li, J., Yao, Y., Lothenbach, B. and De Belie, N. (2023b) Carbonation of blast furnace slag concrete at different CO_2 concentrations: carbonation rate, phase assemblage, microstructure and thermodynamic modelling. *Cement and Concrete Research*. 169, 107161. https://doi.org/10.1016/j.cemconres.2023.107161.

Liu, Z. and Meng, W. (2021) Fundamental understanding of carbonation curing and durability of carbonation-cured cement-based composites: a review. *Journal of CO_2 Utilization*. 44, 101428. https://doi.org/10.1016/j.jcou.2020.101428.

Liyew, G., Lee, N., Park, S., Lee, H.K., Park, J.J. and Kim, H.K. (2024) Understanding mechanism on carbonation curing for Portland cement through phase profiling via QXRD analysis and thermodynamic modeling. *Journal of CO_2 Utilization*. 87, 102919. https://doi.org/10.1016/j.jcou.2024.102919.

Lo, Y. and Lee, H.M. (2002) Curing effects on carbonation of concrete using a phenolphthalein indicator and Fourier-transform infrared spectroscopy. *Building and Environment*. 37(5), pp. 507–514. https://doi.org/10.1016/s0360-1323(01)00052-x.

Lu, B., He, P., Liu, J., Peng, Z., Song, B. and Hu, X. (2021) Microstructure of Portland cement paste subjected to different CO_2 concentrations and further water curing. *Journal of CO_2 Utilization*. 53, 101714. https://doi.org/10.1016/j.jcou.2021.101714.

Luo, W., Li, B., Xu, M., Pang, C., Lester, E. and Kow, K.W. (2023) Accelerated curing of cement mortar: in-situ carbonation utilising CO_2-impregnated faujasite. *Construction and Building Materials*. 388, 131639. https://doi.org/10.1016/j.conbuildmat.2023.131639.

Lv, C. and Liu, J. (2023) Alkaline degradation of plant fiber reinforcements in geopolymer: a review. *Molecules*. 28(4), 1868. https://doi.org/10.3390/molecules28041868.

Lv, Z.-Y., Pei, C. and Zhu, J.-H. (2025) Review on functional fibre-reinforced concrete: properties, applications and advances. *Proceedings of the Institution of Civil Engineers: Structures and Buildings*. 178(9), pp. 759–797. https://doi.org/10.1680/jstbu.25.00025.

Ma, W., Yan, L. and Kasal, B. (2025) Intensive exploration: the application potential of flax fibre/textiles as reinforcement in cementitious composites. *Journal of Cleaner Production*. 507, 145457. https://doi.org/10.1016/j.jclepro.2025.145457.

Madera, C.C.R. (2018) *Implementación de algoritmos de inteligencia artificial y procesamiento digital de imágenes en la determinación de la profundidad de carbonatación en estructuras de concreto*. Undergraduate thesis. Bogotá: Universidad Militar Nueva Granada.

Manaia, J.P., Manaia, A.T. and Rodriges, L. (2019) Industrial hemp fibers: an overview. *Fibers*. 7(12), 106. https://doi.org/10.3390/fib7120106.

Mantovani, M.P., Arruda Filho, A.B., Meneghetti, L.C. and Lima, P.R.L. (2025) Impact of hornification treatment on the pull-out behavior of natural fiber fabric. In: *RILEM Bookseries*. Vol. 60. Cham: Springer, pp. 204–212. https://doi.org/10.1007/978-3-031-92777-5_17.

Masoodi, R. and Pillai, K.M. (2012) A study on moisture absorption and swelling in bio-based jute-epoxy composites. *Journal of Reinforced Plastics and Composites*. 31(5), pp. 285–294. https://doi.org/10.1177/0731684411434654.

Mechtcherine, V. and Lieboldt, M. (2011) Permeation of water and gases through cracked textile reinforced concrete. *Cement and Concrete Composites*. 33(7), pp. 725–734. https://doi.org/10.1016/j.cemconcomp.2011.04.001.

Mehdizadeh, H. and Ling, T.C. (2025) Hydration and strength of cement paste containing metastable vaterite derived from recycled concrete fines and CO_2. *Cement and Concrete Research*. 194, 107891. https://doi.org/10.1016/j.cemconres.2025.107891.

Mejia-Ballesteros, J.E., Savastano, H., Fiorelli, J. and Marmol, G. (2025) Impact of carbonation and fiber hornification on the performance of fiber-cements. *Low-Carbon Materials and Green Construction*. 3(1), 16. https://doi.org/10.1007/s44242-025-00077-7.

Merta, I., Poletanovic, B., Dragas, J., Carevic, V., Ignjatovic, I. and Komljenovic, M. (2022) The influence of accelerated carbonation on physical and mechanical properties of hemp-fibre-reinforced alkali-activated fly ash and fly ash/slag mortars. *Polymers*. 14(9), 1799. https://doi.org/10.3390/polym14091799.

Meyer, V., De Cristofaro, N., Bryant, J. and Sahu, S. (2018) Solidia cement: an example of carbon capture and utilization. *Key Engineering Materials*. 761, pp. 197–203. https://doi.org/10.4028/www.scientific.net/kem.761.197.

Miller, S.A., Juenger, M., Kurtis, K.E. and Weiss, J. (2024) Cement and alternatives in the Anthropocene. *Annual Review of Environment and Resources*. 49(1), pp. 309–335. https://doi.org/10.1146/annurev-environ-112621-070104.

Miyauchi, M. (2023) Water adsorption on hydrophilic fibers and porous and deliquescent materials: cellulose, polysaccharide, silica, inorganic salt, sugar alcohol, and amino acid. *ACS Omega*. 8(46), pp. 44212–44220. https://doi.org/10.1021/acsomega.3c06642.

Mo, L., Zhang, F. and Deng, M. (2016) Mechanical performance and microstructure of the calcium carbonate binders produced by carbonating steel slag paste under CO_2 curing. *Cement and Concrete Research*. 88, pp. 217–226. https://doi.org/10.1016/j.cemconres.2016.05.013.

Mo, W., Chen, K., Yang, X., Kong, F., Liu, J. and Li, B. (2022) Elucidating the hornification mechanism of cellulosic fibers during the process of thermal drying. *Carbohydrate Polymers*. 289, 119434. https://doi.org/10.1016/j.carbpol.2022.119434.

El Mogahzy, Y.E. (2009) Structure and types of yarn for textile product design. In: *Engineering textiles*. Cambridge: Woodhead Publishing, pp. 240–270. https://doi.org/10.1533/9781845695415.2.240.

Monazami, M. and Gupta, R. (2022) Effect of curing age on pull-out response of carbon, steel, and synthetic fiber embedded in cementitious mortar matrix. *Journal of Materials in Civil Engineering*. 34(10), 04022275. https://doi.org/10.1061/(asce)mt.1943-5533.0004426.

Monkman, S. and MacDonald, M. (2017) On carbon dioxide utilization as a means to improve the sustainability of ready-mixed concrete. *Journal of Cleaner Production*. 167, pp. 365–375. https://doi.org/10.1016/j.jclepro.2017.08.194.

Monkman, S., MacDonald, M., Hooton, R.D. and Sandberg, P. (2016) Properties and durability of concrete produced using CO_2 as an accelerating admixture. *Cement and Concrete Composites*. 74, pp. 218–224. https://doi.org/10.1016/j.cemconcomp.2016.10.007.

Morales-Florez, V., Findling, N. and Brunet, F. (2012) Changes on the nanostructure of cementitious calcium silicate hydrates (C–S–H) induced by aqueous carbonation. *Journal of Materials Science*. 47(2), pp. 764–771. https://doi.org/10.1007/s10853-011-5852-6.

Morandeau, A., Thiéry, M. and Dangla, P. (2014) Investigation of the carbonation mechanism of CH and C–S–H in terms of kinetics, microstructure changes and moisture properties. *Cement and Concrete Research*. 56, pp. 153–170. https://doi.org/10.1016/j.cemconres.2013.11.015.

Mukhopadhyay, S. and Khatana, S. (2015) A review on the use of fibers in reinforced cementitious concrete. *Journal of Industrial Textiles*. 45(2), pp. 239–264. https://doi.org/10.1177/1528083714529806.

Müller, B., Grengg, C., Schallert, V., Sakoparnig, M., Staudinger, C., Breininger, J., Mittermayr, F., Ungerböck, B., Borisov, S.M., Dietzel, M. and Mayr, T. (2018) Wide-range optical pH imaging of cementitious materials exposed to chemically corrosive environments. *RILEM Technical Letters*. 3, pp. 39–45. https://doi.org/10.21809/rilemtechlett.2018.72.

Muzyczek, M. (2020) The use of flax and hemp for textile applications. In: *Handbook of natural fibres*. Cambridge: Elsevier, pp. 147–167. https://doi.org/10.1016/b978-0-12-818782-1.00004-3.

Naaman, E.A. (2000) Optimized geometries of fiber reinforcements of cement, ceramic and polymeric based composites. *Cement and Concrete Composites*. 22(4), pp. 311–313. https://doi.org/10.1016/s0958-9465(00)80011-6.

Nahum, L., Peled, A. and Gal, E. (2020) The flexural performance of structural concrete beams reinforced with carbon textile fabrics. *Composite Structures*. 239, 111917. https://doi.org/10.1016/j.compstruct.2020.111917.

Nascimento, K.M., Freire, R.T.S., Ribeiro Borges, P.H., Christoforo, A.L. and Panzera, T.H. (2023) Fiber-reinforced concrete (FRC) for civil engineering applications. In: *Advanced fibre-reinforced polymer (FRP) composites for structural applications*. Cambridge: Elsevier, pp. 541–568. https://doi.org/10.1016/b978-0-12-820346-0.00008-3.

Niu, L., Wu, S., Andrew, R.M., Shao, Z., Wang, J. and Xi, F. (2025) Global and national CO_2 uptake by cement carbonation from 1928 to 2024. *Earth System Science Data*. 17(5), pp. 2231–2247. https://doi.org/10.5194/essd-17-2231-2025.

Oinam, Y., Ju, S., Shin, M. and Pyo, S. (2023) Influence of cellulose micro-fibers on hydration characteristics of cementless UHPC using CaO-activated GGBFS. *Construction and Building Materials*. 389, 131747. https://doi.org/10.1016/j.conbuildmat.2023.131747.

Onuaguluchi, O. and Banthia, N. (2016) Plant-based natural fibre reinforced cement composites: a review. *Cement and Concrete Composites*. 68, pp. 96–108. https://doi.org/10.1016/j.cemconcomp.2016.02.014.

Orlowsky, J., Beßling, M. and Kryzhanovskyi, V. (2023) Prospects for the use of textile-reinforced concrete in buildings and structures maintenance. *Buildings*. 13(1), 189. https://doi.org/10.3390/buildings13010189.

Osman, A.I., Hefny, M., Abdel Maksoud, M.I.A., Elgarahy, A.M., David, J. and Rooney, D.W. (2021) Recent advances in carbon capture, storage and utilisation technologies: a review. *Environmental Chemistry Letters*. 19, pp. 797–849. https://doi.org/10.1007/s10311-020-01133-3.

Pacheco-Torgal, F. and Jalali, S. (2011) Cementitious building materials reinforced with vegetable fibres: a review. *Construction and Building Materials*. 25(2), pp. 575–581. https://doi.org/10.1016/j.conbuildmat.2010.07.024.

Pae, J., Kim, W.K. and Moon, J. (2024) Mineral carbonation performance of wollastonite-blended cementitious composites through in-situ CO_2 mixing. *Construction and Building Materials*. 438, 137160. https://doi.org/10.1016/j.conbuildmat.2024.137160.

Pamenter, S. and Myers, R.J. (2021) Decarbonizing the cementitious materials cycle: a whole-systems review of measures to decarbonize the cement supply chain in the UK and European contexts. *Journal of Industrial Ecology*. 25(2), pp. 359–376. https://doi.org/10.1111/jiec.13105.

Pan, X., Shi, Z., Shi, C., Ling, T.C. and Li, N. (2017a) A review on concrete surface treatment. Part I: types and mechanisms. *Construction and Building Materials*. 132, pp. 578–590. https://doi.org/10.1016/j.conbuildmat.2016.12.025.

Pan, X., Shi, Z., Shi, C., Ling, T.C. and Li, N. (2017b) A review on surface treatment for concrete. Part II: performance. *Construction and Building Materials*. 133, pp. 81–90. https://doi.org/10.1016/j.conbuildmat.2016.11.128.

Papadakis, V.G., Vayenas, C.G. and Fardis, M.N. (1991) Fundamental modeling and experimental investigation of concrete carbonation. *ACI Materials Journal*. 88(4), 363–373. https://doi.org/10.14359/1863.

Parrott, L.J. (1994) A study of carbonation-induced corrosion. *Magazine of Concrete Research*. 46(166), pp. 23–28. https://doi.org/10.1680/macr.1994.46.166.23.

Pei, C., Zeng, Y., Kong, S., Zhang, D., Li, H. and Zhu, J. (2021) Pull-out performance of anchored carbon-fiber bundles in cementitious matrix. *Journal of Composites for Construction*. 25(6), 04021057. https://doi.org/10.1061/(asce)cc.1943-5614.0001175.

Peled, A., Bentur, A. and Yankelevsky, D. (1994) Woven fabric reinforcement of cement matrix. *Advanced Cement Based Materials*. 1(5), 216–223. https://doi.org/10.1016/1065-7355(94)90027-2.

Peled, A., Mobasher, B. and Bentur, A. (2017) *Textile reinforced concrete*. Boca Raton, FL: CRC Press. https://doi.org/10.1201/9781315119151.

Pereira-De-Oliveira, L.A., Castro-Gomes, J.P. and Nepomuceno, M.C.S. (2012) Effect of acrylic fibres geometry on physical, mechanical and durability properties of cement mortars. *Construction and Building Materials*. 27(1), pp. 189–196. https://doi.org/10.1016/j.conbuildmat.2011.07.061.

Phung, Q.T. (2015) Effects of carbonation and calcium leaching on microstructure and transport properties of cement pastes. In: *Proceedings of the 4th International Conference on Self-Healing Materials (ICSHM 2013)*. Ghent, Belgium, pp. 196–200. Available at: http://hdl.handle.net/1854/LU-6913935 (Accessed: day month year).

Phung, Q.T., Maes, N., Jacques, D., Bruneel, E., Van Driessche, I., Ye, G. and De Schutter, G. (2015) Effect of limestone fillers on microstructure and permeability due to carbonation of cement pastes under controlled CO_2 pressure conditions. *Construction and Building Materials*. 82, pp. 376–390. https://doi.org/10.1016/j.conbuildmat.2015.02.093.

Pidun, K. and Schulze, M. (2015) Designed textile reinforced concrete elements for architectural facade applications. *Applied Mechanics and Materials*. 719–720, pp. 171–176. https://doi.org/10.4028/www.scientific.net/amm.719-720.171.

Pizzol, V.D., Mendes, L.M., Frezzatti, L., Savastano, H. and Tonoli, G.H.D. (2014) Effect of accelerated carbonation on the microstructure and physical properties of hybrid fiber-cement composites. *Minerals Engineering*. 59, pp. 101–106. https://doi.org/10.1016/j.mineng.2013.11.007.

Pourasee, A., Peled, A. and Weiss, J. (2011) Fluid transport in cracked fabric-reinforced cement-based composites. *Journal of Materials in Civil Engineering*. 23(8), pp. 1227–1238. https://doi.org/10.1061/(asce)mt.1943-5533.0000289.

Prabhu, L., Krishnaraj, V., Sathish, S., Gokulkumar, S., Karthi, N., Rajeshkumar, L., Balaji, D., Vigneshkumar, N. and Elango, K.S. (2021) A review on natural fiber reinforced hybrid composites: chemical treatments, manufacturing methods and potential applications. *Materials Today: Proceedings*. 45, pp. 8080–8085. https://doi.org/10.1016/j.matpr.2021.01.280.

Praneeth, S., Guo, R., Wang, T., Dubey, B.K. and Sarmah, A.K. (2020) Accelerated carbonation of biochar reinforced cement–fly ash composites: enhancing and sequestering CO_2 in building materials. *Construction and Building Materials*. 244, 118363. https://doi.org/10.1016/j.conbuildmat.2020.118363.

Preinstorfer, P., El Kadi, M., Dittel, G., Ghiassi, B., Müller, S., et al. (2024) Article of RILEM TC 292-MCC: bond behaviour of textile-reinforced concrete—a review. *Materials and Structures*. 57(4), pp. 1–21. https://doi.org/10.1617/s11527-024-02339-5.

Qiu, Q. (2020) A state-of-the-art review on the carbonation process in cementitious materials: fundamentals and characterization techniques. *Construction and Building Materials*. 247, 118503. https://doi.org/10.1016/j.conbuildmat.2020.118503.

Rafiee, A., Rajab Khalilpour, K., Milani, D. and Panahi, M. (2018) Trends in CO_2 conversion and utilization: a review from process systems perspective. *Journal of Environmental Chemical Engineering*. 6(5), pp. 5771–5794. https://doi.org/10.1016/j.jece.2018.08.065.

Ragalwar, K., Heard, W.F., Williams, B.A., Kumar, D. and Ranade, R. (2020) On enhancing the mechanical behavior of ultra-high performance concrete through multi-scale fiber reinforcement. *Cement and Concrete Composites*. 105, 103422. https://doi.org/10.1016/j.cemconcomp.2019.103422.

Rahbar, R.S., Shoushtary, S.A.M., Abdouss, M. and Khosroushahy, A. (2006) Production and characterisation of multifilament yarns made from polypropylene containing small amounts of oxidised polypropylene. *Journal of Chemical Research*. 2006(2), pp. 121–126. https://doi.org/10.3184/030823406776330945.

Rahman, F.A., Aziz, M.M.A., Saidur, R., Bakar, W.A.W.A., Hainin, M.R., Putrajaya, R. and Hassan, N.A. (2017) Pollution to solution: capture and sequestration of carbon dioxide (CO_2) and its utilization as a renewable energy source for a sustainable future. *Renewable and Sustainable Energy Reviews*. 71, pp. 112–126. https://doi.org/10.1016/j.rser.2017.01.011.

Ralston, N., Gupta, S. and Moini, R. (2024) 3D-printing of architected calcium silicate binders with enhanced and in-situ carbonation. *Virtual and Physical Prototyping*. 19(1). https://doi.org/10.1080/17452759.2024.2350768.

Ramakrishna, G. and Sundararajan, T. (2005) Studies on the durability of natural fibres and the effect of corroded fibres on the strength of mortar. *Cement and Concrete Composites*. 27(5), pp. 575–582. https://doi.org/10.1016/j.cemconcomp.2004.09.008.

Raupach, M. and Morales Cruz, C. (2016) Textile-reinforced concrete. In: *Textile fibre composites in civil engineering*. Oxford: Elsevier, pp. 275–299. https://doi.org/10.1016/b978-1-78242-446-8.00013-6.

Ravichandran, D., Prem, P.R., Kaliyavaradhan, S.K. and Ambily, P.S. (2022) Influence of fibers on fresh and hardened properties of ultra high performance concrete (UHPC): a review. *Journal of Building Engineering*. 57, 104922. https://doi.org/10.1016/j.jobe.2022.104922.

Ren, F., Zhou, C., Zhang, Z., Dreimol, C.H. and Angst, U. (2025) Effect of accelerated carbonation on long-term water absorption behavior of cement-based materials. *Materials and Structures*. 58(1), 16. https://doi.org/10.1617/s11527-024-02533-5.

RILEM (1988) CPC-18: measurement of hardened concrete carbonation depth. *Materials and Structures*. 21(6). https://doi.org/10.1007/bf02472327.

Rodriguez-Blanco, J.D., Shaw, S. and Benning, L.G. (2011) The kinetics and mechanisms of amorphous calcium carbonate (ACC) crystallization to calcite, via vaterite. *Nanoscale*. 3(1), pp. 265–271. https://doi.org/10.1039/c0nr00589d.

Rostami, V., Shao, Y., Boyd, A.J. and He, Z. (2012) Microstructure of cement paste subject to early carbonation curing. *Cement and Concrete Research*. 42(1), pp. 186–193. https://doi.org/10.1016/j.cemconres.2011.09.010.

Ruifrok, A.C. and Johnston, D.A. (2001) Quantification of histochemical staining by color deconvolution. *Analytical and Quantitative Cytology and Histology*. 23(4), pp. 291–299.

Sadrolodabaee, P., Claramunt, J., Ardanuy, M. and de la Fuente, A. (2021) A textile waste fiber-reinforced cement composite: comparison between short random fiber and textile reinforcement. *Materials*. 14(13), 3742. https://doi.org/10.3390/ma14133742.

Saetta, A.V., Schrefler, B.A. and Vitaliani, R.V. (1993) The carbonation of concrete and the mechanism of moisture, heat and carbon dioxide flow through porous materials. *Cement and Concrete Research*. 23(4), 761–772. https://doi.org/10.1016/0008-8846(93)90030-D.

Saillio, M., Baroghel-Bouny, V., Pradelle, S., Bertin, M., Vincent, J. and d'Espinose de Lacaillerie, J.B. (2021) Effect of supplementary cementitious materials on carbonation of cement pastes. *Cement and Concrete Research*. 142, 106358. https://doi.org/10.1016/j.cemconres.2021.106358.

Saini, K., Matsagar, V.A. and Kodur, V.R. (2024) Recent advances in the use of natural fibers in civil engineering structures. *Construction and Building Materials*. 411, 134364. https://doi.org/10.1016/j.conbuildmat.2023.134364.

De Santis, S., Carozzi, F.G., de Felice, G. and Poggi, C. (2017) Test methods for textile reinforced mortar systems. *Composites Part B: Engineering*. 127, pp. 121–132. https://doi.org/10.1016/j.compositesb.2017.03.016.

De Santis, S. and De Felice, G. (2015) Tensile behaviour of mortar-based composites for externally bonded reinforcement systems. *Composites Part B: Engineering*. 68, pp. 401–413. https://doi.org/10.1016/j.compositesb.2014.09.011.

Santos, S.F., Schmidt, R., Almeida, A.E.F.S., Tonoli, G.H.D. and Savastano, H. (2015) Supercritical carbonation treatment on extruded fibre–cement reinforced with vegetable fibres. *Cement and Concrete Composites*. 56, pp. 84–94. https://doi.org/10.1016/j.cemconcomp.2014.11.007.

Sanyal, T. (2017) Jute, jute fiber, and jute yarn. In: *Jute geotextiles and their applications in civil engineering*. Singapore: Springer, pp. 7–17. https://doi.org/10.1007/978-981-10-1932-6_2.

Šavija, B. and Luković, M. (2016) Carbonation of cement paste: understanding, challenges, and opportunities. *Construction and Building Materials*. 117, pp. 285–301. https://doi.org/10.1016/j.conbuildmat.2016.04.138.

Schiavon, J.Z. and Andrade, J.J. de O. (2023) Comparison between alternative chemical treatments on coir fibers for application in cementitious materials. *Journal of Materials Research and Technology*. 25, pp. 4634–4649. https://doi.org/10.1016/j.jmrt.2023.06.210.

Scrivener, K., Snellings, R. and Lothenbach, B. (2018) *A practical guide to microstructural analysis of cementitious materials*. 1st edn. Boca Raton, FL: CRC Press. https://doi.org/10.1201/b19074.

Seifritz, W. (1990) CO_2 disposal by means of silicates. *Nature*. 345(6275), 486. https://doi.org/10.1038/345486b0.

Sen, T. and Jagannatha Reddy, H.N. (2013) Strengthening of RC beams in flexure using natural jute fibre textile reinforced composite system and its comparative study with CFRP and GFRP strengthening systems. *International Journal of Sustainable Built Environment*. 2(1), pp. 41–55. https://doi.org/10.1016/j.ijsbe.2013.11.001.

Shafei, B., Kazemian, M., Dopko, M. and Najimi, M. (2021) State-of-the-art review of capabilities and limitations of polymer and glass fibers used for fiber-reinforced concrete. *Materials*. 14(2), 409. https://doi.org/10.3390/ma14020409.

Shah, V., Scrivener, K., Bhattacharjee, B. and Bishnoi, S. (2018) Changes in microstructure characteristics of cement paste on carbonation. *Cement and Concrete Research*. 109, pp. 184–197. https://doi.org/10.1016/j.cemconres.2018.04.016.

Shao, Y., Rostami, V., He, Z. and Boyd, A.J. (2013) Accelerated carbonation of Portland limestone cement. *Journal of Materials in Civil Engineering*. 26(1), pp. 117–124. https://doi.org/10.1061/(asce)mt.1943-5533.0000773.

Shi, C., He, F. and Wu, Y. (2012) Effect of pre-conditioning on CO_2 curing of lightweight concrete block mixtures. *Construction and Building Materials*. 26(1), pp. 257–267. https://doi.org/10.1016/j.conbuildmat.2011.06.020.

Shi, C., Tu, Z., Guo, M.Z. and Wang, D. (2017) Accelerated carbonation as a fast curing technology for concrete blocks. In: *Sustainable and nonconventional construction materials using inorganic bonded fiber composites*. Cambridge: Woodhead Publishing, pp. 313–341. https://doi.org/10.1016/b978-0-08-102001-2.00015-2.

Shi, X.C. and Shui, Z. (2023) Effect of eggshell powder addition on the properties of cement pastes with early CO_2 curing and further water curing. *Construction and Building Materials*. 404, 133231. https://doi.org/10.1016/j.conbuildmat.2023.133231.

Sidhu, G.S., Guleria, H., Sharma, D. and Goyal, S. (2023) Strength and permeation characteristics of pervious concrete subjected to accelerated carbonation curing. *Journal of Sustainable Cement-Based Materials*. 12(10), pp. 1242–1254. https://doi.org/10.1080/21650373.2023.2213241.

Signorini, C., Nobili, A., Liebscher, M., Zhao, J., Ahmed, A.H., Köberle, T. and Mechtcherine, V. (2024) Assessing the stress-transfer capability of mineral impregnated PBO yarns in a limestone calcined clay cement-based (LC3) matrix. *Composites Part B: Engineering*. 276, 111364. https://doi.org/10.1016/j.compositesb.2024.111364.

Silva, F. de A., Filho, R.D.T., Filho, J. de A.M. and Fairbairn, E. de M.R. (2010) Physical and mechanical properties of durable sisal fiber–cement composites. *Construction and Building Materials*. 24(5), pp. 777–785. https://doi.org/10.1016/j.conbuildmat.2009.10.030.

da Silva, T.R., de Matos, P.R., Tambara Júnior, L.U.D., Marvila, M.T. and de Azevedo, A.R.G. (2023) A review on the performance of açaí fiber in cementitious composites: characteristics and application challenges. *Journal of Building Engineering*. 71, 106481. https://doi.org/10.1016/j.jobe.2023.106481.

Silveira, R.G. da and Isaia, G.C. (2022) Proposal of a digital image analysis method for determining the carbonated front in concretes. *Ambiente Construído*. 22(3), pp. 275–298. https://doi.org/10.1590/s1678-86212022000300619.

Siqueira, I.S., Filho, R.D.T. and Koenders, E. (2015) Influence of cellulose pulp fiber addition on the hydration of cementitious pastes with silica fume. In: *Proceedings of the International Conference on Bio-Based Building Materials (ICBBM 2015)*. Clermont-Ferrand, France. Paper 77. https://doi.org/10.26168/icbbm2015.77.

Skocek, J., Zajac, M. and Ben Haha, M. (2020) Carbon capture and utilization by mineralization of cement pastes derived from recycled concrete. *Scientific Reports*. 10(1), 62503. https://doi.org/10.1038/s41598-020-62503-z.

Snellings, R., Chwast, J., Cizer, Ö., De Belie, N., Dhandapani, Y., Durdzinski, P., Elsen, J., Haufe, J., Hooton, D., Patapy, C., Santhanam, M., Scrivener, K., Snoeck, D., Steger, L., Tongbo, S., Vollpracht, A., Winnefeld, F. and Lothenbach, B. (2018) RILEM TC-238 SCM recommendation on hydration stoppage by solvent exchange for the study of hydrate assemblages. *Materials and Structures*. 51(6), pp. 1–4. https://doi.org/10.1617/s11527-018-1298-5.

Song, Q., Guo, M.Z., Wang, L. and Ling, T.C. (2021) Use of steel slag as sustainable construction materials: a review of accelerated carbonation treatment. *Resources, Conservation and Recycling*. 173, 105740. https://doi.org/10.1016/j.resconrec.2021.105740.

Spadea, S., Farina, I., Carrafiello, A. and Fraternali, F. (2015) Recycled nylon fibers as cement mortar reinforcement. *Construction and Building Materials*. 80, pp. 200–209. https://doi.org/10.1016/j.conbuildmat.2015.01.075.

Steiner, S., Lothenbach, B., Proske, T., Borgschulte, A. and Winnefeld, F. (2020) Effect of relative humidity on the carbonation rate of portlandite, calcium silicate hydrates and ettringite. *Cement and Concrete Research*. 135, 106116. https://doi.org/10.1016/j.cemconres.2020.106116.

Su, Y., Qian, C., Rui, Y. and Feng, J. (2021) Exploring the coupled mechanism of fibers and bacteria on self-healing concrete from bacterial extracellular polymeric substances (EPS). *Cement and Concrete Composites*. 116, 103896. https://doi.org/10.1016/j.cemconcomp.2020.103896.

Suescum-Morales, D., Fernández-Rodríguez, J.M. and Jiménez, J.R. (2022) Use of carbonated water to improve the mechanical properties and reduce the carbon footprint of cement-based materials with recycled aggregates. *Journal of CO_2 Utilization*. 57, 101886. https://doi.org/10.1016/j.jcou.2022.101886.

Tao, Y., Hadigheh, S.A. and Wang, Z. (2024) Void geometry analysis and multifaceted characterisation of cementitious mortar reinforced with short carbon and glass fibres: a comparative study. *Journal of Building Engineering*. 89, 109283. https://doi.org/10.1016/j.jobe.2024.109283.

Tausif, M., Cassidy, T. and Butcher, I. (2018) Yarn and thread manufacturing methods for high-performance apparel. In: *High-performance apparel: materials, development, and applications*. Oxford: Elsevier, pp. 33–73. https://doi.org/10.1016/b978-0-08-100904-8.00003-1.

Teune, I.E., Schollbach, K., Florea, M.V.A. and Brouwers, H.J.H. (2023) Carbonation of hydrated cement: the impact of carbonation conditions on CO_2 sequestration, phase formation, and reactivity. *Journal of Building Engineering*. 79, 107785. https://doi.org/10.1016/j.jobe.2023.107785.

Thiéry, M., Villain, G., Dangla, P. and Platret, G. (2007) Investigation of the carbonation front shape on cementitious materials: effects of the chemical kinetics. *Cement and Concrete Research*. 37(7), pp. 1047–1058. https://doi.org/10.1016/j.cemconres.2007.04.002.

Thomas, B.C. and Jose, Y.S. (2022) Impact of sisal fiber reinforced concrete and its performance analysis: a review. *Evolutionary Intelligence*. 15(2), pp. 865–875. https://doi.org/10.1007/s12065-019-00230-9.

Tolêdo Filho, R.D., Ghavami, K., England, G.L. and Scrivener, K. (2003) Development of vegetable fibre–mortar composites of improved durability. *Cement and Concrete Composites*. 25(2), pp. 185–196. https://doi.org/10.1016/s0958-9465(02)00018-5.

Tolêdo Filho, R.D., Scrivener, K., England, G.L. and Ghavami, K. (2000) Durability of alkali-sensitive sisal and coconut fibres in cement mortar composites. *Cement and Concrete Composites*. 22(2), 127–143. https://doi.org/10.1016/S0958-9465(99)00039-6.

Tonoli, G.H.D., Belgacem, M.N., Siqueira, G., Bras, J., Savastano, H. and Rocco Lahr, F.A. (2013) Processing and dimensional changes of cement based composites reinforced with surface-treated cellulose fibres. *Cement and Concrete Composites*. 37(1), pp. 68–75. https://doi.org/10.1016/j.cemconcomp.2012.12.004.

Tonoli, G.H.D., Pizzol, V.D., Urrea, G., Santos, S.F., Mendes, L.M., Santos, V., John, V.M., Frías, M. and Savastano, H. (2016) Rationalizing the impact of aging on fiber–matrix interface and stability of cement-based composites submitted to carbonation at early ages. *Journal of Materials Science*. 51(17), pp. 7929–7943. https://doi.org/10.1007/s10853-016-0060-z.

Tonoli, G.H.D., Santos, S.F., Joaquim, A.P. and Savastano, H. (2010) Effect of accelerated carbonation on cementitious roofing tiles reinforced with lignocellulosic

fibre. *Construction and Building Materials*. 24(2), pp. 193–201. https://doi.org/10.1016/j.conbuildmat.2007.11.018.

Tu, Z., Guo, M.Z., Poon, C.S. and Shi, C. (2016) Effects of limestone powder on $CaCO_3$ precipitation in CO_2-cured cement pastes. *Cement and Concrete Composites*. 72, pp. 9–16. https://doi.org/10.1016/j.cemconcomp.2016.05.019.

Tuutti, K. (1982) *Corrosion of steel in concrete*. PhD thesis. Stockholm: KTH Royal Institute of Technology.

Urrea-Ceferino, G.E., Rempe, N., dos Santos, V. and Savastano Junior, H. (2017) Definition of optimal parameters for supercritical carbonation treatment of vegetable fiber-cement composites at a very early age. *Construction and Building Materials*. 152, pp. 424–433. https://doi.org/10.1016/j.conbuildmat.2017.06.182.

Vega, F., Baena-Moreno, F.M., Gallego Fernández, L.M., Portillo, E., Navarrete, B. and Zhang, Z. (2020) Current status of CO_2 chemical absorption research applied to CCS: towards full deployment at industrial scale. *Applied Energy*. 260, 114313. https://doi.org/10.1016/j.apenergy.2019.114313.

Ventura, H., Álvarez, M.D., Gonzalez-Lopez, L., Claramunt, J. and Ardanuy, M. (2022) Cement composite plates reinforced with nonwoven fabrics from technical textile waste fibres: mechanical and environmental assessment. *Journal of Cleaner Production*. 372, 133652. https://doi.org/10.1016/j.jclepro.2022.133652.

Villagrán-Zaccardi, Y.A., Egüez-Alava, H., De Buysser, K., Gruyaert, E. and De Belie, N. (2017) Calibrated quantitative thermogravimetric analysis for the determination of portlandite and calcite content in hydrated cementitious systems. *Materials and Structures*. 50(3), pp. 1–10. https://doi.org/10.1617/s11527-017-1046-2.

Villain, G., Thiéry, M. and Platret, G. (2007) Measurement methods of carbonation profiles in concrete: thermogravimetry, chemical analysis and gammadensimetry. *Cement and Concrete Research*. 37(8), pp. 1182–1192. https://doi.org/10.1016/j.cemconres.2007.04.015.

Vollpracht, A., Gluth, G.J.G., Rogiers, B., Uwanuakwa, I.D., Phung, Q.T., Villagran Zaccardi, Y., Thiel, C., Vanoutrive, H., Etcheverry, J.M., Gruyaert, E., Kamali-Bernard, S., Kanellopoulos, A., Zhao, Z., Martins, I.M., Rathnarajan, S. and De Belie, N. (2024) Report of RILEM TC 281-CCC: insights into factors affecting the carbonation rate of concrete with SCMs revealed from data mining and machine learning approaches. *Materials and Structures*. 57(9), pp. 1–33. https://doi.org/10.1617/s11527-024-02465-0.

Wang, D., Xiao, J. and Duan, Z. (2022) Strategies to accelerate CO_2 sequestration of cement-based materials and their application prospects. *Construction and Building Materials*. 314, 125646. https://doi.org/10.1016/j.conbuildmat.2021.125646.

Wang, L., Ma, C., Li, Y., Zhang, M. and Liu, J. (2025) The microstructure evolution of cement paste and steel corrosion behavior under natural and accelerated carbonation: CO_2 concentration, temperature and humidity. *Construction and Building Materials*. 490, 142433. https://doi.org/10.1016/j.conbuildmat.2025.142433.

Wawrzyńczak, D., Majchrzak-Kucęba, I., Pevida, C., Bonura, G., Nogueira, R. and de Falco, M. (2022) *The carbon chain in carbon dioxide industrial utilization technologies*. Boca Raton, FL: CRC Press. https://doi.org/10.1201/9781003336587.

Wei, J. and Meyer, C. (2015) Degradation mechanisms of natural fiber in the matrix of cement composites. *Cement and Concrete Research*. 73, pp. 1–16. https://doi.org/10.1016/j.cemconres.2015.02.019.

Wilberforce, T., Olabi, A.G., Sayed, E.T., Elsaid, K. and Abdelkareem, M.A. (2021) Progress in carbon capture technologies. *Science of the Total Environment*. 761, 143203. https://doi.org/10.1016/j.scitotenv.2020.143203.

Wong, H.S., Head, M.K. and Buenfeld, N.R. (2006) Pore segmentation of cement-based materials from backscattered electron images. *Cement and Concrete Research*. 36(6), pp. 1083–1090. https://doi.org/10.1016/j.cemconres.2005.10.006.

Wu, B. and Qiu, J. (2022) Incorporating hollow natural fiber (HNF) to enhance CO_2 sequestration and mechanical properties of reactive magnesia cement (RMC)-based composites: feasibility study. *Journal of CO_2 Utilization*. 57, 101874. https://doi.org/10.1016/j.jcou.2021.101874.

Wu, C., Pan, Y. and Yan, L. (2023) Mechanical properties and durability of textile reinforced concrete (TRC): a review. *Polymers*. 15(18), 3826. https://doi.org/10.3390/polym15183826.

Wu, H., Shen, A., Cheng, Q., Cai, Y., Ren, G., Pan, H. and Deng, S. (2023) A review of recent developments in application of plant fibers as reinforcements in concrete. *Journal of Cleaner Production*. 419, 138265. https://doi.org/10.1016/j.jclepro.2023.138265.

Wu, H., Shen, A., Ren, G., Ma, Q., Wang, Z., Cheng, Q. and Li, Y. (2023) Dynamic mechanical properties of fiber-reinforced concrete: a review. *Construction and Building Materials*. 366, 130145. https://doi.org/10.1016/j.conbuildmat.2022.130145.

Wu, S., Shao, Z., Andrew, R.M., Bing, L., Wang, J., Niu, L., Liu, Z. and Xi, F. (2024) Global CO_2 uptake by cement materials accounts 1930–2023. *Scientific Data*. 11(1), 4234. https://doi.org/10.1038/s41597-024-04234-8.

Xian, X., Mahoutian, M. and Shao, Y. (2023) Production of concrete pipes by carbonation curing in an inflatable enclosure. *Construction and Building Materials*. 363, 129861. https://doi.org/10.1016/j.conbuildmat.2022.129861.

Xian, X., Zhang, D., Lin, H. and Shao, Y. (2022) Ambient pressure carbonation curing of reinforced concrete for CO_2 utilization and corrosion resistance. *Journal of CO_2 Utilization*. 56, 101861. https://doi.org/10.1016/j.jcou.2021.101861.

Xian, X., Zhang, D. and Shao, Y. (2021) Flue gas carbonation curing of cement paste and concrete at ambient pressure. *Journal of Cleaner Production*. 313, 127943. https://doi.org/10.1016/j.jclepro.2021.127943.

Xie, Y., Hill, C.A.S., Xiao, Z., Militz, H. and Mai, C. (2010) Silane coupling agents used for natural fiber/polymer composites: a review. *Composites Part A: Applied*

Science and Manufacturing. 41(7), pp. 806–819. https://doi.org/10.1016/j.compositesa.2010.03.005.

Xu, M., Zhang, Y., Yang, S., Mo, L. and Liu, P. (2023) Effects of internal CO_2 curing provided by biochar on the carbonation and properties of steel slag-based artificial lightweight aggregates (SALAs). *Cement and Concrete Composites*. 142, 105197. https://doi.org/10.1016/j.cemconcomp.2023.105197.

Yan, J. and Zhang, Z. (2019) Carbon capture, utilization and storage (CCUS). *Applied Energy*. 235, pp. 1289–1299. https://doi.org/10.1016/j.apenergy.2018.11.019.

Yang, F., Lai, C., Liu, L., Chen, Z., Jia, H., Zhu, J., Jiang, Z., Shi, C. and Liu, J. (2024) A new method for improving the resistance of cement-based materials to carbonic acid water corrosion: carbonation curing and further water curing. *Construction and Building Materials*. 422, 135733. https://doi.org/10.1016/j.conbuildmat.2024.135733.

Yang, K.H., Jung, Y.B., Cho, M.S. and Tae, S.H. (2015) Effect of supplementary cementitious materials on reduction of CO_2 emissions from concrete. *Journal of Cleaner Production*. 103, pp. 774–783. https://doi.org/10.1016/j.jclepro.2014.03.018.

Yang, X. and Wang, X.Y. (2021) Strength and durability improvements of biochar-blended mortar or paste using accelerated carbonation curing. *Journal of CO_2 Utilization*. 54, 101766. https://doi.org/10.1016/j.jcou.2021.101766.

Yeh, C.H., Wu, J.H. and Yang, T.C. (2024) Drying shrinkage and mechanical strength of cementitious composites with alkali-treated Makino bamboo fibers. *Journal of Natural Fibers*. 21(1). https://doi.org/10.1080/15440478.2024.2321531.

Yoshioka, K., Obata, D., Nanjo, H., Yokozeki, K., Torichigai, T., Morioka, M. and Higuchi, T. (2013) New ecological concrete that reduces CO_2 emissions below zero level: new method for CO_2 capture and storage. *Energy Procedia*. 37, pp. 6018–6025. https://doi.org/10.1016/j.egypro.2013.06.530.

You, X., Hu, X., He, P., Liu, J. and Shi, C. (2022) A review on the modelling of carbonation of hardened and fresh cement-based materials. *Cement and Concrete Composites*. 125, 104315. https://doi.org/10.1016/j.cemconcomp.2021.104315.

Younsi, A., Turcry, P. and Aït-Mokhtar, A. (2022) Quantification of CO_2 uptake of concretes with mineral additions after 10-year natural carbonation. *Journal of Cleaner Production*. 349, 131362. https://doi.org/10.1016/j.jclepro.2022.131362.

Younsi, A., Turcry, P., Aït-Mokhtar, A. and Staquet, S. (2013) Accelerated carbonation of concrete with high content of mineral additions: effect of interactions between hydration and drying. *Cement and Concrete Research*. 43, pp. 25–33. https://doi.org/10.1016/j.cemconres.2012.10.008.

Yue, Z., Dhandapani, Y., Adu-Amankwah, S. and Bernal, S.A. (2023) Influence of slag chemistry on the carbonation of sodium sulfate-activated slag cements. In: *RILEM Bookseries*. Vol. 44. Cham: Springer, pp. 451–461. https://doi.org/10.1007/978-3-031-33187-9_42.

Zajac, M., Irbe, L., Bullerjahn, F., Hilbig, H. and Ben Haha, M. (2022) Mechanisms of carbonation hydration hardening in Portland cements. *Cement and Concrete Research*, 152, 106687. doi:10.1016/j.cemconres.2021.106687.

Zajac, M., Skibsted, J., Skocek, J., Durdzinski, P., Bullerjahn, F. and Ben Haha, M. (2020) Phase assemblage and microstructure of cement paste subjected to enforced, wet carbonation. *Cement and Concrete Research*, 130, 105990. doi:10.1016/j.cemconres.2020.105990.

Zeng, W., Wang, W., Wang, Q., Li, M., Zhang, L. and Tong, Y. (2024) Effect of macro fibres on the permeability and crack surface topography of layered fibre-reinforced concrete. *Materials*, 17(8), 1733. doi:10.3390/ma17081733.

Zevenhoven, R. and Fagerlund, J. (2010) Mineralisation of carbon dioxide (CO_2). In: *Developments and Innovation in Carbon Dioxide (CO_2) Capture and Storage Technology*. Oxford: Elsevier, pp. 433–462. doi:10.1533/9781845699581.4.433.

Zhan, B., Poon, C.S. and Shi, C. (2013) CO_2 curing for improving the properties of concrete blocks containing recycled aggregates. *Cement and Concrete Composites*, 42, pp. 1–8. doi:10.1016/j.cemconcomp.2013.04.013.

Zhang, D., Cai, X. and Jaworska, B. (2020a) Effect of pre-carbonation hydration on long-term hydration of carbonation-cured cement-based materials. *Construction and Building Materials*, 231, 117122. doi:10.1016/j.conbuildmat.2019.117122.

Zhang, D., Ghouleh, Z. and Shao, Y. (2017) Review on carbonation curing of cement-based materials. *Journal of CO_2 Utilization*, 21, pp. 119–131. doi:10.1016/j.jcou.2017.07.003.

Zhang, D. and Shao, Y. (2016) Early-age carbonation curing for precast reinforced concretes. *Construction and Building Materials*, 113, pp. 134–143. doi:10.1016/j.conbuildmat.2016.03.048.

Zhang, D. and Shao, Y. (2019) Enhancing chloride corrosion resistance of precast reinforced concrete by carbonation curing. *ACI Materials Journal*, 116(3), pp. 3–12. doi:10.14359/51714461.

Zhang, K., Yio, M., Wong, H.S. and Buenfeld, N.R. (2024a) Development of more accurate methods for determining carbonation depth in cement-based materials. *Cement and Concrete Research*, 175, 107358. doi:10.1016/j.cemconres.2023.107358.

Zhang, M. and Deng, M. (2022) Tensile behaviour of textile-reinforced composites made of highly ductile fibre-reinforced concrete and carbon textiles. *Journal of Building Engineering*, 57, 104824. doi:10.1016/j.jobe.2022.104824.

Zhang, P., Wittmann, F.H., Zhao, T. and Lehmann, E.H. (2010) Neutron imaging of water penetration into cracked steel-reinforced concrete. *Physica B: Condensed Matter*, 405(7), pp. 1866–1871. doi:10.1016/j.physb.2010.01.065.

Zhang, Y., He, S., Liang, X., Liang, M., Çopuroğlu, O. and Schlangen, E. (2025) Characterisation of the transitional zone between fully carbonated and non-carbonated

areas in slag-rich cement paste after long-term natural exposure. *Cement and Concrete Research*, 198, 107986. doi:10.1016/j.cemconres.2025.107986.

Zhang, Z., Pan, S.Y., Li, H., Cai, J., Olabi, A.G., Anthony, E.J. and Manovic, V. (2020b) Recent advances in carbon dioxide utilisation. *Renewable and Sustainable Energy Reviews*, 125, 109799. doi:10.1016/j.rser.2020.109799.

Zhang, Z., Zheng, K., Chen, L. and Yuan, Q. (2024b) Review on accelerated carbonation of calcium-bearing minerals: carbonation behaviours, reaction kinetics and carbonation efficiency improvement. *Journal of Building Engineering*, 86, 108826. doi:10.1016/j.jobe.2024.108826.

Zhou, Y., Fan, M. and Chen, L. (2016) Interface and bonding mechanisms of plant fibre composites: an overview. *Composites Part B: Engineering*, 101, pp. 31–45. doi:10.1016/j.compositesb.2016.06.055.

Zhuge, Y., Ong, P.B., Wong, H.S. and Myers, R.J. (2024) Natural fibre-enhanced CO_2 transport and uptake in cement pastes subjected to enforced carbonation. *Journal of CO_2 Utilization*, 90, 102983. doi:10.1016/j.jcou.2024.102983.

Appendix 1. Supporting tables for literature review

Table A1.1. Effects of supplementary cementitious materials on carbonation reactions.

SCM type	Primary microchemical effect	Observed carbonation consequence
Fly ash (HVFA)	Reduces portlandite via pozzolanic reaction; lowers Ca availability	Faster apparent carbonation depth in colorimetric tests; enhanced C-S-H carbonation under accelerated CO_2; potential underestimation/confounding in accelerated tests (Van den Heede, De Schepper and De Belie, 2019; Wei et al., 2020)
Slag (GGBFS)	Alters Ca/Si ratio and incorporates Al into C-S-H/C-A-S-H	Increased decalcification susceptibility; calcite + vaterite common; denser post-carbonation microstructures observed (Wei et al., 2020)
Silica fume	Strongly lowers Ca/Si and refines pore structure	Less portlandite to carbonate; C-S-H carbonation and silica gel formation dominate; microstructure densification but complex kinetics (Wei et al., 2020)
Metakaolin	Introduces Al in hydrates and consumes portlandite	Alters nucleation and may promote different carbonate morphologies and greater C-S-H decalcification (Saillio et al., 2019)

Table A1.2. Effects of key exposure and material parameters on carbonation rate in cement-based materials under enforced carbonation, summarised from the literature (Castellote et al., 2008; Ashraf, 2016; Ashraf, Olek & Atakan, 2016; Morandeau, Thiéry & Dangla, 2014; Šavija & Luković, 2016; Yang et al., 2015; von Greve-Dierfeld et al., 2020; Liu & Meng, 2021; Zhang, Ghouleh & Shao, 2017)[1]

Parameter	Typical range reported	Effect on carbonation rate	Main mechanism
CO_2 concentration	1–100 vol.% CO_2	Higher CO_2 concentration increases	Increased CO_2 diffusion gradient and

[1] The effects of individual parameters are interdependent. For example, the influence of CO_2 concentration and temperature on carbonation rate is strongly moderated by the moisture state of the pore system, as adequate pore water is required for CO_2 dissolution while sufficient gas-filled porosity is needed for CO_2 transport.

		carbonation rate up to a limit	higher CO_2 availability for dissolution
Relative humidity (RH)	40–90% RH	Maximum carbonation rate typically observed at intermediate RH (~50–70%)	Balance between CO_2 diffusion (favoured at low RH) and CO_2 dissolution in pore water (favoured at high RH)
Temperature	20–80 °C	Higher temperature generally increases carbonation rate	Enhanced reaction kinetics and faster CO_2 diffusion
CO_2 pressure	0.1–1 MPa	Increased pressure accelerates carbonation	Higher CO_2 solubility and penetration depth
Moisture state (degree of saturation or pre-conditioning)	Dry to fully saturated	Partially saturated state favours fastest carbonation	Enables both gas transport and aqueous reaction
Curing age at carbonation onset	Fresh to >28 days	Early-age carbonation proceeds faster than late-age carbonation	Higher availability of reactive calcium phases and open pore structure
Cement type	OPC, blended cements	Lower portlandite content generally reduces carbonation rate	Reduced $Ca(OH)_2$ buffer capacity
Water-to-binder ratio (w/b)	0.30–0.60	Higher w/b increases carbonation rate	Increased porosity and gas permeability
Pore structure	Fine vs coarse pores	Coarser, connected pores increase carbonation rate	Enhanced CO_2 transport pathways
Carbonation duration	Hours to days (enforced)	Carbonation rate decreases with time	Progressive pore blocking by carbonation products

Appendix 2. Image analysis trials and sensitivity analysis

Section 2A1: Past image analysis trials

With natural fibre yarns embedded in the centre of the cement paste, carbonation develops with contrasting geometries and intensities. The boundary between stained and unstained regions is rarely circular and is frequently disrupted by fibre bundles, stray filaments, and surface roughness. Some discs exhibit sharp colour transitions, whereas others show diffuse fronts or mottled textures. Such variability makes it difficult to identify carbonation boundaries using simple thresholding on RGB channels.

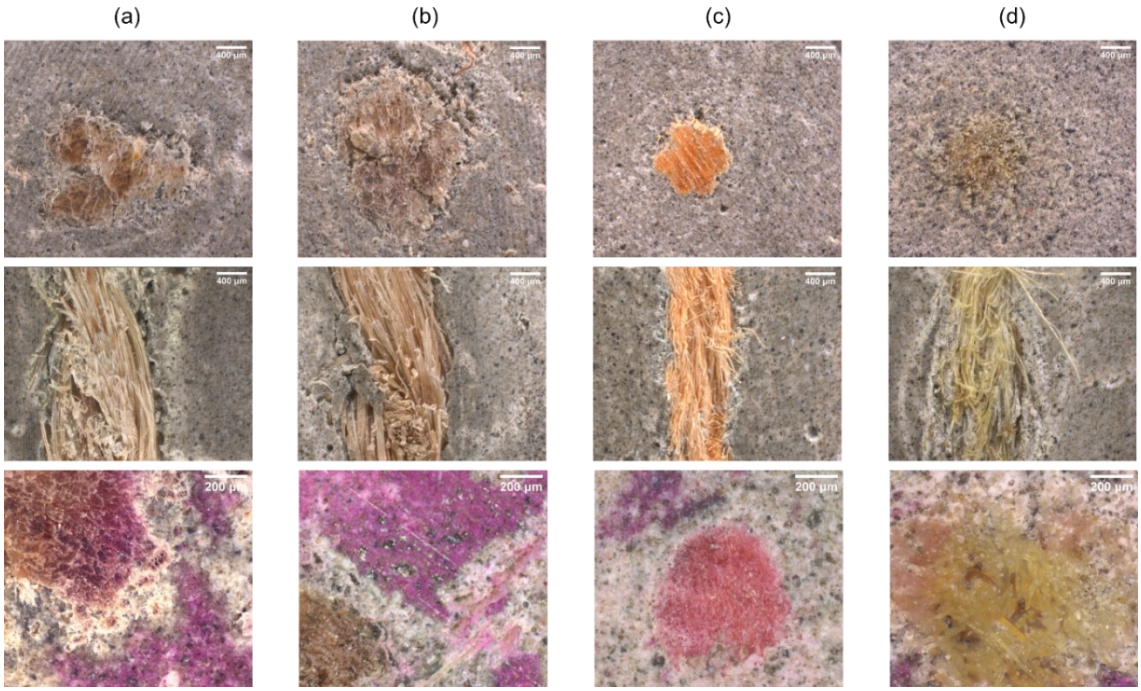


Figure A2.1. Cross-sectional (top), vertical (middle) interface bond and phenolphthalein-stained cross-sections of (a) jute, (b) hemp, (c) cotton, and (d) wool fibre string and cement matrix (darkfield, Zeiss Axio Imager Z2m digital microscope).

Microscopy of fibre–cement interfaces (*Figure A2.1*) further illustrates the challenge. Different fibres bond differently to the matrix: jute and hemp show gaps and distinct bundle edges; cotton bonds closely with no obvious voids; and wool forms diffuse,

irregular boundaries. Carbonation often develops preferentially around these regions, creating heterogeneous colour fields. Stray fibres and microstructural defects appear as bright or dark features unrelated to carbonation, making simple intensity-based segmentation unreliable.

To examine whether thresholding methods could cope with this complexity, the RGB channels of a representative stained disc (J-D7-20) were separated (*Figure A2.2*). Although the green channel provides stronger contrast than the red or blue channels, global thresholding on the green channel produced inconsistent and often unrealistic segmentation outputs. As shown in *Figures A1.2 (e)-(f)*, auto threshold or overflow segmentation method either overestimated carbonation or produced boundaries corrupted by noise. This reflects the nature of phenolphthalein staining, where the transition is gradual rather than sharp, and where stray fibres, saw marks, pores, and roughness produce pixel intensities that overlap with stain signals.

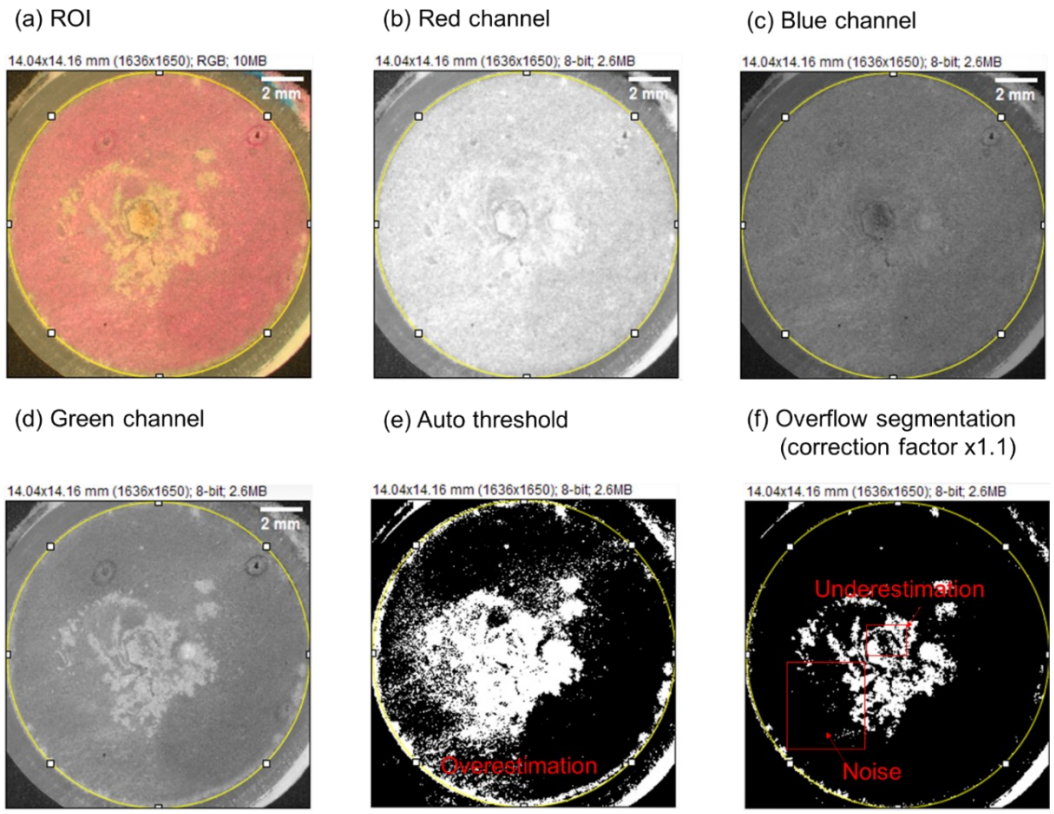


Figure A2.2. (a) Region of interest of a carbonated jute yarn sample (J-D7-20); (b-d) Colour channel split images in red, blue and green; (e-f) binary images obtained by different thresholding methods using ImageJ Tool.

A systematic evaluation of sixteen global thresholding methods confirmed these limitations (*Table A2.1*; *Figure A2.3*). Despite being widely used in image analysis, these

methods produced highly divergent results. Several overestimated the carbonated area by +10% to +290%, while others underestimated specific regions or generated fragmented masks dominated by artefacts. Even the best-performing thresholds could not delineate the carbonation front reliably.

Table A2.1. Application of various global (histogram-derived) threshold methods on the green channel of a carbonated jute yarn sample (J-D7-20) using ImageJ Tool.

No.	Method	Threshold value	Area (%)	Accuracy assessment	Source
1	Huang	145	+12.7%	Overestimation	(Huang & Wang, 1995)
2	Huang2	149	+9.33%	Overestimation	(Huang & Wang, 1995),16bit
3	Intermodes	90	+205%	Not applicable	(Prewitt & Mendelsohn, 1966)
4	Isodata	96	+153%	Not applicable	(Ridler & Calvard, 1978)
5	Li	139	+18.2%	Overestimation	(Sezgin & Sankur, 2004; Li & Tam, 1998; Li & Lee, 1993)
6	Maxentropy	107	+86.2%	Not applicable	(Kapur, Sahoo & Wong, 1985)
7	Mean	137	+20.3%	Overestimation	(Glasbey, 1993)
8	MinError	170	−6.36%	Relatively accurate with noises/underestimation	(Kittler & Illingworth, 1986)
9	Minimum	82	+290%	Not applicable	(Prewitt & Mendelsohn, 1966)
10	Moments	130	+28.2%	Overestimation	(Tsai, 1985)
11	Otsu	143	+14.4%	Overestimation	(Otsu, 1979)
12	Percentile	136	+21.4%	Overestimation	(Doyle, 1962)
13	RenyiEntropy	107	+86.2%	Not applicable	(Kapur, Sahoo & Wong, 1985)
14	Shanbhag	143	+14.4%	Overestimation	(Shanbhag, 1994)
15	Triangle	168	−4.86%	Relatively accurate with noises/underestimation	(Zack, Rogers & Latt, 1977)
16	Yen	107	+86.2%	Not applicable	(Yen, Chang & Chang, 1995; Sezgin & Sankur, 2004)

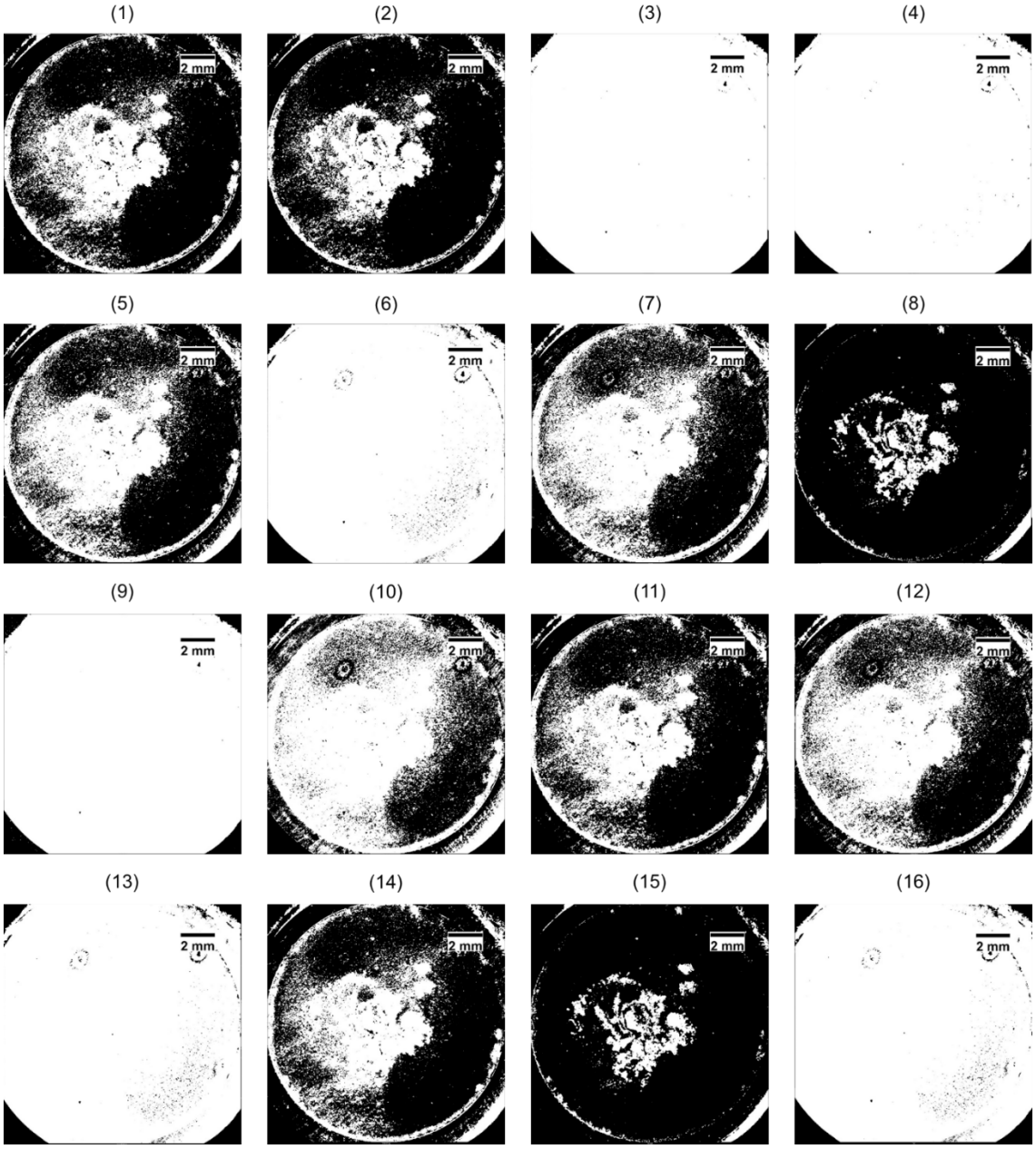


Figure A2.3. Application of various global (histogram-derived) threshold methods on the green channel in Figure A2.2(d) (J-D7-20) using ImageJ Tool.

These inconsistencies arise because the embedded fibres, microplastic fragments, saw marks, and surface roughness introduce localised intensity variations that push global thresholds beyond their intended assumptions. When applied to high-resolution images of small specimens, these issues are amplified: small artefacts disproportionately affect pixel distributions, and the histogram no longer reflects the true separation between carbonated and uncarbonated regions.

Section 2A2: Sensitivity analysis

Table A2.2. Difference in effective carbonation radius ($\Delta r_{carbonated}$) and carbonated area fraction ($\Delta f_{carbonated}$) derived from threshold with different correction factor (1.0 – 1.4) to manual threshold counterparts.

	f =1.0		f =1.1		f =1.2		f =1.25		f =1.3		f =1.4	
	$\Delta r_{carbonated}$	$\Delta f_{carbonated}$	$\Delta r_{carbonated}$	$\Delta f_{carbonated}$	$\Delta r_{carbonated}$	$\Delta f_{carbonated}$	$\Delta r_{carbonated}$	$\Delta f_{carbonated}$	$\Delta r_{carbonated}$	$\Delta f_{carbonated}$	$\Delta r_{carbonated}$	$\Delta f_{carbonated}$
SJ-D7-0	0.06	0.01	0.05	0.00	0.02	0.00	0.03	0.02	0.12	0.04	0.69	0.20
SJ-D7-10	2.56	0.37	1.09	0.12	0.40	0.04	0.14	0.01	0.11	0.01	0.77	0.06
SJ-D7-20	0.78	0.08	0.33	0.03	0.04	0.00	0.26	0.02	0.47	0.03	0.96	0.06
SJ-D7-30	1.51	0.15	0.62	0.05	0.18	0.01	0.01	0.00	0.19	0.01	0.59	0.03
SJ-D7-40	1.15	0.09	0.41	0.02	0.08	0.00	0.06	0.00	0.18	0.01	0.47	0.02
SJ-D5-0	0.07	0.02	0.06	0.02	0.03	0.01	0.02	0.01	0.12	0.03	0.79	0.20
SJ-D5-10	1.84	0.19	1.08	0.09	0.60	0.04	0.38	0.02	0.16	0.01	0.41	0.03
SJ-D5-20	2.49	0.31	0.95	0.09	0.10	0.01	0.27	0.02	0.58	0.04	1.21	0.06
SJ-D5-30	1.88	0.16	0.61	0.04	0.02	0.00	0.20	0.01	0.38	0.02	0.74	0.02
SJ-D5-40	1.38	0.06	0.43	0.01	0.16	0.00	0.08	0.00	0.02	0.00	0.10	0.00
SJ-D7-0	0.06	0.02	0.04	0.01	0.01	0.00	0.08	0.02	0.22	0.06	0.96	0.25
SJ-D7-10	1.21	0.13	0.65	0.06	0.27	0.02	0.06	0.00	0.15	0.01	0.75	0.05
SJ-D7-20	0.93	0.09	0.56	0.05	0.28	0.02	0.12	0.01	0.04	0.00	0.55	0.03
SJ-D7-30	0.97	0.06	0.36	0.02	0.11	0.00	0.01	0.00	0.08	0.00	0.31	0.01
SJ-D7-40	1.59	0.06	0.42	0.01	0.17	0.00	0.11	0.00	0.06	0.00	0.01	0.00
SJ-D7-0	0.03	0.01	0.03	0.01	0.01	0.00	0.01	0.00	0.06	0.02	0.57	0.15
SJ-D7-10	2.00	0.21	1.27	0.11	0.67	0.05	0.40	0.03	0.17	0.01	0.30	0.02
SJ-D7-20	1.37	0.09	0.86	0.04	0.57	0.02	0.41	0.01	0.26	0.01	0.06	0.01
SJ-D7-30	1.05	0.04	0.51	0.01	0.28	0.00	0.17	0.00	0.09	0.00	0.05	0.00
SJ-D7-40	0.77	0.03	0.34	0.01	0.12	0.00	0.02	0.00	0.06	0.00	0.21	0.00

References in Appendix 2

Doyle, W. (1962) Operations Useful for Similarity-Invariant Pattern Recognition. *Journal of the ACM (JACM)*. 9 (2), 259–267. doi:10.1145/321119.321123.

Glasbey, C.A. (1993) An Analysis of Histogram-Based Thresholding Algorithms. *CVGIP: Graphical Models and Image Processing*. 55 (6), 532–537. doi:10.1006/CGIP.1993.1040.

Huang, L. & Wang, M.J. (1995) Image thresholding by minimizing the measures of fuzziness. *Pattern Recognition*. 28 (1), 41–51.

Kapur, J.N., Sahoo, P.K. & Wong, A.K.C. (1985) A new method for gray-level picture thresholding using the entropy of the histogram. *Computer Vision, Graphics, and Image Processing*. 29 (3), 273–285. doi:10.1016/0734-189X(85)90125-2.

Kittler, J. & Illingworth, J. (1986) Minimum error thresholding. *Pattern Recognition*. 19 (1), 41–47. doi:10.1016/0031-3203(86)90030-0.

Li, C.H. & Lee, C.K. (1993) Minimum cross entropy thresholding. *Pattern Recognition*. 26 (4), 617–625. doi:10.1016/0031-3203(93)90115-D.

Li, C.H. & Tam, P.K.S. (1998) An iterative algorithm for minimum cross entropy thresholding. *Pattern Recognition Letters*. 19 (8), 771–776. doi:10.1016/S0167-8655(98)00057-9.

Otsu, N. (1979) A Threshold Selection Method from Gray-Level Histograms. *IEEE Trans Syst Man Cybern*. SMC-9 (1), 62–66. doi:10.1109/TSMC.1979.4310076.

Prewitt, J.M.S. & Mendelsohn, M.L. (1966) The analysis of cell images. *Annals of the New York Academy of Sciences*. 128 (3), 1035–1053. doi:10.1111/J.1749-6632.1965.TB11715.X.

Ridler, T.W. & Calvard, S. (1978) Picture thresholding using an iterative selection method. *IEEE Transactions on Systems, Man and Cybernetics*. SMC-8 (8), 630–632. doi:10.1109/TSMC.1978.4310039.

Sezgin, M. & Sankur, B. (2004) Survey over image thresholding techniques and quantitative performance evaluation. *https://doi.org/10.1117/1.1631315*. 13 (1), 146–165. doi:10.1117/1.1631315.

Shanbhag, A.G. (1994) Utilization of Information Measure as a Means of Image Thresholding. *CVGIP: Graphical Models and Image Processing*. 56 (5), 414–419. doi:10.1006/CGIP.1994.1037.

Tsai, W.H. (1985) Moment-preserving thresolding: A new approach. *Computer Vision, Graphics, and Image Processing*. 29 (3), 377–393. doi:10.1016/0734-189X(85)90133-1.

Yen, J.C., Chang, F.J. & Chang, S. (1995) A New Criterion for Automatic Multilevel Thresholding. *IEEE Transactions on Image Processing*. 4 (3), 370–378. doi:10.1109/83.366472.

Zack, G.W., Rogers, W.E. & Latt, S.A. (1977) Automatic measurement of sister chromatid exchange frequency. *The journal of histochemistry and cytochemistry : official journal of the Histochemistry Society*. 25 (7), 741–753. doi:10.1177/25.7.70454.

Appendix 3. Supplementary information on carbonation geometry and phase evolution in yarn-embedded cement pastes

This appendix provides supplementary visual and thermogravimetric data supporting the analysis of carbonation behaviour in cement pastes containing natural fibre yarns. The figures presented here complement the results in Chapter 5.

FigureA3.1 presents a matrix of phenolphthalein-stained cement paste discs containing natural fibre yarns, arranged to show the evolution of carbonation geometry with depth (0–50 mm) and carbonation duration (1, 3, 5, and 7 days) for different yarn types.

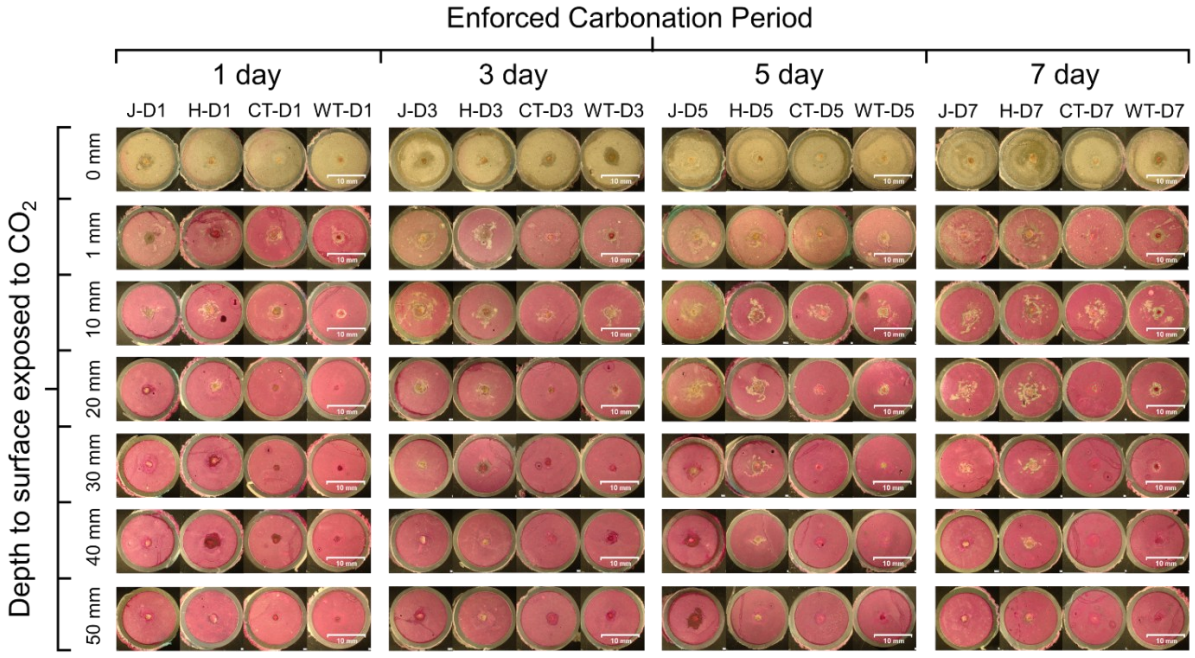


Figure A3.1. Carbonated area geometry of jute (J), hemp (H), thick cotton (CT) and thick wool (WT) embedded samples at 0-50 mm depths after 1, 3, 5, and 7 days of carbonation curing.

Across all fibre types, discs taken close to the CO_2-exposed surface show extensive colourless regions, indicating advanced carbonation, while deeper sections retain a

predominantly pink colour, corresponding to higher alkalinity and lower carbonation extent. With increasing carbonation duration, the colourless regions progressively extend both radially and along the yarn axis, demonstrating the development of depth-dependent carbonation profiles.

Distinct fibre-dependent patterns are evident. Bast fibre yarns (jute and hemp) exhibit broader and less uniform carbonation zones surrounding the yarn, with irregular fronts that persist to greater depths as curing time increases. In contrast, cotton and wool yarns show more localised and compact carbonation regions, typically confined to the immediate vicinity of the yarn and diminishing more rapidly with depth.

At later curing stages (5–7 days), near-surface discs are almost fully carbonated regardless of fibre type, whereas differences between yarns remain visible at intermediate and deeper depths. Overall, the images illustrate that carbonation is strongly depth-dependent and that yarn type influences both the extent and geometry of carbonation fronts, supporting the depth-resolved and fibre-specific analysis presented in the main text.

Figure A3.2 shows TG–DTG curves of reference and hemp-embedded cement paste specimens after 1, 3, 5, and 7 days of enforced carbonation, with measurements taken at depths of 0–50 mm from the CO_2-exposed surface.

Across all curing durations, near-surface discs exhibit larger carbonate-related mass loss than deeper sections, indicating a clear depth-dependent carbonation gradient. Hemp-embedded samples show more pronounced carbonate decomposition peaks than reference samples, particularly at early ages (1–3 days) and shallow depths, consistent with higher CO_2 uptake. With increasing curing time, carbonate-related peaks increase initially and then approach a plateau between 5 and 7 days, reflecting a reduced carbonation rate at later stages.

These trends are consistent with the depth-resolved carbonation patterns observed by phenolphthalein staining (*Figure A3.1*) and image analysis, and indicate that hemp yarn incorporation influences the extent and distribution of carbonation under enforced carbonation conditions.

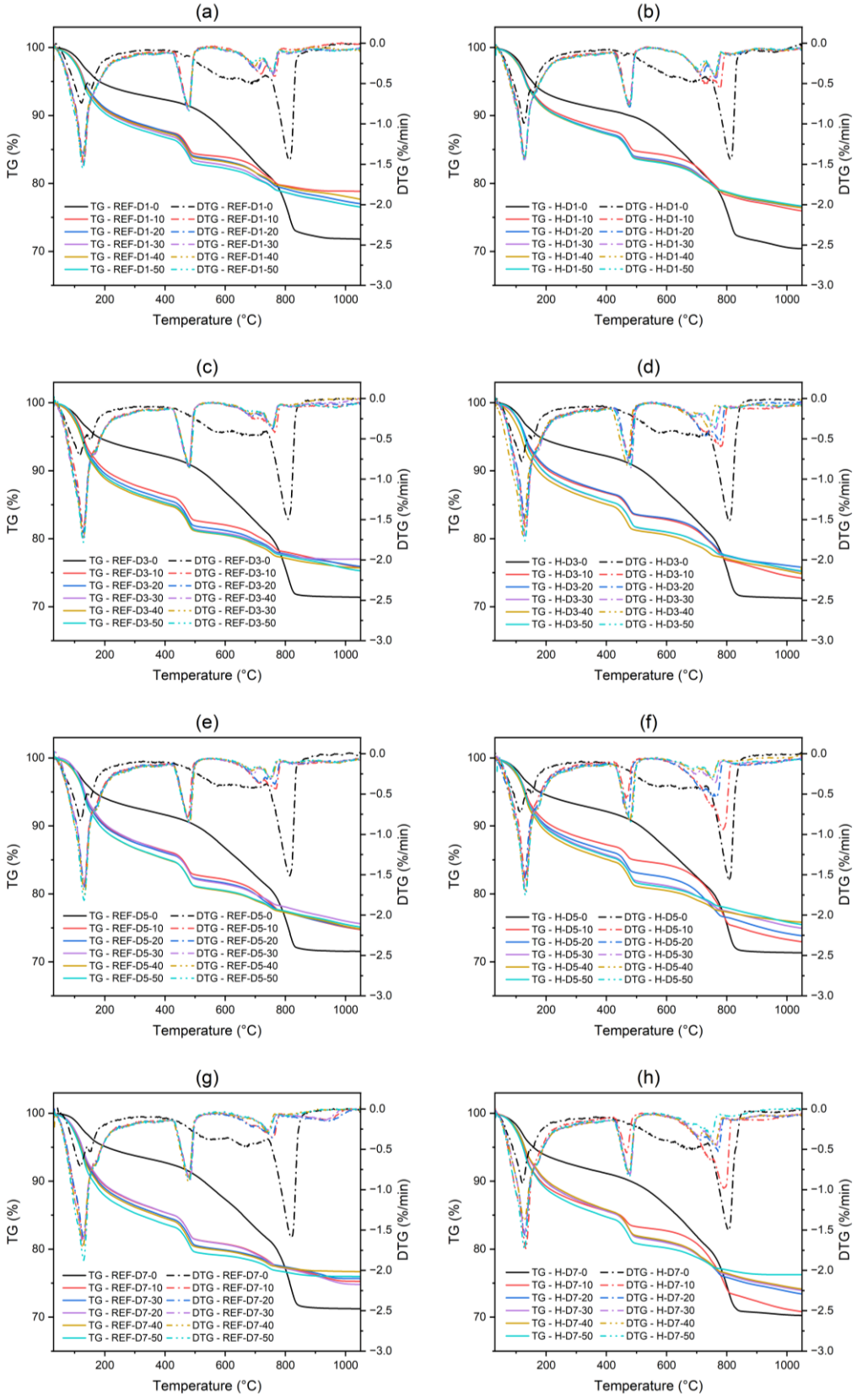


Figure A3.2. TGA-DTG curves of reference and hemp-embedded samples subjected to CO_2 curing for 1,3,5 and 7 days; (a) 1-day carbonation curing on reference sample; (b) 1-day carbonation curing on hemp-embedded sample; (c) 3-day carbonation curing on reference sample; (d) 3-day carbonation curing on hemp-embedded sample; (e) 5-day carbonation curing on reference sample; (f) 5-day carbonation curing on hemp-embedded sample; (g) 7-day carbonation curing on reference sample. (h) 7-day carbonation curing on hemp-embedded sample.

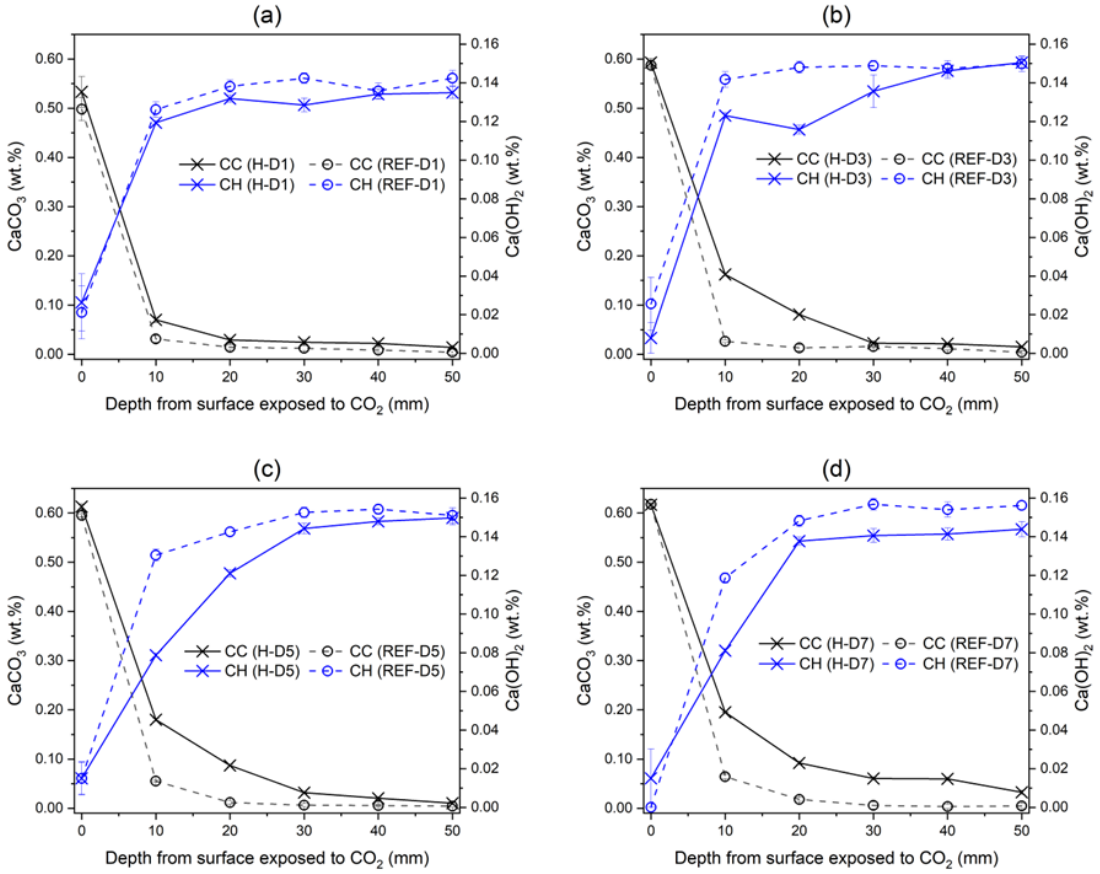


Figure A3.3. Evolution of calcium carbonate (CC) and calcium hydroxide (CH) content of hemp-embedded and reference samples subjected to CO_2 curing for (a) 1, (b) 3, (c) 5, (d) 7 days. The weight percentages are normalised to per gram of anhydrous cement.

Figure A3.3 summarises the changes in calcium carbonate (CC) and calcium hydroxide (CH) contents in both hemp-embedded and reference cement samples subjected to CO_2 curing over 1-7 days of forced carbonation. The weight percentages are normalised to the initial mass of cement (M_{cement}), which is calculated using Equation 3.1. Throughout all curing periods, there was a significant increase in CC content near the surface exposed to CO_2, beginning from 3 days of forced carbonation, with a corresponding decrease in CH. These trends were also observed in the image analysis results shown in *Figure 5.2*.

Figure A3.4 presents representative fluorescence microscopy images of resin-impregnated yarn cross-sections for (a) jute, (b) hemp, (c) cotton, and (d) wool.

Clear differences in yarn internal structure and fibre packing are evident. Jute and hemp yarns show relatively open and heterogeneous fibre arrangements with pronounced inter-fibre voids, whereas cotton and wool yarns exhibit more compact packing and a more uniform distribution of fibres. These differences in internal porosity and packing provide

qualitative context for the distinct carbonation geometries observed around different yarn types in the main text, particularly the broader and more irregular carbonation regions associated with bast fibre yarns.

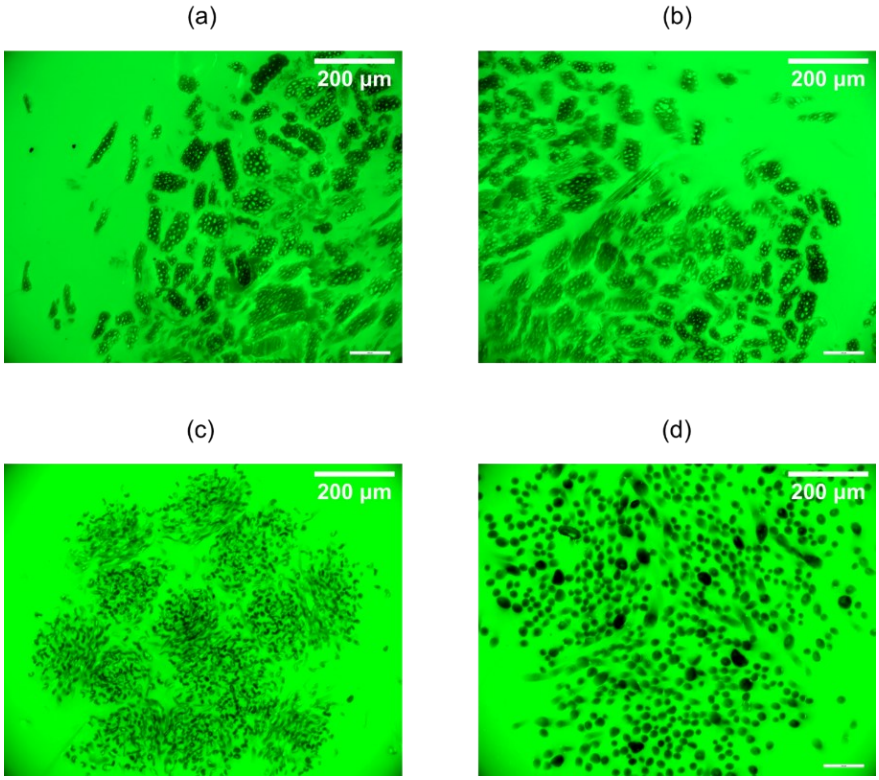


Figure A3.4. Example resin impregnated sample under fluorescence microscopy. (a) jute, (b) hemp, (c) cotton, and (d) wool fibre yarn.

Appendix 4. Supplementary characterisation results supporting carbonation and hydration behaviour of yarn-cement composites

Figure A4.1 shows the normalised heat flow and cumulative heat release profiles for pastes containing oven-dried and pre-saturated yarns. All samples exhibited a single dominant hydration peak between 6–10 hours, typical of C3S hydration. Minor variations were observed: saturated jute (SJ) and acrylic (SA) produced slightly broader, delayed peaks and marginally higher cumulative heat (~304 J/g) than their oven-dried counterparts (~295 J/g). However, these differences were within 3 %, confirming negligible impact of fibre type or moisture state on hydration kinetics.

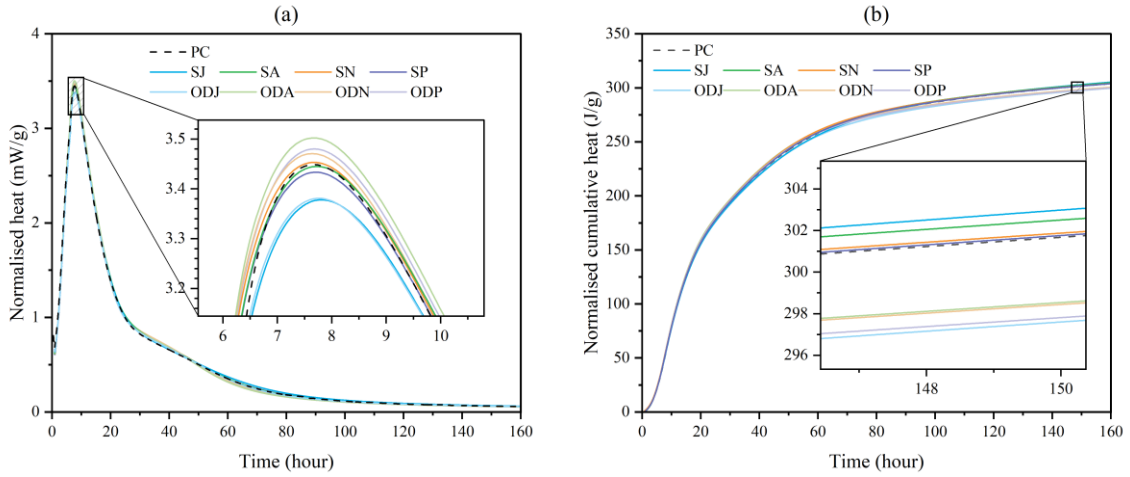


Figure A4.1. Isothermal conduction calorimetry results for pastes containing oven-dried (ODJ, ODN, ODA, ODP) and saturated (SJ, SN, SA, SP) yarns, alongside a paste control (PC). (a) Normalised heat flow curves over 7 days. (b) Normalised cumulative heat release over 7 days.

Thermogravimetric (TG) and derivative thermogravimetric (DTG) analyses were performed to assess portlandite decomposition and carbonate formation in representative yarn–cement composites under air and enforced carbonation curing. Measurements were

conducted for the saturated jute (SJ), oven-dried jute (ODJ), and reference paste (REF) systems at depths of 0–40 mm after 1 and 7 days of exposure. *Figure A4.2* presents the TG–DTG profiles for the SJ composite as a representative example. These results confirm that carbonation proceeds progressively from the CO_2-exposed surface and is most pronounced in moisture-rich systems such as SJ, while the ODJ and REF specimens show comparatively lower carbonate formation and retain stronger CH peaks.

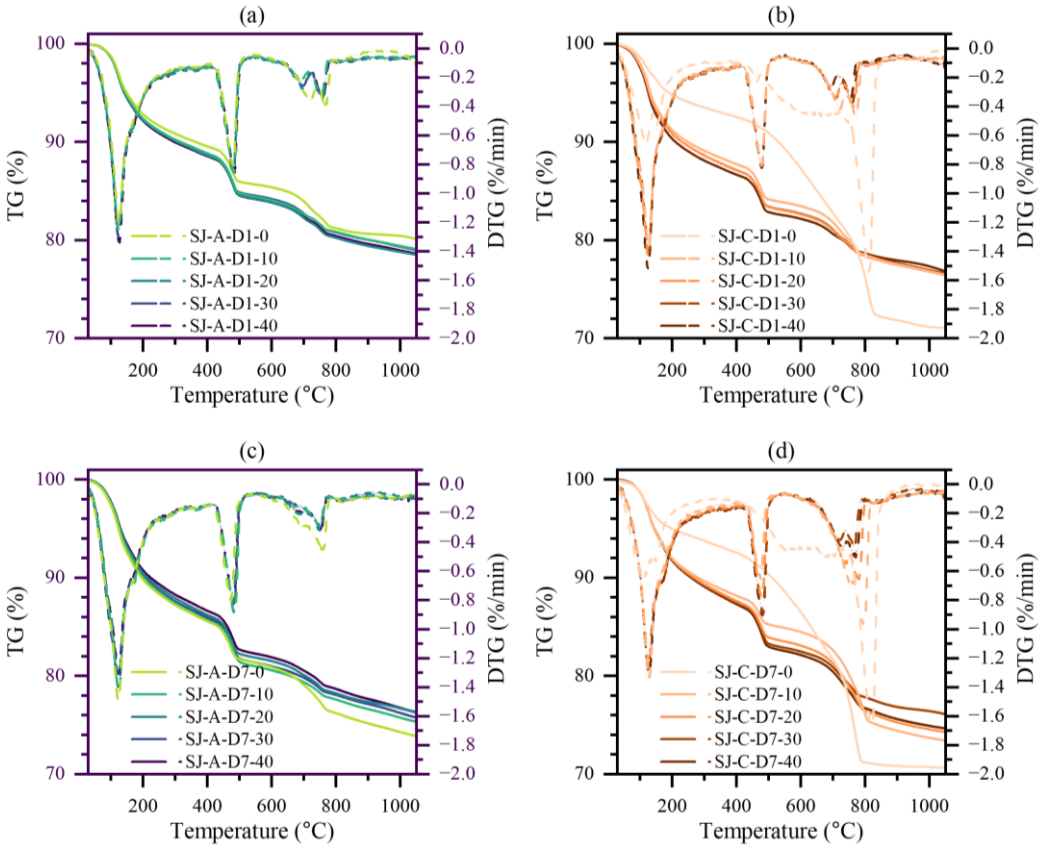


Figure A4.2. Thermogravimetric analysis of selected yarn-cement paste composites. (a–d) TG and DTG curves of saturated jute (SJ) paste at different depths (0–40 mm) under (a) 1-day air curing and (b) 1-day enforced carbonation, (c) 7-day air curing and (d) 7-day carbonation

Quantitative analysis of phase assemblages (*Figure A4.3a–d*) reinforces the trends observed in carbonated area fraction and CO_2 uptake (Section 3.1). At the CO_2-exposed surface (0–1 mm), vaterite accounts for up to 29 wt.% of the total crystalline calcium carbonate formed, indicating early-stage metastable carbonate precipitation under prolonged exposure. However, in deeper sections of the cylinder (e.g., 10–40 mm), vaterite proportions drop to 3–11 wt.%, with calcite becoming increasingly dominant. Among synthetic fibres, nylon was selected as a representative case; its XRD profiles and

quantified phase assemblage closely resemble the reference paste, showing no significant changes in either hydration or carbonation product formation.

Under air curing, the DoH was consistent across systems, varying only slightly between samples: 81.5 % for the reference paste, 84.5 % for saturated jute (SJ), 82.4 % for oven-dried jute (ODJ), and 82.6 % for nylon (N). These values suggest that fibre inclusion at the tested volume fractions exerts only a marginal influence (< 3 %) on bulk hydration. The slightly higher DoH for SJ is attributed to weak internal curing from lumen-retained moisture. Overall, the QXRD results confirm that carbonation in moisture-retentive composites proceeds through progressive portlandite depletion and carbonate accumulation, with phase assemblage trends consistent with the carbonation-to-hydration ratios presented in the main text (*Figure 6.5*).

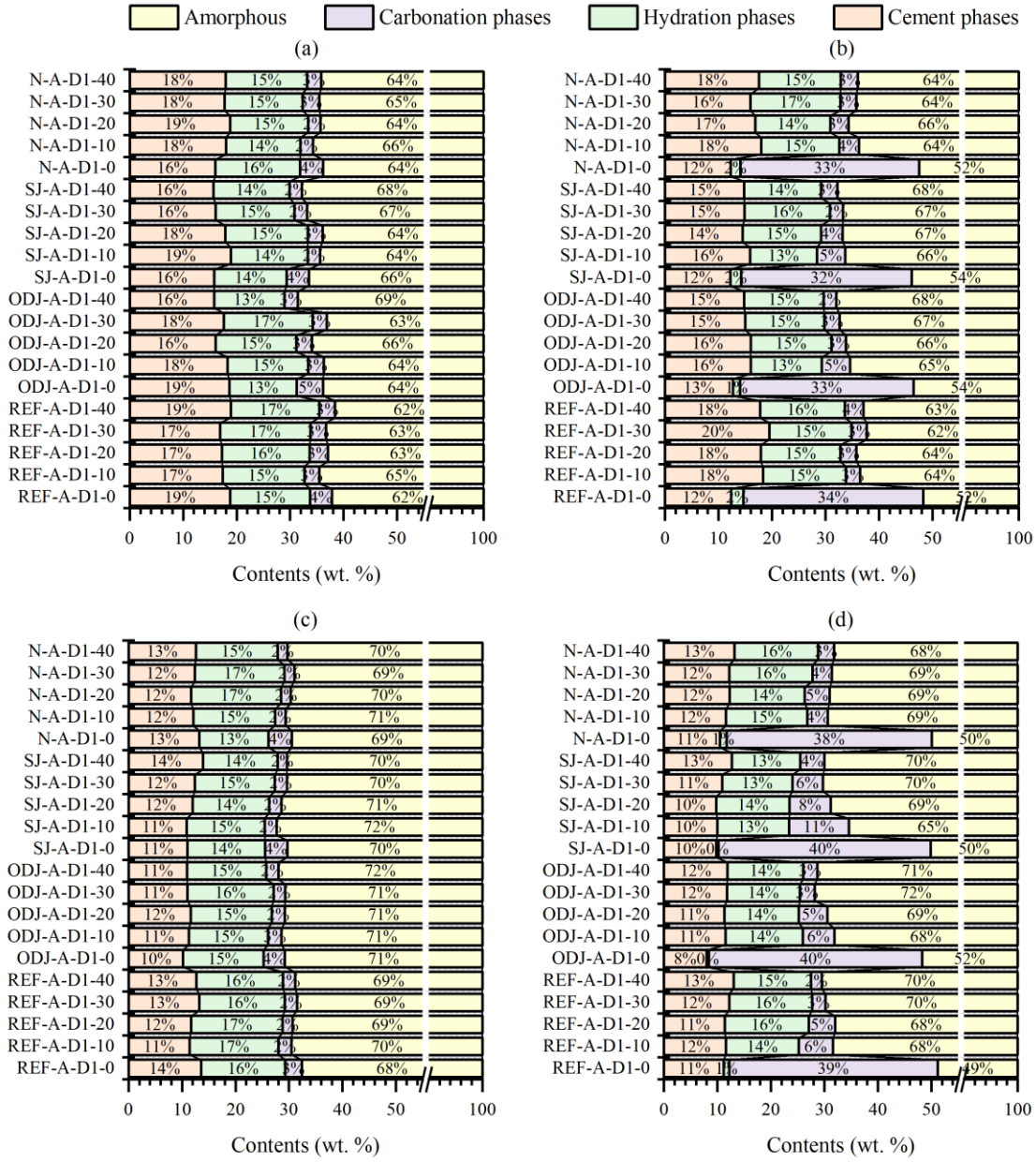


Figure A4.3. Stacked phase assemblages (wt.%) obtained by quantitative XRD of (a) 1-day air-cured; (b) 1-day carbonation cured; (c) 7-day air-cured; (d) 7-day carbonation-cured.

Figure A4.4 presents pore area fraction (μ_p) profiles as a function of depth for air-cured and carbonated specimens after 7 days. The data show that air-cured samples exhibit relatively uniform μ_p across depth and microstructural zones, whereas carbonation curing introduces depth-dependent variations, most notably in regions adjacent to the yarn. Differences between jute- and nylon-containing composites highlight the role of fibre type in modifying local pore structure under carbonation curing.

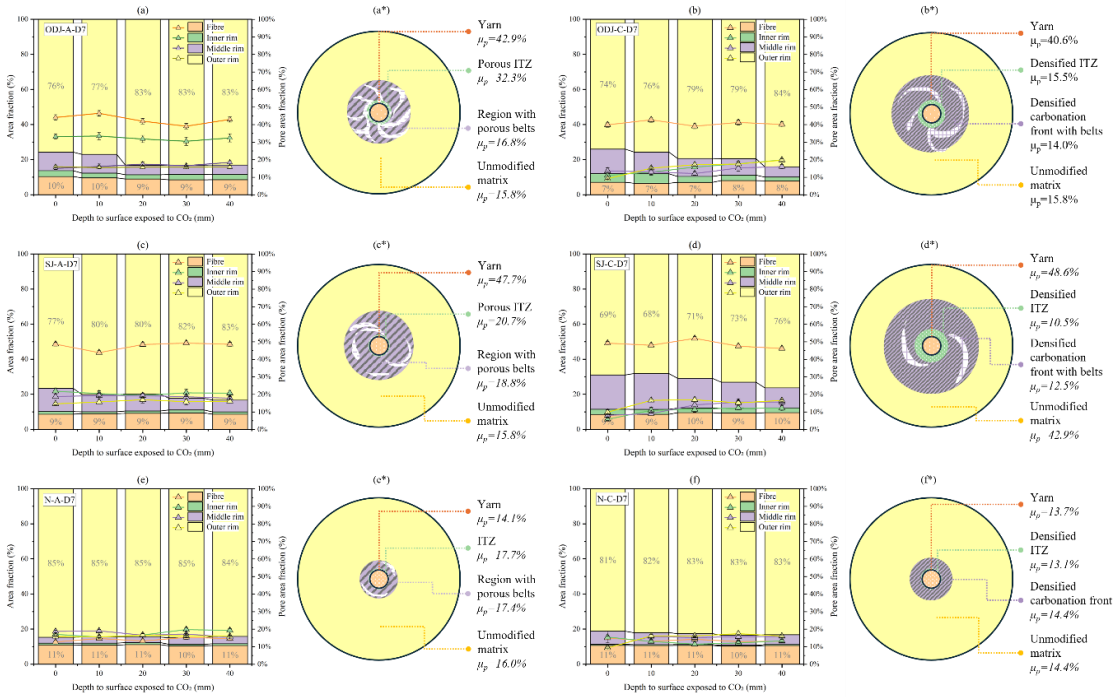


Figure A4.4. Pore area fraction (μ_p) distributions in yarn–cement composites after 7 days of air curing and enforced carbonation. Graphs (a–f) present μ_p (%) as a function of depth (1–41 mm), segmented into four characteristic microstructural zones: yarn (I), inner rim (II), middle rim (III), and outer rim (IV). The left y-axis shows the relative area of each zone (stacked bars), while the right y-axis denotes μ_p within each zone (scatter lines) across depths. Accompanying schematics (a*–f*) illustrate the radial positions of each zone and corresponding average μ_p. Samples include: (a, a*) ODJ-A-D7; (b, b*) ODJ-C-D7; (c, c*) SJ-A-D7; (d, d*) SJ-C-D7; (e, e*) N-A-D7; and (f, f*) N-C-D7.

Appendix 5. Supplementary compressive strength results for yarn-reinforced cement paste cubes

Additional composite configurations with in-plane yarn spacing of 2.5 mm were fabricated to evaluate the effect of very tight mesh geometry on compressive strength and CO_2 uptake (*Figure A5.1*). The preparation procedure followed the same protocol described in Section 7.2.2 of the main text. Due to the high fibre content (> 6 vol.% for 2.5–2L), paste placement and compaction were more difficult, and local air entrapment occurred within the inter-yarn gaps. These specimens were tested under identical curing and loading conditions as the main series.

Given that the effective carbonation radius in all systems was within 2–3 mm (*Figure 6.4*), the 2.5 mm mesh spacing approaches the limit where carbonation fronts from adjacent yarns overlap. As a result, these geometries offer little differentiation in CO_2 transport behaviour and were excluded from further analysis in the main text.

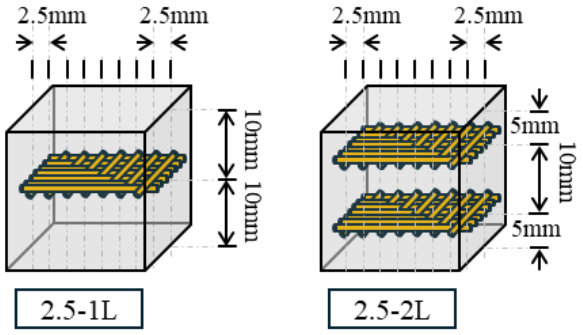


Figure A5.1. Schematic illustration of the additional 2.5 mm mesh configurations used to assess the influence of extreme yarn spacing on fibre volume and mechanical response.

Table A5.1 summarises the compressive strength of yarn–cement composites subjected to air curing and enforced carbonation for 1, 3, and 7 days across all mesh configurations. The data provide a complete overview of early-age strength evolution prior to any post-curing treatment.

Table A5.1. Compressive strength of yarn–cement composites under air and carbonation curing at 1, 3, and 7 days for all mesh configurations.

Fibre type	Mesh	Compressive strength/mPa															
		Air curing								Carbonation curing							
		1-d			3-d			7-d			1-d			3-d			7-d	
ODJ	10-1L	42.0	±	2.39	57.7	±	1.28	65.8	±	3.14	60.4	±	2.50	67.8	±	7.49	77.6	±	4.80
	5-1L	39.9	±	3.09	47.4	±	4.39	57.0	±	3.24	50.2	±	5.25	60.2	±	5.84	75.3	±	6.50
	2.5-1L	44.5	±	3.37	38.7	±	3.37	45.5	±	6.69	43.8	±	6.04	53.1	±	1.08	56.8	±	11.1
	10-2L	38.7	±	2.81	48.2	±	1.39	53.9	±	6.50	44.2	±	5.30	64.1	±	3.51	63.5	±	7.46
	5-2L	30.2	±	0.892	38.7	±	1.81	41.8	±	1.20	37.1	±	5.22	51.7	±	3.12	52.4	±	2.09
	2.5-2L	30.5	±	1.34	31.2	±	2.09	39.4	±	4.61	32.3	±	2.08	45.5	±	1.92	43.2	±	9.14
	10-3L	37.8	±	3.57	37.9	±	3.84	50.8	±	10.30	43.5	±	1.17	54.1	±	4.90	60.6	±	6.81
	5-3L	20.8	±	1.17	28.8	±	3.27	32.7	±	0.752	34.9	±	2.67	39.0	±	1.05	39.4	±	1.07
SJ	10-1L	44.0	±	3.23	51.2	±	2.36	57.8	±	7.96	55.3	±	0.807	64.2	±	7.98	80.1	±	5.46
	5-1L	41.1	±	2.71	41.9	±	2.36	40.5	±	4.51	37.9	±	1.47	65.2	±	6.93	75.2	±	7.79
	2.5-1L	29.2	±	5.33	33.0	±	6.13	38.2	±	7.89	38.4	±	1.41	52.9	±	2.87	57.6	±	4.81
	10-2L	35.9	±	5.02	45.9	±	1.91	46.3	±	7.41	45.1	±	1.98	49.4	±	10.1	61.0	±	4.93
	5-2L	29.1	±	5.67	30.5	±	4.60	42.7	±	3.06	36.7	±	2.37	44.9	±	4.28	55.4	±	2.26
	2.5-2L	31.7	±	4.26	18.7	±	2.06	18.7	±	2.52	27.1	±	4.33	27.4	±	6.83	36.9	±	9.65
	10-3L	37.3	±	2.61	47.2	±	1.49	42.3	±	2.49	50.7	±	0.53	54.9	±	3.22	56.1	±	6.68
	5-3L	20.7	±	0.496	30.7	±	2.36	33.9	±	1.23	36.3	±	3.09	42.0	±	2.93	43.1	±	2.97
N	10-1L	46.8	±	1.14	51.4	±	2.79	59.6	±	1.16	45.8	±	6.65	73.2	±	6.96	77.2	±	5.46
	5-1L	45.5	±	3.17	55.0	±	1.09	61.3	±	4.74	50.5	±	3.17	63.5	±	5.16	75.7	±	2.34
	2.5-1L	31.3	±	3.88	41.8	±	0.95	48.1	±	4.90	42.9	±	5.17	49.6	±	2.56	66.4	±	3.94
	10-2L	31.1	±	0.438	47.8	±	6.85	55.5	±	4.47	37.6	±	3.92	65.1	±	3.96	58.1	±	4.47
	5-2L	34.7	±	7.07	36.8	±	10.2	52.2	±	1.64	48.7	±	2.80	45.7	±	8.14	55.5	±	6.89
	2.5-2L	32.4	±	2.89	28.1	±	2.98	46.9	±	2.68	32.9	±	1.76	35.9	±	4.47	42.2	±	7.51
	10-3L	34.9	±	0.873	53.1	±	1.06	46.0	±	3.91	47.6	±	0.785	52.1	±	1.00	64.7	±	2.62
	5-3L	33.2	±	2.18	36.9	±	1.50	36.5	±	4.69	38.3	±	1.52	39.8	±	1.50	41.3	±	4.97